Hierarchical structures of aligned carbon nanotubes as low-density energy-dissipative materials

Thesis by

Jordan R. Raney

In Partial Fulfillment of the Requirements

for the Degree of

Doctor of Philosophy

California Institute of Technology

Pasadena, California

2012

(Defended March 5, 2012)

To those who depend on me, and to those on whom I depend.

Acknowledgments

This work would not have been possible without the efforts, guidance, friendship, and support of many people, inside and outside of Caltech.

Professionally, I foremost must acknowledge and thank my advisor, Professor Chiara Daraio. Through her patient mentoring she has helped me to become a better researcher. In addition to this role as a research advisor, she has also shared much wisdom about life in the academic world—through her words, but more importantly through her consistent, impeccably professional example each day. I also thank all of the members of the Daraio group for their helpful comments about my research over the last few years.

Thanks also to the members of my dissertation committee, Prof. William L. Johnson, Prof. Kaushik Bhattacharya, and Prof. Guruswami Ravichandran, for their willingness to serve in this capacity, and for their helpful comments to improve this work. I am also grateful to Professor Ravichandran for his professional guidance and support, in addition to his role on the committee.

I am grateful to Professor Abha Misra, now of the Indian Institute of Science (Bangalore), who was a post-doc in the group when I first joined. Several of the practical laboratory procedures that were vital to the research contained herein were initially developed by her efforts. Additionally I thank Professor Luigi de Nardo, from Politecnico di Milano, who was a visiting researcher in the group when I joined. He taught me much about practical experimental issues. Thanks also go to Professor Jinkyu Yang, a former post-doc in the group and now of the University of South Carolina, for his patient support related to the dynamic experiments used here as well as for his professional advice.

I am indebted to Professor Fernando Fraternali of the University of Salerno for sharing his deep knowledge as well as for his professional advice. He and several of his students (Ada Amendola, Lucia Senatore, and Ilenia Farina) also displayed enormous personal generosity toward us when my family and I visited southern Italy and the University of Salerno. We are grateful to them for facilitating a time there that was satisfying professionally and personally, and grateful to the University of Salerno's Department of Civil Engineering for the invitation and hospitality.

In addition to those already named, I thank the other talented individuals who have contributed in vital ways to the work presented here. This includes Anna E. Craig, Ludovica Lattanzi, Ada Amendola, Richard Y. Wang, Dr. Thomas Blesgen, Dr. Hong-Li Zhang, and Prof. Daniel E. Morse. I have enjoyed working with each and hope our joint efforts can continue in the future.

My time and research at Caltech have been graciously supported by a few organizations and grants that I want to gratefully acknowledge here. My first year of study was supported by an L.S. Clark Fellowship awarded by Caltech. Subsequent work was supported by the Army Research Office and U.S. Department of Defense by way of a National Defense Science & Engineering Graduate (NDSEG) Fellowship, with costs associated with research materials supported by the Institute for Collaborative Biotechnologies, under contract W911NF-09-D-0001 with the Army Research Office. I am also grateful to the California Institute of Technology and the John and Ursula Kanel Charitable Foundation for an additional generous scholarship that proved to be an enormous help.

I also thank the administrative personnel for their ample logistical support during my time at Caltech. This especially includes Christy Jenstad and Pam Albertson in the Materials Science Option and Jennifer Stevenson, Dimity Nelson, and Denise Ruiz in Aerospace. I also thank the support from the Graduate Studies Office and the impressively efficient Office of the Registrar.

The California Institute of Technology is truly a special place. My time here has been extremely fulfilling, and I hope that the Institute is forever able to continue in its capacity as the greatest academic institution of scientific research on the face of

the planet (which I say in all seriousness).

On a more personal level, I will be forever grateful for the years of love, support, and prayer from my parents, Les and Joelle Raney. Becoming a parent during my time at Caltech has given me a deeper understanding of the love that one has for a child, and has deepened my appreciation even more for their sacrifices on my behalf and on that of my brothers. They have provided a wonderful example to follow, as their parents provided to them. I am therefore also grateful for the faithful lives of my grandparents, Floyd and Maxine Brown and Robert and Dorothy Raney, all of whom have now passed, and for Erma Raney, who has provided a grandmother's love and care.

Additionally, I am infinitely grateful to the guys who, before I even came to Caltech, were there in the darkest times, the quality of friends and band of brothers that everyone should have. Indirectly, it is their support that allowed me to ever even make it to Caltech to begin the work presented here. Two of these men are in fact my brothers—Chad and Kyle Raney—their selflessness and encouragement over many years has sustained me through all challenges. The others became brothers by, at various times and in various ways, fighting the fight on my behalf when I had given up: Tom Kidd, Chris Hill, Erik Tisthammer, and Mike Mellema. God is gracious to have provided such as these.

I am forever grateful for all of the people who, prior to my time at Caltech, believed in me when I didn't, encouraging me to put one foot in front of the other, to continue the march forward even when the path seemed tortuous or meaningless. Others shared words and wisdom that I needed to hear at vital points along the path, with Fr. Alan Crippen and Dr. Bob Osburn springing immediately to mind. Such conversations gave light and hope. Eventually the path itself transitioned from what seemed like a journey through a thick jungle to a peaceful walk through hills, pastures, and hamlets, in a land where a good Shepherd King reigns. The burden is easy and the yoke is light.

Of all people on earth I most thank my wife, Carolyn. She possesses the gift of encouragement, among many other gifts. She has the rare courage to take a different

road than most, and inspires by her selflessness. She has been a continual source of life and joy to me, reminding me each day why we're doing what we're doing. None of this work would have occurred without her, as her companionship has proven prerequisite to any endeavor I begin. I am also grateful to our children Daniel and Catherine who have brought much joy (and a healthy impetus toward graduating from life as a student).

With a humble and grateful heart I praise God for providing all that was necessary and more for this effort.

Abstract

Carbon nanotubes (CNTs) are known to have remarkable properties, such as a specific strength two orders of magnitude higher than that of steel. It has remained a challenge, however, to achieve useful bulk properties from CNTs. Toward that goal, here we develop low-density bulk materials (0.1–0.4 g cm^{-3}) entirely or nearly entirely from CNTs. These consist of nominally-aligned arrays of CNTs that display a dissipative compressive response, with a notable stress-strain hysteresis. The compressive properties of CNT arrays are examined in detail. This analysis reveals interesting features in the mechanical response, such as strain localization (resulting from a gradient in physical properties along the height), recovery after compression, non-linear viscoelasticity, and behavior under repeated compression that depends on the strain of previous cycles (similar to the Mullins effect in rubbers). We observe that in compression the energy dissipation of these materials is more than 200 times that of polymeric foams of comparable density.

Next, materials based on CNT arrays are studied as exemplary of hierarchical materials (materials with distinct structure at multiple length scales). Hierarchical materials have pushed the limits of traditional material tradeoffs (e.g., the typical trend that increased strength requires increased weight). Techniques are developed to separately vary the structure of CNT arrays at nanometer, micrometer, and millimeter length scales, and the effects on the bulk material response are examined. Structure can be modified during CNT synthesis, such as by varying the composition of the flow gas or by manipulating the input rate of chemical precursors; it can also be modified post-synthesis, e.g., by the *in situ* synthesis of nanoparticles in the interstices of the CNT arrays or by the assembly of multilayer structures of multiple CNT arrays

connected by polymeric or metallic interlayers.

Finally, a mathematical model is applied to capture the complexities of the mechanical response. This one-dimensional, multiscale, bistable spring model is able to match the global stress-strain response as well as local effects such as strain localization and Mullins-like behavior. A technique is developed to reliably discern the model's material parameters based on *in situ* optical data from the experiments.

Contents

List of Figures

List of Tables

Chapter 1

Introduction

1.1 Goals and objectives

Material selection for almost any application involves tradeoffs between a beneficial quality (e.g., increased material strength) and an undesirable property (e.g., increased weight). Recently, hierarchical materials have been developed that push the limits of these traditional tradeoffs, giving increases in beneficial material qualities with minimal increases in accompanying negative material qualities. Hence, techniques to control structure at multiple length scales have received increasing interest among researchers.

Of course, in addition to understanding how nano/micro structure affects bulk properties, one must choose wisely the material that is to be structured. The remarkable characteristics of carbon nanotubes (CNTs) have long been known (the specific strength, or strength-to-weight ratio, is more than two orders of magnitude greater than that of steel, as a prime example) [1], making them a potentially excellent starting point from which to design novel materials. However, it has proven a challenge to obtain a semblance of the excellent characteristics of individual CNTs in bulk scale materials. A variety of approaches have been taken to achieve macroscopic benefits from CNTs, and this work is a contribution toward that same end.

This effort is therefore intended to have twofold relevance. At an applied level, it is hoped that this work will contribute toward the design of materials that benefit from CNTs at bulk scales. At a more fundamental level, this effort is also intended to

contribute toward the scientific goal of better understanding how structure at multiple length scales affects bulk material properties.

Specific goals include the following:

- To characterize the mechanical properties of CNT arrays.
- To contribute to an improved understanding of the mechanisms responsible for the dissipative response of CNT arrays in compression.
- To design new processes to tailor the properties of CNTs and CNT arrays.
- To elucidate process-structure-property relationships as they relate to materials based on CNT arrays.

1.2 Overview of dissertation

The remainder of this chapter represents a general introduction to CNTs and structures of CNTs. This will lay the foundation for Chapter 2, which will discuss the mechanical properties of CNT arrays in their as-synthesized state, as well as discuss the common experimental approaches used throughout this dissertation. Once the mechanics of conventional CNT arrays is discussed, two chapters will follow that discuss different ways in which the structure and thereby the properties of CNT arrays can be tailored. The first of these chapters, Chapter 3, discusses techniques to tailor properties by controlling parameters *in situ* during CNT synthesis. Chapter 4 follows with a discussion of tuning the properties of CNT arrays after CNT synthesis is complete.

Chapter 5 follows, discussing the creation of multilayer structures of CNT arrays, introducing a new level of structural hierarchy. Chapter 5 deals with multiple layers of CNT arrays connected with polymer interlayers (Section 6.3 undertakes a related discussion about multilayer CNT array structures connected by copper foil interlayers). Chapter 6 introduces our use of a one-dimensional model based on elements with bistable potentials connected in series, and explains a procedure to identify the

material parameters for the model based on *in situ* experimental observations. We show that this model succeeds in capturing both the global stress-strain response of the material as well as the strain localization that arises due to inhomogeneities in the structures. Finally, a concluding chapter (Chapter 7) summarizes the present work and introduces a few possible avenues for future extensions of it. (Appendix A, based on a recent collaborative effort, provides additional mathematical details about the model that we employ in Chapter 6, especially regarding the extension of the model that is discussed in Section 6.2. The main themes of the dissertation can be understood without the details of Appendix A, but it is included for the sake of completeness and for the interested reader.)

The techniques described herein can be used to separately vary the structure of CNT arrays at nanometer, micrometer, and millimeter length scales. To illustrate the control over structural hierarchy, the top left panel in Figure 1.1 shows a multilayer structure, similar to those constructed in Chapter 5 and Section 6.3, consisting of four different CNT arrays. This figure serves as a useful summary of the structural hierarchy in these materials, and also as a graphical table of contents for the experimental processes developed to control that structure (i.e., Chapters 3 to 6).

The procedures discussed in Chapter 3 affect two levels of hierarchy and illustrate the importance of synthesis conditions to the resulting CNT properties. Section 3.1, corresponding to the bottom right panel in Figure 1.1, specifically discusses the role of H_2 gas in affecting changes in CNT diameter (by changing the number of CNT walls) and the resulting mechanical properties of CNT arrays. Section 3.2, corresponding to the top right panel of Figure 1.1, is a study of the tailoring of strain localization and the compressive response of CNT arrays by synthesizing them with microscale heterogeneities (in density and alignment) during the growth process. Chapter 4 discusses the modification of CNT arrays after synthesis by the *in situ* synthesis of metal oxide particles on the surfaces of individual CNTs, corresponding to the bottom left panel of Figure 1.1. Chapter 5 and Section 6.3 are studies of multilayer CNT foams in which multiple CNT arrays have been connected via polymeric or metallic interlayers, respectively, with an example of a multilayer structure in the top

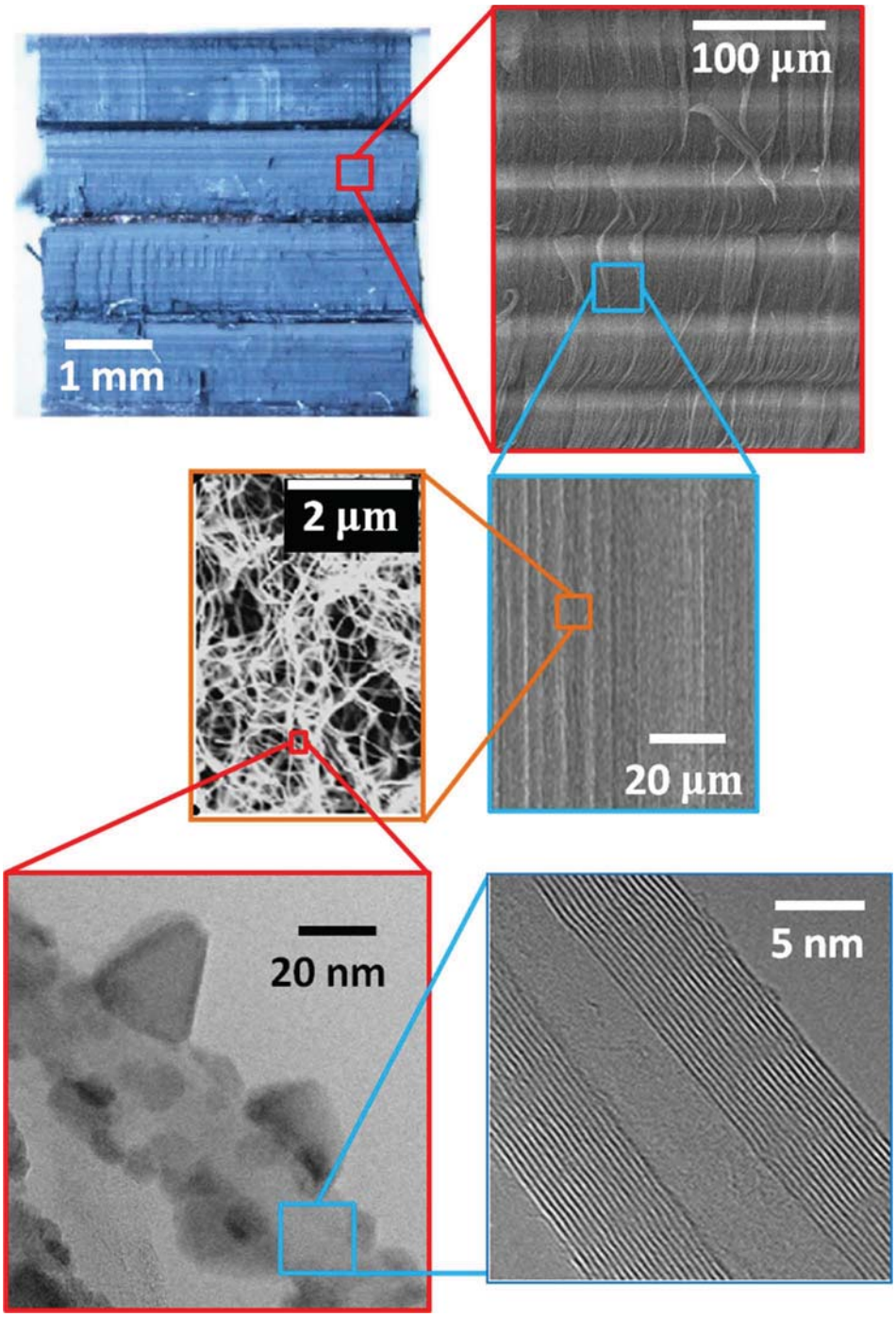

Figure 1.1: Structural hierarchy in multilayer carbon nanotube-based materials, depicting the control of structure from nanometer to millimeter length scales based on the several processes discussed in this dissertation

left of Figure 1.1.

Together these procedures allow the bulk density of the material to be tuned by

almost an order of magnitude and certain compressive mechanical properties such as energy dissipation to be tuned by over a factor of 40. Additionally, these procedures allow for the control of the density distribution along the height of the material, resulting in controlled strain localization (at both the microscale and macroscale) and energy dissipation. Thus the several processes developed here control structure, and the structure controls the bulk properties. It is intended that this traditional interest of materials science—the relationships between synthesis process, structure, and properties—contributes to an understanding of a non-traditional material.

Each of these chapters is a discussion of some facet of the general problem of the construction of lightweight, energy-dissipative materials based on aligned arrays of CNTs. Most of these chapters, or their constitutive sections, have been, or are in the process of becoming, published as stand-alone papers. Each chapter therefore can be read independently, and includes a brief introduction that goes into more detail about the particular problem being addressed.

1.3 Carbon nanotubes

Though the history of carbon nanotube (CNT) synthesis extends back farther than 1991 (see [2, 3]), it was the paper by Iijima of that year [4] that sparked the flurry of research that has followed on the topic in the years since. A CNT can be thought of as a hollow cylindrical fullerene made up, in its perfect form, entirely of sp^2-bonded carbon atoms. In appearance, a perfect CNT can be pictured as a sheet of graphene that is rolled into a cylinder (though CNT synthesis is entirely different). In actuality, CNTs deviate from this ideal picture, becoming collapsed when energetically favorable [5], dynamically deviating from a non-circular cross section due to the influence of other CNTs [6], or exhibiting a number of defects [7] (which are often characterized via Raman spectroscopy [8]).

Just as a CNT can be pictured as a rolled-up sheet of graphene, which is made entirely of hexagonally-patterned carbon atoms, the symmetry axis of the cylinder can have any number of orientations with respect to those hexagons in the 2D plane.

This orientation is referred to as a CNT's chirality, and has enormous impact on some of its physical properties (see the extensive discussion by Dresselhaus et al. [9]). Most noteworthy, chirality determines whether a CNT is electrically conducting or semiconducting [10]. It also affects mechanical properties such as Young's modulus and the Poisson ratio (with these effects being particularly noticeable for narrow-diameter CNTs [11]) but such effects are of much smaller magnitude relative to the effects on electrical properties [12].

CNTs are often observed to exist in multi-wall form, in which a large number of cylinders are ordered concentrically. In ideal form, in which the CNTs would not have defects, the shear strength between adjacent walls is remarkably low (around 0.08–0.3 MPa) [13]. This is because adjacent CNT walls only interact via van der Waals interactions except in the case of defect-related bridging from wall to wall (e.g., via an sp^3 covalent bond).

Interwall spacing in multi-wall CNTs is typically about 0.34 nm, but can be up to 10% higher than this, depending on diameter and the number of walls [13]. This is related to the fact that the strain energy of a CNT is proportional to the inverse square of the diameter [13]. In fact, this sets a lower limit on CNT diameter at roughly 0.5 nm, as the strain energy for CNTs of smaller diameter than that would exceed that of the chemical bonds [14]. Because of these large changes in strain energy, CNT reactivity, which is typically very low as a result of the stable conjugated sp^2 bonds that they are made of, is a function of diameter as well as of mechanical deformation [15].

The electrical, thermal, and mechanical properties of individual CNTs are remarkable. For example, the tensile strength of a CNT wall is 100 times greater than aluminum and the Young's modulus is approximately 1 TPa [13]. CNTs can be thermally stable up to approximately 3000 K in vacuum [16]. As mentioned above, they have excellent thermal (3000–6000 W m^{-1} K^{-1}) [17, 18] and electrical conductivity (up to 1000 times the electrical conductivity of copper) [9]. The low density of CNTs also gives them an advantageous specific strength relative to other materials. For example, CNTs are 100 times stronger than steel but have one sixth of the weight

(these numbers depend on the size and number of walls of the CNTs) [19]. Thus, there is no doubt that CNTs have outstanding properties—the challenge is in being able to utilize them in such a way that some of those outstanding properties can be realized in macroscopic systems.

1.3.1 Synthesis of carbon nanotubes

There are a number of ways to synthesize CNTs, which developed rapidly following Iijima's 1991 paper [4]. Besides the arc discharge method that Iijima used, others have synthesized CNTs typically via laser ablation (see, e.g., [20]) or chemical vapor deposition (CVD), which can be either of the plasma-enhanced variety (e.g., [21]) or be merely thermal based. Thermal CVD, in particular, has received much attention for the ease with which large quantities of aligned CNTs are synthesized (and is also deemed the most likely of current approaches to be amenable to industrial mass-production [22]). For this reason, the remainder of the discussion of CNT synthesis in this dissertation will be specific to thermal CVD.

Certain metals, namely Fe, Co, and Ni, were for some time known to catalyze graphitic carbon in thermal CVD systems [23]. It had been observed that if a flow of certain types of hydrocarbons (acetylene, ethylene, etc.) was passed over a thin film of one of these metals in a CVD furnace at sufficient temperatures, that planar layers of graphitic carbon would be formed. Sinnott et al. identified three necessary features of the metal in order for it to lead to these graphitic layers [23]: first, it must have good catalytic activity for the initial breaking down of the hydrocarbon source into simpler carbon compounds; second, it must be able to form metastable carbides; finally, it must allow rapid diffusion of carbon into its interior. Eventually this interior buildup leads to the precipitation of carbon in graphitic form, and if the metal "catalyst" is of the right shape (i.e., particulate and of diameter $\sim$ 1–50 nm) it can lead to continuous precipitation in tubular form [23].

For the purpose of synthesizing CNTs, the metal catalyst can be either deposited as a thin film on an appropriate substrate prior to placing the substrate in the furnace

(referred to as the "fixed" or "pre-deposited" catalyst approach), or it can be deposited during synthesis (the "vapor phase", "floating", or "continuous" catalyst approach). In the former case, the thin-film catalyst must be broken up into nanoparticles for CNT growth to take place (as per the discussion above). This is usually controlled by a combination of gas composition, "pre-treatment" time (i.e., the flow of some gas combination prior to flowing hydrocarbons into the furnace), and/or temperature (see, for example, the work by Nessim et al. [24]). Though the deposition of the catalytic thin film adds an extra step, this approach can result in very pure CNTs and generally gives additional control of the ultimate CNT morphology (e.g., the catalyst film thickness is a significant contributor to determining CNT diameter [21] and number of walls [25]). In contrast, the vapor-phase approach (see, e.g., the work by Andrews et al. [26] and the diagram in Figure 1.2) has the fewest steps but also less purity than CNTs synthesized by fixed catalyst (it also has a few additional features, however, as will be discussed in Chapter 2 and elsewhere). This approach is usually accomplished by using metallocenes as metal precursors. These compounds are comprised of a metal atom sandwiched between two aromatic rings. Metallocenes generally decompose at temperatures less than 500 °C [27], at which point the metal atom is free. These atoms must congregate to form islands large enough to initiate CNT growth. (CNTs can also be synthesized in thermal CVD systems by using a powdered catalyst [22], however this results in disordered, entangled CNTs rather than the nominally aligned systems desired for this study; the powdered approach will therefore not be discussed further.) Most of the discussion in this work will focus on CNTs that have been synthesized by the vapor-phase approach, but the fixed-catalyst approach will be discussed in contrast occasionally, as there are significant differences in morphology and various physical properties of the CNTs that result.

Both the fixed- and vapor-phase catalyst approaches require careful tuning of the synthesis parameters, such as substrate, gas composition, gas flow rate, temperature, etc. (which, when properly tuned, result in arrays of aligned CNTs, oriented normal to the substrate surface). While early CNT researchers were faced with these many parameters as obstacles to successful CNT synthesis, the hundreds of research pa-

pers that they have generated on this topic in the last two decades now allow these parameters to be thought of as opportunities for tunability. Though there are still some disagreements about the effects of certain parameters, there is now a detailed understanding about how most affect CNT morphology and properties, allowing the synthesis of customizable CNTs within well-defined limits. In this section, the effects of some of these parameters will be briefly discussed in turn.

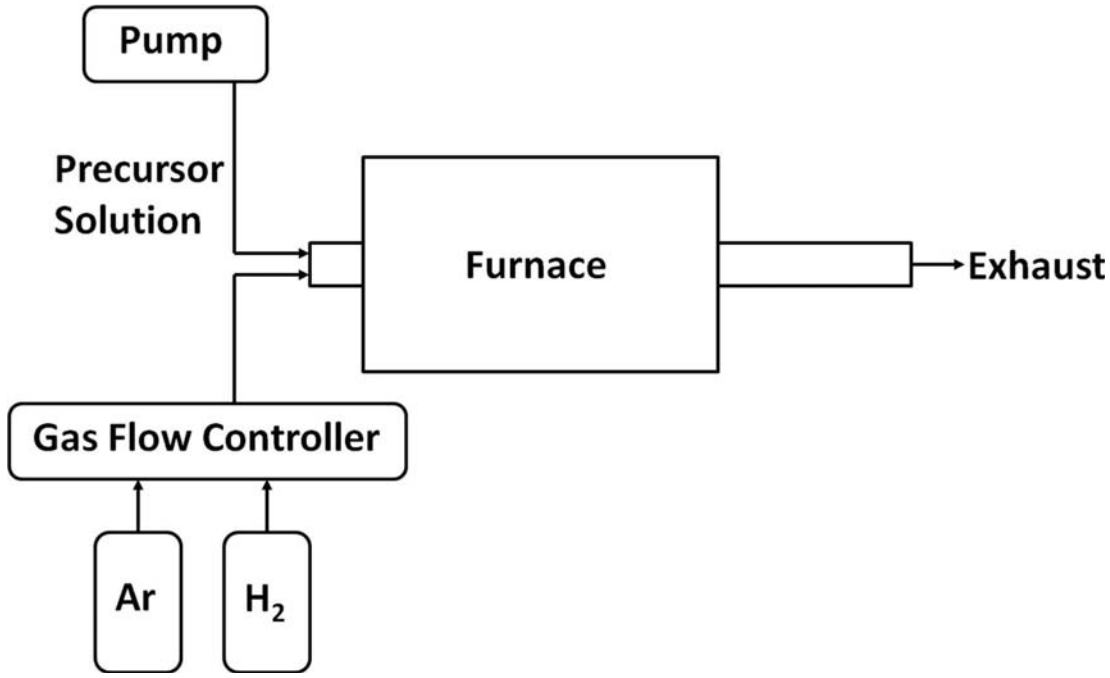

Figure 1.2: Experimental setup for the synthesis of carbon nanotube array samples

As mentioned above, metallocenes are typically used in vapor-phase catalyst systems. Most frequently, ferrocene is used for this purpose, consisting of an iron atom between two five-member aromatic rings of carbon [26]. Some have studied the use of substituted versions of ferrocene, with other compounds attached to the carbon rings, however it has been observed that the concentration of the ferrocene (or ferrocene-like compound) matters more than its detailed chemical structure [28] since the rings become pyrolyzed prior to reaching the substrate anyway. What matters most strongly is the quantity of metallocene and the choice of metal atom in the metallocene, not the structure of the aromatic rings. Since many standard cyclic aromatic hydrocar-

bons exist in liquid form at room temperature (e.g., benzene, xylene, and toluene), interact strongly with metallocenes, and act as carbon precursors for CNT growth, metallocenes are frequently dissolved in these prior to CNT growth. These solutions can then be injected into the furnace as a complete source for both catalyst and carbon, removing the need for hydrocarbon gases. The earliest groups typically used xylene for this type of CNT synthesis [26], though we have chosen to use toluene as it has been shown to result in a somewhat higher CNT yield [29].

In both the fixed-catalyst and vapor-phase approaches CNT synthesis takes place on a support substrate. In common practice, such substrates have been silicon-based, taking advantage of the low cost of such materials. There are notable exceptions, involving the direct synthesis of CNTs on other materials such as graphitic foams [30] or metallic surfaces [31]. However, the literature has focused on CNTs synthesized on Si-based materials, which can then be later removed from the Si-based substrate and transfered to other materials if desired. CNT synthesis has been shown to work best on oxidized portions of Si [32]. It has been observed that CNT synthesis directly on Si is inhibited by the formation of silicides (e.g., $FeSi_2$), which deactivates the metal catalyst [33]. An oxide layer provides an effective barrier to the movement of atoms, protecting the metal catalyst (with the properties of this oxide buffer layer, such as crystallinity or density, also playing a role in catalyst longevity [34]). In fact, this has allowed researchers to pattern CNT growth, simply by creating a pattern of Si and oxidized Si, the former inhibiting CNT growth and the latter allowing it [33]. It has also been observed that the structure of the substrate can play an important role, with porous Si allowing for a higher growth rate and narrower diameter (and narrower-diameter distribution of) CNTs [35]. In our case, we use a standard thermally-oxidized silicon wafer, with 1 μm of oxide.

In addition to the possibility that Si can deactivate the catalyst through the formation of silicides, it can also be deactivated by the build-up of amorphous or graphitic [22] barriers of carbon on the catalyst particles, preventing new hydrocarbon molecules from reaching the interior of the catalyst. In the case of fixed catalyst systems this was historically an important obstacle to overcome, since there is no

way to provide new catalyst as old catalyst becomes deactivated in these systems (in contrast with vapor phase systems). Most researchers divide the CNT synthesis process into four stages (with some objections, e.g., Ref. [36]): (1) formation of adsorbed surface carbon on catalyst particles; (2) dissolution of carbon precursors; (3) diffusion of carbon through metal particles; and (4) precipitation of the carbon in the form of CNTs. Many have argued that step 3, the diffusion of carbon into the catalyst particle, is the rate-limiting step [29, 37–39]. It has been suggested that there is an "encapsulation point" at which catalyst particles are deactivated by encapsulated carbon, corresponding to the point at which the rate of carbon adsorption (step 1) exceeds the rate of diffusion through the metal particles (step 3) [37]. For this reason, it has been noted that CNT growth and yield are better for low partial pressures of the carbon source (e.g., xylene) [26, 37]. In fact, product yield has been observed to be independent of concentration up to the "encapsulation concentration" [37]. Above this point defective CNTs [37] and amorphous carbon [26] predominate. Great strides have been made in preventing this by fine tuning the flow gases during synthesis. For example, providing hydrogen or an oxidizing agent during synthesis can prevent the formation of carbonaceous barriers around catalyst particles, allowing even fixed-catalyst systems to generate CNTs approaching 1 cm in length (see, e.g., Ref. [25]).

Composition of the flow gas affects more than merely catalyst longevity, however, as it also influences CNT morphology. For example, while hydrogen can prevent the build-up of carbon on catalysts and thereby prevent their deactivation, it also results in CNTs of lower mean diameter with fewer walls. This has been observed for both vapor-phase- (see Ref. [40] and Section 3.1) and fixed- [41–43] catalyst systems (though in the latter case there are some additional complexities due to the necessity of breaking up the catalyst thin film into nanoparticles [24]). Including hydrogen in the flow gas has also been observed to result in CNTs with fewer surrounding amorphous impurities [43] and to improve yield [30]. The presence of an oxidizing agent has been shown to have similar effects, especially in preventing the formation of amorphous carbon [25, 42, 44]. Including a small amount of water is one way to do this [45]. This approach has been shown to result in improved alignment of CNTs

and less amorphous carbon, but at the cost of a larger quantity of defects and non-continuous graphite layers [30, 34]. Another approach is to include a small amount of air [38] or acetic acid (which converts to CO_2 at high temperature) in the system [46]. These approaches were both observed to increase the length of CNTs and to prevent amorphous impurities.

Other additives can also play a vital role in the resulting CNT properties. For example, the inclusion of thiophene in the precursor mixture (which acts as a source of sulfur) results in CNTs with Y junctions and poor alignment, which is attributed to pentagonal defects (i.e., the formation of adjacent pentagon-heptagon pairs rather than the hexagons formed by sp^2-bonded carbon when no defects are present) [47]. Another example is pyridine, which can lead to helical CNTs [48]. When dichlorobenzene is used, the alignment of CNTs that would typically result is disrupted and instead a material of randomly interconnected CNTs is obtained [49]. Other such variations exist in the literature, allowing extensive customizability of CNTs.

The flow rate of the carrier gas is also important, with higher flow rates up to a certain point giving higher yield of CNTs, resulting in CNT growth over a larger area of the substrate (rather than predominantly clustered near the entrance of the gas feed into the heating zone of the furnace) [50, 51]. This is related to the fact that the CNT properties (or even whether or not there are CNTs) vary as a function of position in the CVD furnace [51]. CNT samples have been observed to vary in bulk density [52], height [50], and amount of contaminant [53] depending on substrate position in the furnace and sample position on the substrate. Abbaslou et al. found that 40% of the Fe particles in their toluene/ferrocene vapor phase catalyst system were deposited in the first 10 cm of the heating zone of their furnace [37]. Interestingly, they found that this region corresponded to narrower-diameter but higher-areal-density CNTs. Others have also conducted studies of how reaction kinetics vary along the window of the furnace (e.g., [54]). Higher flow rates lead to CNTs with higher average lengths [51, 55]. It has also been claimed that higher flow rates of the carrier gas lead to better-aligned bundles of CNTs and low rates to more random orientations [56].

Usually a low catalyst concentration is considered to result in purer CNTs [57]

with lower diameters on average [26, 28, 57, 58] and possibly narrower diameter distributions as well [58]. Since it has been convincingly shown that catalyst particle size and CNT diameter are closely related [30, 59], it can be concluded that higher concentrations of the catalyst precursor result in larger catalyst particles rather than merely a larger number of small particles. It has also been suggested that lower catalyst concentration might also be important in order to obtain straighter (rather than helical) CNTs [30]. The growth rate of the CNTs is observed to decline when either too high or too low of a catalyst concentration is utilized [60].

Reports have varied regarding the optimal synthesis temperature at which the growth rate is at a maximum (typically 750–800 °C, but as low as 650 and as high as 900 °C) [57]. There are also contradictory reports about the effect of temperature on CNT morphology, with claims that increasing temperatures lead to decreased [47, 57] or increased [58, 61] CNT diameters, with some reports suggesting no change in diameter or other morphological characteristics [29, 39]. The data can be difficult to interpret, since different conditions not only lead to different rates of catalytic activity, but also to different rates of pyrolytic activity [39, 60]. Higher diameters at higher temperatures could result from increased mobility of the catalyst particles (allowing improved agglomeration), but could also be a result of increased formation of pyrolyzed carbon into partially-graphitic layers around the CNTs [58]. In general, it is thought that higher temperatures lead to improved crystalline quality of the CNTs [39, 41] (similarly, it has also been suggested that crystalline quality of the individual CNT walls can be improved via annealing, as evidenced by changes in density and increases in oxidation temperature after performing such a procedure [56, 62]). However, at very high temperatures, between 1000 and 1100 °C, it has been noted that acetylene (which can be a byproduct of the pyrolysis of aromatic carbons) is consumed to form polycyclic aromatic hydrocarbons (PAHs) and soot, as evidenced by a thick, brown oil/tar in the furnace tube [63, 64].

Two 2005 studies revealed that vapor-phase-catalyst thermal CVD systems result in CNTs via bottom-up synthesis, in which new CNT synthesis always takes place at the substrate [65, 66]. That is, new CNT growth takes place underneath whatever

CNTs are present already, lifting them upward away from the substrate. CNT growth can be completely halted (and even the substrates temporarily removed from the furnace) and then a new growth cycle can be begun again, initiating CNTs under the previously synthesized CNTs. It has been noted that as the CNTs grow there is a resulting barrier to the substrate of increasing thickness, resulting in a decay in the CNT growth rate with time [58, 60].

1.3.2 Mechanics of carbon nanotubes

As discussed earlier, CNTs are known to have remarkable physical properties, including more than just their mechanical properties. However, the scope of this dissertation is limited primarily to the bulk mechanical properties of CNT-based materials. For this reason, this section gives an overview of the mechanical properties of individual CNTs, a necessary background to understanding the mechanical behavior of bulk systems of CNTs.

Due to their small size, the first studies of the mechanics of individual CNTs consisted of two main approaches: simulation/modeling and observation using transmission electron microscopy (TEM). Both approaches have limitations. Simulation was and remains limited by computation time. TEM allowed for observations of CNTs contorted in various interesting ways that gave clues about mechanical properties, but it did not easily allow for direct manipulation. Despite such limitations, these first studies noted the tremendous flexibility of single- and double-walled CNTs [67]. Iijima et al. noted that above a critical bending angle (which depends on CNT diameter) kinks form; however, the CNT returns to its original configuration upon release [67]. Similarly, Yakobson et al. found using molecular dynamics that CNT collapse and buckling at high angles could be quite abrupt, with rapid energy release and morphological reconfiguration, yet without any brittleness or plasticity [68]. Additionally, the snap-back in unloading occurred at slightly lower strains than original snapping during loading, resulting in a small hysteresis. More recently, this elastic shell kinking has been proposed as a mechanism for energy dissipation in CNTs

[69, 70], and is a physical motiviation for the use of elastic bistable springs as a model for the compressive response of materials made up of many CNTs (see Refs. [71, 72] and Chapter 6).

Similar studies were later conducted for thicker, multi-wall CNTs. Low-amplitude, evenly spaced ripples in the CNT walls on the inside of the bend were observed by Falvo et al., even for small bending angles [73]. These rapidly redistributed as the bending angle was changed. The authors concluded that these buckles were intrinsic rather than defect-related. These ripples were subsequently examined by others, with the explanation that such rippling alleviates planar strain energy in the inner, compressed wall, replacing some of the compression of the strong sp^2 bonds that are planar in the CNT walls with flexural modes, with more accomodating out-of-plane bending [74]. Shell finite elements have also been used to computationally reproduce the experimentally observed rippling [75]. Throughout these studies it was observed that local strains as large as 0.16 could be induced without any failure in the CNT walls [73].

CNTs are also observed to exhibit tremendous abilities for elastic deformation radially, with deviation from circular to elliptical (and eventually planar) cross sections under radial pressure [76]. Even van der Waals interactions between two parallel CNTs in contact suffice in inducing non-circular CNT cross sections in certain cases [6]. Some have observed a flattening of the tube as a result of van der Waals interactions between opposite walls of a single tube, which has been suggested as a limitation on the maximum possible diameters of single-wall CNTs (i.e., for CNTs with diameters greater than ~ 3 nm it is energetically favorable to maintain a fully collapsed configuration) [68].

The earliest efforts to experimentally quantify mechanical properties of CNTs such as Young's modulus involved indirect approaches. Treacy et al. devised a clever way to back-calculate estimates for the Young's modulus of CNTs [77]. Using TEM, they searched for isolated CNTs that happened to have one free end over a hole in the TEM substrate, and studied thermal-induced vibrations at different temperatures. By measuring the amplitudes of these vibrations at the free ends of the CNTs

(based on apparent smearing in the images), and treating them as clamped cylindrical cantilevers, they could estimate Young's modulus from an observed effective spring constant. These estimates had large uncertainties (1.8 $\pm$ 1.4 TPa), but did provide important information [77]. Direct experimental measurements were made by Falvo et al., who bent multi-wall CNTs over large angles using an atomic force microscope (AFM), relying on surface interactions to hold the other end of the CNTs in place [73]. Lourie et al. dispersed CNTs onto a slide, and coated this with an epoxy that was allowed to cure [78]. During curing, the epoxy contracted, causing compressive forces on the CNTs. The thicker tubes buckled more smoothly, and revealed wavelike deformations of constant wavelength on the inner side of the bend, whereas thinner tubes collapsed, possibly fracturing or telescoping. From this behavior they obtained compressive strengths between 100 and 200 GPa, two orders of magnitude higher than most fibers [78]. Variations in structural features in multi-wall CNTs, such as chirality, diameter, or number of walls, are observed to have almost no effect on the elastic properties for CNTs in which bending energy is not excessive (i.e., CNTs with diameters greater than $\sim$ 2 nm) [19].

Yu et al. in 2000 succeeded in connecting the two ends of multi-wall CNTs to two different atomic force microscope (AFM) tips, one connected to a stiff cantilever and the other to a more compliant one [79]. By pulling the two AFM tips apart they directly measured the tensile strength of various multi-wall CNTs to be 11–63 GPa, and the Young's modulus to be 270–950 GPa, with no apparent dependence on CNT diameter. The failure strain was measured to be as high as 0.12. Of particular interest, they observed that the failure mode consisted of a break in the outermost wall, calling this "sword-in-sheath" failure [79].

CNTs are multifunctional materials in which, for example, electric currents affect mechanical properties. This has been exploited for applications such as electromechanical oscillators [80] and actuators [81]. Aside from a brief discussion in Section 7.2.1 about electromechanical behavior in our bulk materials, this rich area will not be discussed further here.

1.3.3 Achieving macroscale benefits from carbon nanotubes

Though CNTs have excellent properties individually, the question remains as to how to achieve any sort of benefits at the macroscale from such nanomaterials. This section will review several common approaches that have been taken.

Perhaps the most common approach is to add a small quantity of CNTs as reinforcing fibers in other material matrices to form a composite [82], analogous to the frequent use of carbon fibers. This faces challenges such as CNT agglomeration and poor interfacial adhesion [83]. Dozens of academic papers have been devoted just to the problem of getting uniform dispersion of CNTs in another matrix (see the examples below). The high aspect ratio and strong van der Waals interactions of CNTs lead to a serious problem with clumping, and these deposits end up leading to weak spots in the matrix material rather than to reinforcement [84]. A large variety of techniques have been attempted to facilitate dispersion, from ultrasonication and surfactants to covalent functionalization [85]. If CNTs are shortened they have less tendency to clump, but also are less able to provide the desired reinforcement [86]. Covalent functionalization of the CNT surfaces (so that they better match the molecular structure of the surrounding matrix) is one of the most reliable ways to get successful dispersion of CNTs and good interaction with the matrix [87]. Chemists have successfully devised processes for functionalization of CNT surfaces with a wide variety of molecules [88]. The main disadvantage of this approach is that covalent functionalization necessitates disruption of the same sp^2 bonds that give CNTs their tremendous properties. For this reason, some have proposed approaches that exploit non-covalent means to "functionalize" the CNT surfaces [89], utilizing $\pi - \pi$ interactions to bind to the CNTs and a separate copolymer to interact with the matrix [90]. Even with successful dispersion of individual CNTs into polymeric matrices, most mechanical properties show only modest improvements [83]. Damping behavior, however, has shown improvements of several orders of magnitude, with the extremely high surface area of CNTs leading to a large amount of interfacial friction [83].

A variation in this approach adds an intermediate level of hierarchy between CNTs

and the bulk material, which maintains improved spatial separation of the individual CNTs (to avoid clumping) allowing them to successfully reinforce the matrix and improve properties such as toughness [91–93]. For example, CNTs can be synthesized directly onto SiC fibers, which are subsequently used in woven composites. This has been shown to improve the mechanical, electrical, and thermal properties relative to traditional composites [91].

Others have taken advantage merely of the geometrical fact that CNTs have enormous surface-to-volume ratios, synthesizing CNTs on the surface of a material to increase the overall surface-to-volume ratio rather than incorporating the CNTs into the interior. For example, one group synthesized CNTs within the voids of graphitic foams in order to improve the surface area of the foams by two to three orders of magnitude [30]. This increase in surface area combined with the excellent thermal conductivity of CNTs could lead to applications where efficient thermal dissipation is desired [30].

Rather than incorporating CNTs with other materials at all, some have created bulk materials entirely or nearly entirely from just CNTs (as we do here). These include one-dimensional yarns [94], two-dimensional ultrathin sheets [95] or thicker "bucky paper" [96] (which can consist of aligned or disordered CNTs), and various three-dimensional configurations [97] (ordered "arrays" or "forests" of CNTs, of course, comprise a special category to which most of this dissertation is addressed, beginning in Section 1.4). The review by Liu et al. discusses all of these categories in detail [97]. To give one impressive example of these structures, CNTs have been successfully spun into yarns, taking inspiration from millennia of human experience with fibers from wool and cotton. Using the procedure of Zhang et al., yarns can be synthesized of 1–10 μm diameter with maximum strengths up to 460 MPa [98]. Their process could be used to obtain a length of roughly 50 m of such yarn from 1 cm^2 of aligned multi-wall CNTs. Due to the tremendous properties of the individual CNTs, the yarns were able to be made into multi-ply fibers or tied tightly into knots without degradation [98].

One can also think of other interesting, non-mechanical applications for CNTs as

components in larger systems. These could relate to field emission [35], microsensors for non-destructive evaluation [99], flexible electronics [100], aerogels [101], electrochemical applications [102, 103], etc., and have been widely proposed. However, these other areas are outside the scope of this work and will not be discussed in detail here.

1.4 Aligned arrays of carbon nanotubes

Aligned arrays of carbon nanotubes have garned much interest due to their interesting physical properties (e.g., a compliant, dissipative compressive response, both thermal and electrical conductivity, and structurally dependent hydrophobicity/philicity [104]), which will be discussed throughout this work. Additionally, aligned CNTs are quite simple and inexpensive to synthesize. In fact, if one uses the standard thermal chemical vapor deposition techniques that were discussed earlier (Sec. 1.3.1), the resulting structure consists of aligned CNTs (see Figure 1.3 for a typical example). These materials have been proposed for many plausible applications, such as through-wafer interconnects [105], thermal interfaces [106, 107], viscoelastic dampers [108], biomimetic dry adhesives [109, 110], brushes [111] (e.g., for electrical motors [112]), etc. They can additionally be bonded or anchored to other surfaces, which could be useful for a variety of applications [113, 114]. Also of note, the alignment of the CNTs results in anisotropic properties that could be useful for certain applications as well. For example, the electrical and thermal conductivities can be an order of magnitude lower for CNT arrays in the directions perpendicular to the CNTs relative to the direction parallel with them [115].

In the remainder of this section, first the effect of the synthesis approach on the structure and properties of CNT arrays will be discussed, followed by a discussion of the uses of CNT arrays as components in other materials (rather than as stand-alone structures such as those that will be studied for most of the rest of this dissertation). An extensive discussion of the mechanical properties of CNT arrays (based on our experimental investigations and those described in the literature) will be given in Chapter 2. Various techniques for modifying the structure of materials based on CNT

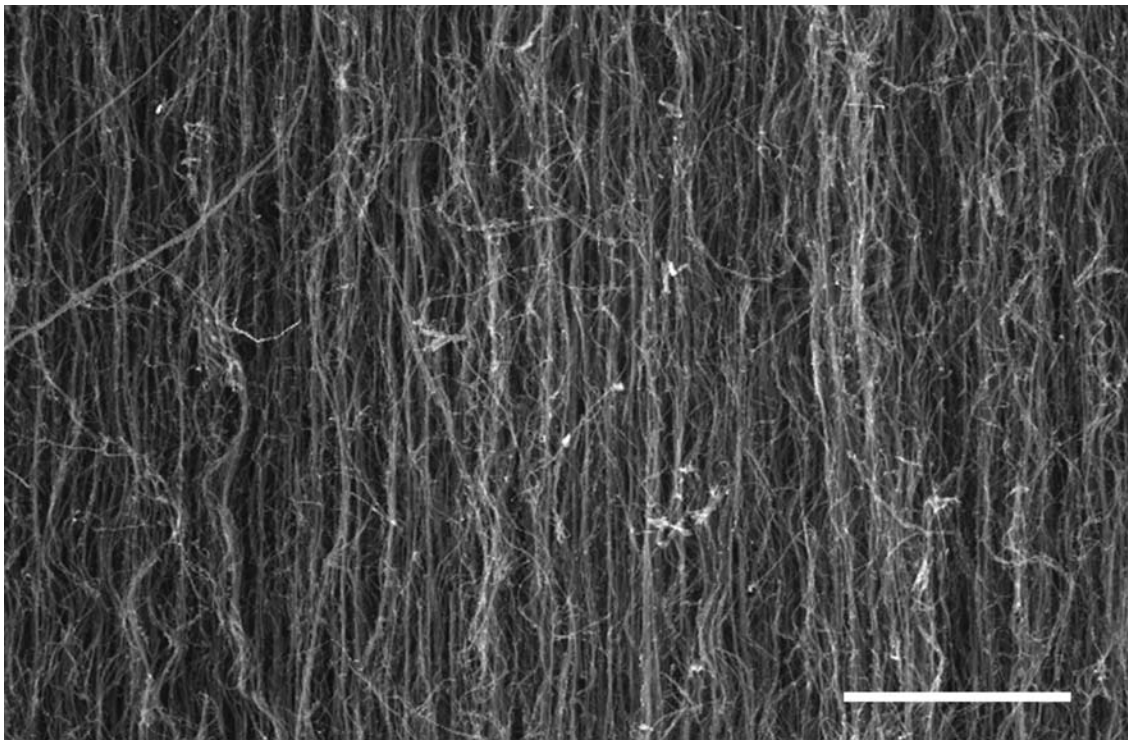

Figure 1.3: A typical CNT array synthesized via vapor phase catalyst thermal chemical vapor deposition (the standard synthesis procedure used throughout this dissertation and detailed in Section 2.1); the scale bar represents 5 μm

arrays, and for thereby controlling bulk mechanical properties, will be developed (i.e., Chapters 3 to 5). The modeling of the mechanical properties of these structures will be investigated later as well (see Chapter 6 and Appendix A).

1.4.1 Effect of synthesis approach

Following the taxonomy devised in the review by Seah et al. [32] (in which many additional details can be found), aligned CNTs can be directly synthesized by one-stage (i.e., the "vapor phase" or "floating catalyst" approach discussed earlier) or two-stage processes (i.e., the "fixed catalyst" or "pre-deposited catalyst" approach). In general, the one-stage processes are less expensive but also result in lower quality CNTs, whereas the two-stage processes allow increased tuning of the CNTs at additional monetary cost and time. Thermal chemical vapor deposition (CVD) is widely regarded as the synthesis technique of choice for bulk and tailorable synthesis

of aligned CNTs, and it allows for both one- and two-stage processes. To reiterate, the one-stage thermal CVD approach involves the continual deposition of catalyst into the furnace's reaction zone during synthesis. The two-stage thermal CVD approach involves first depositing a thin film of catalyst and then conducting CNT synthesis as a later separate step in which only a carbon source and other optional additives are injected into the reaction zone (i.e., no catalyst is injected). Most of the results in this work follow the one-stage process, using ferrocene as a catalyst precursor and toluene as a carbon source, which are injected simultaneously into the heating zone during synthesis.

Most of the general CNT synthesis details mentioned earlier (Sec. 1.3.1) also apply here, as the techniques discussed earlier nearly all result in aligned CNTs. Thermal CVD systems can be used to generate arrays of various characteristics, on a variety of surfaces. Of special note are the differences in microstructure and mechanical properties that result from floating catalyst techniques (e.g., Refs. [26, 111, 116–118]) versus fixed/pre-deposited catalyst (e.g., Refs. [119–121]). In general, the former result in CNTs of larger average diameter (20–80 nm) and a larger number of walls than do the latter (average diameter 5–15 nm). As a result, the porosities of the arrays also differ significantly, with the floating catalyst arrays being roughly 85–90% porous volume (translating to bulk densities of roughly 0.3 g cm^{-3}) [116, 117] and the fixed catalyst arrays being roughly 95–99% porous volume (translating to bulk densities of roughly 0.05 g cm^{-3}) [121]. Porosity has been calculated or measured in various ways. These have included scanning electron microscopy (SEM)-based approximations of CNT diameter and intertube spacing [117]; comparisons of array bulk density with theoretical calculations [119]; and direct measurements of internal surface area [28]. Of course, the internal surface area of CNT arrays decreases with increasing CNT diameter [28], and so also greatly differs for arrays synthesized by the two different approaches. Perhaps most striking is the difference in mechanical properties between the two types of arrays, which will be addressed in Chapter 2.

Various synthesis parameters can be used to directly impact the microstructure of the arrays during synthesis (e.g., as implied in Section 1.3.1, when techniques were

discussed for varying the diameters/number of walls of individual CNTs directly). For example, Abbaslou et al. found that high carbon concentrations led to arrays with more entangled CNTs [37]. Sometimes the array structure can be varied after synthesis instead. For example, aligned CNTs can be directly densified to a desired level by laterally compressing the material from the two orthogonal directions that are perpendicular to the long CNT axes [122]. Both categories of approaches will be followed at different points in this dissertation (especially in Chapters 3 and 4, respectively). As examples in the first category (approaches used during CNT synthesis), the quantity of hydrogen used during synthesis affects both the structure and the properties of the resulting material (see Ref. [40] and Section 3.1). Similarly, changing the feed rate of carbon/catalyst precursors during synthesis gives control over the density distribution along the height of the structure, resulting in interesting strain localization effects when the CNT arrays are later compressed (Section 3.2). As examples in the second category, post-synthesis techniques discussed herein include synthesis of nanoparticles in the array interstices (Chapter 4).

Changes in the morphology of CNT arrays are often difficult to quantify, especially since many properties vary along the height of the structure (i.e., along the lengths of the individual CNTs). Quoting a single value for such parameters as defect density [25], alignment [65], CNT diameter [38], or quantity of contamination [37], which are known to vary along the height of the structure, therefore, does not completely characterize a CNT array sample. Some have attempted to quantify changes in morphology (e.g., CNT tortuosity or alignment) with various image analysis techniques, but with very limited success [123, 124]. A better approach is to experimentally measure these quantities, such as by small-angle x-ray scattering (SAXS) [125] or x-ray microdiffraction [65]. SAXS has been used successfully to study variations in diameter and orientation of arrays of CNTs, using a beam size of order 100 μm (suggesting that this length scale sits appropriately between the nanometer scale of the structure of individual CNTs and the millimeter scale of CNT arrays) [125]. Though these techniques allow estimates of tortuosity, alignment, porosity, etc., as a function of height, it has remained an active area of research to understand how these parameters relate

to the global and local mechanical response of the system.

There are a couple process-structure relationships that are directly relevant to the work contained here. Studies have noted that an increase in feed rate of catalyst and carbon source leads to CNTs of decreased diameter [28, 47, 51]. An increased feed rate has also been observed to give a lower CNT yield (as % weight of the solution) and shorter CNTs [50, 51] but also narrower diameter distributions and improved alignment [47]. Thus, the feed rate of carbon/catalyst precursors is an important parameter (and in fact in certain cases the carbon feed rate can actually be used to select between single- and multi-walled CNTs [126]). This is an important observation for later discussions (especially Section 3.2).

In addition to feed rate, another important parameter is the continuity or discreteness of the injection of the carbon/catalyst precursor. Typically precursors are fed into the reaction zone at a constant rate, but it has been shown that pulsed, dropwise, or other discontinuous approaches can also work in certain cases, and affect structure. These discontinuous approaches have been used in both vapor-phase-catalyst (e.g., Refs. [65, 66] and Section 3.2) and fixed-catalyst (e.g., pulsed acetylene gas [127]) approaches. Jackson et al. used *in situ* optical techniques to measure growth as it occurred [127]. Their short bursts (0.2 s of hydrocarbon injection every 10 s) resulted in a "banded" structure, with bands of sub-μm length. In the case of these short bursts it is found that the CNTs can be continuous across the separate layers, in contrast with other reports that used much larger pauses [65, 66]. Our own data show that the continuity of the CNTs across layers may be a function of the length of time of the pause between input events (Section 3.2). Orientiation of the CNTs is also observed to vary with the height along the array, with lateral entanglement of CNTs occurring near the boundaries between layers [65, 127]. These have higher carbon density, as verifed by Z-contrast scanning transmission electron microscopy (Z-STEM), and correspond to the early part of the growth that results from each pulse [127].

As noted previously (Section 1.3.1), CNT arrays synthesized by thermal CVD typically grow in bottom-up fashion [65, 66], with newer growth at the base. Because

of the increasing thickness of the CNTs with time there is an increasing diffusion barrier to continued CNT growth. In the case of fixed catalyst systems there is an additional factor resulting from the gradual loss of catalyst particles (i.e., particles become deactivated by carbonaceous covering). In the case of vapor-phase catalyst systems there is an additional factor resulting from increased substrate crowding with time. In either case, CNT growth slows down with time, and therefore discontinuous growth techniques, as described above, lead to layers of decreasing height toward the base of the structure when the same growth time is used for each layer [127].

Additional effects such as temperature and gas composition are important, as discussed earlier (Section 1.3.1), and affect the properties of CNT arrays as they affect the properties of individual CNTs.

1.4.2 Aligned CNTs as components in other materials

In addition to being studied as standalone materials (as in most of the rest of this dissertation), aligned arrays of CNTs have been incorporated into or coupled with other materials. This has most commonly been done with applications of damping or interlaminar shear resistance in mind. For example, Suhr et al. integrated aligned CNTs with epoxy and investigated the damping behavior of the resulting composite by imposing shear [128]. They found an order of magnitude improvement in the loss factor damping ratio over epoxy alone, concluding that the enhanced damping resulted from frictional energy dissipation and interfacial sliding (energy loss because of both CNT-CNT contact and CNT-polymer contact) as others have observed in similar materials [83]. They noted that the dissipation effect is so large as a result of the very large interfactial area (100 m^2 g^{-1}) that arises from the small size of CNTs. Similar to the case for individual CNTs dispersed in polymeric matrices (Section 1.3.3), the elastic modulus and glass transition temperature of the epoxy did not change appreciably [128]. Abot et al. built a laminate structure using arrays of multi-wall CNTs to increase interlaminar shear resistance by bridging the interfaces between layers (finding the greatest improvement for the shortest CNTs, $\sim$ 100 μm

in their case) [129, 130].

Several other groups have infiltrated various polymers into the interstices of arrays of CNTs [131–136], despite the many challenges that arise due to dependencies on viscosity, location of polymer-array contact, drop size, array porosity, etc. [132]. Due to capillarity effects, polymer infiltration takes place more rapidly into the array from the top or bottom (where the CNT ends are) than it does from the sides. García et al. synthesized short (40–70 μm), patterned CNTs and then submerged them into the polymer SU-8, which penetrated the array to coat the individual CNTs. Upon curing, they tested the composite in compression with a diamond flat punch and observed a factor of three increase in Young's modulus relative to a CNT array without polymer reinforcement [133]. Ci et al. infiltrated poly(dimethyl siloxane) into the interstices of long arrays of CNTs (> 3 mm) and observed order-of-magnitude increases in shear modulus and damping behavior [131]. Improved energy dissipation was also observed in compression, due to polymer reinforcement of the buckling CNTs and increased energy dissipation due to interfacial effects [131]. Similarly, Shin et al. infiltrated their multi-wall CNT arrays with a polyurethane solution to develop a strong, stretchable, electrically conductive polyurethane composite [137]. In all of these cases, one of the main concerns is getting polymer uniformly into the interstices without formation of voids, etc. [132], which is much easier to accomplish when the CNT arrays are shorter. Instead of directly infiltrating the aligned CNTS with polymer, some have applied polymer via a CVD polymerization process [136]. Tawfick et al., for example, applied polymer based on poly-p-xylylene with different functionalizations and of different thicknesses (10–27 nm) depending on time in CVD, resulting in roughly doubled stiffness [136].

Rather than filling the interstices of CNT arrays uniformly with polymer, other groups have constructed multilayer structures in which the CNT arrays are largely unmodified except for their boundaries, at which points they are in some way bound to other materials [138]. One group embedded catalyst into vermiculite and then synthesized numerous aligned CNT arrays in the material by flowing ethylene and hydrogen at high temperature, separating vermiculite layers by aligned multi-wall

CNTs of order ten μm length [139]. The resulting structure was capable of repeated compression to 90 % volume reduction. Others have synthesized millimeter-scale CNT arrays and then stacked them vertically with different types of interlayers, including polymer (see Ref. [140] and Chapter 5) and metal foils (see Ref. [72] and Section 6.3). In these latter cases, strain localization was observed due to different characteristics of the CNT layers [40, 52].

1.5 Toxicity and potential health hazards

Only in recent years have the potential health hazards of nanomaterials begun to be widely studied. Recommendations for how to detect [141] and handle (e.g., Ref. [142]) nanomaterials in a laboratory or occupational environment are relatively new or still being developed. Though carbon is not commonly a cause of worry in terms of causing chemical disruptions of biologically important processes, there is still concern about carbon-based nanomaterials based on their physical or geometrical potential for toxicity. In particular, it has been noted that CNTs and CNT bundles of certain sizes closely resemble the size, aspect ratio, and fibrous structure of asbestos [143].

Jaurand et al. concluded in their review that, "CNTs elicit tissue and cell responses similar to those observed with asbestos fibres" based on the animal/cellular studies available in the literature [143]. Their review encompassed a variety of CNT types and sizes. Of particular relevance to this dissertation, CNTs that are similar in morphology to those used here (i.e., CNT diameters of 40–60 nm, the same as those used here, and lengths up to 500 μm, only slightly shorter than those used here) caused inflammation and thickening of alveolar lining in rats and had long persistency *in vivo* (at least three months) [143], based on the work of Liu et al. [144]. Because of the precedence of asbestos toxicity via airways, there is especially concern about the effects of nanomaterials entering the body via this pathway [145]. There is also a likelihood that nanomaterials could travel to a variety of other places in the body, such as lymph nodes and kidneys. A recent study used the renal cells of mice to investigate CNT toxicity in kidneys, and noted changes in protein expression and cell

function that are cause for concern [146].

When dangerous fibers like those of asbestos reach the lung, inflammatory cells produce a variety of substances, including reactive oxygen species (ROS) and reactive nitrogen species (RNS) [143]. It is thought that metal, especially iron, as a contaminant on such fibers can encourage the formation of ROS and RNS [143]. This is especially disconcerting knowing that iron is perhaps the most common catalyst type used for CNT synthesis, and is strewn throughout CNT arrays on the surfaces of the individual CNTs when vapor-phase methods are used (although at least one study has argued that CNT defects drive acute toxicity more than the presence of metal contaminant [147]). One potentially important difference between CNT fibers and asbestos fibers, however, is that the former are usually hydrophobic and the latter are hydrophilic [143]. It is unknown whether this could affect either the acute or the long-term toxicities of CNTs.

Just as with asbestos fibers, CNT fibers have length-dependent toxicity as observed in mice [148]. In general, thin fibers with lengths of at least 4–8 μm have been suggested to result in the most active toxicological activity [143]. Below this range, macrophages are able to engulf the CNTs. At the higher ranges they cannot, leading to "frustrated phagocytosis" [148]. In these cases, there can be a chronic inducement toward inflammation and the formation of granulomas, with long-term health effects [148].

Very recent work with human epithelial cells has given some reason for optimism [149]. The authors noted that, unlike asbestos fibers, even large quantities of the multi-wall CNTs used in the study did not cause immediate cell death, though high levels of ROS and other indications of cell damage were observed [149]. Exposure for up to six months did not result in cumulative problems, or any issues that developed with time. The CNTs in this study were purified, however, in contrast to most CNTs, which are typically contaminated with various transition metals.

It has been shown that in certain cases there is very little particle shedding during synthesis of CNT arrays and subsequent handling [150]. This is helped by the strong van der Waals interactions between CNTs. It is likely, based on this result, that

handling CNTs in array form is safer than doing so in powder form. It is unclear, however, if this result fully applies in the case of CNT arrays synthesized via vapor-phase approaches [150].

There is enough reason for concern, and therefore caution is in order. Though CNTs have been definitely implicated in acute toxicity [144] there is also a possibility of longer-term health effects that could take years or decades to unfold. CNTs are thought to be biopersistent, but more research needs to be done to know exactly to what extent this is the case [143], since acute toxicity may or may not imply a potential for longer-term health problems [147, 149]. In the author's opinion, direct contact between CNTs and those studying them should be avoided through whatever laboratory equipment is necessary for this, to include fume hoods, glove boxes, and respirators with appropriate filters to prevent researchers from breathing in nanoparticles.

Chapter 2

Experimental investigation of the mechanical properties of carbon nanotube arrays

The goal of this chapter is twofold. First, the experimental approaches that were commonly taken in the course of this dissertation will be discussed (Section 2.1). Second, the mechanical properties of typical unmodified CNT arrays will be discussed to lay the framework for the remainder of the dissertation (which will discuss several different ways in which the substructure and thereby the properties of the CNT arrays can be controlled). Quasistatic compression and viscoelastic measurements (based on creep and stress relaxation tests) will be discussed in Sections 2.2 and 2.3, respectively.

2.1 Experimental approaches used throughout the dissertation

2.1.1 Sample synthesis

The work of this dissertation is based on vapor phase (floating) catalyst synthesis of CNT arrays, through the use of ferrocene as a catalyst precursor and toluene as a carbon source (Figure 1.2). In all cases, a solution of ferrocene and toluene is used at a concentration of 0.02 g ml^{-1} and is injected into a furnace held at a temperature of 827 °C where pieces of a thermally oxidized silicon wafer are waiting as the substrates

for what will become CNT arrays. Substrates are typically several square centimeters in size, limited only by the diameter of the quartz furnace tubes (in our case, this is approximately 4 cm) and the length of the heating zone (approximately 15 cm, though this is difficult to estimate precisely due to changes in temperature near the outsides of the zone). Various feed rates of the precursor solution are used, though this is typically 1 ml min^{-1} unless stated otherwise. The flow gas used is nearly always pure argon (flowing at 800 sccm), except of course for in Section 3.1 (and Ref. [40]), where using different quantities of hydrogen in the flow gas is specifically studied. Typically a total of 50 ml of the precursor solution is injected in a single growth cycle, though this also differs from chapter to chapter, depending on the desired height of the samples. After passing through the furnace the exhaust gas passes through a bubbler (at atmospheric pressure) to prevent backflow of atmospheric gases into the reactor, and then passes into the exhaust collector in a fume hood. Following the above synthesis procedure leads to CNT arrays as pictured in Figure 1.3.

CNT array samples are removed from the growth substrate prior to additional testing or modification, typically with cross-sectional areas of 10–20 mm^2. Depending on the exact synthesis parameters used and also on the original location of the sample on its substrate [40, 52], sample density and height are typically 0.1–0.35 g cm^{-3} and 0.8–1.5 mm, respectively.

2.1.2 Compression measurements

Standard mechanical tests include quasistatic compression using a commercial materials test system (Instron E3000). This system was coupled with optics and a four probe electrical measurement system in order to understand how deformation and electrical characteristics were changing during compression (Figure 2.1).

This system was used primarily to obtain stress-strain data at low strain rates (10^{-4} to 10^{-1} s^{-1}). The resultant compressive stress-strain measurements were used to calculate parameters such as the loading/unloading modulus, strain recovery, peak stress, and energy dissipation per unit volume (by integrating the area of the stress-

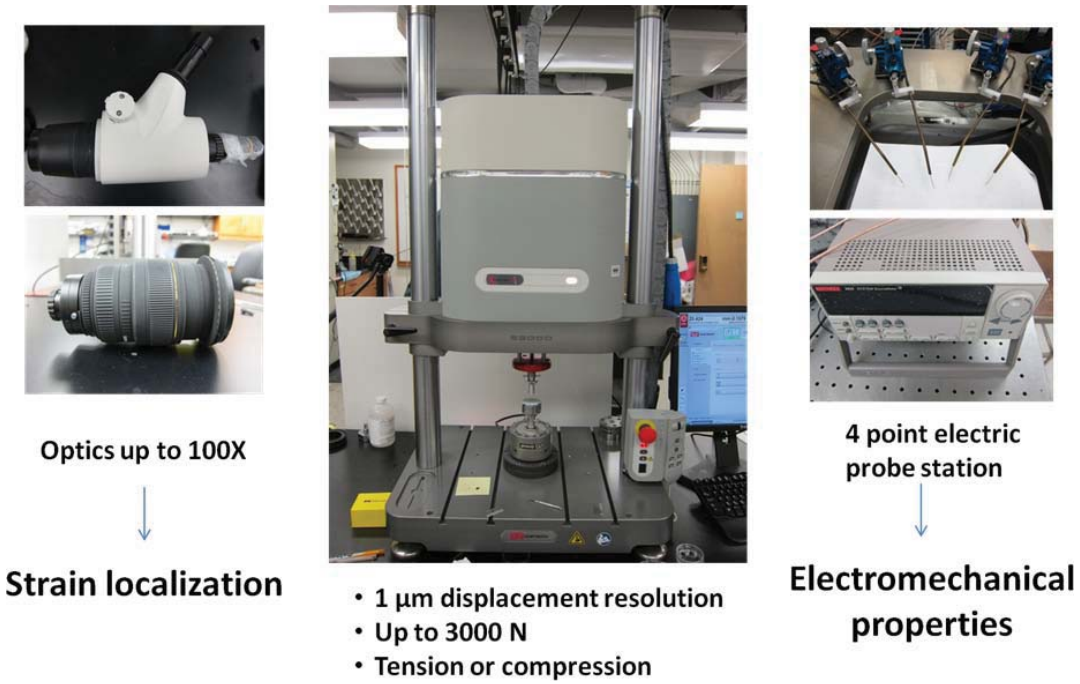

Figure 2.1: Experimental setup for quasistatic mechanical measurements

strain hysteresis); this sort of analysis was conducted for almost every chapter in this dissertation. At times this same apparatus was used to measure time-dependent properties based on creep or stress relaxation tests; in these cases tests were allowed to run for 8 hours or so (see, e.g., Section 2.3 or Ref. [151]).

The quasistatic test system was coupled with *in situ* optics for two studies in particular (see the discussions in Chapter 5 and Section 6.3), in which multilayer structures were investigated. In these cases the optics were used to characterize the location and extent of strain localization during compression. The quasistatic test system was coupled with the electric probe station for the work in Chapter 5, in which it was desirable to understand how the electrical resistance changes during compression, and also in the preliminary work presented in Section 7.2.1 that shows electrical current resulting in electromechanical stiffening of the material.

2.1.3 Impact measurements

Another type of mechanical test that was frequently performed was a simple impact test using a steel sphere (diameter $^3/_8$ inch, mass 3.47 g) dropped from 2–30 centimeters in height (Figure 2.2). A switch was used to simultaneously release the striker and activate a high-speed camera (Phantom V12.1). This recorded images at 20 kHz to allow for an accurate measure of the restitution coefficient (i.e., the ratio of the incoming speed of the striker to the outgoing speed of the striker) based on image analysis.[1] This procedure readily allowed the calculation of the energy dissipated during contact between the striker and the sample. Namely, by the conservation of energy:

$$D = \frac{1}{2}mv_i^2 - \frac{1}{2}mv_f^2 \tag{2.1}$$

where D represents the energy dissipated during the collision, m is the striker mass, and v_i and v_f represent the incoming and outgoing speeds of the striker immediately before and after contact with the sample, respectively.

Additionally, a piezo sensor (PCB Piezotronics B01 or B02, depending on the drop height) was placed under the sample, opposite the striker impact point, allowing for a force-time profile to be recorded (see Sections 3.2 and 7.2.2 for specific examples). Though it is a simplification, this force-time profile was treated as representative of the uniform stress state throughout the sample (i.e., as though the sample were being quasistatically compressed). With this assumption, and its direct consequence that the force profile being measured by the sensor is the instantaneous force acting on the steel striker, Newton's second law can then be employed to obtain displacement-time or force-displacement information for the striker. I.e., since $F(t) = m\ddot{x}$, numerically integrating the force data, $F(t)$, which is known directly from the sensor, can provide both velocity and, if integrated twice, displacement as a function of time. Importantly, the first integration constant, corresponding to the initial velocity of the striker immediately prior to making contact with the sample, can be directly

[1] I am grateful to Dr. Jinkyu Yang, now a professor at the University of South Carolina, who originally created the image analysis routines and also provided important help regarding the assembly and use of the apparatus used for impact tests.

measured by the high-speed camera (the second constant can merely be set to zero, defining the position of the sample surface as zero).

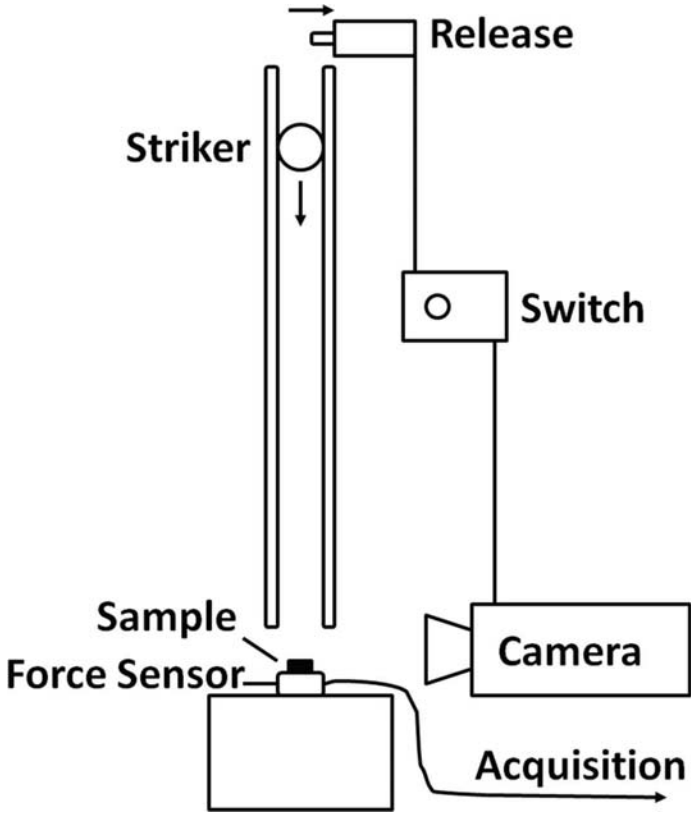

Figure 2.2: Experimental setup for impact tests

This approach is used extensively in Section 3.2 and for the preliminary work discussed in Section 7.2.2.

2.2 Quasistatic compressive response of CNT arrays

Cao et al. first noted that arrays of aligned CNTs behave similar to foams under compression [117].[2] Structures based on these materials have been shown to dissipate more than two orders of magnitude more energy in compression than typical polymeric foams of comparable density (see Ref. [140] and Chapter 5), and show an almost complete absence of a Poisson effect [109]. Arrays of CNTs exhibit a stress-strain

[2] Part of the material in this section was adapted from the introduction of our prior work [152].

hysteresis in compression analogous to that of open cell foams (Figure 2.3), with three-regime behavior (a linear elastic regime followed by a plateau associated with buckling and finally a densification regime) [117, 153]. In addition to the hysteretic stress-strain relationship, the mechanical response includes several noteworthy features. These include strain localization during compression [120, 154]; strain recovery after compression [117]; a diminishing hysteresis area (i.e., diminishing energy dissipation) and peak stress for the first few compressive cycles [40, 117]; and an abrupt shift in stress-strain behavior to that of the pristine material when a previous value of maximum strain is exceeded.

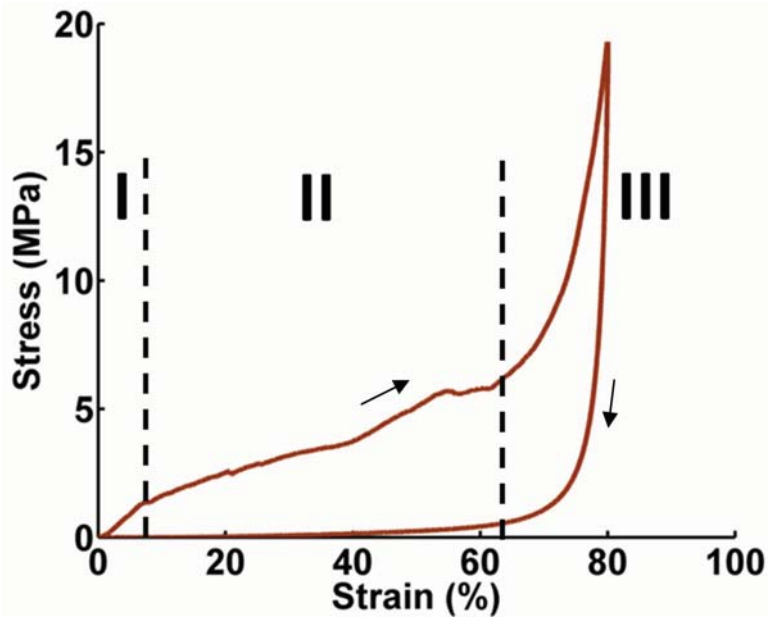

Figure 2.3: A typical stress-strain relationship for CNT arrays in quasistatic compression (arrows indicate the directions of loading and unloading); analogous to open cell foams, three regions of behavior are observed: I, a linear region; II, a plateau associated with the formation of buckles; and III, densification

Strain localization has long been noted during the compression of CNT arrays [117, 120, 155], with uniaxial compression typically resulting in the imposed strain being entirely accommodated by the formation of buckles at the base of the structure, with *base* being defined as the side that was nearest to the growth substrate during synthesis. This behavior is observed whether the CNTs remain bound to the

substrate [120, 154] or are removed from it to create a freestanding structure [117], and is therefore generally thought to be a result of a gradient in physical properties that originate with the growth process. The result of this is that the CNT arrays undergo coordinated buckling of many individual CNTs [156], leading to the formation of collective buckles laterally across the entire width of the structure, which form sequentially from the base upward [120].

A variety of behaviors has been observed for strain recovery, with some groups reporting that CNT arrays recover most of their original height after large compressive deformation (e.g., Refs. [40, 114, 117, 118, 157]) while others have reported an almost complete absence of strain recovery (e.g., Refs. [109, 120, 156, 158–161]). In the past [154], it has been noted that the former category has consisted of CNTs that were synthesized by a vapor phase catalyst technique by which catalyst is continually deposited during the synthesis process, whereas the latter has consisted of CNTs that were synthesized by a fixed catalyst approach in which CNTs grow from the surface of a catalyst thin film that is deposited prior to the start of synthesis. However, recently a process was reported that allows for either behavior to be obtained for fixed-catalyst-synthesized CNTs [119]. In that study, the authors terminated the growth of their CNT arrays after they had reached 1 mm thickness, and then flowed pure ethylene into the furnace for various amounts of time, observing the pyrolytic formation of additional walls (i.e., graphitic layers) around the CNTs. If this ethylene treatment was provided the CNTs recovered after compression, a fact that the authors attribute to changes in CNT surface roughness (which would disrupt the van der Waals interactions between CNTs), and if it was not the CNTs did not recover [119]. This explanation is in contrast with that of Ge et al., who hypothesized that strain recovery or lack thereof was entirely a function of CNT diameter [158]. I.e., they showed how small-diameter CNTs (in their case, 8 nm) have much higher adhesion relative to bending stiffness, resulting in CNT–CNT interaction that was not able to be overcome by the elasticity of the individual CNTs. In contrast, thick CNTs (such as the 40-nm-diameter CNTs of Ref. [117]) have much higher bending stiffness, and therefore a lower importance of adhesive effects relative to this bending stiffness

[158]. The physical basis for the strain recovery or lack of recovery remains an active area of investigation. The recovery of CNT arrays has been shown to be very rapid [117, 119], sometimes as high as 5 mm s^{-1} from even 0.9 compressive strain (with *strain* being defined as the total compressive displacement normalized by the original sample height—i.e., 0.9 strain is 90% compression relative to the original height) [119].

Even for the CNT arrays that are observed to recover well from compression, repeated loading and unloading of the material results in a slight permanent residual strain and also a hysteretic response of decreased area (and therefore less dissipated energy) and decreased peak stress for later cycles relative to earlier cycles. After thousands of compressive cycles to 0.85 strain, Cao et al. reported roughly 15% residual strain [117]. Most of the decrease in hysteresis area occurs within a few cycles, at which point the material behaves with a steady-state response that is mostly unchanged for any number of later cycles [40, 117] (see especially the study of the fatigue behavior of CNT arrays by Suhr et al. [118]). This initial decrease in energy dissipation for the first several cycles is often referred to as *preconditioning*, and is observed in many rubbery (e.g., [162]) and biological materials (e.g., [163]). We observe that the preconditioning effect in CNT arrays undergoing compression is a local effect, which only occurs up to the maximum compressive strain that is reached. When the maximum strain of all previous cycles is exceeded in a later cycle, immediately the stress-strain response returns to the primary loading path of the pristine material.

These observations in sum are analogous to the Mullins effect in certain rubbers [162], which has been observed in indentation experiments on CNTs in the past [114] as well as for compression of CNT arrays in our recent work [152, 164]. Namely, the Mullins effect is defined to involve a stress-softening behavior that includes three observations (see, for example, Refs. [165, 166]): first, the stress measured at a given fixed value of strain will be lower on unloading than it is on loading (defining a hysteresis); second, for repeated loading and unloading to a given maximum strain, a decreasing maximum stress will be observed for the first several cycles until a steady-state hysteresis is eventually reached; and finally, despite this hysteresis of

declining area, when a loading path reaches a higher strain than the maximum strain of all previous cycles an immediate return to the primary loading path is observed (i.e., the stress-strain curve of the pristine material). All three of these elements are present in a wide series of experiments that we performed on different samples and varying architectures of CNT arrays, including single-layer and multilayer structures [40, 72, 140] (the effect will be discussed more in Section 6.2). For the sake of example, Figure 2.4[3] shows the stress-strain response that we recorded through quasistatic compression tests on a single-layer CNT foam, which was compressed three times to a maximum overall strain of $\epsilon = 0.4$ and then three times to a maximum strain of $\epsilon = 0.8$.

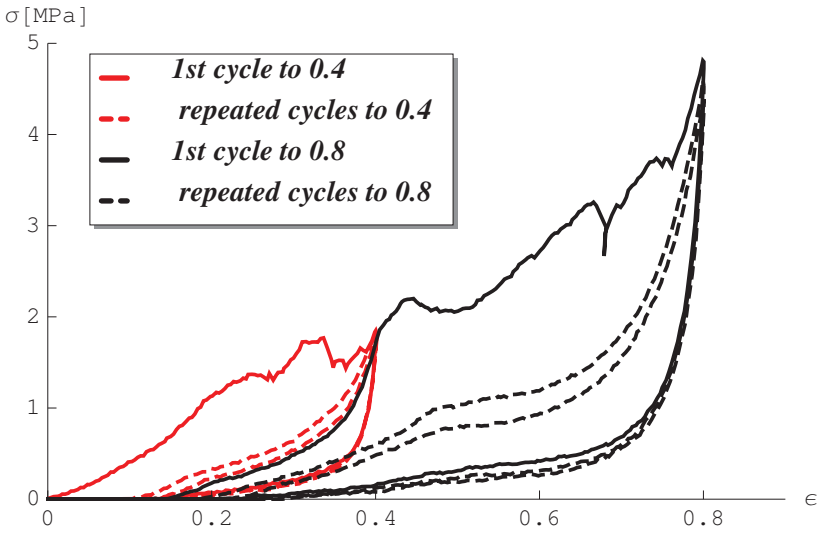

Figure 2.4: The stress-strain response of a single-layer CNT sample for repeated loading to different compressive strains

Even when the structure of individual CNTs is held relatively constant, the morphology of a CNT array, and hence the interaction of those CNTs, is of vital importance in determining the properties of the final material. For example, the lateral interaction of the nominally aligned CNTs in these arrays is an important parameter for determining array behavior (such as compressive modulus [167]), and it has been observed to vary with total array height, with taller arrays often showing more

[3] This figure is reproduced from our recent work, Ref. [152].

lateral entanglement [168]. Arrays as short as 50 nm [169] and as long as several millimeters [157] have previously been examined. The mechanical responses of these extreme cases have been very different, with the former short sample being made up of non-interacting parallel CNTs and the latter of highly entangled CNTs.

The local rearrangements and buckling associated with preconditioning and the Mullins-like behavior of the CNTs give rise to an important mechanism for energy dissipation during the first few compressive cycles. The material continues to exhibit a hysteretic response after preconditioning, however, and therefore the mechanisms of energy dissipation must be enumerated separately for both the preconditioning (and the associated Mullins-like strain dependence) as well as the steady-state response of the material for later compressive cycles. The energy dissipation observed in compressed CNT arrays is a result of the interplay of several distinct mechanisms, including friction and entanglement between CNTs. Additionally, individual CNTs have been observed in axial compression to undergo elastic shell buckling, with an unstable kinking regime associated with negative stiffness and resulting dissipation [69, 70]. This latter mechanism leads to a form of rate-independent hysteresis (or "transformational plasticity") at the macroscopic scale, which is similar to that observed in metals, shape memory alloys, and open-cell foams (refer, e.g., to [170, 171] and to the references therein). A similar rate-independent mechanism arises from the rapid breaking and formation of van der Waals interactions between CNTs, as recently observed by Yang et al. [172]. These mechanisms provide a physical basis for the model that is utilized and developed later (Chapter 6 and Appendix A) and are likely responsible for the impressive temperature-independent viscoelastic properties [173] and the strain rate independence (Section 6.2) that have been observed for bulk CNT-based materials.

With the above considerations related to the structure at nanometer and micrometer length scales, the analogy between CNT arrays and more traditional foams is primarily limited to the macroscopic phenomenological response of the systems to compression. Notably, CNT arrays are structures made up of structures (nanoscale tubules) unlike most foams, which typically consist of a traditional matrix material

(e.g., a polymer such as polyurethane or a metal such as aluminum) that is structured to include voids. There are indeed scaling effects as the size of these voids (i.e., the porosity of the bulk material) is changed. However, there are also effects (referred to as *intrinsic effects* by Gibson and Ashby [153]) which are derivative from the cell-wall material itself. For example, any strain rate dependence in the bulk material used to make the cell walls of a foam carries over to contribute a strain rate dependence to the resulting foam. The sp^2-bonded CNTs allow for relatively strong π-π and van der Waals interactions between adjacent CNTs, which have been observed to rapidly break and re-form [172]. This results in interesting new physics that would not be observed in traditional foams due to the *intrinsic* properties of the materials, regardless of scaling. For example, CNT-based materials show temperature-independent viscoelasticity over a range of more than 1000 K due to the structure of the CNTs and the mechanisms (primarily van der Waals forces) that govern their interactions [173], which is unprecedented for more traditional materials. The strain-rate independent deformation referenced above [172] (and our own data in Section 6.2) serves as another example of this fundamental difference arising from the intrinsic effects of the materials—a difference that would exist irrespective of scaling.

It is observed that many of the compressive properties of CNT arrays (such as loading modulus, energy dissipation, and peak stress) vary substantially from sample to sample, even when synthesized during the same growth cycle. We found that this variability correlated well with the bulk density of the samples (Figures 2.5 and 2.6), defined simply as the mass divided by the total volume of the sample (including interstitial space between CNTs and the volume enclosed by CNTs) (see Section 3.1 and Refs. [40, 52]).[4]

It turns out that the samples can vary in bulk density by up to a factor of two even within the same growth substrate (although typically it is closer to 10-20%). We quantified this effect statistically for many different growth substrates, and we observed that the density is always highest for the part of the substrate nearest the

[4]Figures 2.6 and 2.7 are from our previously published work [52] and are reprinted here with permission.

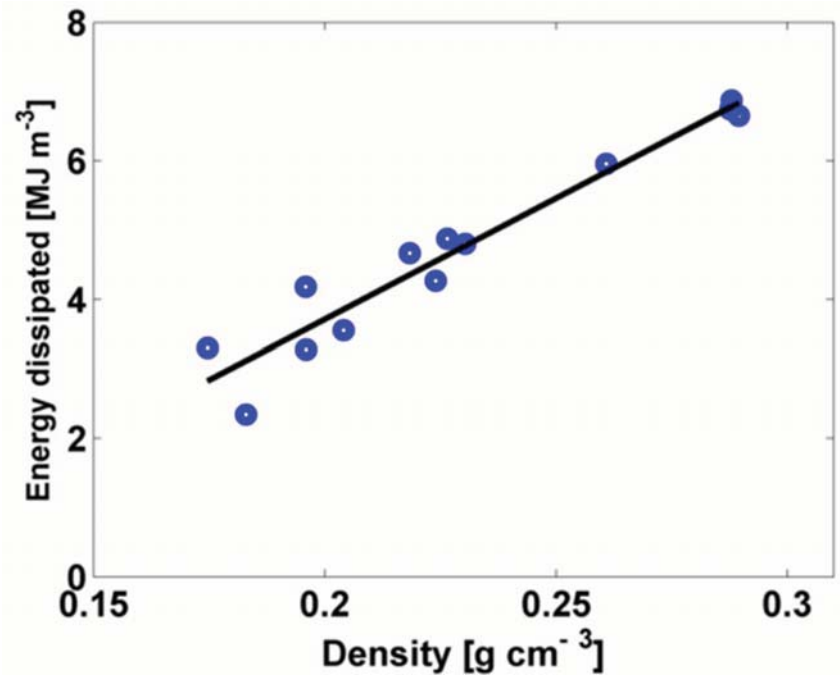

Figure 2.5: Energy dissipation (per unit volume) as a function of sample bulk density; measurement uncertainty is of less size than the circular data markers

inlet of the gases into the furnace (Figure 2.7). This has potential to allow for tailoring of the mechanical properties of materials based on CNT arrays. If a softer material is desired, CNT arrays should be selected from the side of the substrate farthest from the entrance of the gases into the furnace (i.e., the samples with the lowest density). Discussions related to this possibility are presented later (e.g., Sections 3.1, 6.3, and 7.2.2).

Instead of speaking in terms of bulk density, the relative density is a common measure often used in discussions of foams [153]. The relative density is defined as the bulk density of the porous material normalized by the density of the solid material from which it derives. For most of this dissertation, the analysis is conducted in terms of bulk density rather than relative density in order to avoid the ambiguities associated with the definition of the density of the solid material in our case. That is, our "foams" are constructed of a porous arrangement of members that are themselves structures (tubular graphite) rather than a solid material. Depending on the number of walls of the CNTs, the "solid density" of fully-densified CNTs varies. If one preferred to

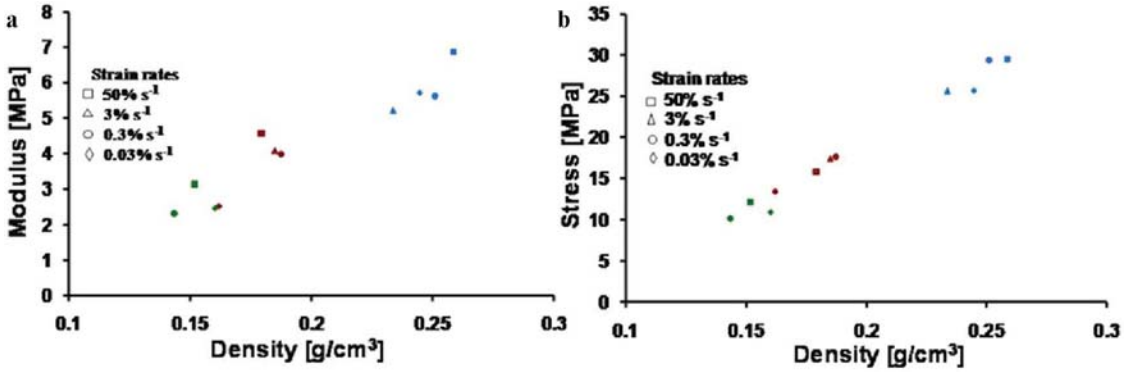

Figure 2.6: (a) Loading modulus and (b) peak stress (at 0.8 strain) as a function of sample bulk density; measurement uncertainty is accurately characterized by the size of the data markers

use relative density, therefore, the simplest approach would be to use the density of graphite ($\sim$2.15 g cm^{-3}) as the solid density. This would mean that our typical CNT arrays of 0.1 to 0.3 g cm^{-3} would have relative densities in the range $\sim$0.047–0.14. Regardless of whether one prefers bulk density or relative density, the important thing is that many of the mechanical properties trend linearly with variations in these.

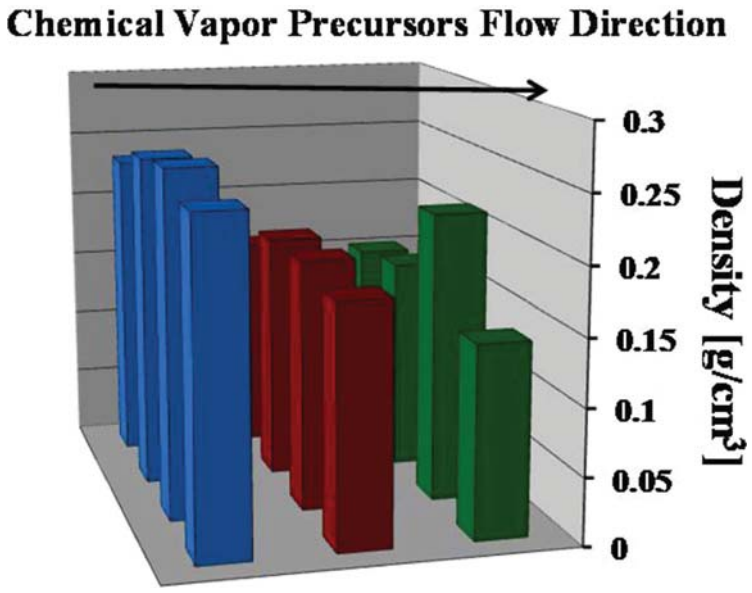

Figure 2.7: Bulk density of CNT samples according to their original position on their growth substrate

Figure 2.6 was discussed earlier in the context of understanding the effect of a

sample's bulk density on its compressive properties. That figure also includes information regarding strain rate, however. In that particular study [52], as well as in another previous work of ours [140], strain rate was not observed to have any effect for the first compressive cycle. However, as noted earlier, it is known that the behavior associated with deformation and energy dissipation differ from the first compressive cycle to later cycles. Therefore the strain rate dependence must be checked for both the first loading cycles of CNT array samples as well as subsequent preconditioned cycles in case the fundamental dissipative mechanisms differ. Such an analysis will be conducted in Section 6.2.

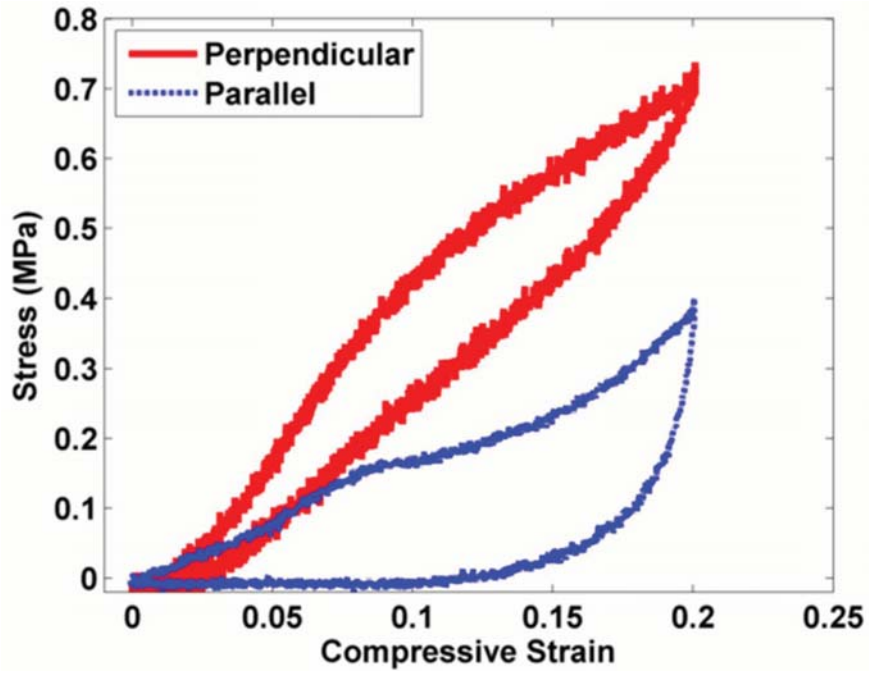

Figure 2.8: Comparison of the compressive response of CNT arrays that are loaded to small strains either perpendicular to or parallel with the CNT alignment direction

Given the clear physical anisotropy that exists in CNT arrays, with CNT bundles nearly parallel to one another from bottom to top of the structure, it is no surprise that there is also anisotropy in the mechanical properties. Loading the material either perpendicular to or parallel with the CNT alignment direction results in qualitatively similar behavior, however, including the formation of a stress-strain hysteresis, recovery from compressive strain, and preconditioning effects for repeated loading that

are associated with the Mullins-like behavior discussed earlier. Figure 2.8 shows the compressive response for loading in both of these directions for small strains. Notice that compression perpendicular to the direction of CNT alignment results in a more rapid rise in stress for a given strain, and produces a hysteresis of smaller area in the strain domain of Figure 2.8. For these two reasons, it is clear that for damping applications that involve small strains, loading CNT arrays parallel with the alignment direction results in superior protection. For dissipative applications it is generally desirable for the hysteresis to be as large as possible yet also as flat as possible (in the plateau region), to prevent stress spikes exceeding some application-dependent protective threshold.

The picture changes somewhat for large strains, however (see Figure 2.9), with the hysteresis area for each compression mode becoming comparable. More interesting perhaps is the pattern of rising and falling stress for the parallel case and the lack thereof in the perpendicular case (Figure 2.9). This is a direct consequence of the fact that loading in parallel with the alignment results in a non-reversible reorientation of the individual CNTs in order to allow for collective buckling [156] (the non-reversible nature of this reorientation means that the rising/falling stress pattern is not present even in the parallel loading case after the first compressive cycle—see Section 6.2). Because of this reorientation and subsequent structural buckling, it is also observed that loading in parallel results in less strain recovery than does perpendicular loading (i.e., in which no structural buckling is taking place). For example, in a typical experiment to a strain of $\epsilon = 0.5$ there would be residual strains of ~ 0.04 and 0.12 for the perpendicular and parallel cases, respectively. Related to this is the fact that there is a much larger change in mechanical properties (such as hysteresis area) from the first cycle to later cycles for parallel loading than there is for perpendicular loading. In fact, though parallel loading usually dissipates more energy than perpendicular loading for low or moderate strains for the first cycle, after several cycles the perpendicular case can exceed the parallel case.

The structure and properties of CNT arrays can be altered by a variety of processes, some of which will be discussed in upcoming chapters of this work, and these

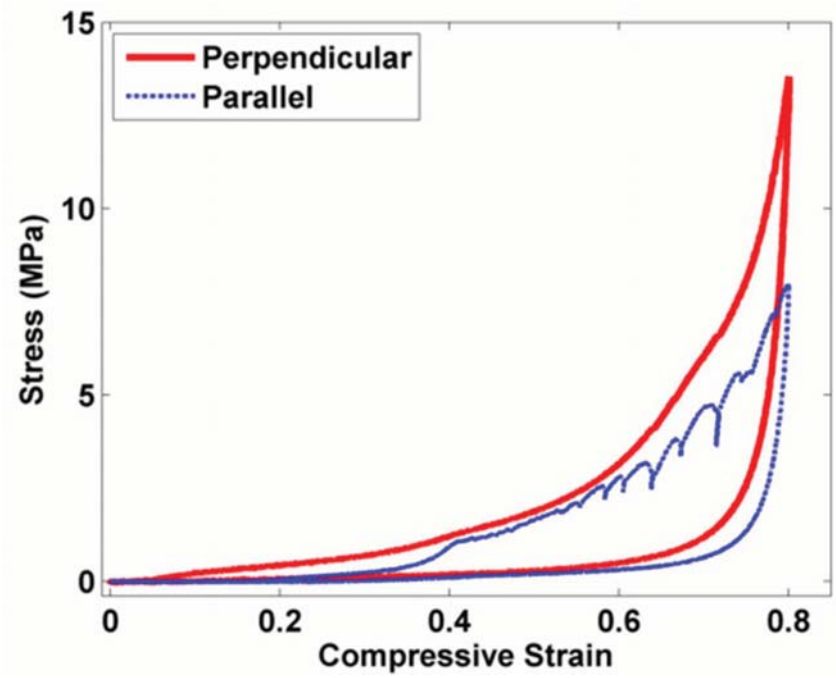

Figure 2.9: Comparison of the compressive response of CNT arrays that are loaded to large strains either perpendicular to or parallel with the CNT alignment direction

can change the typical mechanical response for CNT arrays which has been discussed above. For example, after synthesis is complete individual CNTs can be thickened with additional graphitic or partially-graphitic layers [119, 174]. In addition to affecting whether or not a CNT array will recover after compression [119], as discussed earlier, this thickening has also been noted to be a way in which various properties of the arrays can be tuned. Li et al. noted the ability to increase CNT diameters and the bulk density of CNT arrays by an order of magnitude, resulting in an increased modulus of three orders of magnitude and increased electrical conductivity by a factor of five [174]. Detailed discussions about modifying the mechanical properties of CNT arrays begin in Chapter 3.

2.3 Viscoelasticity of CNT arrays based on creep and stress relaxation tests

Time-dependent properties have been observed both for indentation [159, 175, 176] and compression [151, 157] of CNT arrays. Indentation tests revealed viscoelastic behavior in arrays of CNTs [176] which has been attributed to "tilting and twisting" of the individual tubes [177]. Deck et al. observed a viscoelastic response in millimeter-scale aligned CNTs under compression [157] which was later studied in more detail by Lattanzi et al. (see Ref. [151]), and presented here in part. The viscoelastic behavior of CNT-based structures is unique relative to most viscoelastic materials for its temperature invariance over a very large range (a range of $\sim$ 1200 °C) [173, 178, 179]. This is remarkable when compared to typical polymeric viscoelastic damping materials, usually only effective from around 0 to 100 °C [108, 180].

Under a spherical indenter CNT forests have been shown to undergo time-dependent creep deformation [159], and viscoelastic relaxation due to the thermally activated change in nanotube contacts [175].[5] Dense CNT brushes have been shown to exhibit a viscoelastic response under dynamic indentation for loads below the critical CNT buckling load [176]. Zhang et al. [159] have shown a dependence of creep strain rate on the density of CNT forests, reporting a lower creep deformation in denser material.

Here, we describe the bulk time-dependent response of millimeter-long CNT arrays. We performed bulk creep and stress relaxation tests and fit the results with a time power-law. We tested the viscoelastic response of all samples at different strain and stress levels. For the stress-relaxation tests, strains of ϵ = 0.1, 0.2, 0.4, 0.6, and 0.8 were applied at a strain rate of 0.03 s^{-1} and held for 3x10^4 s. Creep tests were performed using stress values of 1, 4, 8, 12, 15, and 18 MPa, which were initially applied at a stress rate of 1 MPa s^{-1} and held for 3x10^4 s.

The creep behavior for CNT arrays is shown in Figure 2.10. The increase in foam

[5] The remainder of this section is adapted from our recent work, Ref. [151] by L. Lattanzi, J.R. Raney, L. de Nardo, A. Misra, and C. Daraio. LDN and CD designed the study. LL synthesized samples and performed the mechanical tests with support by JRR and AM. LL wrote the manuscript with support from JRR. All authors contributed to analysis of the results.

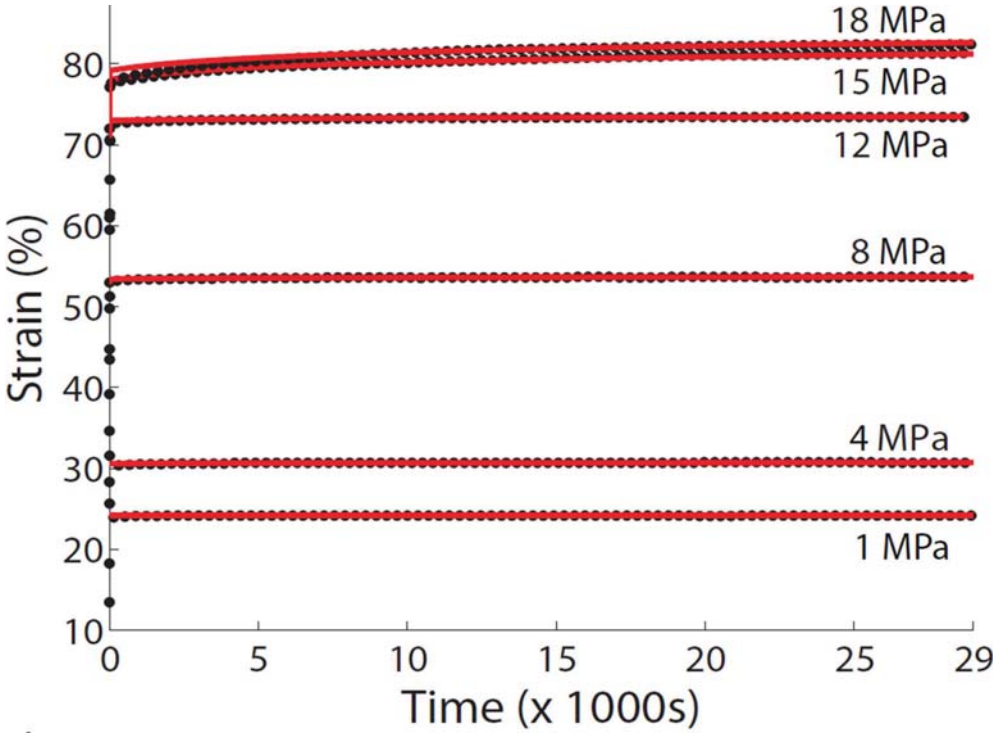

Figure 2.10: Experimental creep response (points) and power law curve fitting (solid lines)

deformation over time with a step-constant load exhibits a short primary stage and a long secondary stage in which the strain rate is constant. Results obtained from the stress-relaxation tests are reported in Figure 2.11. All samples show a decrease in stress with time and an increase of stress values for increasing step strain levels.

The progressive deformation under step-constant stress (Figure 2.10) and the decrease in stress over time with a step-constant strain (Figure 2.11) confirm the time-dependent behavior typical of viscoelastic materials [181]. During compression, CNTs change their alignment, becoming less oriented, breaking van der Waals forces, and creating new tube–tube interactions [118]. Such behavior can be compared to the conformational changes observed in polymer chains. The parallels between CNTs and polymers have been proposed by Green et al., who explored the structure, properties, and rheology of CNTs, referring to the material as "the ultimate polymer" [182].

A more accurate description of the viscoelastic behavior can be obtained by studying the dependence of relaxation rate on strain levels and of the creep rate on stress

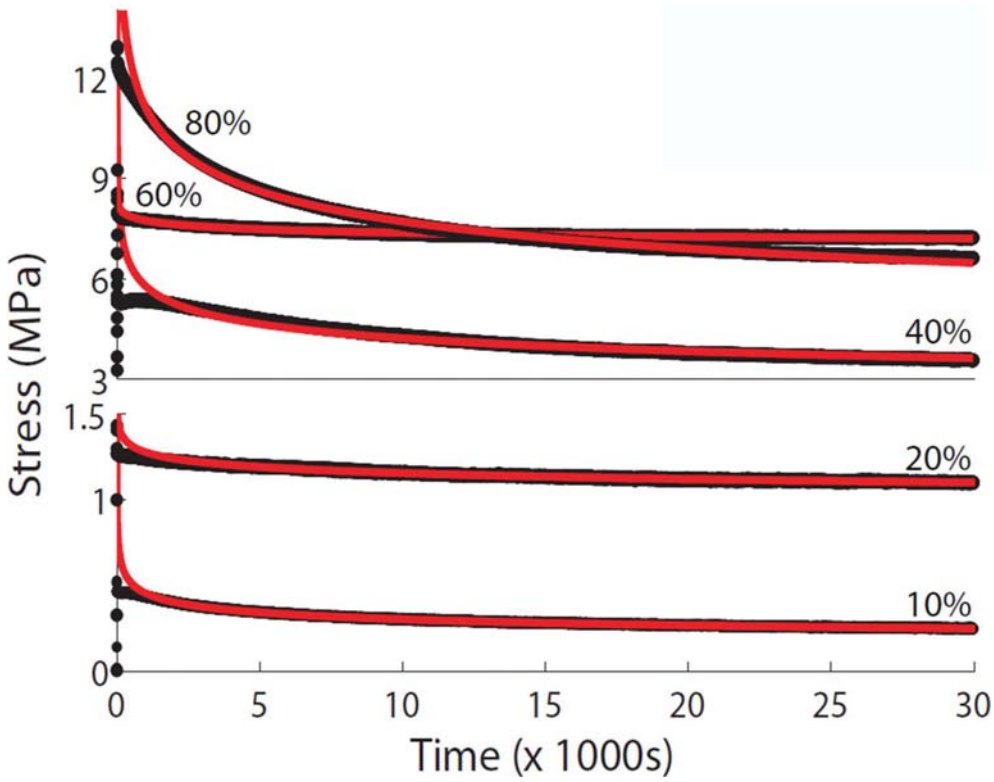

Figure 2.11: Experimental stress relaxation response (points) and power law curve fitting (solid lines)

levels [181]. For linear viscoelastic materials, the relaxation/creep rate does not depend on the strain/stress level, being characterized by a constant value. In contrast, nonlinear viscoelastic behavior is strongly dependent on the strain/stress level [181]. Many theories have been developed to study nonlinear viscoelasticity (e.g., Ref. [183]). Because of the complexity of these nonlinear theoretical formulations, empirical approaches are often used [183] to describe the main features of the creep [181] and stress relaxation behavior [184] of viscoelastic materials. Here we use power functions of time to fit the creep (Eq. 2.2) and stress relaxation (Eq. 2.3) tests:

$$\epsilon(t) = K_{cr} t^n \tag{2.2}$$

$$\sigma(t) = K_{sr} t^m \tag{2.3}$$

where $\epsilon(t)$ and $\sigma(t)$ are the strain and stress as a function of time, respectively, and K_{cr} and K_{sr} are the power-law coefficients. The values n and m are dimensionless power-law exponents that indicate the relaxation rate of creep and stress-relaxation tests, respectively [184]. Figures 2.10 and 2.11 show creep and stress-relaxation test results: the points represent the experimental data while the solid lines represent the power function fit. The results confirm that the power-law gives a good representation of creep and stress relaxation behavior. The values of the power-law exponents n and m are summarized in Tables 2.1 and 2.2, respectively.

Stress (MPa)	1	4	8	12	15	18
n x 10^3	0	3.0 ± 1.7	2.8 ± 1.4	3.6 ± 1.1	10 ± 2.1	13.8 ± 3.1

Table 2.1: Creep exponent n (Power-law exponent). Table reports the values plotted in Figure 2.12a

Strain	0.05	0.1	0.2	0.4	0.6	0.8
m x 10^2	-16.0 ± 2.0	-19.0 ± 2.8	-2.0 ± 1.7	-8.0 ± 1.7	-2.0 ± 0.58	-14.6 ± 1.1

Table 2.2: Relaxation exponent m (Power-law exponent). Table reports the values plotted in Figure 2.12b

The creep exponent n varies as a function of applied stress, presenting three distinct regions (Figure 2.12a). At low stress values ($\sigma < 4$ MPa), freestanding CNTs show a near 0 creep exponent, suggesting the absence of secondary creep. At such low stress values, freestanding CNTs instantly deform and maintain the step strain for the entire 3x10^4 s. The absence of creep suggests that at low stress values CNT arrays do not show a viscoelastic response. The second region is characterized by a critical stress ($\sigma \sim 4$ MPa) at which freestanding CNTs exhibit secondary creep showing a creep exponent of ~ 0.004 and a viscoelastic response. The results suggest that until a certain stress, ~ 12 MPa, n does not depend on the stress levels, showing the same value at each applied step stress (4, 8, 12 MPa). The quasi-horizontal trend of n suggests an almost linear viscoelastic behavior of freestanding CNTs for stress in the 4–12 MPa range. In the third region (highest stress values of Figure 2.12a), the creep rate increases by nearly an order of magnitude, reaching the values of 0.01 for

15 MPa and ~ 0.015 for 18 MPa. The different creep exponent values observed in this third region suggest that the linear viscoelastic approach is valid up to a critical stress level, which is referred to as the linear viscoelastic threshold, here ~ 12 MPa. Above this stress level the response of the material becomes nonlinear.

Figure 2.12b shows the relaxation exponent m vs. strain for CNT arrays. Results again show a response characterized by three different regions: an initial portion (up to $\epsilon = 0.1$) characterized by a relaxation exponent nearly -0.2; the next, from $\epsilon = 0.2$ to $\epsilon = 0.6$, in which the magnitude of m decreases by nearly an order of magnitude ($-0.05 < m < 0$), and finally an increase in the magnitude of the relaxation exponent for the applied step deformation $\epsilon = 0.8$. Results show that at low strain values ($\epsilon = 0.05$ and $\epsilon = 0.1$), the viscoelastic response is significant, while at strain values ranging from $\epsilon = 0.2$ to $\epsilon = 0.6$, CNT forests do not show any appreciable viscoelasticity. The decrease in the magnitude of m is probably caused by the increased adhesive interactions between the nanotubes when squeezed together, as previously observed by Pathak et al., studying the viscoelasticity of dense carbon nanotube brushes by nanoindentation tests [176]. Pathak et al. explained such behavior by comparing CNT foams to polymers, like rubber, where an increase in cross-linking leads to a decrease of the viscoelastic response. This also corresponds with the observations of coordinated buckling at those strain levels made by Zbib et al. [156]. During compression of CNT arrays, the individual CNTs begin somewhat randomly oriented (though still mostly along the vertical), but for buckling to take place the CNTs reorient and more closely align, ultimately forming collective buckles [156]. On the contrary, the increased magnitude of m at $\epsilon = 0.8$ corresponds to a densification regime in which these ordered buckles can crack and separate, explaining an increase in viscoelasticity at this point.

Comparing the values of the relaxation and creep exponents, it is clear that the relaxation proceeds faster than creep, confirming the nonlinear viscoelasticity of both freestanding and anchored CNTs [185]. Previous studies demonstrate that nonlinearity causes relaxation to proceed more rapidly than creep [185]. By contrast, in a linear material, power-law creep and relaxation curves have the same slope [185].

In the same study from which this section is derived (Ref. [151]) we also analyzed the viscoelasticity of CNT arrays that had been anchored in polymer (specifically, both the top and the bottom were anchored into ~ 50 μm thin films of (poly)dimethyl siloxane). The partial anchoring of CNT arrays in thin polymer films has been previously reported [114, 138]. Anchored CNT arrays have been shown to behave as excellent light-weight, energy-absorbing systems [114, 140]. A similar procedure is used in Chapter 5 to connect multiple layers of CNT arrays. However the changes in viscoelastic behavior caused by these layers were minimal (the most noteworthy differences were that in the case of the polymer-anchored CNT arrays there was a non-zero creep rate for small stresses due to the viscoelasticity of the polymer, and also the three regime behavior illustrated in Figure 2.12 was less distinct). The interested reader is therefore directed toward the original report (Ref. [151]) if more details regarding these differences are desired.

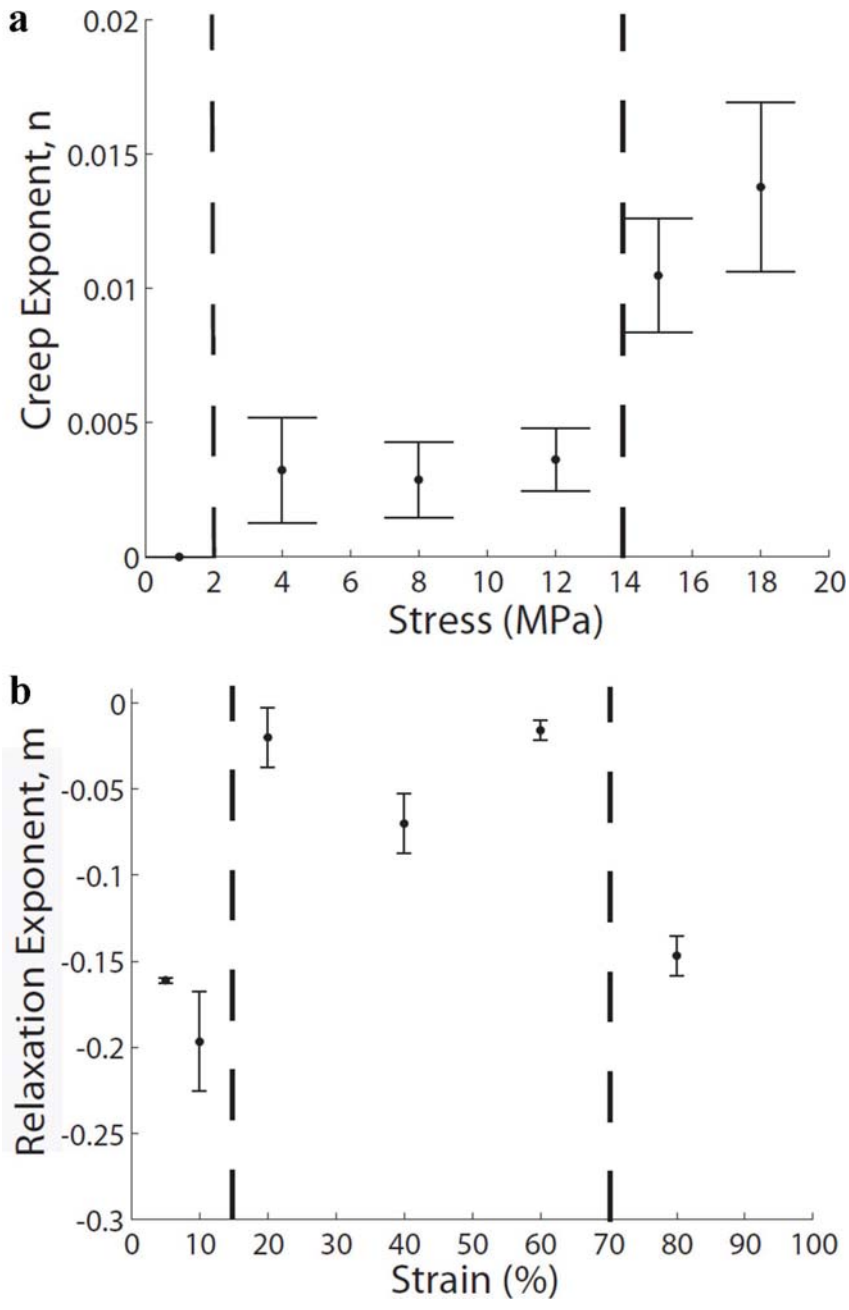

Figure 2.12: (a) Creep exponent n vs. stress and (b) relaxation exponent m vs. strain

Chapter 3

In situ tailoring of the microstructure and properties of arrays during CNT synthesis

This chapter derives from two recent papers about the tuning of structure (and thereby the tuning of mechanical properties) of CNT arrays. The uniting feature of the two approaches is that they are both used during CNT synthesis to affect the resulting array properties (approaches used after CNT synthesis are discussed in Chapters 4 and 5). The first study looks at the effect of hydrogen concentration in the furnace gas during synthesis (Section 3.1). Typically we used 100% argon at 1 atm as the flow gas, but here hydrogen was added in different quantities, proving to be a means to affect the CNT diameter distribution and, as an effect, the bulk density and mechanical properties of the CNT arrays. The second study looks at the effect of the injection rate of the carbon/catalyst precursor solution into the furnace (Section 3.2). Typically a constant rate of 1 ml min^{-1} was used, however in this section we varied the input rate during synthesis. This allowed the density and alignment of CNTs to be controlled along the height of the CNT arrays, affecting certain dynamic properties as well as the way in which strain is localized in compression.

3.1 Effect of the hydrogen concentration used during synthesis

Abstract

We synthesize vertically aligned arrays of carbon nanotubes (CNTs) in a chemical vapor deposition system with floating catalyst, using different concentrations of hydrogen in the gas feedstock[1]. We report the effect of different hydrogen concentrations on the microstructure and mechanical properties of the resulting material. We show that a lower hydrogen concentration during synthesis results in the growth of stiffer CNT arrays with higher average bulk density. A lower hydrogen concentration also leads to the synthesis of CNT arrays that can reach higher peak stress at maximum compressive strain, and dissipate a larger amount of energy during compression. The individual CNTs in the arrays synthesized with a lower hydrogen concentration have, on average, larger outer diameters (associated with the growth of CNTs with a larger number of walls), but present a less uniform diameter distribution. The overall heights of the arrays and their strain recovery after compression have been found to be independent of the hydrogen concentration during growth.

3.1.1 Introduction

While the potential applications of carbon nanotubes (CNTs) have garnered much attention [1], the full realization of macroscale benefits from these nanoscale objects remains an active area of research. Chemical vapor deposition (CVD) is one of several approaches used to synthesize CNTs, commonly chosen for its high growth yield [26, 186, 187]. The vertically aligned CNTs (VACNTs) resulting from this process have been proposed for use in a number of applications due to their unique structure, including field-emission electron sources [188], brushes for electrical motors [112], as

[1] This section has been previously published as Ref. [40] by J.R. Raney, A. Misra, and C. Daraio and is here reproduced with the publisher's permission. JRR and CD designed the study. AM performed transmission electron microscopy and Raman spectroscopy. JRR synthesized samples, performed the mechanical testing, conducted scanning electron microscopy, and wrote the manuscript. All authors contributed to the analysis of the results.

well as fatigue-resistant foams [118]. In the CVD growth process, the catalyst, usually iron, can be deposited onto an oxidized silicon substrate prior to the CVD process [187]. Alternatively, an appropriate catalyst precursor, such as ferrocene, can be floated into the system along with a carbon source [26]. This latter approach results in an increased quantity of catalyst particles throughout the resulting material. The continuous deposition of catalyst, however, allows for easier synthesis of tall VACNT arrays, suitable as bulk materials, when compared to the predeposited approach, which requires more elaborate synthesis procedures to obtain tall growth (compare Refs [26, 117, 187, 189]).

The mechanical properties also differ between CNTs grown with pre-deposited catalyst and those grown with floating catalyst [154]. For example, the floating catalyst approach has been shown to produce VACNTs that exhibit a foam-like hysteresis during compressive deformation followed by recovery to nearly their original height even after large strains [117]. Such recovery is not typically observed for VACNTs grown with predeposited catalyst (neither as a bulk material nor in the form of micro pillars) [120, 154, 189], with a recent study concluding that this is a result of differences in CNT surface roughness [119]. The foam-like response of VACNTs synthesized by the floating catalyst approach has already been exploited in the development of electrically conductive VACNT-based composites that absorb more than two orders of magnitude the amount of energy absorbed by typical polymeric foams of comparable bulk density [140].

Despite these promising characteristics, controlling the VACNT properties during synthesis remains a challenge. There have been a large number of studies regarding the optimization of predeposited catalyst CVD synthesis of VACNTs. Progress has been made in understanding how such factors as temperature [187], catalyst layer thickness [25], spacing of catalyst particles [190], various pretreatments of the substrate surface [24], and gas composition [42] can be altered to control certain microstructural properties of the resulting VACNTs. It has also been shown for this type of process that hydrogen can serve an important role in controlling the diameter of the resulting CNTs, as a result of breaking up the deposited catalyst layer into

smaller particles [24], and that it can also help prevent the formation of amorphous carbon impurities [41, 43].

In the floating catalyst case, there have been several studies about how gas composition affects the quality of synthesis [37, 38, 46]. The effect of hydrogen on the properties of individual CNTs has received some attention, but no systematic analysis has been performed to address its impact on bulk mechanical properties. One study of a xylene-based floating catalyst system, for example, concluded that depending on the precise hydrogen concentration present during growth the ensuing product could be soot, carbon fibers, carbon nanotubes, or nothing at all, over a relatively narrow range of hydrogen amounts [191]. However, the extreme hydrogen sensitivity observed in [191] might be setup dependent, or intrinsic to xylene-based systems.

In the present study the effect of hydrogen concentration on the growth of VACNTs is investigated for a toluene-based floating catalyst system. It is found that multi-wall VACNTs of consistent quality are obtained regardless of the hydrogen concentration (examined from 0% to 50% of the total gas feedstock); however the microstructure and mechanical properties change substantially. The purpose of this study is therefore twofold: (i) to explore how the microstructure of arrays of VACNTs depends on hydrogen concentration during synthesis, and (ii) how this changing microstructure affects the bulk mechanical properties of the VACNT arrays. The ability to tune the mechanical properties by altering the hydrogen concentration to be used during synthesis raises the possibility of constructing composite materials with desired strength and deformation properties. For example, this approach could be used to create multilayer materials similar to those reported elsewhere [130, 140] but in which the localization of deformation under compressive loading can be predetermined and controlled [72].

3.1.2 Experimental

Vertically aligned arrays of multi-wall CNTs were synthesized by floating catalyst thermal chemical vapor deposition at atmospheric pressure. The system utilized a

long quartz furnace tube with a 4.1 cm internal diameter and a $\sim$ 15 cm heating zone. The temperature of the heating zone was 827 °C. A thermally oxidized Si wafer was used as the substrate for CNT growth. A solution of ferrocene (the Fe catalyst precursor) and toluene (the carbon source) were mixed at a ratio of 0.02 ml^{-1}. A total of 50 ml of this solution was injected into the furnace at $\sim$ 1 ml min^{-1}. Synthesis cycles were performed with different quantities of hydrogen, varying from 0 to 400 sccm in 80 sccm increments (corresponding to concentrations from 0% to 50% of the total gas flow), with argon flow adjusted correspondingly from 800 to 400 sccm to maintain a total combined gas flow rate of 800 sccm. The amount of hydrogen used was fixed during each synthesis cycle. The result of this process was arrays of VACNTs with total thickness (i.e., height along the CNT axis) of $\sim$ 1 mm. These thick VACNT arrays were resilient against handling and could be physically manipulated. Prior to any mechanical testing, VACNTs on their growth substrate were sectioned into square areas of $\sim$ 16 mm^2. The VACNTs were subsequently removed from the growth substrate, to which they were only weakly bonded, with a razor blade. The mass of each sample was measured with a microbalance. The sample height (along the long CNT axis) was determined using a commercial materials tester (Instron E3000). A small preload of about 0.2 N ($\sim$ 0.12 MPa for our samples) was used on all samples to ensure uniform contact. The apparatus measures displacement in 1 μm increments, resulting in an uncertainty of $\sim$ 0.1% for our samples ($\sim$ 1 mm thick). The volume of each sample was obtained by multiplying the sample height by the corresponding cross-sectional area. Bulk density was then calculated by dividing the mass by the corresponding volume of each sample. The average bulk density of samples grown with no hydrogen in the feedstock was 0.229 g cm^{-3}. However the bulk density was observed to vary with the sample's spatial position in the growth substrate. Higher densities were observed for CNTs grown on substrate areas closer to the entrance of the flowing gases, as reported elsewhere [52].

Quasistatic cyclic axial compression was performed with the same apparatus (Instron E3000), along the axis of the VACNTs. The stress-strain response was measured up to a set maximum compressive strain of 0.8 (chosen to avoid exceeding the force

capacity of the apparatus), with a constant strain rate of 0.01 s^{-1} for both loading and unloading.

Scanning electron microscopy (SEM) was conducted with a FEI Sirion at 15 kV on as-grown samples that had been removed from the growth substrate. Transmission electron microscopy (TEM) was performed using a FEI TF30UT at 300 kV. Samples were prepared for TEM by placing a small amount of the VACNTs into isopropyl alcohol and sonicating until the CNTs were dispersed. A small drop of this solution was placed on a TEM grid and the isopropyl alcohol was evaporated. Raman spectroscopy was performed with a Renishaw M1000 Micro Raman Spectrometer System using an Ar ion laser of wavelength 514.5 nm on samples removed from the substrate.

3.1.3 Results and discussion

After completing synthesis of VACNTs using six different hydrogen concentrations (0–50% in 10% increments) the resulting samples were characterized by SEM and TEM, as shown in Figure 3.1. The SEM image in Figure 3.1a shows the aligned nature of the CNTs as synthesized. SEM images at higher magnification for samples synthesized with no hydrogen (Figure 3.1b) and maximum hydrogen (Figure 3.1c) reveal a clear decline in the average diameter as the hydrogen concentration is increased. Likewise, TEM images in Figure 3.1d and Figure 3.1e display representative features of CNTs synthesized with no hydrogen and maximum hydrogen, respectively. Note the reduced number of walls present in CNTs produced with more hydrogen.

We relied on high-resolution SEM to statistically quantify variations in the CNT diameters. For consistency, we acquired images of the CNTs at the vertical midpoint of the growth area, to measure the CNT diameters from the same location in every sample. Results are shown in Figure 3.2a. The standard deviation of the diameter distribution corresponding to a particular hydrogen concentration also drops significantly with increasing hydrogen concentration (inset of Figure 3.2a). That is, a higher concentration of hydrogen during synthesis results in CNTs with a lower average diameter and an increased uniformity of diameters. This effect is in agreement with

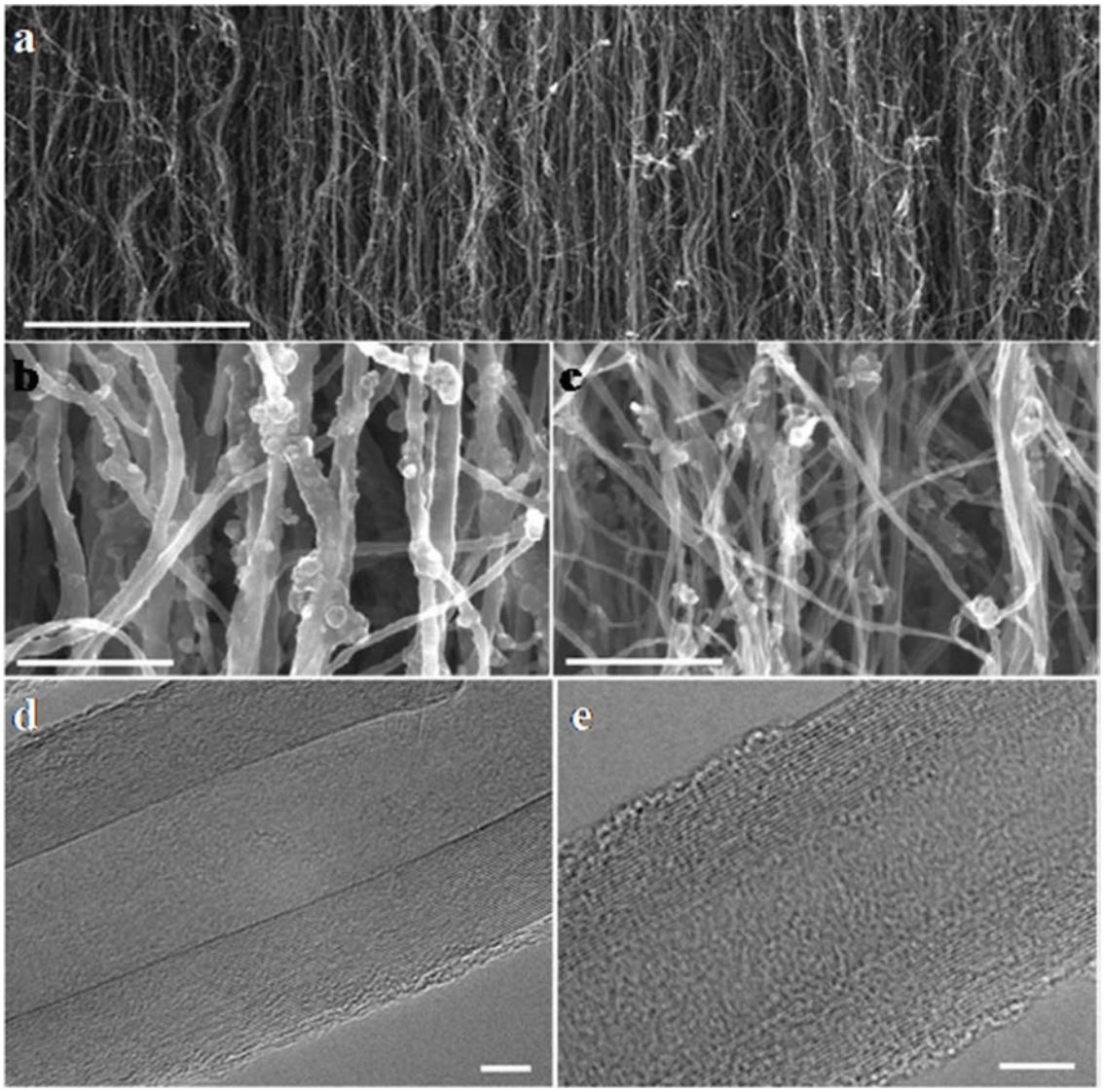

Figure 3.1: (a) SEM image of a typical sample showing the mostly aligned nature of VACNTs as synthesized; scale bar is 5 μm. (b and c) High-resolution SEM images of CNTs grown with no hydrogen and those grown with 400 sccm (50%) hydrogen, respectively; scale bars are 500 nm. (d and e) TEM images of characteristic CNTs synthesized with no hydrogen and with 400 sccm (50%) hydrogen, respectively; scale bars are 5 nm

observations made in the case of floating catalyst synthesis of single-wall CNTs [192].

At the macroscale, the average height of the VACNTs does not change significantly with variations in the hydrogen concentration. However, their bulk density presents visible changes when the amount of hydrogen is varied in the feedstock (Figure 3.2b).

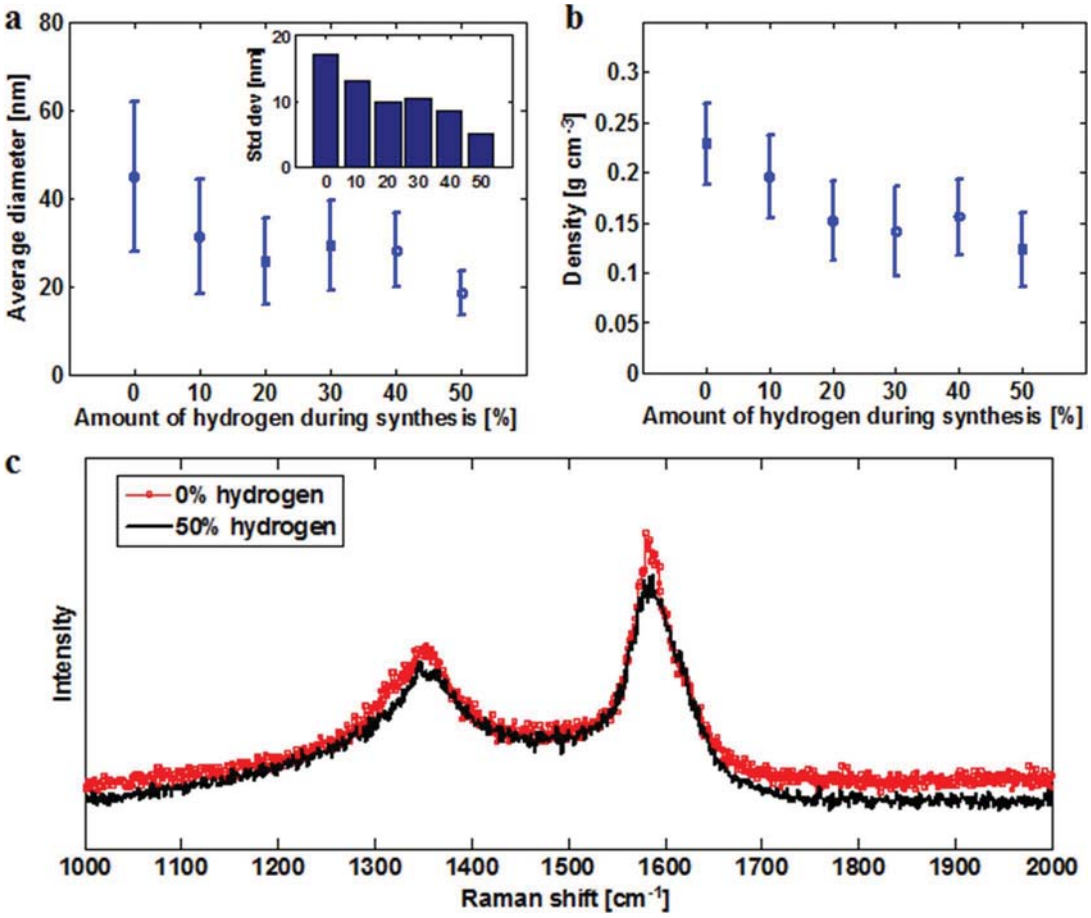

Figure 3.2: (a) Average CNT diameter for each hydrogen concentration tested, as measured with high-resolution SEM; the standard deviations of the respective diameter distributions are shown in the inset to emphasize the narrowing of the diameter distributions for increasing amounts of hydrogen. (b) Average bulk density of the CNT samples as a function of the hydrogen concentration. (c) Representative Raman spectra for samples grown with 0% (top curve) and 50% hydrogen (bottom curve). The D peak (left) is defect induced, and the G peak (right) corresponds to in-plane displacement of graphitic carbon

The average sample density for each hydrogen concentration was determined by taking the average bulk density over all samples grown on a substrate (about 20 samples for each hydrogen concentration). Variations in the mean sample densities are shown in Figure 3.2b. It is evident that the decline in average CNT diameter that is observed for increased amounts of hydrogen in the synthesis process is reflected by a decrease of the average bulk density of the samples. Error bars in Figure 3.2b are related to the variation in density that arises during growth in different areas of the substrate

(see Section 3.1.2).

We used SEM images to characterize the areal density of the CNTs (number of CNTs grown per unit area). The areal density stays the same or increases with the use of a higher concentration of hydrogen during synthesis, verifying that the reduction of bulk densities is not simply a result of a decline in the number of CNTs. High-resolution transmission electron microscopy (HRTEM) analysis of the individual multi-wall tubes revealed that the core diameter (the diameter of the innermost wall), does not statistically change with hydrogen concentration. A similar effect was observed in studies of floating catalyst systems with other additives instead of hydrogen [46], and also in studies of the effects of hydrogen in plasma-enhanced CVD systems [193]. The decline in the CNTs' outer diameters, from an average of $\sim$ 46 nm for 0% hydrogen to $\sim$ 19 nm for 50% hydrogen, corresponds to a change in the number of walls from $\sim$ 56 for 0% hydrogen to $\sim$ 18 for 50% hydrogen. The observed trend in the decline of CNTs' diameters is in agreement with earlier reports for CNTs grown in a CVD system with a predeposited catalyst [24, 41, 43]. It has been shown that introducing hydrogen into thermal CVD systems narrows Fe catalyst particles and that this results in CNTs of smaller diameters [37, 59, 194]. We expect that this effect is the primary reason why our CNTs become narrower with increasing hydrogen concentration in the furnace (in addition to the fact that the hydrogen may inhibit pyrolytic contributions to increasing CNT diameter). In order to rule out the possibility of hydrogen-induced etching as the cause of the observed smaller diameters, we placed already-synthesized CNTs back in the presence of hydrogen in synthesis conditions: we did not observe any perceptible etching or narrowing of the CNTs. Thus, the hydrogen alters the CNT diameters only when it is present during synthesis.

It was a concern that increasing hydrogen concentrations could cause defects in the CNT walls [195]. Raman spectroscopy measurements were performed to provide more quantitative information on the possible formation of defects induced by hydrogen (e.g., Figure 3.2c). Results showed the presence of the typical peaks associated with Raman spectra of multi-wall CNTs. The D peak (the left peak in Figure 3.2c) is associated with lattice defects and particle-size effects [196]. The G peak (the right

peak in Figure 2c) is associated with in-plane displacement of graphitic carbon (e.g., Figure 3.2c) [196]. The ratio of the intensity of these peaks is often used as an indicator of the quality of CNTs (e.g., Ref. [22]). It was found, however, that changing the hydrogen concentration resulted in no significant changes in this ratio. It is likely that the many walls (15–70) of our CNTs make them resilient against the marginal etching effects of hydrogen [193].

We performed quasistatic cyclic compression tests (see Section 3.1.2) to characterize variations in the mechanical properties of the VACNTs induced by the presence of hydrogen during the synthesis process (and by the related microstructural changes). All samples tested were of similar size and geometry, though it should be noted that VACNTs appear to exhibit compressive behavior that is independent of the geometry of the array [154]. Typical results for a loading and unloading cycle obtained from a sample grown with 0% hydrogen are shown in Figure 3.3a and for a sample grown with 50% hydrogen in Figure 3.3b. The stress-strain relationship for floating catalyst VACNTs under compression has been previously observed to exhibit a characteristic three-regime deformation behavior with hysteretic recovery [117], quite similar to classical foams [153]. This dissipative, hysteretic behavior is thought to be a result of friction that arises as the CNTs slide past one another [117, 118]. The three deformation regimes correspond to: (i) an initial linear elastic region for small strains, (ii) a plateau region associated with buckling for intermediate strains, and (iii) a final "densification" stage for high strains [118]. The representative results reported in Figure 3.3a and b for our samples show that an increased hydrogen concentration during synthesis results in a stress-strain relationship that more closely conforms to that expected for an ideal foam, with three distinct regions with different behaviors [153], and a more distinct plateau region with lower peak stresses.

H_2 conc. (%)	0	10	20	30	40	50
Avg. stress at 0.8 strain (MPa)	32.3 ± 5.9	19.8 ± 4.4	9.9 ± 3.3	8.6 ± 1.8	6.5 ± 1.8	5.9 ± 1.8
Avg. energy dissip. (MJ m^{-3})	4.73 ± 1.45	3.21 ± 0.83	1.82 ± 0.57	1.51 ± 0.48	1.31 ± 0.31	1.08 ± 0.44

Table 3.1: Effect of H_2 concentration on peak stress and energy dissipation

We relate this phenomenon to the observed changes in the microstructure of the

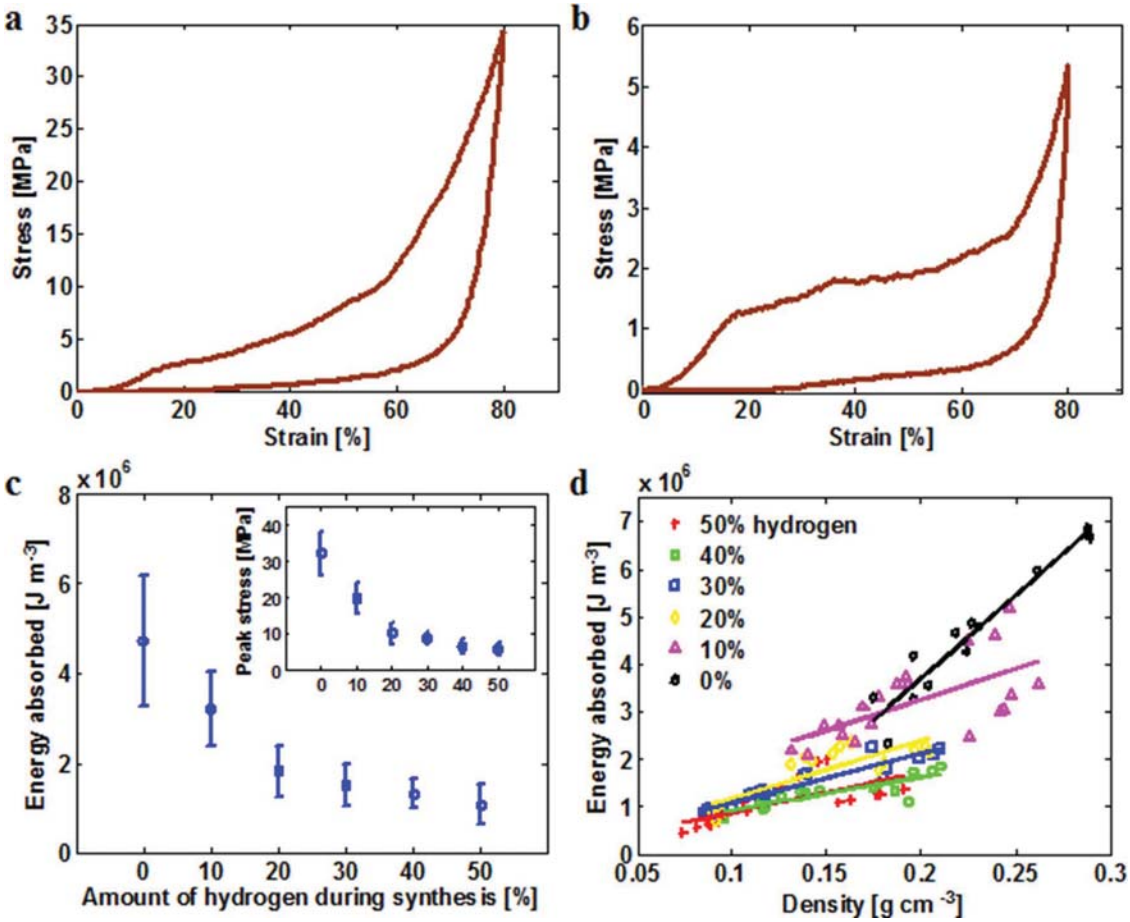

Figure 3.3: (a and b) Characteristic stress-strain curves obtained for the first cycle during quasistatic compression for the case of no hydrogen and that of 50% hydrogen, respectively. (c) Average energy absorbed per unit volume calculated for the first compressive cycle for each hydrogen concentration. The inset shows the variation of the peak stress values obtained at maximum (0.8) strain as a function of the hydrogen concentration used during growth. (d) Energy absorbed in the first compressive cycle plotted as a function of density for all concentrations of hydrogen

VACNTs, and particularly to the different diameter distribution associated with each hydrogen concentration. As shown in Figure 3.2a and the inset therein, an increased amount of hydrogen during synthesis leads to the growth of VACNTs presenting a much narrower diameter distribution, and therefore a more uniform microstructure. If the CNTs are approximated as Euler columns, as they can be when their length greatly exceeds their radius [11], their critical buckling stress is expected to be proportional to the square of the radius. An array of Euler columns of different diameters will not buckle at a single stress value. As a consequence, CNTs that are synthesized with a large amount of hydrogen (i.e., with small diameter variations within the array, e.g., a diameter distribution with a standard deviation of less than 5 nm for the 50% hydrogen case) should buckle more uniformly compared to those synthesized without hydrogen (i.e., with a much wider diameter distribution, with a standard deviation of 17 nm). This analysis is in qualitative agreement with the results displayed in Figure 3.3a, where the stress-strain curve for the VACNTs grown with no hydrogen shows a progressive buckling behavior (i.e., an approximate plateau regime with a gradual increase of stress) over a broad stress range between 2 and 10 MPa. In contrast, VACNTs synthesized with 50% hydrogen (Figure 3.3b) display a more uniform buckling behavior (i.e., a distinct plateau regime) over a much narrower stress range, between 1.3 and 2.5 MPa. It was observed that VACNTs synthesized at all hydrogen concentrations recover approximately the same amount of strain (about 0.1 residual strain after the first compressive cycle to a maximum strain of 0.8) for all samples, regardless of hydrogen concentration.

The energy absorbed per unit volume by the VACNTs during a particular compressive cycle was calculated by integrating the area within the hysteresis loop in the stress-strain curve, and was compared among samples grown with different amounts of hydrogen. An increased amount of hydrogen during growth correlates not only with CNTs of narrower diameters but also with reduced energy absorption during compression (Figure 3.3c). The decline in energy absorbed appears to reach a plateau level when the amount of hydrogen used during synthesis increases to 40–50%. The peak stress obtained at maximum strain, 0.8, follows the same trend (see Table 3.1 and the

inset of Figure 3.3c). We attribute this decline in energy absorption and peak stress to the observed variation in the microstructural properties (i.e., the variation in the bulk density of the VACNT arrays and in the individual CNT diameters/number of walls). This decrease in peak stress and energy dissipation that occurs for the VACNTs synthesized with larger amounts of hydrogen matches the decreased diameters of the CNTs themselves (and hence a decrease in the force they can bear) rather than a decline in CNT quality, as noted in the Raman analysis.

As described earlier, the density of the VACNT arrays taken from a given substrate varies with position (higher densities are measured for samples taken from areas of the growth substrate closer to the entrance of the gases in the furnace). For any given hydrogen concentration, the energy absorption of each VACNT array depends nearly linearly on this density variation (see Figure 3.3d). A similar relationship has been observed for VACNTs in the variation of peak stress with density [52]. However, it is interesting to note that two VACNT samples with the same bulk density, but synthesized with different concentrations of hydrogen, will typically absorb slightly different amounts of energy in compression, revealing that bulk density alone is not a sufficient predictor of mechanical properties. That is, a separate linear relationship between bulk density and energy absorption exists for each hydrogen concentration utilized (Figure 3.3d).

It was shown in the past that VACNTs exhibit a preconditioning effect under compression [117, 118, 140] such that the first one or two cycles differ somewhat in their mechanical properties from later cycles. For example, earlier studies [118] showed a decline in energy dissipation (i.e., the area of the stress-strain hysteresis) from the first to subsequent cycles, although these later cycles rapidly reached a steady-state response, showing resilience against fatigue. In addition to looking at the mechanical properties of the first compressive cycle, we performed cyclic compressive tests to characterize the response of the CNT arrays at steady state. In our samples, the material response in compression reached steady-state by the third cycle. We compared the samples' behavior at the third cycle with that of the first cycle (in which preconditioning effects are substantial). The steady-state energy absorption and peak

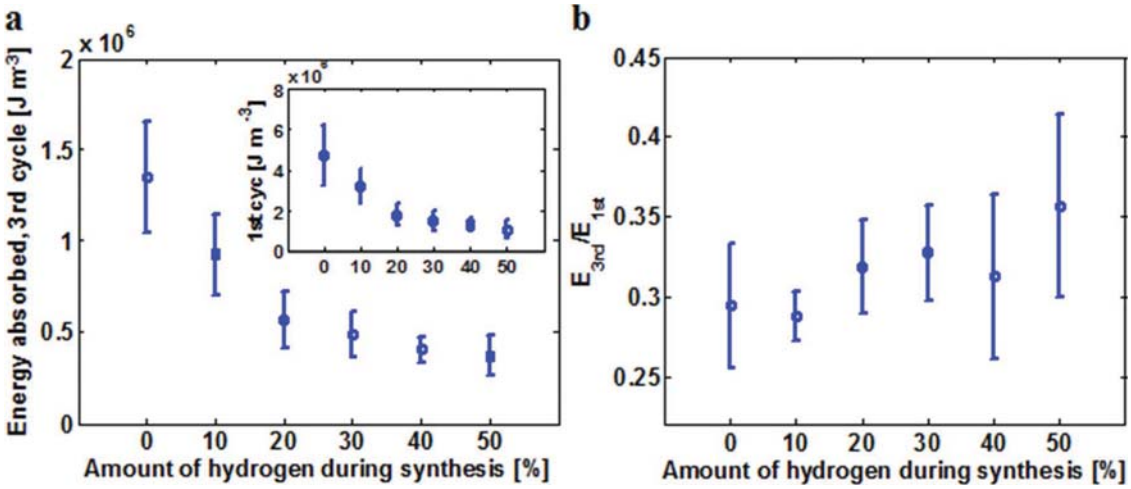

Figure 3.4: (a) Average energy absorbed during the third cycle plotted as a function of the amount of hydrogen during synthesis. The inset shows the average energy absorbed during the first cycle as a comparison. (b) Ratio of average energy absorbed during the third cycle to that absorbed during the first cycle as a function of the amount of hydrogen during synthesis

stress values showed roughly the same decline with increased hydrogen concentration as observed for the first cycle (e.g., compare the plot in Figure 3.4a for the third cycle with the inset in the same figure). As expected, each VACNT sample displayed a softening and a drop in energy absorption from the first to the third cycle due to preconditioning effects. However, there is a slight decline in the size of this drop for samples synthesized with increasing hydrogen concentration (Figure 3.4b). That is, the drop in energy dissipation from the first to later cycles associated with preconditioning becomes slightly smaller with increasing hydrogen concentration during synthesis. This is consistent with the observed constitutive response of the materials (compare Figures 3.3a and b).

3.1.4 Summary

We report that controlling the amount of hydrogen during floating catalyst chemical vapor deposition of vertically aligned arrays of carbon nanotubes has important structural and mechanical effects. Using a lower hydrogen concentration in the furnace feedstock leads to the growth of stiffer CNT arrays with higher average bulk density, a

less uniform diameter distribution, and larger average CNT diameters (i.e., due to the growth of individual CNTs with a larger number of walls). A lower hydrogen concentration also leads to the synthesis of CNT arrays that can reach significantly higher peak stresses at maximum strain, and that can absorb increased amounts of energy during compression. Both the overall height of the arrays and their strain recovery after compression have been found to be independent of hydrogen concentration during growth.

We also found that the stress-strain curves for samples synthesized without hydrogen do not present the clear three-regime deformation behavior characteristic of CNT foams, likely a result of the non-uniformity of the associated CNTs. In contrast, samples synthesized with higher amounts of hydrogen better conform to the stress-strain behavior exhibited by ideal foams. This study shows that using different concentrations of hydrogen during synthesis allows for the tuning of microstructural properties of VACNTs, including the ability to control the distribution of CNT diameters and the number of CNT walls, and consequently their mechanical response. This contributes to an understanding of the tunability of CNT-based materials, at microstructural and bulk levels, and it is expected to facilitate the design of new materials with tunable mechanical properties for many potential applications, such as protective foams and novel laminar structural composites.

Acknowledgments

The authors thank Prof. Julia R. Greer and Prof. A. John Hart for conversations leading to this work. This work is supported by the Institute for Collaborative Biotechnologies, under contract W911NF-09-D-0001 with the Army Research Office. JRR also gratefully acknowledges support from the Department of Defense via a National Defense Science & Engineering Graduate (NDSEG) Fellowship.

3.2 Control of input rate of precursor solution to obtain microstructural heterogeneities

Abstract

Arrays of aligned carbon nanotubes (CNTs) under compression are known to exhibit a dissipative hysteretic response similar to classical foams[2]. Here, we control the microstructure of the arrays during synthesis using a variable supply of carbon source and catalyst. We control CNT alignment and density along the array height, creating bands of high- and low-density regions. We study the dynamic response of these materials and show the ability to tailor the location and extent of strain localization under compression. We show that the synthesis procedures described herein allow for construction of CNT arrays with improved protection and energy dissipation in impact tests.

3.2.1 Introduction

Arrays of aligned carbon nanotubes (CNTs) have been observed to present a dissipative, hysteretic response under compression, much like open cellular foams [117]. In addition to dissipating significantly more energy during compressive deformation than commercial polymeric foams of comparable density (0.15 to 0.35 g cm^{-3}) [140], these materials are also thermally and electrically conductive and have therefore been proposed as multifunctional millimeter-scale low-density protective layers [117, 140]. These systems have received much attention for being functionally graded in their as-synthesized state, possessing variations in such properties as average CNT diameter [38], density [155], alignment [65], presence of contamination [37], and defect density [198] along their height. When these structures are subjected to compression along the long CNT axes these gradients in structural properties are associated with strain

[2]This section has been submitted for publication and is referred to as Ref. [197] by J.R. Raney, R.Y. Wang, and C. Daraio herein. JRR and CD designed the study. JRR and RYW synthesized samples and performed the mechanical testing. JRR conducted scanning electron microscopy and wrote the manuscript. All authors contributed to the analysis of the results.

localization and sequential collapse [117, 154]. More specifically, as an array undergoes increasing compressive strain it proceeds through a sequence of buckling events in which each buckle is completely formed prior to the formation of a new buckle, with the non-buckling region undergoing no apparent deformation [120]. This buckling is observed to take place from the base, defined as the side nearest the growth substrate, where the density also is lowest [120, 155]. Such functionally graded properties are often challenging to obtain in macroscopic systems, but are a desirable feature for foams used for protection against impact [199]. Graded properties can improve a material's resistance to damage [200] and are frequently observed in natural systems [201]. The aforementioned graded structure of arrays of CNTs is therefore an interesting feature that may allow such materials to serve as low-density protective foams. Limited low-energy impact tests have been performed in the past and shown that similar systems undergo nonlinear deformation and exhibit energy dissipation during impact [114, 202]. Here we devise a simple method to further control the deformation and dissipation properties of CNT arrays, which has not been previously reported.

Vapor phase (or "floating catalyst") thermal chemical vapor deposition (CVD) allows for the production of large quantities of millimeter-scale well-aligned CNTs on unmodified, inexpensive quartz surfaces [26]. The low-density (0.15 to 0.35 g cm^{-3}) CNT arrays that result can be repeatedly compressed to large strains (> 0.8) and hysteretically recover nearly completely [118]. The microstructure and the resulting bulk mechanical properties of these systems have been shown to be tailorable to some extent. For example, the choice of hydrogen concentration used in the flow gas during synthesis affects the average CNT diameter as well as the bulk density and resulting mechanical properties of the array [40]. In another study it was shown that partially-graphitic layers of pyrolyzed carbon can be formed around the CNTs, greatly increasing both the bulk density and the stiffness of the array [174]. Others have combined CNT arrays with other materials to affect overall structural properties, either by infiltrating CNT arrays with polymer [131] or nanoparticles (see Chapter 4 or Ref. [203]), or by incorporating them into multilayer structures [72, 114, 140].

These studies on tailoring CNT arrays tend to focus on understanding and en-

gineering the bulk physical properties of millimeter-scale arrays of CNTs through uniformly modifying the microstructure. While some work has been done to heterogeneously alter the microstructure of CNT arrays [65, 127], no work to date has examined how this could be used to affect the mechanical response of the arrays. Here, we introduce microscale heterogeneities during the synthesis process by varying the input rate of catalyst and carbon precursor solution during sample growth. We observe that these heterogeneities can be arranged to tailor compressive strain localization along the height of the array and thereby improve impact energy dissipation.

3.2.2 Results and discussion

When high injection rates (several ml min^{-1}) are used in bursts of a few minutes or less we observe that a corresponding softer region results in the final CNT structure. Using high-resolution scanning electron microscopy (SEM) (see, for example, the images and similar analysis presented in Ref. [40] and Section 3.1) we observe that the CNTs in these softer regions have a lower average diameter than the CNTs in regions synthesized with slower injection rates (~ 30 nm for the former and ~ 43 nm for the latter), but have statistically similar areal densities (as estimated by a count of the number of CNTs per unit length across the structure). This narrowing of CNT diameter with increasing injection rate of precursor solution has been observed previously [47, 51]. At the other extreme, the precursor input rate can be set to zero by pausing the injection system, depriving the heating zone simultaneously of any new carbon or catalyst. If the system is starved of precursor solution in this way, higher density regions of lateral entanglement (poor CNT alignment) arise [65, 127].

An input rate profile corresponding to a particular CNT growth cycle is shown in Figure 3.5a, in which a typical constant input rate of 0.8 ml min^{-1} is used (the normal growth or "control" case for the purposes of this work). In contrast, a variable input rate profile is shown in Figure 3.5b, in which the input rate alternates between "excess" (8 ml min^{-1}) and "starvation" (0 ml min^{-1}). Scanning electron microscope (SEM) images corresponding to each case are shown in Figures 3.5c and 3.5d, respectively.

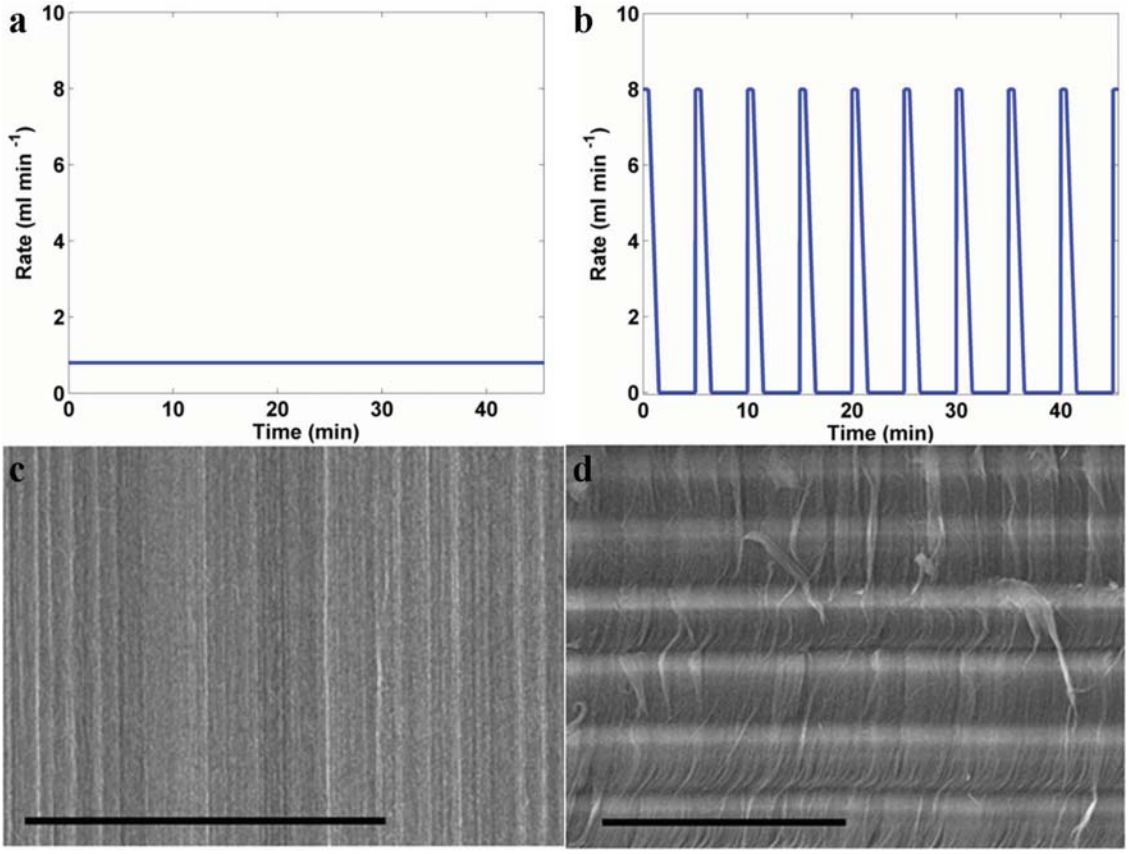

Figure 3.5: The input solution for synthesis of the CNTs consists of 0.02 g ml^{-1} ferrocene in toluene, which can be injected at a constant rate, as in (a), or at a variable rate, such as in (b); the constant input rate displayed in panel a corresponds to the uniform, aligned microstructure displayed via SEM in (c) (scale bar is 100 μm) and the cyclic input rate represented in panel b corresponds to the banded microstructure displayed in (d) (scale bar is 200 μm)

Note the uniform, aligned arrangement of the former, corresponding to the constant input rate, and the distinct horizontal bands of the latter, corresponding to an input rate varying between excess and starvation.

As is typical for arrays of CNTs synthesized using floating catalyst techniques [40, 114, 117, 118], these arrays recover to most of their original height even after large quasistatically-applied compressive strains (see Figure 3.6 for representative stress-strain data measured in quasistatic compression). In order to observe the manner of collapse in the system under compression, we designed a steel vise to hold the arrays in a compressed state during SEM imaging. Figure 3.7a shows an array corre-

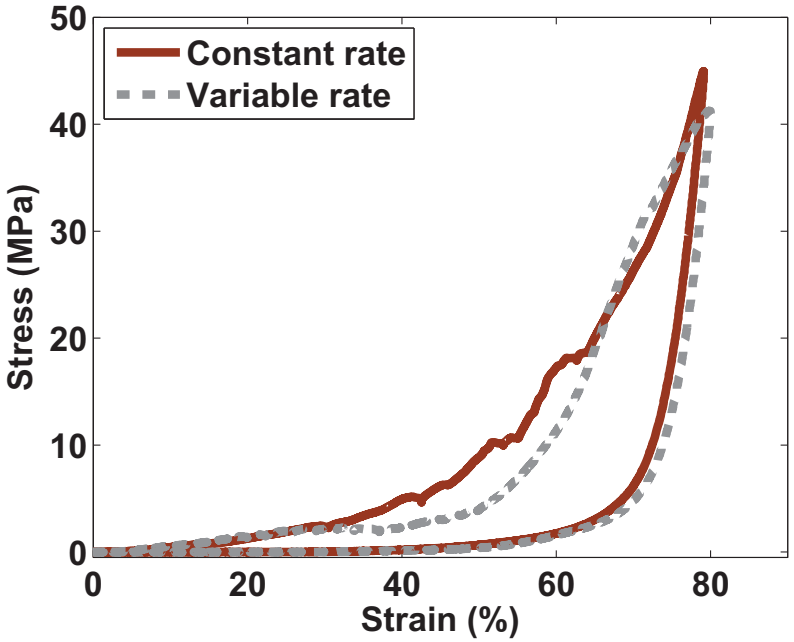

Figure 3.6: Typical quasistatic stress-strain curves for CNT arrays under compression; the solid line is for the control case with no intentional bands, whereas the dotted line is for a sample for which a discrete band was synthesized near the center of the structure

sponding to the input rate profile given in Figure 3.5b in the uncompressed steel vise. Figure 3.7b shows the same CNT array compressed by the vise to approximately 0.35 strain. Figures 3.7c and 3.7d give higher resolution SEM images of the uncompressed and compressed states, respectively. It is evident from the changes in Figure 3.7d relative to Figure 3.7c that the compressive strain is predominantly localized in the dark bands. Comparing the height of the dark band in Figure 3.7d to its height in Figure 3.7c, as indicated by the vertical dashed lines, shows that the local strain in this particular dark band is about 0.42, about 20% higher than the global strain for the full CNT array of 0.35.

Additional samples were synthesized with different carbon/catalyst solution input rate profiles. For the simplest cases, samples were synthesized with only one of the low-density bands described above. This was accomplished by using a three-part input rate profile using the programmable syringe pump. The three steps (I–III)

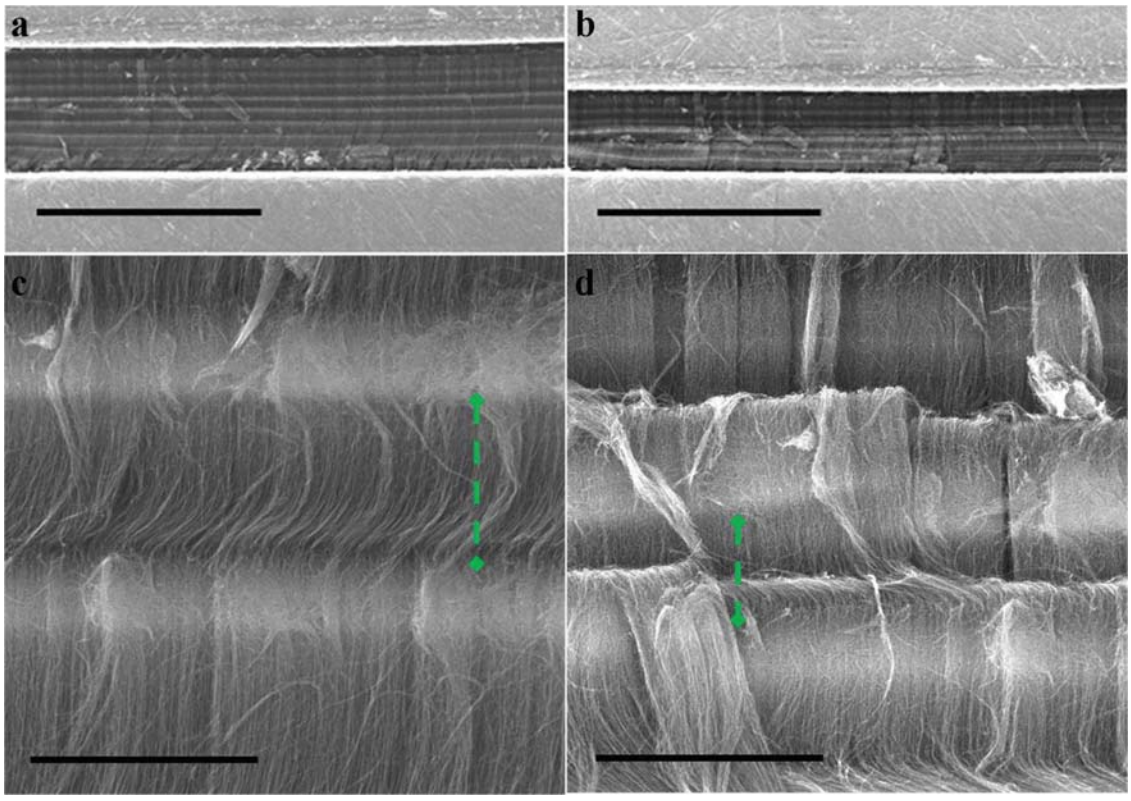

Figure 3.7: (a–b) A banded CNT structure (as synthesized according to the input profile displayed in Figure 3.5b) in a steel vise in uncompressed and compressed states, respectively (scale bars are 1 mm); (c–d) the microstructure in the uncompressed and compressed states, respectively (scale bars are 50 μm), revealing how the buckling takes place predominantly in the darker, more aligned regions; the vertical dashed lines are visual aids for observing the strain localization taking place in the dark bands

are depicted in Figure 3.8a: (I), a typical constant input rate of 0.8 ml min^{-1} was used; (II), a higher constant input rate of 5 ml min^{-1} was used in order to provide carbon/catalyst in excess (for two minutes in most cases); and (III), the same constant input rate as in step I (0.8 ml min^{-1}) was used. Two main categories of samples were synthesized: The first category of samples was synthesized with a pause in the precursor input rate between steps I/II and between steps II/III. These samples are referred to as the "discrete" band case because of the sharp boundaries that resulted between the low-density band and the rest of the structure (see Figure 3.8a). The other category of samples was synthesized with no pauses between the three steps

and is therefore referred to as the "continuous" case, due to the lack of apparent sharp boundaries between the low-density band and the rest of the structure (see Figure 3.8b).

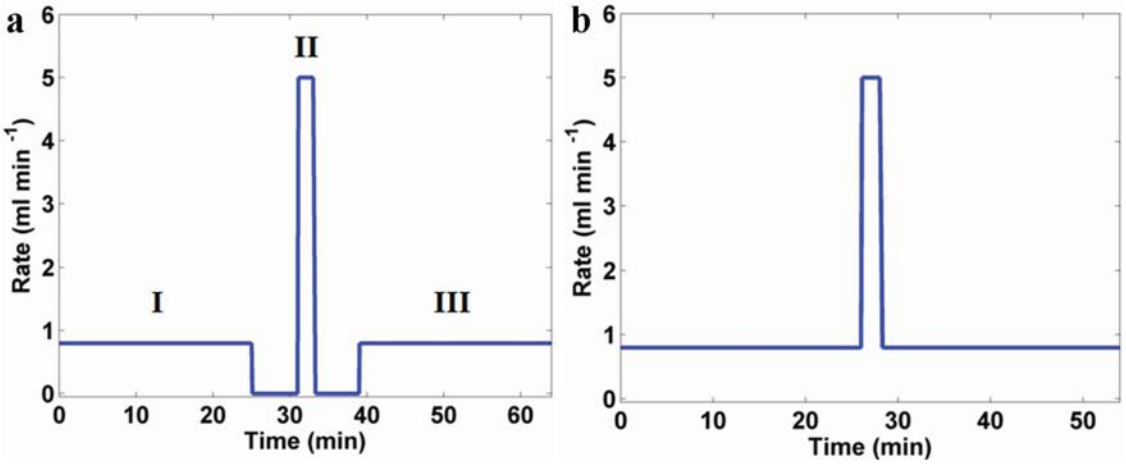

Figure 3.8: (a) The input rate of the precursor feedstock as a function of time that is used for synthesis of a single "discrete" band, and (b) the same for a "continuous" band that does not have the same noticeably sharp boundaries

Other groups have synthesized banded CNT arrays by starting and stopping the injection of the solution of carbon source and catalyst [204] or by dropwise synthesis [204, 205]. In these studies, however, the layers were found to separate easily [204]. In our case we find that there is excellent continuity and adhesion between layers for both our discrete and continuous cases. This was quantified by testing the samples in tension (see Figure 3.9 for a diagram of the setup). This is in agreement with an earlier report for a fixed catalyst system using a pulsed carbon source to synthesize sub-micron size bands [127]. Two factors are likely to promote improved continuity and adhesion even in the discrete case. First, rather than abruptly shutting off the injection of precursor solution, some residual evaporation of precursor continues for roughly half a minute due to the buildup of a small pool of precursor in our system directly in front of the heating zone of the furnace. This would act as a buffer to allow for a gradual halt to CNT growth (presumably allowing some CNTs to continue growing for a short time, ultimately bridging separated layers). This also explains why the higher density regions, e.g., the lighter bands pictured in the SEM image

in Figure 3.7c, have a gradient in brightness as a function of height. Second, rather than pausing the system for 10–15 minutes [65, 204] or even longer [66], as others have done, we kept the precursor flow off for only a few minutes at a time. If we completely stopped the input of the precursors for more than 10–15 minutes then the layers readily separated even with light handling. Thus the continuity of the CNTs between layers (and, as a result, the interlayer strength) appears to depend on the time that the structure is deprived of precursors.

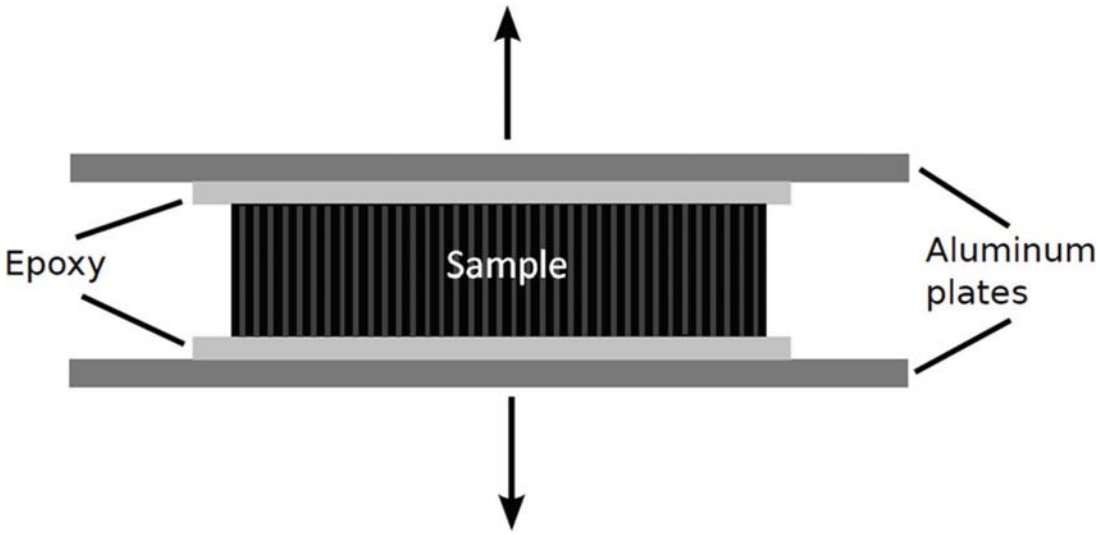

Figure 3.9: CNT arrays were tested in tension by bonding the top and bottom to aluminum plates using epoxy and pulling the plates apart with an Instron E3000; in all cases debonding occurred at the epoxy/aluminum boundary prior to sample delamination (tested up to 1–2 MPa)

By changing the relative times for step I and step III illustrated in Figure 3.8a (i.e., the normal synthesis rate before and after the low-density band, respectively), the ultimate location of the low-density region could be adjusted along the height of the CNT array. This allowed for the control of where, along the height of the structure, the strain was localized during compression. Note that because of the bottom-up synthesis mechanism of floating catalyst CNTs [65, 66], periods of excess precursor solution that occur earlier during synthesis correspond to low-density regions higher on the structure (further from the substrate). Other input rate profiles were used to construct samples with multiple low-density bands (by repeating steps

II and III in the above scheme multiple times), samples with low-density bands of different thicknesses (by varying the length of time for step II above), and samples with increased discreteness between low-density and normal-density regions (by varying the amount of time that the input of precursor solution was paused between steps I/II and between steps II/III above).

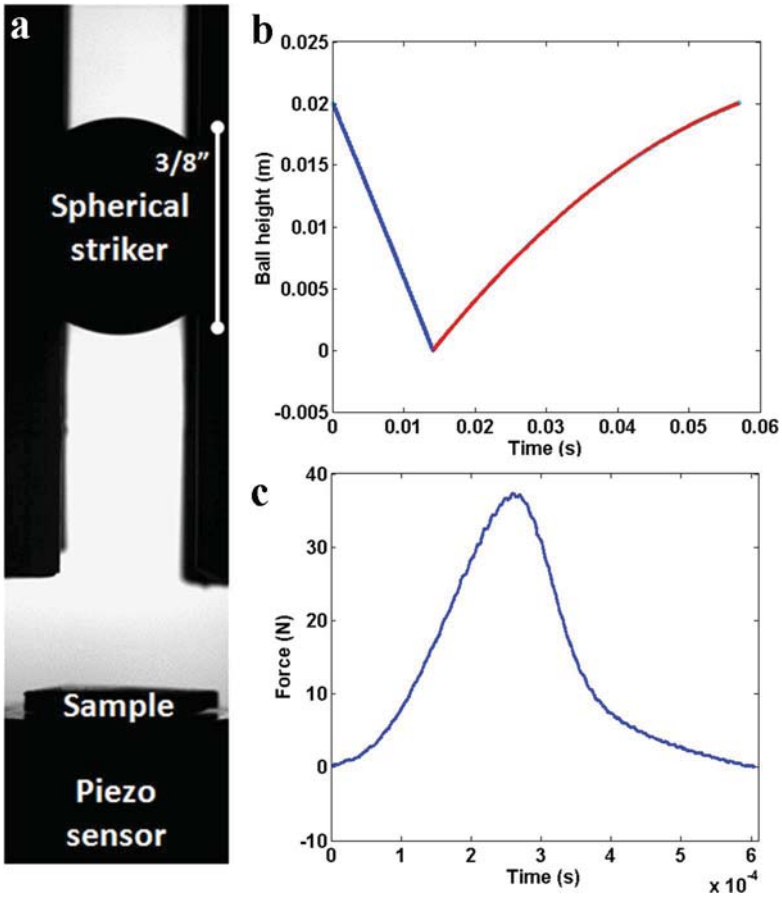

Figure 3.10: (a) A frame taken from the high-speed camera with labels indicating the striker, sample, and force sensor; (b) a representative plot of the trajectory of the spherical striker, as extracted from a series of hundreds of sequential images similar to that seen in a; (c) a representative force-time curve extracted from the piezo sensor during a typical test

In addition to the quasistatic observations (i.e., the SEM images in Figure 3.7 and the stress-strain data presented in Figure 3.6), impact tests were performed in order to study the dynamic response of these systems (Figure 3.10) using a similar technique as in previous work [114, 202]. The testing apparatus was activated with

a switch that simultaneously triggered a solenoid to release the striker and started a high-speed camera recording at 20 kHz (Figure 3.10a). The falling striker was imaged continuously by the camera before, during, and after impact, allowing the calculation of the striker's trajectory (e.g., Figure 3.10b) and its incoming and outgoing velocities. The ratio of the outgoing velocity to the incoming velocity defines the unitless coefficient of restitution, which varied from approximately 0.4 to 0.6 for our CNT arrays, depending on the density and internal distribution of that density. The apparatus included a force sensor underneath the sample, activated by the onset of dynamic force as a result of the striker's impact. This gives a force-time profile for each test (e.g., Figure 3.10c).

By knowing the incoming and outgoing velocities of the striker, the difference between the kinetic energy of the striker immediately before impact and that immediately after was readily calculated. By the requirements of energy conservation, this difference in kinetic energy for each collision represents the amount of energy dissipated during impact. The percent of incoming striker kinetic energy that was dissipated in each test was used as a figure of merit for the different types of samples. Figure 3.11a compares the average amount of striker kinetic energy dissipated as a result of impact for "control" samples (constant precursor input rate of 0.8 ml min^{-1}), "discrete" samples (input profile given in Figure 3.8a), and "continuous" samples (input profile given in Figure 3.8b). Both types of modified samples dissipate significantly more energy than the control case and show only a small difference relative to one another. Though Figure 3.11a corresponds to impact events from drop heights of 12.25 cm, we did not see any dependence on striker velocity within the margin of uncertainty of our tests for the drop heights used (from $\sim$ 3 cm to $\sim$ 15 cm, corresponding to impact velocities of 0.77–1.72 m s^{-1} and approximate initial strain rates at contact of 0.73×10^3–1.64×10^3 s^{-1}).

The low-density regions act to improve impact energy dissipation in multiple ways. First, the low-density bands result in larger displacement during contact. This is illustrated in Figure 3.11b, where the average penetration depth during contact of the spherical striker into the sample is given for each sample type. The penetration depth

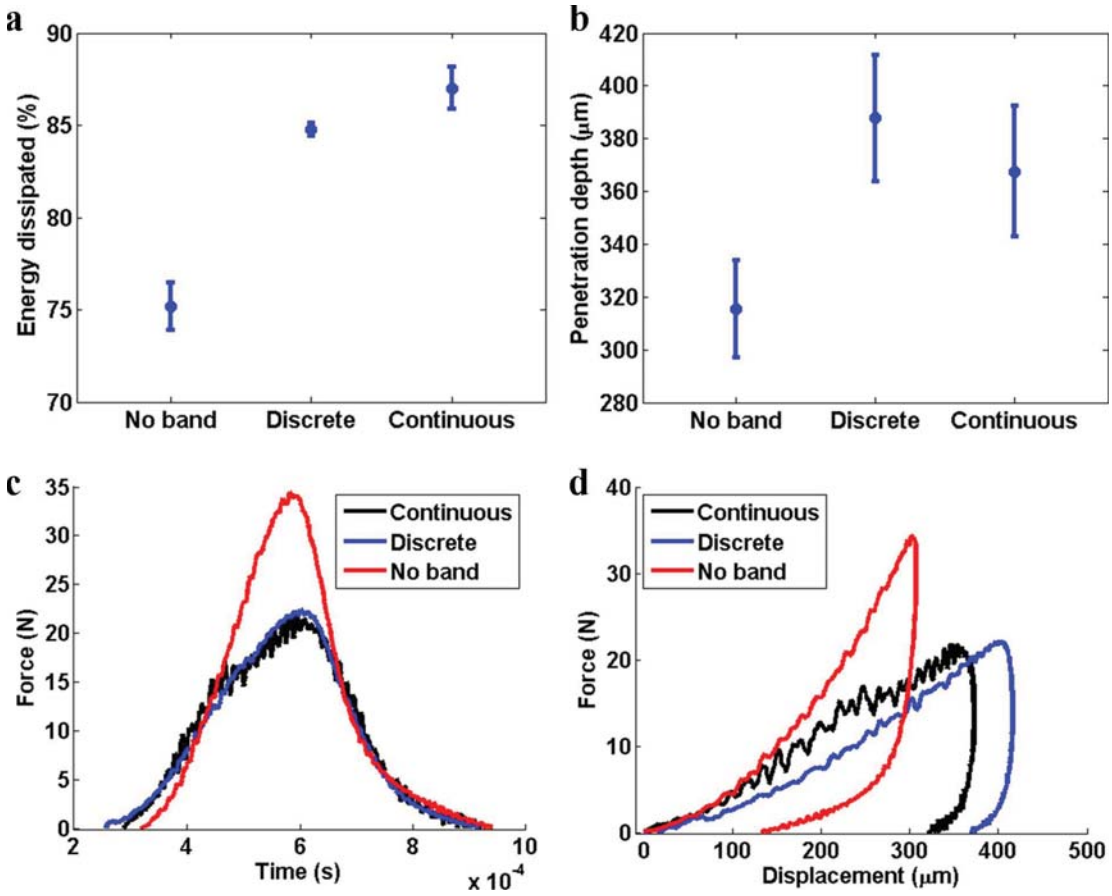

Figure 3.11: (a) Average energy of the striker that is dissipated during an impact test (drop height 12.25 cm) for samples with no bands (the control case), one "discrete" band with sharp boundaries, and one "continuous" band with gradual boundaries; (b) average penetration depth of the striker for the test and sample types in a; (c) representative force-time curves for the three sample types; (d) representative force-displacement data for the same

was calculated using the force-time data from the piezo sensor (e.g., Figure 3.11c) and the Newtonian equations of motion for the striker. That is, the data for force as a function of time gathered at the sensor is approximated as the instantaneous force on the impacting sphere (ignoring the effects of stress-wave propagation as a first-order approximation). Striker velocity as a function of time is determined by integrating this data in Newton's second law, using the incoming velocity of the striker as determined by the high-speed camera as the integration constant corresponding to the initial velocity. Finally, this is integrated once more to obtain displacement as

a function of time, with the initial position (onset of force) defined as zero position. The striker displacement into the samples is $\sim$ 20–30% higher for the samples with bands than for those without (Figure 3.11b). This increased displacement means that the force during impact acts over a longer distance, with a larger portion of the structure deforming and thereby dissipating energy. This has been shown to be an important cause of energy dissipation in other structures with variations in density, such as functionally-graded honeycombs [206]. Accordingly, the trend for energy dissipation (Figure 3.11a) closely matches that for penetration depth (Figure 3.11b). Figure 3.11d plots representative force-displacement curves for the different types of samples, revealing that the enhanced energy dissipation for the banded samples corresponds to lower peak forces (an important metric for protecting objects behind a foam layer from impact) and higher displacements.

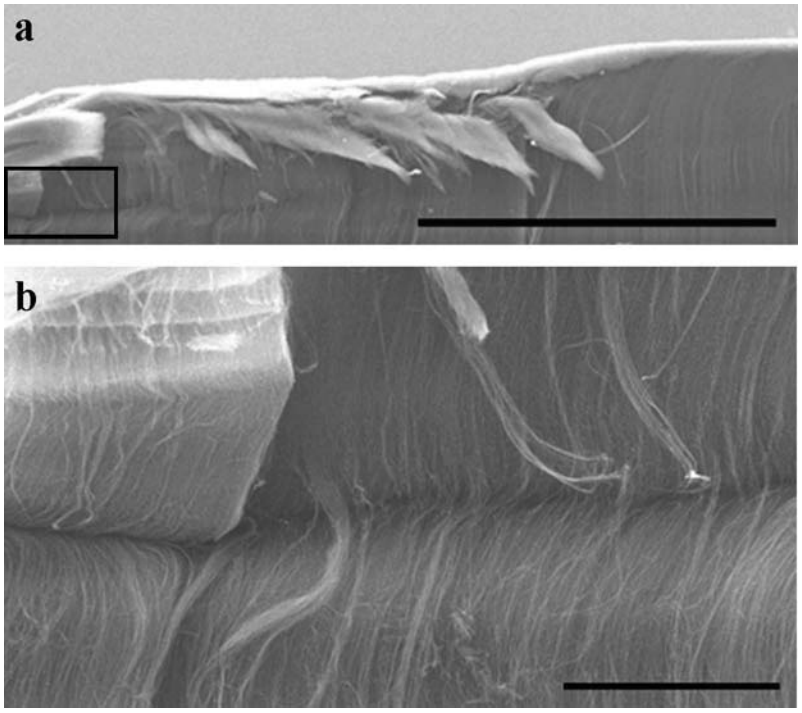

Figure 3.12: (a) A CNT array, synthesized to have one soft region, impacted six times on the left portion of the image (scale bar is 1 mm) and then sectioned by a razor blade to show the compaction internal to the structure; (b) a closer view of the region enclosed by the rectangle in part a showing compaction in the softer region (scale bar is 100 μm)

A second contribution to energy dissipation that results from the low-density bands is a slight increase in localized permanent deformation in samples containing them. This was confirmed with SEM imaging after the impact tests (see the permanent deformation for a banded sample pictured in Figure 3.12; this was not observed for the control samples). This was also confirmed by repeated impact events in the same location for each sample, which revealed that after the first one or two impact events the sample performance quickly declines (as concluded by decreased energy dissipation and increased peak force), becoming approximately the same as the control samples'. In this way the softer region appears to become somewhat compacted, losing its benefit after a few strikes (but always performing at least as well as the control samples despite this). It is important to note that this compaction is highly localized. If the striker impacts a portion of the sample even a couple millimeters from a previous impact site then dissipation proceeds as if the sample had not been impacted previously.

In addition to the effect on impact energy dissipation that arises from increased striker displacement and sample permanent deformation, we also expect the bands to have a third effect due to resulting changes in stress-wave propagation. It has been observed in other systems with layers of varying densities that these can greatly affect stress-wave propagation in high (blast loading) [207] and moderate (low-kinetic-energy impact tests such as ours) [208] strain rate conditions. Depending on how the stress wave amplitude compares to the local yield stress, the variations in density can result in changes to both the shape of the stress wave as well as the net energy dissipated [209]. This may be a factor in our systems but it requires further study to understand its relative importance, as little has been reported regarding stress wave propagation in aligned CNTs. Given the high correlation of improvement in energy dissipation with penetration depth (Figures 3.11a and 3.11b, respectively), we expect that increases in penetration depth play the largest role in the increase in energy dissipation at the tested strain rates.

We also studied how the thickness of the band affects the mechanical performance by changing the amount of time during synthesis that the high input rate of precursor

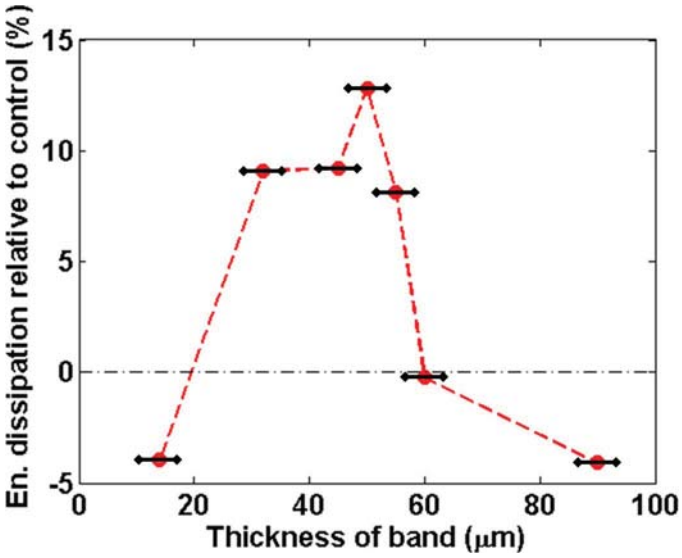

Figure 3.13: The thickness of the low-density band affects the energy dissipation of the structure under impact (the horizontal line at 0 indicates the average performance of samples with no bands); the horizontal bars indicate the uncertainty of the band thickness due to variations within any given sample

solution was used (i.e., step II in Figure 3.8a). The resulting samples were tested under impact, and the band sizes were determined using SEM (all samples were of discrete type in order to facilitate accurate measurement of band height). The results are given in Figure 3.13. Note that for very short or very thick bands the performance of the samples under impact actually becomes worse than the control case. The best performance is found for bands in the 30–55 μm range. We expect that the optimal band size could vary if strain rate changed significantly, since the density profile for optimal energy dissipation can change with the amplitude of the stress wave [209]. It is also worth noting that some samples of the continuous type performed better than the maximum performance given in Figure 3.13, dissipating up to 20% more energy than the control case. Such tests were not included due to the difficulty of accurately measuring the band thickness in the continuous case.

3.2.3 Conclusions

By varying the input rate of the precursor solution (containing both the carbon source and the catalyst precursor necessary for CNT synthesis) into a CVD furnace, CNT arrays can be synthesized with a heterogeneous structure. Higher precursor input rates lead to softer regions (with lower average CNT diameter), which are observed to buckle earlier than higher-density regions when the structure is subject to compression. As a result, strain can be controllably localized in a compressed CNT array. The presence of these low-density regions leads to improved energy dissipation under impact but also tends to increase the permanent deformation or damage that results from such an event. Despite this, even after damage has occurred, the samples with the low-density regions still perform at least as well as control samples. We found that impact energy dissipation is dependent on the thickness of these low-density bands. The number of bands is also expected to affect the mechanical performance, but we did not produce a sufficient number of samples of the proper height and density to statistically verify this with our experiments.

3.2.4 Experimental

Synthesis of CNT arrays: A floating catalyst thermal chemical vapor deposition system was used to synthesize the CNT arrays. Specifically, we synthesized millimeter-scale arrays of CNTs on thermally oxidized Si substrates using a CVD system in a flow of argon at 827 °C. As reported in detail elsewhere [40], we typically use a 0.02 g ml^{-1} solution of ferrocene (Fe catalyst precursor) in toluene (carbon source), at an input rate of approximately 0.8 to 1 ml min^{-1}; however, in this study, we used non-constant input rates for the precursor solution, controlled by a programmable syringe pump. As described in the main text, higher input rates corresponded to lower-density regions of CNT growth. This fact was used to synthesize CNT arrays of different architectures, as discussed.

Quasistatic mechanical deformation: We designed a small steel vise to hold the CNT arrays at various strains for desired intervals. This allowed for imaging with scanning

electron microscope (SEM), in this case using a FEI Quanta 200F at 30 kV. Other cyclic quasistatic compression tests were performed using a commercial materials test system (Instron E3000) at a strain rate of 0.01 s^{-1} to a maximum strain of 0.8, with strain being defined as the total displacement normalized by the total height of the sample (i.e., samples compressed to 0.8 strain are only 20% of their original height at maximum strain).

Impact tests: A steel sphere of $^3/_8$ inch diameter and mass 3.47 g was dropped from heights of 3 to 15 cm onto samples synthesized using different feed rate profiles. Samples used for testing were 1.05±0.10 mm in thickness and 0.287±0.044 g cm^{-3} in bulk density. Though samples of a wider range of heights (0.6–1.4 mm) and bulk densities (0.15–0.35 g cm^{-3}) were synthesized, only those near to the height and density specified above were used in the analyses, in order to avoid introducing additional variables that are known to affect the mechanical response of the CNT arrays [40]. The testing apparatus was activated with a switch that simultaneously triggered a solenoid to release the striker and started a Phantom V12.1 high-speed camera recording at 20 kHz (Figure 3.10a). This recorded the motion of the striker throughout the impact event, and allowed calculation of its restitution coefficient using image correlation routines. The apparatus included a force sensor (PCB Piezotronics) underneath the sample, which was activated by the onset of dynamic force as a result of the striker's impact. A computer was used to record the resulting voltage-time data during impact, and voltage was mapped to force using the manufacturer's and our own calibration data.

Acknowledgments

The authors thank Dr. Jinkyu Yang for his support with the impact tests and Lauren C. Montemayor for her assistance with the assembly of the synthesis apparatus. This work is supported by the Institute for Collaborative Biotechnologies, under contract W911NF-09-D-0001 with the Army Research Office. JRR also gratefully acknowledges support from the Department of Defense via a National Defense Science and Engineering Graduate (NDSEG) Fellowship.

Chapter 4

Tailoring array properties after synthesis: synthesis of nanoparticles on CNT surfaces

Abstract

In the past, aligned arrays of carbon nanotubes (CNTs) have been observed to exhibit a foam-like dissipative response in compression, garnering attention for possible mechanical applications[1]. Nanoparticles have previously been integrated with graphitic materials for electrochemical applications. Here, we synthesize nanoparticles of SnO_2 and MnO_2 in the interstices of aligned arrays of CNTs without altering the ordered structure of the arrays, and we characterize their mechanical response. We report that CNT arrays with embedded particles present superior energy dissipation relative to unmodified CNT arrays. In addition, energy dissipation, strain recovery, and structural failure (observed after repeated loading) depend on particle type (SnO_2 versus MnO_2).

[1]This chapter has been published as Ref. [203] by J.R. Raney, H.L. Zhang, D.E. Morse, and C. Daraio herein. CD and DEM initiated and designed the study. JRR synthesized CNT samples, performed mechanical tests, conducted electron microscopy, and wrote the manuscript. HLZ performed nanoparticle synthesis in the CNT samples and characterized the resulting structures with thermogravimetric analysis and x-ray diffraction. All authors contributed to the analysis of the results and to the manuscript.

4.1 Introduction

The remarkable mechanical properties of carbon nanotubes (CNTs) have received much attention [13], leading to many efforts to design materials that realize macroscale advantages through integrating these nanoscale structures [97]. Among the approaches taken, it has been noted that nominally aligned arrays (or "forests") of millimeter-scale CNTs can be readily synthesized via standard chemical vapor deposition (CVD) techniques. These materials exhibit behavior similar to fatigue-resistant, open-cellular foams under compression [117, 118], with significant recovery from deformation and orders of magnitude superior energy dissipation relative to commercial foams of comparable density (0.1–0.3 g cm^{-3}) [140].

Recent attempts have been made to understand structure-property relationships for these materials, such as how the bulk mechanical response is affected by various structural features [40, 119, 174]. In these studies, synthesis parameters were altered to obtain CNT arrays with different features, allowing the study of how CNT surface roughness [119], CNT diameter distribution [40], or partially-graphitic layering around individual CNTs [174] affects the bulk mechanical response. The control of these synthesis parameters, combined with the modification of CNT arrays after synthesis (such as by the infiltration of polymer into array interstices [131] or by the incorporation of surfactants and nanoparticles via solvent wetting [52]), allows for tuning of the mechanical response, such as array stiffness and energy dissipation, under compression.

Here we develop a novel approach for modifying the mechanical response of CNT arrays post-synthesis. Namely, we reinforce the CNT arrays by coating the individual CNT surfaces or filling the interstices of the arrays with metal oxide particles. We adopt two different procedures to synthesize MnO_2 and SnO_2 particles in the CNT arrays. For the synthesis of MnO_2 particles, we use a solution-based approach, as described in more detail later. For the synthesis of SnO_2 particles, we use a kinetically-controlled catalytic synthesis approach, similar to that used in the past for growing Sn particles *in situ* in graphitic anodes for electrochemical applications [210]. In both

cases, the particles are synthesized *in situ* in the CNT arrays. In contrast, most work in the past involving nanoparticle modification of CNTs has been performed on disordered arrangements of CNTs that have first been dispersed in solution (often an acid) and then filtered. Such procedures have been performed to synthesize particles on disordered arrangements of CNTs such as ZnO [211], Au [212], Ni [213], $CaCO_3$ [214], Cu [215], and others [216]. Specifically relevant to this work, SnO_2 nanoparticles have been integrated with disordered arrangements of CNTs in the past using CVD [217] and solution-based techniques [218]. MnO_2 particles have also been integrated with disordered CNTs [219, 220]. Such materials have already been created in the past for various electrochemical applications, such as aqueous supercapacitors [221]. Thus, these materials based on disordered agglomerates of surface-modified CNTs are useful for certain applications, and do not require the infiltration of particles deep inside CNT arrays, which can be a challenge for many synthesis approaches. While dispersing the CNTs into disordered arrangements prior to modification avoids the problem of needing to obtain good particle infiltration into the arrays, it necessitates the loss of the ordered structure of CNT arrays. For most applications, such a CNT powder must be integrated into another, usually polymeric, matrix. This process has many challenges of its own, such as the difficulty in obtaining uniform dispersion of the CNTs in the matrix [85].

Here, we seek to improve the mechanical performance of CNT arrays without disrupting their ordered structure. We investigate the mechanical stability of these hybrid CNT-nanoparticle structures, which could be useful in multifunctional applications. Inorganic materials have been infiltrated into ordered CNT arrays previously. A sol-gel process has been used to create a CNT-glass composite, but the focus was on enhancing thermal and electrical conductivities of the arrays [222]. Low pressure CVD has also been used, but only for very short CNT arrays (~ 50 μm) due to difficulties in getting reactions to take place more than a few tens of microns deep in the array [223]. More recently a vapor-assisted technique has been used to successfully synthesize TiO_2 uniformly in short CNT arrays, a procedure possibly generalizable to other types of oxides in the future [224]. However, none of these studies examined

how the presence of the nanoparticles affects the mechanical properties of CNT arrays, which is important for understanding issues such as mechanical stability. Here we obtain dispersion of particles deep within millimeter-scale arrays without altering the crystalline structure of the individual CNTs or the ordered arrangement of them. In addition to modifying the CNT arrays we test them under quasistatic compression to examine how energy dissipation, strain recovery, loading/unloading modulus, and permanent damage are affected by the modifications. Understanding these mechanical properties is also a necessary first step toward the use of materials based on nanoparticle-CNT array structures in relevant applications, such as electrochemical applications that have recently been investigated [225].

4.2 Experimental

We synthesized arrays of multi-wall carbon nanotubes (CNTs) using a thermal chemical vapor deposition (CVD) system and a floating catalyst approach described in the past [26, 40]. Our growth substrate was thermally oxidized Si placed in a CVD furnace set to 827 °C. We injected a 0.02 g ml^{-1} solution of ferrocene (a precursor of Fe, a catalyst for CNT synthesis) and toluene (a carbon source for CNT synthesis) at a rate of 1 ml min^{-1} using a syringe pump into the heating zone, with Ar as a carrier gas. This approach results in continued deposition of new catalyst, and thereby continued initiation of new CNT growth, throughout the synthesis process. CNT array samples (with typical heights of 1–1.5 mm, areal cross sections of 10–20 mm^2, volume occupied by CNTs $\sim$ 10%, and individual CNT diameters of 40–50 nm, as characterized by transmission electron microscopy in our previous work [40]) were removed from their growth substrates using a razor blade. The mass for each of these samples was measured using a microbalance, and this was used to calculate the bulk density, both before and after synthesis of the oxide particles.

Loading of SnO_2 particles followed steps similar to those discussed in previous work [210]. CNT array samples were first added to aqueous $SnCl_2$ (0.2 M, 5 ml), with 0.6 ml of acetone added to aid absorption into the array. After soaking for

46 h at room temperature, the CNT samples were fully wetted with the $SnCl_2$ solution and placed in a sealed container that contained an open solution of ammonia (2%wt.). The ammonia vapor gradually diffused to the sample, initiating hydrolysis of the $SnCl_2$ solution contained inside the CNT array. The samples were then removed and washed with deionized water, followed by further heat treatment in N_2 at 450 °C for 1 h at the heating rate of 5 °C min^{-1}, yielding the final CNT/SnO_2. To load MnO_2 particles into the CNT arrays, we soaked the CNT samples in aqueous $KMnO_4$ (0.2 M, 5 ml) for 46–120 h (with the variation in time controlling the loading amount) at room temperature. During the soaking, MnO_4^- spontaneously reduced to MnO_2 on the surface of the CNTs, which acted as a reducing agent [220]. After soaking, the sample was subjected to further heat treatment in N_2 at 450 °C for 1 h at a heating rate of 5 °C min^{-1}, yielding the final CNT/MnO_2. Whether modifying the CNT arrays with SnO_2 or MnO_2, there was no observable change in the dimensions of CNT arrays (as can sometimes be observed due to solvent wetting effects). Scanning electron microscopy (SEM) was used to obtain images of sample structure at different magnifications and locations for each sample. By counting the number of CNTs crossing a horizontal line at different locations it was determined there were no statistically significant changes in the spacing of individual CNTs.

Two samples with SnO_2 and five samples with MnO_2 were synthesized following the procedures above, and compared to the performance of three unmodified control samples. Samples were repeatedly compressed quasistatically, using a commercial materials test system (Instron E3000), to 0.8 strain (with strain being defined as the displacement normalized by sample height; i.e., 0.8 strain is equivalent to compressing the sample until it is only 20% of its original height). This compression occurred at a strain rate of 0.03 s^{-1} (i.e., 3% of the original sample height every second). For each modified CNT array an unmodified "control" sample was tested that had been removed from the growth substrate directly adjacent to it, and therefore had almost the exact same height, density, mean CNT diameter, etc., prior to modification. Energy dissipation per unit volume was obtained by integrating the area of the stress-strain hysteresis for each loading cycle. The loading modulus was calculated by

examining the initial slope of the stress-strain curve. The unloading modulus was similarly calculated by taking the slope of the stress-strain curve after unloading from maximum strain had just begun (corresponding to a drop in stress to $^2/_3$ of the maximum stress).

Thermogravimetric analysis (TGA, Mettler-Toledo 851e instrument) was conducted at 550 °C in air to quantify the amount (wt. %) of particle loading for each modified sample. The type of oxide was determined after synthesis of the particles using x-ray diffraction (XRD, Philips X'PERT MPD with Cu Kα radiation). Samples were characterized with scanning electron microscopy using a FEI Quanta 200F, and transmission electron microscopy using a FEI TF30UT at 300 kV.

4.3 Results and discussion

After synthesizing oxide nanoparticles in the CNT arrays with various loadings (i.e., different quantities of SnO_2 or MnO_2 as quantified by wt. %) following the procedures described in the experimental section, samples were characterized with scanning electron microscopy (SEM) and transmission electron microscopy (TEM). Figure 4.1 compares SEM images of an unmodified array (Figure 4.1a) with one modified with SnO_2 (Figure 4.1b) and two instances of arrays modified with MnO_2 (Figures 4.1c,d). These images illustrate that the way in which the nanoparticles modify the CNT arrays depends strongly on particle type (i.e., SnO_2 versus MnO_2). In all cases, the images are representative of the appearance at this scale at every location internal to the arrays at which it was investigated (i.e., there is no apparent formation of separate densified or cell regions, as determined by SEM images at many different locations and magnifications). The SnO_2 particles formed conglomerations in the array interstices, forming pockets of oxide rather than coating the individual CNTs (Figure 4.1b). The MnO_2 particles, in contrast, formed uniformly along the individual CNTs (Figures 4.1c,d). This is in agreement with earlier qualitative observations that MnO_2 forms a more uniform, tightly-bound coating around CNTs than SnO_2 [221]. We expect that the different affinities are a result of the different roles that the CNTs

play in the two different reactions. As described in the experimental section, the synthesis of SnO_2 is performed from aqueous $SnCl_2$ precursor contained in the CNT array, using a hydrolyzing agent (ammonia) to cause the precipitation of Sn(OH)Cl that is converted to SnO_2 in the subsequent heat treatment. In this case, the CNT array just provides a substrate/space to accommodate the SnO_2 but does not play an active role in the reaction. For the synthesis of MnO_2, with aqueous $KMnO_4$ as precursor, the CNTs can take a more active role in the reaction, acting as both a reducing agent and a substrate for MnO_2 precipitation [219, 220]. This results in particles being formed mainly on CNTs, not everywhere in the interstices. Two different examples are given for MnO_2 (Figures 4.1c,d) in which the particle synthesis parameters used were nearly the same yet slightly different morphological features developed. The sample in Figure 4.1c has a lower total amount of MnO_2 loaded relative to the sample in Figure 4.1d due to a shorter soak time in the $KMnO_4$ precursor solution, despite having significantly larger particles. Past observations have shown that the morphology of nanoparticles resulting from the MnO_2 synthesis is highly sensitive to local pH and temperature [220]. Minor variations in these parameters could therefore explain the observed morphological differences. As small as these morphological differences are, they may affect mechanical properties, as discussed later.

TEM images for CNT samples modified with MnO_2 are given in Figure 4.2. High-resolution images reveal the individual walls of the CNTs and the crystalline nature of the attached MnO_2 particles (Figure 4.2a). Approximately a dozen roughly aligned CNTs with many MnO_2 particles are shown entangled together (Figure 4.2b), displaying a similar morphology to that shown in earlier SEM images (i.e., Figure 4.1c). Higher magnification images show the interface between a CNT and particles (Figure 4.2c) and a high-resolution view of one of these particles (Figure 4.2d). The strong interaction between MnO_2 particles and CNTs observed in these images is not seen in the case of SnO_2 particles. It should be noted, however, that, despite the affinity of the MnO_2 particles for the CNTs, TEM did not reveal any damage to the CNT walls or partial embedding of the particles into the walls.

Representative compressive stress-strain responses for samples modified with MnO_2

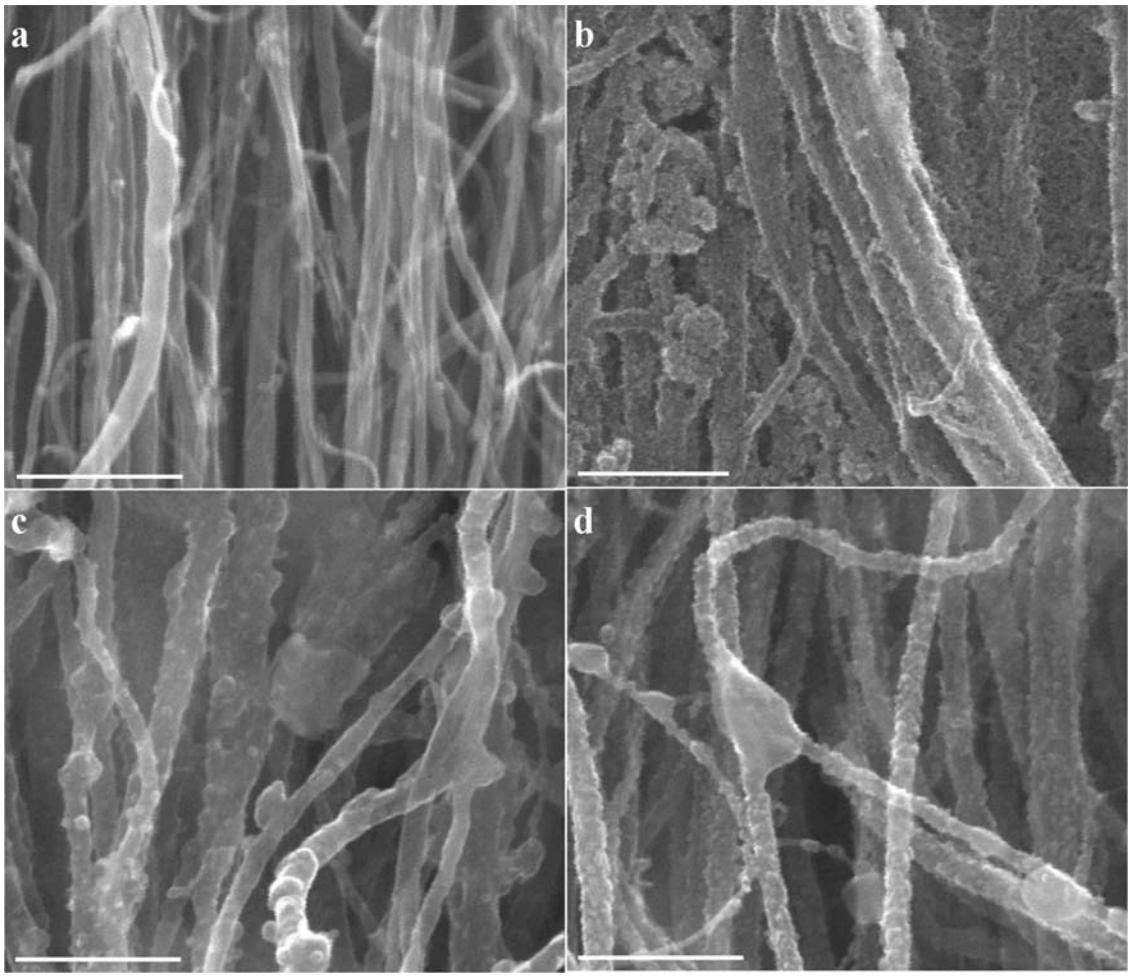

Figure 4.1: Different types of CNT modifications (scale bars are 400 nm); (a) unmodified CNTs; (b) CNT array modified with SnO_2, which has conglomerated in the array interstices; (c–d) two different MnO_2 loadings, both of which predominantly coated the individual CNTs themselves rather than forming conglomerations in the interstices

and SnO_2 are given in Figures 4.3a and 4.3b, respectively, with the response of corresponding control samples indicated by the dashed lines. A hysteretic response was observed in all cases, as is typical for CNT arrays under compression to large strains [117], with separate loading and unloading paths (following the path indicated by the arrows in Figure 4.3a). Similar stress-strain curves were gathered for all samples, and were used to calculate loading modulus (slope of the initial linear region corresponding to small strains), unloading modulus (the slope of the curve at high strain, right after the peak value has been reached and unloading has begun), and energy

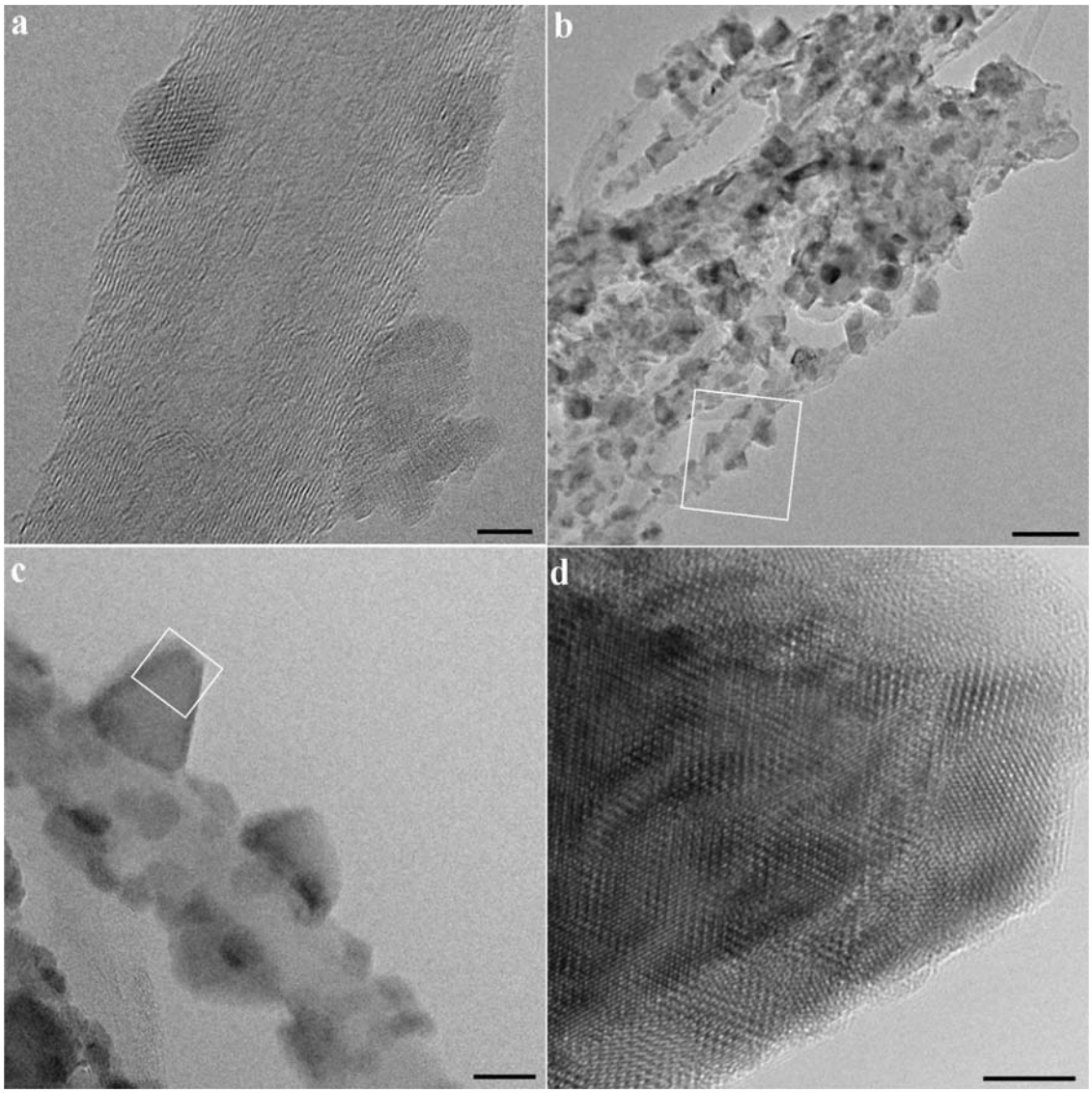

Figure 4.2: Transmission electron microscope images of CNTs modified with MnO_2; (a) high-resolution image showing individual CNT walls and crystalline MnO_2 particles (scale bar is 5 nm); (b) a group of aligned CNTs modified with MnO_2 particles (scale bar is 100 nm); (c) a closer view of a single CNT corresponding to the white box in panel b (scale bar is 20 nm); (d) a high-resolution image of a MnO_2 particle corresponding to the white box in panel c (scale bar is 5 nm)

dissipation. These quantities are summarized in Table 4.1. The area of the stress-strain hysteresis represents the energy dissipated per unit volume. Note the greater improvement in energy dissipation for the sample modified with MnO_2 relative to its control (Figure 4.3a), approximately 100% improvement in this case, as compared

to the sample modified with SnO_2 relative to its control (Figure 4.3b), about 42% improvement in this case. Superior energy dissipation was consistently observed for samples loaded with MnO_2 relative to those loaded with SnO_2.

In addition to these differences resulting from the different particle types, there may be an effect from particle morphology even within a given category of particle type. As mentioned earlier, the slight morphological differences between the samples displayed in Figures 4.1c and 4.1d (both modified with MnO_2) could contribute to the differences in energy dissipation between the two cases, with the former dissipating approximately 70% more energy than the latter during equivalent compression tests. This is noteworthy particularly because the latter sample, with less energy dissipation, was actually loaded with a higher quantity of MnO_2 (40.2 wt. % rather than 34.9 wt. %).

We examined how the samples responded under repeated compressive loading. One of the intriguing properties of as-grown CNT arrays synthesized by floating catalyst CVD is their ability to dissipate energy and to recover much of their original height even after many compressive cycles to high strain (0.8 or higher) [117, 118]. The first cycle generally reaches the highest peak stress and dissipates the largest quantity of energy, with a significant drop in these for the second cycle. After only a few compressive cycles, however, the material begins to reach a steady-state response that does not vary significantly from cycle to cycle [40]. In this study we observed that the response to repeated loading depended strongly on whether the sample was reinforced with MnO_2 or instead with SnO_2. Samples modified with MnO_2 are observed to have higher peak stress and larger hysteresis area (i.e., energy dissipation) than their respective control samples even for repeated compressive cycles (Figure 4.3c). The same is not observed for samples modified with SnO_2, which by the fourth cycle show a nearly identical mechanical response to their respective control samples.

Figure 4.4 illustrates in more detail the significant difference between the response of samples modified with MnO_2 under repeated loading and that of the samples modified with SnO_2. Because the unmodified control samples also show decreased performance with repeated loading, Figure 4.4 shows the responses of modified samples

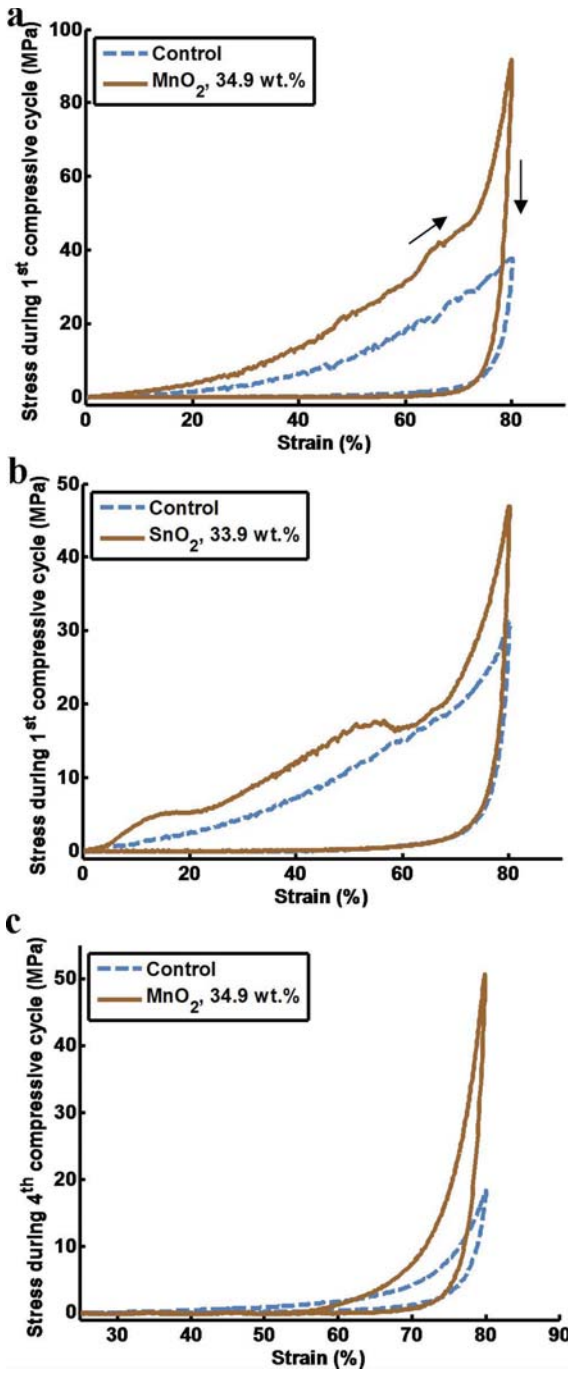

Figure 4.3: Stress-strain relationship of modified CNT arrays relative to their unmodified counterparts; (a–b) the MnO_2-modified samples display a larger improvement in energy dissipation (area of the hysteresis) relative to their control samples than do the SnO_2-modified samples relative to their control samples; (c) by the 4^{th} compressive cycle the samples in panel a both dissipate less energy than in earlier cycles, but the sample reinforced by MnO_2 still has a larger hysteresis than the unmodified sample

relative to this changing response of the control samples. I.e., the first compressive cycles of the modified samples are compared to the first cycles of the unmodified samples, the second compressive cycles for the modified samples to the second cycles of the unmodified samples, etc. Figure 4.4a shows relative energy dissipation for the first four compressive cycles. As already discussed, the sample modified with MnO_2 dissipated approximately 100% more energy than did its control during the first compressive cycle. It continued to dissipate approximately 100% more energy than the control sample in subsequent cycles as well. In the case of samples modified with SnO_2, however, by the fourth compressive cycle the material behaved almost identically to the control, dissipating approximately the same amount of energy and attaining approximately the same peak stress (Figure 4.4a).

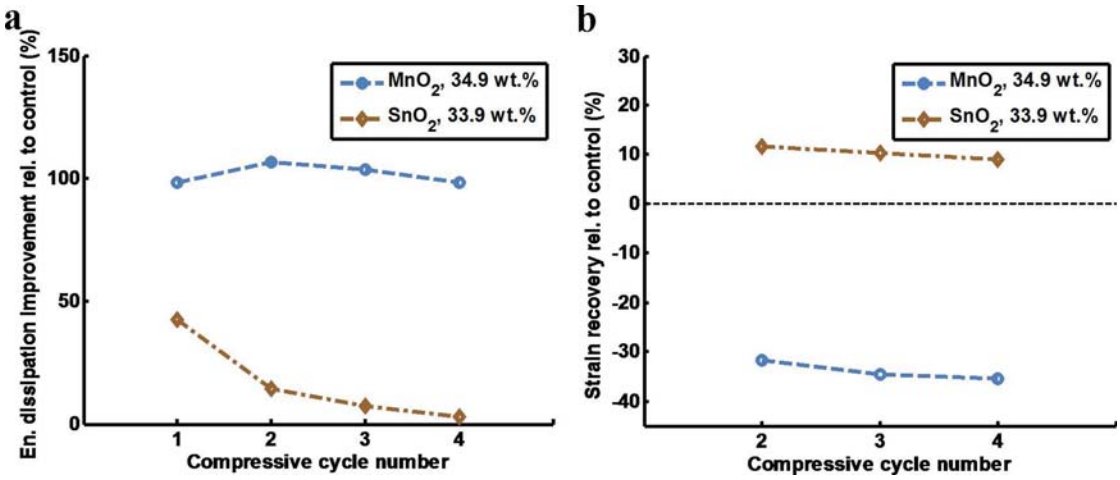

Figure 4.4: Mechanical performance of modified CNT arrays relative to their unmodified counterparts for repeated loading; (a) both MnO_2- and SnO_2-modified samples dissipate more energy during compression than control samples, but the performance improvement for samples with SnO_2 is almost entirely gone by the fourth compressive cycle; (b) though samples with MnO_2 dissipate more energy than both SnO_2 and control samples, they do not recover strain as well after compression

In terms of energy dissipation for repeated loading, it is clear that the properties of CNT arrays modified with MnO_2 particles are superior to those modified with SnO_2, which lose all advantages over their control within a few compressive cycles. However, when strain recovery is considered the samples respond in the opposite manner.

	Loading mod., cyc 1 (MPa)	Loading mod., cyc 4 (MPa)
Control	6.6 ± 3.8	3.1 ± 1.8
SnO_2	41 ± 8	2.4 ± 0.6
MnO_2	9.3 ± 5.6	23 ± 6

	Unloading mod., cyc 1 (MPa)	Unloading mod., cyc 4 (MPa)
Control	1710 ± 330	900 ± 290
SnO_2	2860 ± 230	1090 ± 150
MnO_2	4170 ± 400	3180 ± 190

	En. dissipation, cyc 1 (MJ m^{-3})	En. dissipation, cyc 4 (MJ m^{-3})
Control	6.89 ± 0.49	0.71 ± 0.18
SnO_2	9.71 ± 0.58	0.60 ± 0.05
MnO_2	13.0 ± 1.6	1.40 ± 0.24

Table 4.1: Loading modulus, unloading modulus, and energy dissipation per unit volume of modified and unmodified samples

Figure 4.4b shows the initial heights of the modified samples relative to those of their respective control samples at the beginning of each compressive cycle. This indicates the amount of strain that the CNT array recovers after the previous compressive cycle. With the control samples indicated by the horizontal line at 0% (by definition), it is clear that samples modified with MnO_2 recovered significantly less strain after compression than did either the control samples or those modified with SnO_2. The latter actually recovered slightly more strain after compression than the control samples, which may be related to disruption of some of the lateral entanglement between CNT bundles as a result of the pockets of oxide.

It is also useful to examine the loading and unloading moduli to better understand the compressive response under repeated loading cycles. As summarized in Table 4.1, the initial loading moduli for samples modified with SnO_2 have an average value (41 ± 8 MPa) approximately an order of magnitude higher than those of either the unmodified samples or those modified with MnO_2. However, by the fourth cycle (see Table 4.1) the average loading modulus for samples with SnO_2 has dropped by an order of magnitude to closely match the average value for unmodified samples. In contrast, samples with MnO_2 show a substantial increase in loading modulus after a few cycles. All samples show a dramatic decrease in unloading modulus after the first cycle, though the samples with MnO_2 show a decrease of a smaller relative value.

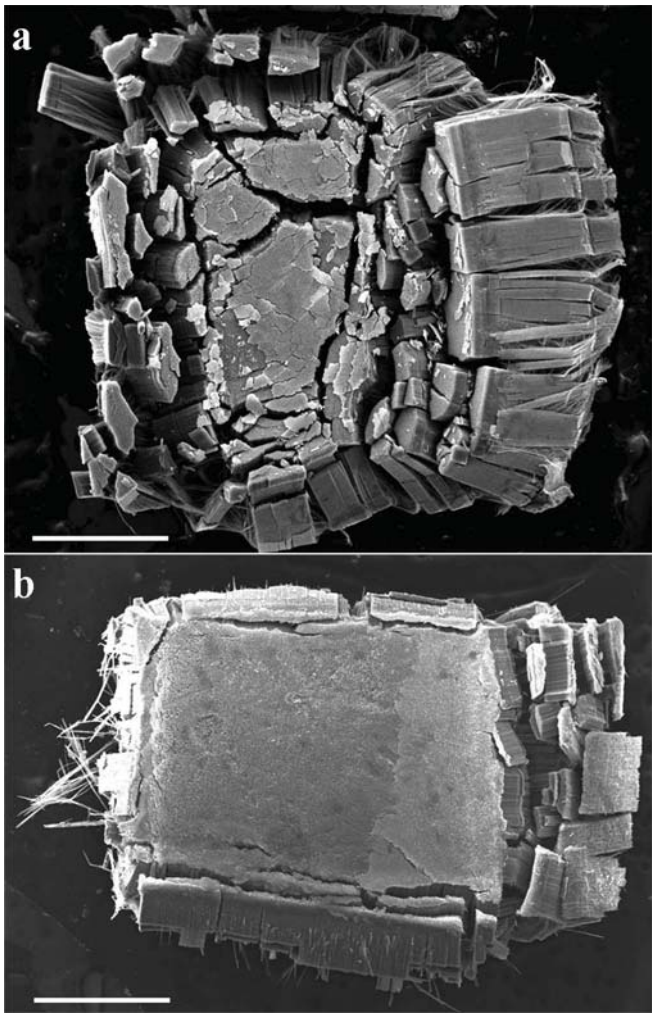

Figure 4.5: Top-down scanning electron microscope images for the assessment of material failure after several compressive cycles to 0.8 strain (scale bars are 1 mm); (a) CNT array modified with SnO_2, exhibiting many lateral cracks; (b) CNT array modified with MnO_2 displaying much less lateral cracking comparatively

The results discussed above and displayed in Figure 4.4 can be explained by returning to the SEM images in Figure 4.1 to understand the different morphologies that result from modifying the CNTs by either SnO_2 or MnO_2. As discussed, the SnO_2 particles appear to form interstitial conglomerations without substantially modifying the individual CNTs (Figure 4.1b) whereas the MnO_2 particles form directly on the individual CNT surfaces (Figures 4.1c,d). It is useful to combine these observations with top down SEM images taken of the samples after they were repeatedly compressed, which indicate how the materials tend to fail (Figure 4.5). Note that the

samples modified with SnO_2 display many lateral cracks that form perpendicular to the long CNT axes (Figure 4.5a). Such behavior is in accordance with the morphology displayed in Figure 4.1b, in which brittle pockets of oxide between elastic CNT bundles would serve as natural locations of fracture. This also explains the high loading modulus obtained in the first cycle, with a large contribution from the oxide deposits, followed by very low values of loading modulus for later cycles, since the oxide deposits would have already failed in brittle fashion (Table 4.1). With these parallel brittle and elastic elements in compression the material fractures into small elastic bundles of CNTs. After the first couple of cycles these elastic bundles no longer interact as strongly with one another, causing the loss of the initial improvement in energy dissipation with repeated loading (Figure 4.4a). Concomitantly, once the oxide is fractured and no longer coupling adjacent CNT bundles, the recovery of the material after compression will be entirely driven by the elastic CNTs, which are known to be highly resilient against bending and buckling [68, 73], not inhibited by the fractured oxide deposits. This results in the large strain recovery for samples modified by SnO_2 shown in Figure 4.4b. In marked contrast, the samples modified with MnO_2 show very little lateral cracking (Figure 4.5b), in accordance with a morphology predominantly consisting of individually modified CNT surfaces (Figures 4.1c,d) rather than large deposits of oxides between separated CNT bundles. With this morphology it would be expected that the mechanical response would be driven by interactions between individual CNTs rather than the material breaking into separated CNT bundles. The result is consistently improved energy dissipation even after repeated compressive loading (Figure 4.4a) but poor strain recovery due to significant entanglement among the individual CNTs in the compressed state (Figure 4.4b). This is also in agreement with the increase in loading modulus for the samples modified with MnO_2 (Table 4.1). Because samples modified with MnO_2 do not recover well from compression, they remain in a densified state. This increased density for later compressive cycles corresponds to an increased loading modulus.

Figure 4.6 illustrates this discussion in the form of diagrams and additional SEM images for clarity. Figure 4.6a represents a sample modified with SnO_2 that is com-

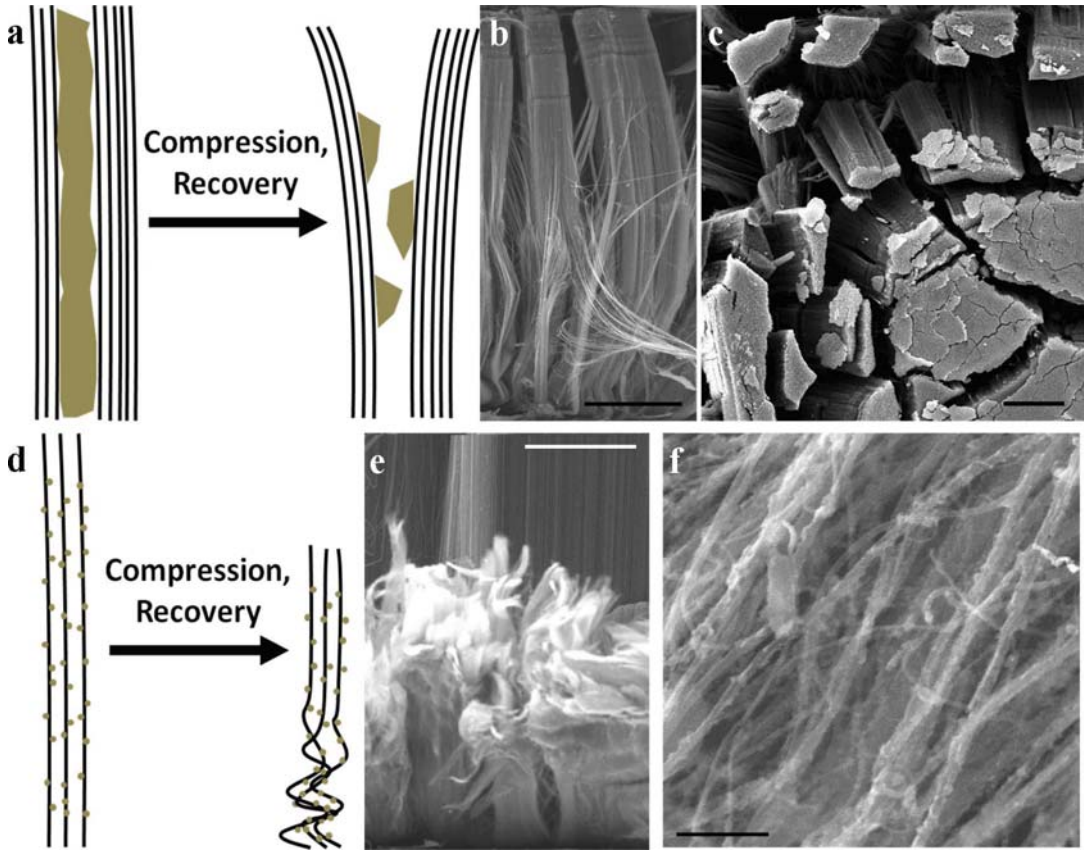

Figure 4.6: CNT morphology before and after compression and recovery for samples modified with SnO_2 (a–c) and MnO_2 (d–f); (a) SnO_2 forms in clumps between CNT bundles, leading to brittle fracture and lateral cracking during compression followed by CNT-driven partial elastic recovery; (b-c) SEM images of a SnO_2-modified CNT array after compression and recovery from both the side and top perspectives, respectively (scale bars are 250 μm); (d) MnO_2 forms as smaller particles along each CNT, leading to entanglement after compression, and less subsequent strain recovery; (e) SEM image taken from the side of a MnO_2-modified CNT array near the base, where compressive deformation predominates (scale bar is 100 μm); (f) an image from the same region as in panel e but at higher magnification (scale bar is 500 nm)

pressed, requiring the brittle fracture of oxide between bundles, followed by recovery driven by the now uninhibited elastic CNT bundles. Figures 4.6b and 4.6c provide a view from the side and top of the CNT array, respectively, using SEM. Notice that the side view shows excellent recovery of the CNT bundles, and the top view shows significant separation of the bundles. In contrast, the samples modified with MnO_2 (Figure 4.6d-f) show little cracking but recover much less of their original height af-

ter compression. Figures 4.6e and 4.6f show significant permanent entanglement of individual CNTs at two different magnifications.

This discussion also explains the existence of plateaus in the stress-strain curves for samples modified with SnO_2 (e.g., Figure 4.3b) which are not observed for the samples modified with MnO_2 (e.g., Figure 4.3a). It is noteworthy that such plateaus are only observed for the first compressive cycle, and are therefore thought to correspond to brittle failure during the formation of lateral cracks through the oxide deposits. It is clear from Figure 4.5b that even the samples modified by MnO_2 display some lateral cracking along the edges of the samples after compressive loading. This can occur to some extent even in unmodified CNT arrays due to a lack of inward lateral support at the edges.

In addition to Sn and Mn oxides we also synthesized Fe oxide and Co oxide particles using corresponding metal salts as precursors and following similar procedures as described earlier. We have also successfully formed metallic particles by subjecting the oxide particles to carbothermal reduction. While we have thereby verified the versatility of the processes described in this study as a proof of concept, further work is necessary, including the synthesis of a larger number of such samples, to understand the systematic effects of these different types of particle loadings on the mechanical properties. It is especially important to understand the integrity of these structures under mechanical stresses by understanding how the affinities of the various types of particles for CNTs might differ from one another, as we have done for SnO_2 and MnO_2.

4.4 Conclusion

We have synthesized SnO_2 and MnO_2 in CNT arrays without disrupting the ordered structure of the individual CNTs or the overall structure of the arrays themselves. Under compression the structures exhibit a hysteretic response, as expected for CNT arrays. The structures modified with nanoparticles dissipate up to twice the amount of energy as unmodified samples. Modifying CNT arrays with SnO_2 results in brittle

deposits of the oxide in the array interstices separated by elastic bundles of CNTs. Compressing these structures results in lateral fracturing through the oxide deposits, followed by elastic recovery of the CNT bundles. After only a few compressive cycles the material with SnO_2 responds similarly to unmodified CNT arrays in compression (as compared by quasistatic stress-strain data and energy dissipation). In contrast to this, when MnO_2 particles are synthesized in CNT arrays by emersion of the CNTs in aqueous $KMnO_4$ the particles form on the individual CNTs themselves. The modifications result in higher energy dissipation during compression and minimal lateral fracturing, even after repeated cycling, but also yield more entanglement of the individual CNTs, resulting in less strain recovery after compression. With electrochemical applications already being developed for similar materials, continued study of the mechanical properties of these systems could lead to useful multifunctional materials with simultaneous mechanical and electrochemical uses.

Acknowledgments

The authors thank Carol Garland for her assistance with transmission electron microscopy. This work is supported by the Institute for Collaborative Biotechnologies, under contract W911NF-09-D-0001 with the Army Research Office. JRR also gratefully acknowledges support from the Department of Defense via a National Defense Science and Engineering Graduate (NDSEG) Fellowship.

Chapter 5

Synthesis and characterization of carbon nanotube-polymer multilayer structures

Abstract

We develop lightweight, multilayer materials composed of alternating layers of polydimethyl siloxane (PDMS) polymer and vertically aligned carbon nanotube (CNT) arrays, and characterize their mechanical response in compression[1]. The CNT arrays used in the assembly are synthesized with graded mechanical properties along their thickness, and their use enables the creation of multilayer structures with low density (0.12–0.28 g cm^{-3}). We test the mechanical response of structures composed of different numbers of CNT layers partially embedded in PDMS polymer, under quasistatic and dynamic loading. The resulting materials exhibit a hierarchical, fibrous structure with unique mechanical properties: They can sustain large compressive deformations (up to ~ 0.8 strain) with a nearly complete recovery and present strain localization in selected sections of the materials. Energy absorption, as determined by the hysteresis

[1] We have published a very similar version of this chapter as Ref. [140] by A. Misra, J.R. Raney, L. de Nardo, A.E. Craig, and C. Daraio. CD designed the study. AM, JRR, LDN, and AEC synthesized samples and performed mechanical tests. AM conducted electron microscopy and electrical characterization. AM wrote the manuscript with assistance from JRR, LDN, and CD. All authors contributed to the analysis of the results. One important difference between Ref. [140] and this chapter is an additional figure and paragraph, which analyze the effect of the polymer interlayers on the compressive properties of CNT arrays, and were derived from another work of ours, Ref. [151]. Published items are reproduced with permission.

observed in stress-strain curves, is found to be 2–3 orders of magnitude larger than that of natural and synthetic cellular materials of comparable density. Conductive bucky paper is included within the polymer interlayers. This allows the measurement of resistance variation as a function of applied stress, showing strong correlation with the observed strain localization in compression.

5.1 Introduction

In recent years, vertically aligned arrays of carbon nanotubes (CNTs) have been developed and considered for use as light-weight energy dispersive materials [117, 226]. CNTs exhibit unique mechanical attributes similar to those found in fibrous materials [131], having excellent compression capability coupled with extreme structural flexibility and recovery [67]. CNTs have the added benefit of presenting a high electrical conductivity, which can be exploited for the creation of multifunctional materials or for active strain monitoring in response to external mechanical loading [81]. The design and functionality of CNT-based structures has evolved and benefited from an understanding of non-linear stress wave mitigation and deformation mechanisms of cellular foams [114, 227].

A common protection scheme that is often adopted for impact mitigation and vibration damping is to utilize layered structures composed of materials with different acoustic impedance [228]. The approach has proven to be quite effective in the design of protective systems in which fiber-reinforced composites [229] or porous foam-like materials are combined with polymers and/or metals [230] to create highly efficient vibration and energy dampers. For practical applications, weight reduction plays an important role and requires the integration of new multifunctional materials based upon microstructural design. These characteristics suggest the use of CNT arrays as lightweight components in the assembly of protective devices against impacts and vibrations.

Preliminary investigations on the mechanical response of CNT arrays partially embedded in polymer have shown enhanced energy absorption capability and sensi-

tivity to large differences in strain rate [114]. In addition, aligned arrays of CNTs grown via thermal chemical vapor deposition have been reported to exhibit graded mechanical properties along their length and a foam-like behavior in compression [117]. The base of CNT arrays (i.e., the side nearer the substrate during synthesis) is generally softer and more prone to buckling and deformation [117]. These properties make CNT arrays excellent candidates as energy-absorbing materials, in particular for dynamic applications.

Multilayer arrays of CNTs are expected to present yet improved protective properties. The synthesis of hybrid materials based on alternating CNT and vermiculite inorganic layers has been reported [139]. Similarly, a multilayer structure consisting of alternating layers of aligned CNTs and metal foils has been described [72]. In both cases, the weak adhesion between the CNT foams and the interlayers limits their protective performance. The present study is focused on the fabrication and characterization of multilayer structures with compliant polymer interlayers, which show complete recovery after large compressive strain, without any damage at the interface between layers. The polymer layers reinforce the resilient aligned CNT bundles and act as an interface material to strengthen the multilayer structure. To evaluate the behavior of these layered structures, we performed mechanical tests with *in situ* electrical measurements and optical microscopy.

Vertically aligned arrays of carbon nanotubes were grown on thermally oxidized silicon by chemical vapor deposition using a one-stage thermal CVD system as described elsewhere [114]. A solution of ferrocene (catalyst) and toluene (carbon source) of 0.02 g ml^{-1} was fed into the furnace, which was at a temperature of 827 °C throughout the process. The overall length of CNT bundles was measured to be $\sim$ 800 μm. The CNT samples were taken off from the substrate using a razor blade, and the bulk density was determined by obtaining dimensions along the three axes and then dividing mass, as measured with a microbalance, by the volume of the CNT block. This density has been measured to be 0.12–0.28 g cm^{-3}.

After growth, a subset of samples was partially anchored in thin poly(dimethylsiloxane) (PDMS) layers. The anchoring was obtained with a multistep process: first

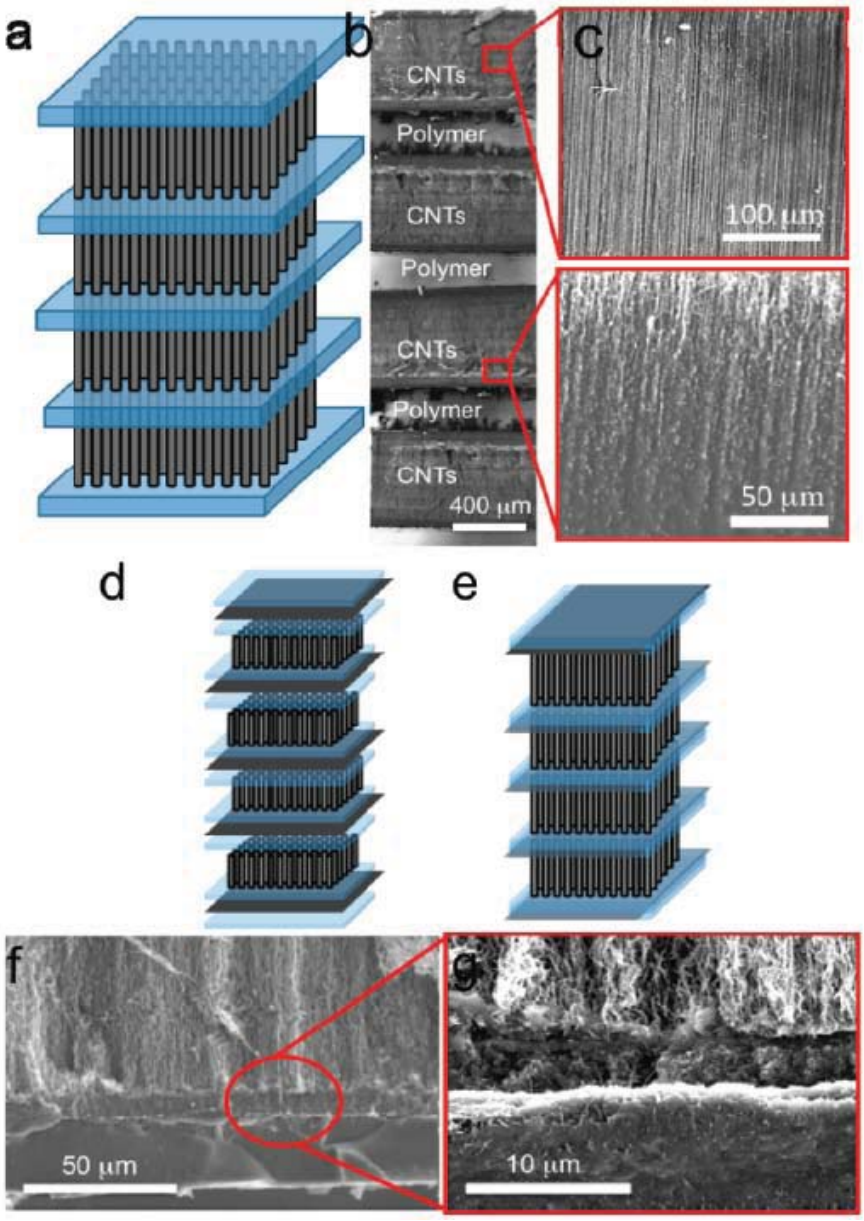

Figure 5.1: Multilayer carbon nanotube–polymer assembly; (a) Schematic diagram of the four-layer carbon nanotube-polymer (PDMS) structure; (b) Optical image of the four-layer carbon nanotube-polymer structure; (c) Scanning electron microscope (SEM) image showing the freestanding and wetted portions of the CNT array; (d) Schematic diagram of the assembly of a multilayered CNT system with embedded polymer–bucky-paper layers; (e) Final arrangement of carbon nanotubes/polymer/bucky-paper film; (f) SEM images showing the interface between the polymer with embedded bucky-paper film and the CNTs; (g) Higher resolution image of the interface

the PDMS was mixed with the curing agent in 10:1 ratio, and then the mixture was spin-coated on a glass slide at 700 rpm, to achieve a 50-μm-thick layer. This thickness was sufficient to connect two CNT bundles (as shown in schematic diagram Figure 5.1a) in a multilayer structure. The first layer of the CNT-polymer multilayer structure was created by embedding the end segments of the carbon nanotubes in a PDMS polymer layer via a substrate transfer method [114]. Figure 5.1a and b show that most of the CNT length is not embedded in the polymer. It was shown earlier that after curing the PDMS and CNT structure at 80 °C, the CNTs adhere well with the PDMS layer [138]. For the fabrication of the multilayer structure, the process was repeated sequentially for each layer in the structure. An image of the final multilayer structure, comprised of four CNT layers separated by polymer interlayers, is displayed in Figure 5.1b. The number of stacking layers can easily be extended utilizing the same fabrication process. The scanning electron microscope (SEM) images in Figure 5.1c and d show close-up views of the polymer-free and embedded portions of the CNT array, respectively. This partial polymer embedding has structural and mechanical advantages in the layered structure: (1) it supports the CNT bases and tips, preventing separation between the layers during deformation, in contrast to what was observed in other reports [139], and (2) it improves mechanical damping due to the compliant polymer matrix [128, 131].

A separate set of samples was prepared including a thin conducting film of entangled CNTs, commonly known as bucky paper (BP), within the polymer layers. The presence of this $\sim$ 10-μm-thick BP provided electrical continuity through each polymer layer and rendered the entire multilayer structure electrically conductive. The BP thin film was obtained by filtration of a CNT suspension in 2-propanol and water (25% vol.). The films were individually sandwiched within PDMS layers, as shown by a schematic diagram in Figure 5.1d (the black layer shows the BP film, and PDMS layers are shown in a light color). The final multilayer CNT assembly is depicted in Figure 5.1e. A SEM image of the interface between the CNT and the polymer with BP is shown in Figure 5.1f, while a close-up view of the contact between the BP film in the polymer and the CNT arrays is shown in Figure 5.1g.

The quasistatic cyclic compressive response of the multilayer CNT-polymer assemblies was investigated using an Instron E3000. Compressive loads were applied along the CNT growth direction, as depicted in the inset schematic diagrams of Figure 5.2a. Displacement controlled compression tests were performed on single- and four-layer CNT assemblies partially embedded in PDMS layers. The goal of these mechanical investigations was to test the stability of the CNT-polymer interfaces and to characterize their ability to recover from large deformations. To ensure reproducibility of the results, measurements were acquired from six different samples for each type of structure (i.e., a single CNT layer in PDMS, both with and without BP film, as well as CNT-PDMS structures with four CNT layers, with and without BP films). The stress-strain response was measured up to a set maximum compressive strain ($\epsilon_{max} = 0.8$), determined so as to avoid reaching the maximum force capacity of the machine, and at two selected strain rates (10^{-2} and 0.5 s^{-1}). We have not observed any strain rate dependence on the compressive behavior of CNT bundles alone in this range of strain rates (i.e., 10^{-3} to 0.5 s^{-1}), when the measured bulk density was accounted for [52].

5.2 Results and discussion

The representative stress-strain responses for three compressive cycles for single- and four-layer CNT structures, without BP films, are shown in Figure 5.2a. Figure 5.2b contains similar curves reporting the response of single-layer structures with and without BP films. Both single- and four-layer structures present a nonlinear loading-unloading path with a hysteretic behavior in loading and unloading. This hysteresis was suggested to be a result of friction between the CNTs [117]. In all cases, a foam-like behavior is evident, similar to that already reported for freestanding vertically aligned CNT arrays [72, 117]. The measured compressive stress-strain curves reveal three different regimes of deformation [72, 117, 231] characterized by (i) an initial linear elastic response at lower strains (less than 0.1), (ii) an intermediate region (between 0.1 and 0.6 strain) in which the deformation increases monotonically with small

variation in the associated stress (a behavior characteristic of coordinated buckling and bending), and (iii) a final rise of the stress to a peak between 20 and 30 MPa (at the peak strain, $\epsilon = 0.8$), resulting from densification and collapse of the overall assembly [139].

To analyze the linear elastic response of the sample, we calculated low strain stiffness by a linear fitting of the initial linear elastic stress increase associated with the first loading cycle in the stress-strain curves (Figure 5.2a and b). We obtained the average value of this stiffness for the single-layer structure $E = 9.9 \pm 1.8$ MPa and an enhanced modulus of 16.3 ± 1.9 MPa for the four-layer structures in Figure 5.2a. However, samples including BP films resulted in a lower modulus for both the single- (9.1 ± 1.7 MPa) and four-layer (12.3 ± 2.0 MPa) structures. The measured lower modulus is likely caused by the increase in thickness of the compliant polymer [232], because structures with no BP have thinner polymer interlayers (~ 50 μm) than those with BP (~ 100 μm), and from the possible presence of slip between CNTs in the BP during compression [233]. Additional effects originating from the composite nature of the polymer/CNTs interface may contribute to the overall response of the samples, but have not been characterized as part of this study.

After the elastic region, the stress-strain response presented a monotonic increase in the stress between 0.1 and 0.6 strain. At strains higher than 0.6 the stress began to increase rapidly, reaching a maximum peak value of ~ 24 MPa at the highest strain (0.8) for single-layer structures with no BP. Four-layer structures with no BP reached a maximum stress of 19 MPa (Figure 5.2a). Because of variation in L/D ratios (where L is the height and D is the lateral dimension of the area of the samples), the deformation mechanisms in compression may differ between samples. This implies that taller specimens might engage in compressive instabilities and non-uniaxial loading. In samples with BP films we observed higher peak stresses for both the single-layer (~ 29 MPa) (Figure 5.2b) and the four-layer structures (~ 23 MPa). The increase of the peak stress level in the structures with BP films can be explained by an enhanced compressive strength due to the reinforcement of the carbon nanotube ends into polymer at the interfaces as compared to the cases of free-standing CNTs and

polymer only as described in an earlier report [131]. According to this report [131], the polymer around CNTs provides a confining effect, which results in strengthening of the composite interface in the structure.

In order to evaluate the effects of PDMS on the buckling behavior of the CNT arrays, we performed SEM analysis on both free-standing and anchored CNTs while the samples were compressed at a fixed strain value of ~ 0.4, using a controlled clamping mechanism. Figures 5.3a–b show the compression of freestanding and sandwiched CNTs, respectively.[2] When uniaxially compressed, freestanding structures start to collapse with zigzag buckles from the bottom (Figures 5.3a and 5.3c), as already observed by Cao et al. [117]. In contrast, the sandwiched CNT arrays buckle differently: the structure collapses by forming zigzag buckles that are then driven outward by the lateral deformation of the PDMS. This is evident in the SEM image in Figure 5.3b and it is explained in the schematic diagram in Figure 5.3d. As another way to quantify the effect of the polymer on the compressive response of CNT arrays, we calculated the ratio between the transverse (lateral) strain and the axial (longitudinal) strain at $\epsilon = 0.6$. For free-standing and anchored CNT arrays, these values were ~ 0.01 and ~ 0.5, respectively.

The residual strain, which corresponds to the permanent deformation in the structure after compression, was observed to be about 0.05 in all samples. Both the peak stress and the hysteresis area were observed to decrease with an increasing number of compressive cycles. Figure 5.2a and b show the first three compressive cycles for each type of sample. There is little difference between the second and third compressive cycles for all samples shown, revealing that after only a couple of cycles the majority of the compressive damage has taken place, with the material nearly in a steady-state response for further cycles. This is in agreement with earlier reports for free-standing CNT forests [117]. A similar characteristic behavior was also observed for multilayer structures with BP films.

The stress-strain curves obtained in the quasistatic tests (Figure 5.2a and b) were used to calculate the energy absorption capabilities of all samples. Depending on

[2] This paragraph, and the associated figure, come from a different work of ours, Ref. [151].

what material the CNT-based structures were being compared to, this quantity was calculated in two different ways. First, we show the energy absorbed during loading only (method 1), for comparison with materials having porous and layered microstructure that permanently deform in loading. Later, we calculate energy absorption as the area enclosed by the hysteresis loop between loading and unloading, to compare the response of our sample with protective materials that completely recover after loading (method 2). For the comparison with permanently deforming materials, we integrated the area under the loading portion of the stress-strain curves and plotted these values (per unit volume) up to a given peak stress as a function of the peak stress (Figure 5.2c). Although the CNT-based materials recover from strain, and therefore a portion of the energy absorption indicated for the CNT-based materials in these plots is a result of elastic energy that will be recovered, it is still useful to make the comparison of how the energy absorption capacity varies as a function of compression (peak stress) during loading. As observed in the stress-strain curves shown in Figure 5.2a and b, the recovery or unloading portion of the hysteresis takes place at very low stress levels, meaning that the elastic strain energy recovered is a small portion of the total energy absorbed during loading. This allowed us to compare the energy absorption capabilities of our CNT-polymer-based materials with the energy absorption of biological materials that also employ a multilayer composite structure with a foam-like interior and a denser exterior region, such as cancelleous bone [153] and lamellar fibers such as cartilage [234]. The data for biological materials were extracted from the reported stress-strain curves given in the references provided [153, 234]. It is evident that the CNT-based materials have comparable or better energy absorption capabilities than cartilage [234], as a function of peak stress, despite having bulk densities between 0.12 and 0.28 g cm^{-3} (as described above) compared to 1.12 g cm^{-3} for cartilage [235]. Interestingly, the CNT-based materials also showed improved energy absorption over cancelleous bone, up to a critical value of measured peak stress ($\sim$ 10 MPa). At higher peak stresses, cancelleous bone shows higher energy absorption than the CNT-based structures, most likely related to its larger density ($\sim$ 1.85 g cm^{-3}) [236] and more complex microstructure. We also cal-

culated the cushion factor [153] as the measured peak stress over energy absorbed for the different CNT-polymer structures. The cushion factor values for all types of tested CNT-polymer structures were plotted against the peak stresses and compared with those for cartilage and bone (Figure 5.2d). In the lower peak stress regime, the cushion factor of CNT structures was found to be higher than the cartilage and bone structures. Among the CNT-polymer structures both the energy absorption and cushion factors have not shown significant differences at any value of peak stress. The energy dissipation in our multi-layer structures is expected to derive from frictional interactions between adjacent, entangled CNTs, in the section of the CNTs not embedded in polymer, and from the presence of a soft and compliant polymer interlayer partially embedding the CNTs. In addition, relative twisting of the CNT bundles may contribute to the energy dissipation, similar to what is observed in the shear interaction of CNT fibers [98, 237].

To evaluate the performance of our CNT-polymer structures in comparison with protective materials presenting large recovery after deformation, we selected different commercially available foams (CFs) obtained from microelectronic packaging and protective padding: cellulose fibers, polyurethane, and rubber. Densities of the CFs varied from 0.02 to 0.2 g cm^{-3}. We compared the CNT-based structures to the CFs by comparing their quasistatic performance. The data are presented for tests performed at a strain rate of 0.05 s^{-1}, though it should be noted that the response was found to be strain-rate independent in this regime as discussed elsewhere [52]. We calculated the peak stress (Figure 5.2e) at maximum (0.8) strain. We also compared energy absorption (Figure 5.2f). In this case we integrated the area of the hysteresis to account for both loading and unloading behavior, since both the CNT-based structures and the CFs recover from deformation. The CNT-polymer structures show a dramatic improvement of up to 3 orders of magnitude higher peak stress and energy absorption capability over CFs at comparable density. Optical microscopic images of the analyzed foam samples and the schematic diagram of CNT structures are depicted in Figure 5.2g.

It is also useful to compare the energy absorption properties of the CNT-based

systems with those of common metallic foams, such as those based on aluminum.[3] This can be challenging, however, due to large variability in the microstructure and the resulting bulk behavior of metal foams. We therefore give only a qualitative comparison of the general behavior here. The most important difference is that typical metal foams undergo plastic deformation of the metallic cell walls during compression, resulting in almost no recovery from deformation to large strains [238]. In contrast, the elasticity of the individual CNTs can result in nearly complete recovery of CNT arrays from large strains (with important exceptions—see, e.g., Ref. [119]). However, during compressive loading aluminum foams behave qualitatively similar to CNT foams of comparable density, with dissipation and plateau stress that are similar or slightly lower than those of CNT arrays [239].

For a detailed characterization of the deformation of multilayer structures, we coupled *in situ* optical measurements to the mechanical testing system. An optical microscope equipped with a digital camera allowed the real-time observation of the deformation of multilayer structures during compression and recovery, as a function of the applied compressive strain (see Figure 5.4a and b). A typical single-cycle compression test is reported in Figure 5.4 with snapshots acquired at different strains during testing. The dashed lines in Figure 5.4a are added to guide the eye for identifying the buckling and recovery response of the individual layers (the dashed lines indicate the location of the polymer interlayers).

Panel 1 in Figure 5.4a shows the pristine structure before compression (as indicated by point 1 in Figure 5.4b). The non-uniform gradual collapse of each layer at 0.3 strain (Figure 5.4b) is shown in panel 2 of Figure 5.4a. Upon reaching 0.5 strain, all layers have begun to collapse (panel 3 in Figure 5.4a, corresponding to point 3 in Figure 5.4b). This response demonstrates the presence of strain localization. At 0.8 strain, the layers show a homogeneous collapse (point 4). Points 5 and 6 show the nearly complete recovery of the structure as the strain returns to zero. A non-uniform recovery is shown in panel 5 of Figure 5.4c. The localized deformation and sequential buckling/recovery of the layers observed during testing is likely to be related to the

[3] This paragraph does not appear in the original paper corresponding to this chapter.

graded stiffness in the microstructure and in the differences in CNT properties from one CNT layer to the next. Such variations have been shown to affect the mechanical properties of CNT arrays [40, 52]. A schematic diagram explaining this phenomenon is shown in Figure 5.4c. This localized deformation of the individual layers is particularly relevant to the energy absorption of structures loaded dynamically [206].

We assessed the dynamic response of the layered CNT-polymer structures by drop ball impact tests (see Methods section) (Figure 5.5a) [202]. We evaluated the force mitigation performance of different CNT structures by comparing the peak force and length of contact time between samples composed of one, two, three, and four layers of CNTs under the same loading conditions (Figure 5.5b). The four-layer structure showed improved force mitigation capability as compared to the single-, double-, and triple-layer materials. In general, the peak force was observed to decrease with increasing number of layers, while at the same time, the contact duration increased. The onset of the deformation in the different layers of the multilayer structure is visible from the presence of "shoulders" in the force-time response, likely indicating the sequential collapse of individual layers and the localization of deformation within selected sections of the material. It is also possible that additional modes of deformation, such as bending, are being excited in these multilayer structures, since the aspect ratio of the samples increases with the number of layers (i.e., the height increases while the cross-sections of the individual samples remain unchanged). However, we saw no evidence for the introduction of new modes in the mechanical responses, which were observed to be independent of the number of layers.

The deformation of the CNT arrays and the effects of residual strain after cyclic compression were monitored via *in situ* and *ex situ* measurements (see Methods section) of electrical resistance across each layer of the CNT-polymer structures (Figure 5.6), assuming a constant contact resistance. The measurement of electrical resistance (Figure 5.6a) during cyclic tests revealed that materials composed of a single layer of CNTs present a decrease in electrical resistance (*in situ*) during loading, and an increase with unloading (Figure 5.6b). The observed variation in electrical resistance may be related to the structural reorganization of the individual CNTs within

the array. It has been suggested that this reorganization results in an overlap of the electron states in adjacent CNT walls, leading to an increase in the accessible number of electrical conduction channels while loading [155]. The distance between adjacent CNTs decreases when the CNTs bend in compression [155]. This may also increase the number of point contacts between CNTs and lower the resistance of the CNT arrays. The variation of resistance, defined as $\frac{\Delta R}{R_0}$, where ΔR is the resistance change between the final and the pristine (R_0) cases, was observed to decrease gradually after each cycle. Interestingly, we also noticed a permanent decrease of the electrical resistance after the load was completely removed, and this decrease can be attributed to the irreversible structural changes occurring in the CNT array structures.

Ex situ electrical measurements were performed on four-layer CNT structures. For this measurement the voltage was fixed at 5 V and the current was measured across each layer before and after the mechanical tests. Measurements were taken between the top layer (fixed electrode) and the successive layers (moving the electrode progressively from one layer to the next), as shown in the schematic diagram (Figure 5.6c). The electrical measurements acquired after performing the mechanical tests showed a significant difference as compared to the measurements acquired from the pristine sample. In particular, the current measured was different in each layer of the structure (Figure 5.6d). This suggests that the individual layers deform differently from one another and undergo different structural rearrangements. In this particular case, the current measured across the first layer was observed to decrease, as opposed to the increase measured across the other layers. This suggests a localization of deformation in the first layer of the structure, in agreement with the optical image shown in Figure 5.4a (panel 6). This effect may arise from the presence of imperfections deriving from the fabrication process.

5.3 Conclusions

We report the design, fabrication, and testing of new lightweight multilayer materials for energy absorption, using structures composed of alternating layers of aligned

carbon nanotubes and polymer (PDMS). The final materials combine a fibrous microstructure with graded mechanical properties. The presence of polymer interlayers provides adhesion and prevents delamination between different layers under mechanical loading. These materials have good energy-absorbing ability (up to three orders of magnitude better than conventional packaging foams of similar density) and present localized deformation within the individual layers composing the structure. The additional ability to include conducting bucky paper within the polymer interlayers provides electrical conductivity across the material's thickness without degradation of the overall mechanical properties. *Ex situ* and *in situ* electrical and optical measurements have been performed, revealing strain localization and differential collapse of the individual layers under compression.

5.4 Methods

Dynamic Mechanical Characterization

The experimental setup for high-strain-rate dynamic tests ($\sim 10^3$ s^{-1}) used a free-falling sphere (4.76 mm diameter, 0.45 g, Bearing-Quality Aircraft-Grade 25, Alloy Chrome Steel precision stainless steel ball, with a surface roughness $\sim$ 50 nm maximum, made from AISI type 52100 steel, McMaster-Carr) as a striker to impact the CNT samples. A calibrated piezosensor (Piezoelectric single sheet, 515 T110-A4-602 provided by Piezo-System, Inc., with soldered 34 AWG microminiature wiring) connected to a Tektronix oscilloscope (TDS 2024B) was used to detect force-time curves under the sample. The impact was generated by dropping the steel sphere from a height of 10 cm, which corresponds to an impact speed of $\sim$ 1.4 m s^{-1}.

Electrical Measurements

Two-point electrical measurements were performed using an Alessi REL-3200 probe station attached to a Keithley-2365 source measure unit system. Bucky paper films were used as conducting electrodes to measure the changes in normalized electrical

resistance during the compression of single layer (*in situ*) [137] and electrical current after recovery of the multilayer structures (*ex situ*). These measurements were monitored to observe changes due to the compression and recovery of the individual layers in both multi- and single-layer samples, similar to the cyclic tests described in Ref. [137], for the measurement of resistance as a function of strain. The electrical current in the direction of the CNT growth was evaluated at a constant voltage of 5 V.

Acknowledgments

We thank H. M. (Chinthaka) Mallikarachchi and S. Lacheteau for their contribution to the experiments. J.R.R. gratefully acknowledges support through a National Defense Science & Engineering Graduate (NDSEG) Fellowship through the Department of Defense. L.D.N. thanks INSTM for travel granting support in "Metamateriali" grant project. C.D. acknowledges support from the Institute for Collaborative Biotechnologies under contract W911NF-09-D-0001 with the Army Research Office.

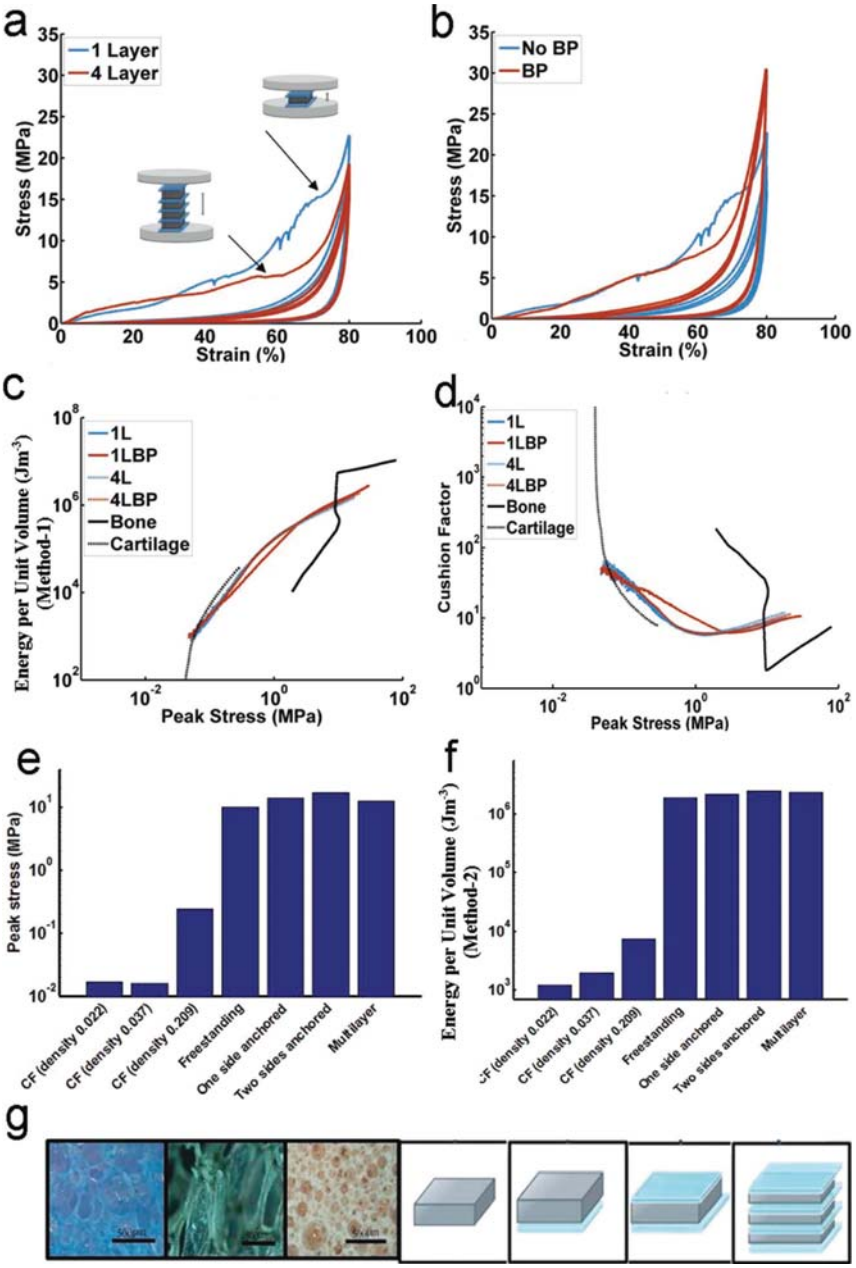

Figure 5.2: Quasistatic mechanical response and energy absorption; (a) Typical stress-strain curves obtained with single- and four-layer structures without insertion of bucky-paper film; (b) Typical stress-strain curves obtained with single-layer structures with and without insertion of bucky-paper films; (c) Energy absorption plots of single- and four-layer structures, calculated using method 1 and compared with cancelleous bone and cartilage; (d) Cushion factor of single- and four-layer structures, compared with those of cartilage and bone; (e–f) Maximum peak stress and energy absorbed per unit volume, calculated using method 2, for commercial foams (CFs) and CNT structures; (g) Optical images of commercial foams with three different densities, 0.022, 0.037, and 0.209 g cm^{-3} from left to right, respectively (scale bar is 500 μm), and the schematic diagram of the CNT structures with and without polymer layers, from left to right, respectively

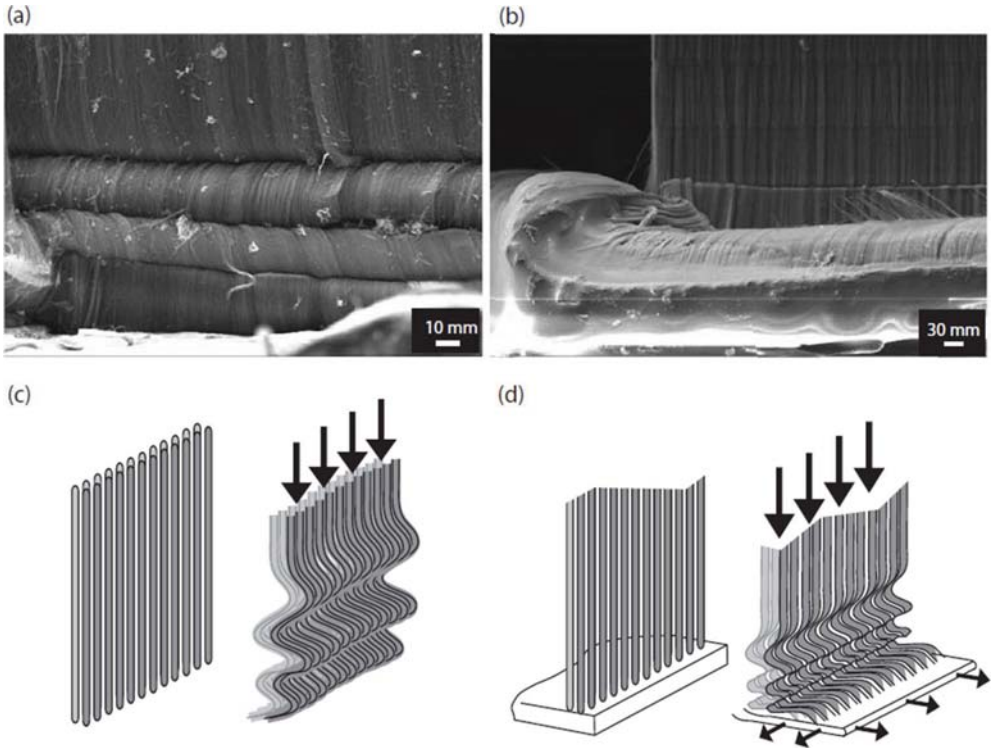

Figure 5.3: Scanning electron microscope (SEM) micrographs of the buckling area in the bottom section of (a) freestanding and (b) double-anchored CNT forests while compressed at $\epsilon = 0.4$. Schematic illustration of the different compressive behavior in (c) freestanding and (d) double-anchored CNT forests

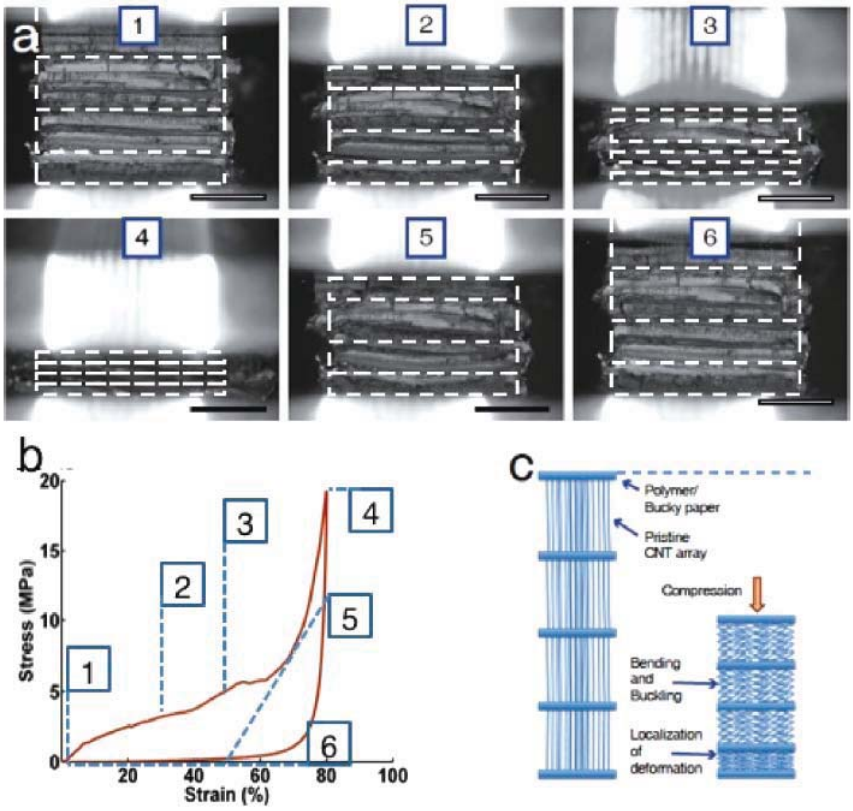

Figure 5.4: *In situ* visualization of the compressive deformation of a multilayer sample; (a) Digital snapshots of the deformed configuration of the four-layer structure corresponding to the different strain levels indicated in panel b. The white lines show the position of polymer, which separates each CNT layer. (b) Stress-strain curve showing the different strain levels corresponding to the snapshots in panel a; (c) Schematic diagram illustrating the localized deformation of the four-layer structure under compression

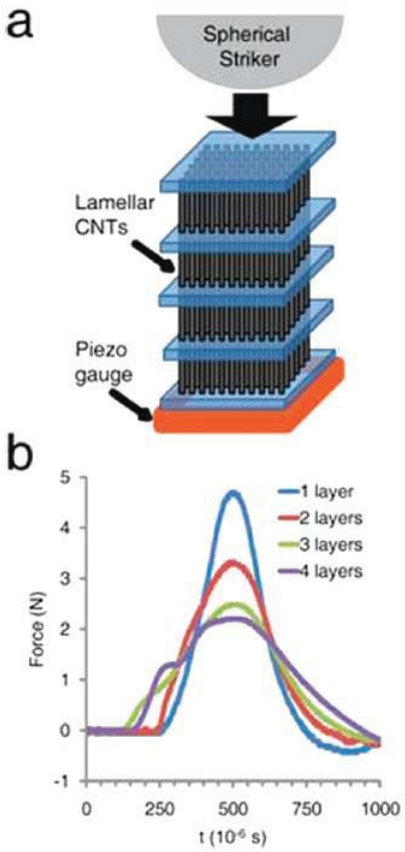

Figure 5.5: Structure-dependent dynamic response; (a) Schematic diagram showing the experimental setup; (b) Force-time plots obtained by impacting the CNT-polymer structures with a stainless steel bead at ~ 1.4 m s^{-1}

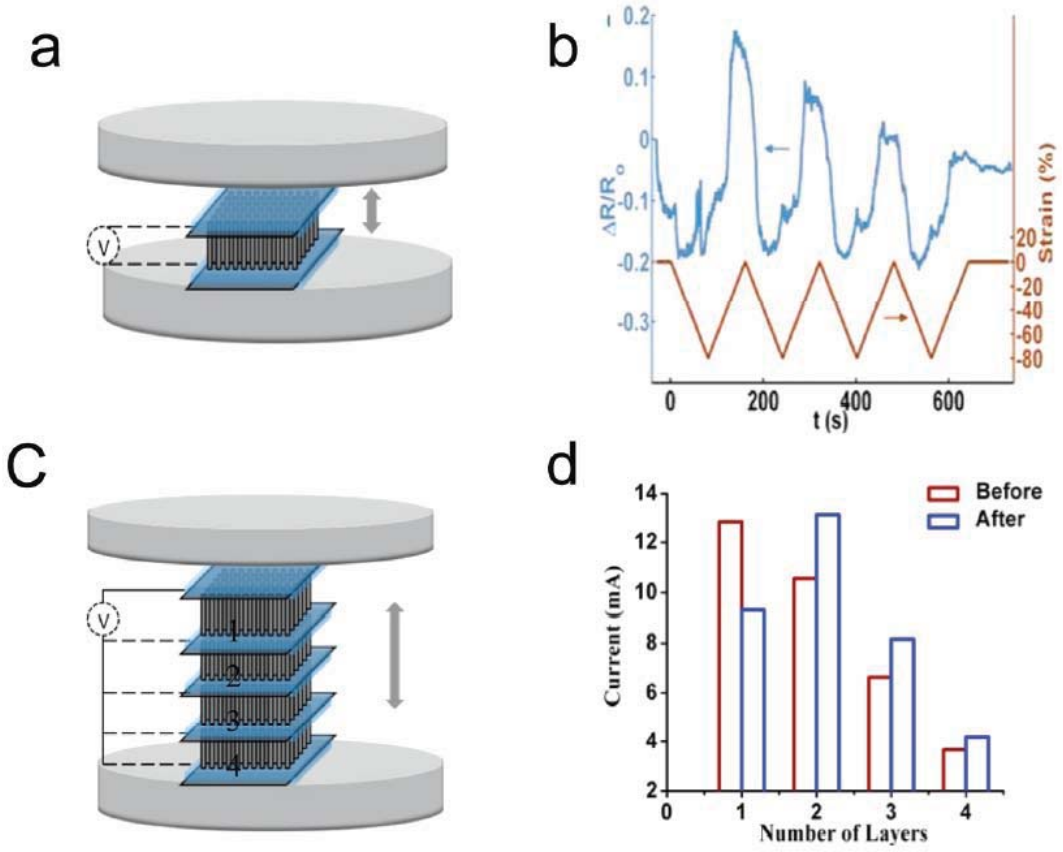

Figure 5.6: *In situ* and *ex situ* electrical response under applied stress; (a) The schematic diagram shows the experimental setup used for *in situ* cyclic compression on a single layer of CNT-polymer; (b) Compressive strain and fractional resistance change ($\frac{\Delta R}{R_0}$) measured (*in situ*) during cyclic compression for an assembly of polymer, bucky paper, and a single layer of carbon nanotubes; (c) Schematic of the experimental setup used for electrical measurement of a four-layer structure; (d) *Ex situ* electrical measurements performed after compressive testing of the multilayer samples. The graph shows the measured electric current before (red color) and after (blue color) compression of the four-layer structure. The dark line shows the constant position of one electrode, and dashed lines show the measurements between sequential layers with respect to the constant electrode

Chapter 6

Modeling the compressive response of CNT arrays

One of the modeling approaches used in early research of the mechanics of CNT arrays (e.g., Ref. [117]) was to treat CNT arrays as non-interacting, parallel Euler columns, mainly with the goal of explaining the buckling of CNT arrays in compression. However, several physical phenomena make such an approach insufficient to explain what is occurring in these systems. First, as has been repeatedly observed experimentally [117, 120, 152, 156], buckling takes place locally, starting from one side of the structure, rather than in the center of the structure, as would be expected for Euler buckling. Second, there is a physical gradient along the height of the structure for a number of parameters, including the CNT diameters themselves (as discussed in Section 1.4.1). Third, though at a mesoscale the CNTs (or rather, CNT bundles) are very aligned, at the submicron scale there is extensive lateral entanglement among CNTs [114]. For these reasons, the nature of the buckling is a local phenomenon, and therefore the model that captures it must account for this reality.

In order to address the above, Fraternali et al. [71] developed a one-dimensional multiscale model based on bistable spring elements in series. This model captures both the local nature of the deformation in compressed CNT arrays as well as the global stress-strain response. First, an overview of the original model by Fraternali et al. [71] will be given in Section 6.1. Then the model will be extended and applied toward two different applications. The first of these, discussed in Section 6.2, involves

an extension of the model to capture some of the more complicated aspects of the mechanics of CNT arrays which were not captured by the original model (e.g., the experimental observations of permanent deformation and of a Mullins-like compressive response, as discussed in Section 2.2). The second application of the model is for our multilayer structures of CNT arrays (similar to those discussed in Chapter 5). In this case, discussed in Section 6.3, an *in situ* procedure is developed that uses experimental information to allow model parameters to be identified more efficiently than otherwise.

6.1 Overview of the multiscale model based on bistable elements in series

We model the strain-rate-independent compressive response of CNT arrays using a one-dimensional model based on a series of bistable springs, following the original work by Fraternali et al. [71]. Importantly, this model is multiscale, which reflects the multiscale nature of the mechanics of CNT arrays as discussed earlier. At the smallest scale the material is modeled by a 1D mass-spring chain of $N+1$ masses $m^0, \ldots, m^N$ connected by N identical bistable microscopic spring elements ($N \geq 2$). Such a series of springs represents an infinitesimal portion of the height along the CNT array structure. The mass m^0 is clamped at the bottom of the chain at position $x^0 = 0$, whereas m^N is on top at position $x^N = L$. The bistable springs are characterized by the axial strains

$$\varepsilon^i = \varepsilon^i(u_N) = \frac{u_N^{i-1} - u_N^i}{h_N}, \qquad i = 1, \ldots, N, \tag{6.1}$$

where u_N^i denotes the axial displacement of the mass m^i (positive upward). The potential V^i and stress σ^i vs. strain ε^i relationship for a generic spring are defined by

$$V^i(\varepsilon^i) = \begin{cases} V_a^i(\varepsilon^i) := -k_0^i[\varepsilon^i + \ln(1-\varepsilon^i)], & \varepsilon^i < \varepsilon_a^i, \\ V_b^i(\varepsilon^i) := c_1 + \sigma_a^i \varepsilon^i + \frac{1}{2} k_b^i (\varepsilon^i - \varepsilon_a^i)^2, & \varepsilon_a^i \le \varepsilon^i \le \bar{\varepsilon}_c^i, \\ V_c^i(\varepsilon^i) := c_2 - k_c^i[\varepsilon^i - \varepsilon_*^i + \ln(1-(\varepsilon^i - \varepsilon_*^i))], & \bar{\varepsilon}_c^i < \varepsilon^i, \end{cases} \tag{6.2}$$

$$\sigma^i(\varepsilon^i) = V^{i\prime}(\varepsilon^i) = \begin{cases} k_0^i \frac{\varepsilon^i}{1-\varepsilon^i}, & \varepsilon^i < \varepsilon_a^i, \\ \sigma_a^i + k_b^i(\varepsilon^i - \varepsilon_a^i), & \varepsilon_a^i \le \varepsilon^i \le \bar{\varepsilon}_c^i, \\ \frac{k_c^i(\varepsilon^i - \varepsilon_*^i)}{1-(\varepsilon^i - \varepsilon_*^i)}, & \bar{\varepsilon}_c^i < \varepsilon^i \end{cases} \tag{6.3}$$

where $k_0^i > 0$, $k_b^i < 0$, $k_c^i > 0$, $\varepsilon_a^i > 0$, and $\varepsilon_c^i \ge \varepsilon_a^i$ are constitutive parameters (five independent parameters); the constants $c_1 < 0$ and $c_2 > 0$ are such that $V_a^i(\varepsilon_a^i) = V_b^i(\varepsilon_a^i)$, $V_b^i(\bar{\varepsilon}_c^i) = V_c^i(\bar{\varepsilon}_c^i)$. This results in

$$\varepsilon_*^i = \varepsilon_c^i - \frac{\sigma_a^i}{k_c^i + \sigma_a^i}, \tag{6.4}$$

$$\bar{\varepsilon}_c^i = \frac{\varepsilon_c^i(k_c^i + \sigma_a^i)}{k_c^i + \sigma_c^i} + \frac{(\sigma_c^i - \sigma_a^i)(k_c^i + \varepsilon_c^i k_c^i + \varepsilon_c^i \sigma_a^i)}{(k_c^i + \sigma_a^i)(k_c^i + \sigma_c^i)}, \tag{6.5}$$

with

$$\sigma_a^i = k_0^i \frac{\varepsilon_a^i}{1-\varepsilon_a^i}, \qquad \sigma_c^i = \sigma_a^i + k_b^i(\bar{\varepsilon}_c^i - \varepsilon_a^i). \tag{6.6}$$

The stress-strain response of a generic microscopic spring (i.e., Eq. 6.3) is graphically illustrated in Figure 6.1. Allowing for dynamic relaxation during compression, such a spring would experience elastic deformation up to some critical strain ϵ_a followed by a dynamic switching event as the instability causes a shift from phase (a) (i.e., as indicated by the path between $\bar{A}$ and A in Figure 6.1) to phase (c) (i.e., as indicated by

the path between $\bar{C}$ and C in Figure 6.1). This snapping is associated with dissipation that results from "transformational plasticity" ("plasticity" which is reversible) [170, 240].

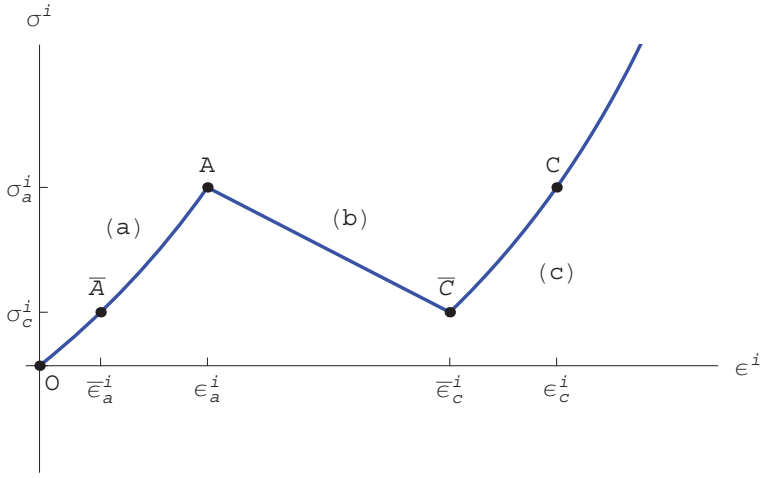

Figure 6.1: Stress σ^i versus strain ε^i relationship in the generic microscopic spring

As detailed in the work by Puglisi and Truskinovsky (Ref. [170]), a chain of identical bistable springs that is compressed to a sufficient strain will result in individual snapping events of single springs (as opposed to simultaneous snapping of multiple springs), following the maximum delay path. The total strain of the chain will remain constant during the rapid snapping of a single spring (as shown in Ref. [170]). Because of this, and the fact that the stress in each spring will be equal at equilibrium, as the snapping spring collapses to an increased strain the remaining $N-1$ springs must relax slightly, leading to a drop in the global stress (Figure 6.2). As $N \to \infty$ for a series of N microscopic springs, this stress drop approaches zero. Following the definition of Fraternali et al. [71], a *mesoscopic* spring element is now defined as such a continuum limit of microscopic springs (these mesoscopic elements will be formally defined in Sections 6.2 and 6.3).

The macroscopic response of the system will result from a series of such mesoscopic springs. Depending on whether the macroscopic system comprises a continuum limit of mesoscopic elements or if instead it comprises a finite number of such elements, each mesoscopic spring can represent an infinitesimal or a finite portion of the height of the CNT array. Each mesoscopic spring can have different properties. In our case, we use

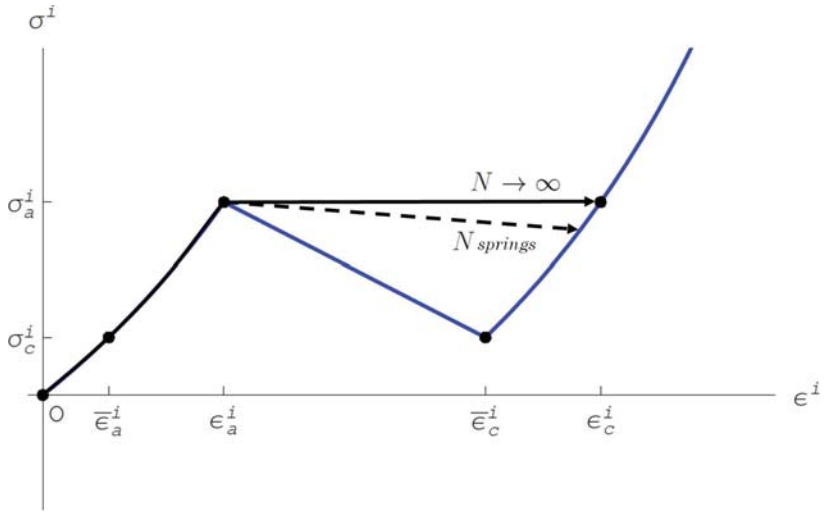

Figure 6.2: The snapping behavior during loading for a generic microscopic spring. The dashed line indicates a loading path associated with a stress drop that occurs for a generic spring during snapping in a finite chain (as a result of the relaxation of the non-snapping springs). The solid line shows the loading path for a chain in which $N \to \infty$, and therefore there is no stress drop

a finite chain of mesoscopic elements, and therefore the series of mesoscopic springs forms a chain with discrete regions of differing mechanical properties. In Section 6.3 this model is integrated with experimental data using *in situ* optics to allow for more rapid determination of model parameters for accurate modeling of experiments, and the model is also extended to the case of multilayer CNT structures.

6.2 Strain-rate-independent dissipative response of carbon nanotube arrays in compression

The previous section introduced a one-dimensional model based on bistable elements in series which is able to capture the global stress-strain response of materials based on CNT arrays as well as the local deformation that is observed in such systems. However, that model assumes that every compressive cycle is equivalent, thereby missing some of the more complicated mechanical behavior that is observed experimentally. This includes the Mullins-like behavior and partial strain recovery of real

CNT arrays, as was discussed in Chapter 2. Here we apply the model of Fraternali et al. to single-layer CNT structures, and extend it so that it is able to capture these additional effects. For detailed derivations and mathematical justifications related to the extended model, which was developed collaboratively, the interested reader is directed to Appendix A.

6.2.1 Introduction

Arrays of nominally-aligned carbon nanotubes (CNTs) have garnered much interest for their use as low-density, compliant (yet thermally and electrically conductive) materials for a variety of applications [97]. They can be readily synthesized using well-established techniques [32], such as thermal chemical vapor deposition [26]. This has allowed their integration into systems as diverse as field effect transistors [241], thermal heat sinks [107], brushes for electrical motors [112], and fatigue-resistant foams [118].

The mechanical behavior of these systems has therefore proven to be of great interest, and has been investigated for arrays of varying morphologies. CNT arrays as short as 50 nm [169] to as tall as several millimeters [157] have been investigated. The response can vary greatly, depending on such factors as CNT diameter distribution [40], CNT surface roughness [119, 174], the density of CNT-CNT contacts [167], and the presence of microstructural heterogeneities [197]. Under compression, the arrays undergo a localized response in which CNTs reorient and form collective buckles one at a time [156]. Compression reveals a hysteretic global stress-strain response, exhibiting viscoelasticity [151] and dissipating mechanical energy [117]. The mechanisms of this energy dissipation, which is at least two orders of magnitude superior to that of commercial polymeric foams of comparable density (~ 0.2 g cm^{-3}) [140], have remained largely uncertain, however.

Under compression, CNT arrays exhibit a complex mechanical response. Due to the well-established gradients in physical properties along the heights of long CNT arrays (e.g., gradients in CNT diameter [38], alignment [65], and contamination [37]),

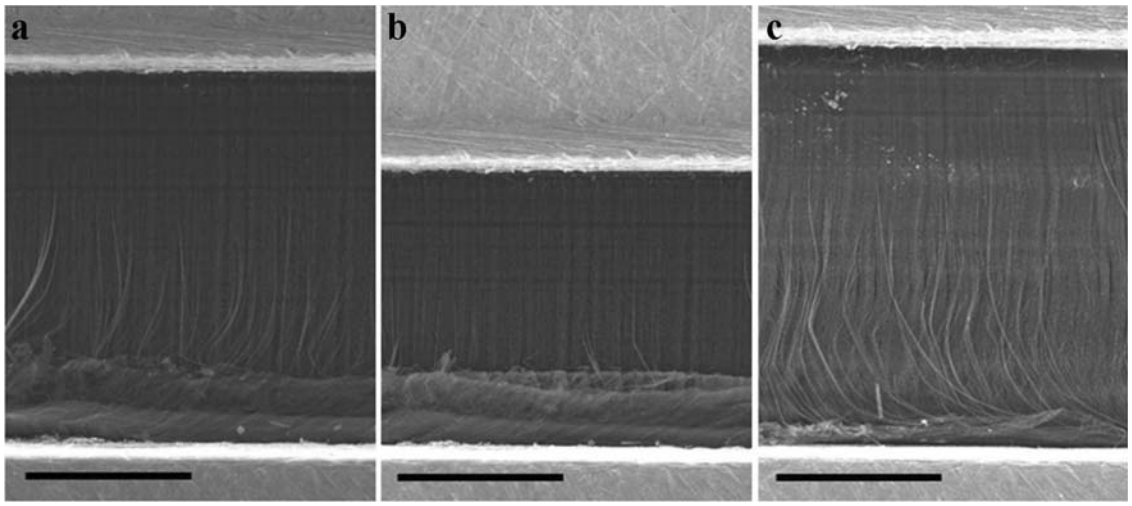

Figure 6.3: (a) A CNT array in a vise is held at low ($\sim$ 0.19) compressive strain and (b) at higher ($\sim$ 0.4) compressive strain, followed by (c) the array after it has recovered much of its original height after release from maximum strain; the scale bars represent 500 μm

a gradient in the mechanical response is observed. Typically, increasing compressive strain is accommodated by the sequential formation of buckles from the base (i.e., substrate-side) of the array [117], as shown in Figure 6.3, and this is true regardless of whether or not the array is still attached to the substrate or has been physically removed.

Upon release of a compressive load, CNT arrays (at least those synthesized by vapor phase catalyst systems [154]) recover most of their original height, allowing for the system to be loaded again. Figure 6.4a shows the stress-strain response for the first few compressive cycles to a maximum strain of 0.4 (i.e., the sample is deformed a total displacement of 40% of its original height), with the primary (first) cycle indicated by the solid line and the subsequent loading cycles indicated by the dashed lines. Notice that there is a large difference between the stress levels of the first compressive cycle and all of the subsequent cycles, but much less difference among the subsequent cycles. These later cycles quickly reach a fully-preconditioned response which would continue with minimal changes for dozens or hundreds of cycles [118].

This preconditioning effect and the local buckling effect discussed above have

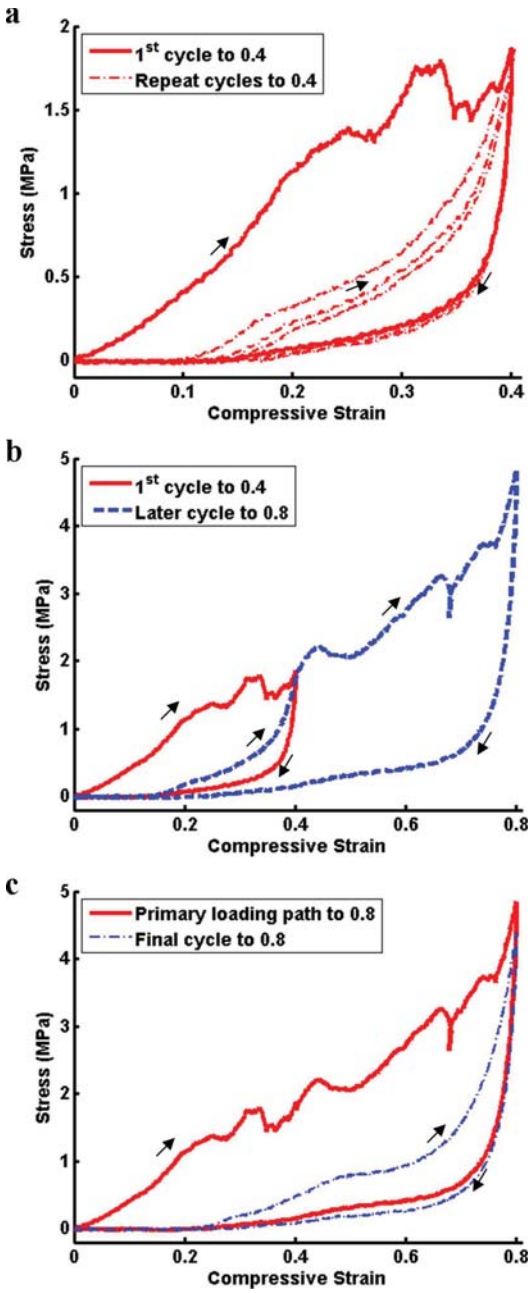

Figure 6.4: (a) Stress-strain response of the 1^{st} (solid line) and 2^{nd}–4^{th} (dashed lines) compressive cycles to 0.4 strain; (b) 1^{st} (solid line) cycle to 0.4 strain and the 4^{th} cycle (dashed), which was the first cycle beyond 0.4 strain, up to 0.8; (c) the primary loading curve (solid) constructed from part b, with the stress for strains 0 to 0.4 obtained from the solid line in part b and that for strains from 0.4 to 0.8 obtained from the dashed line in part b; the dashed line in (c) corresponds to a later cycle to 0.8, after the material exhibits a steady-state response

important ramifications for the mechanical response of the material under repeated loading. In Figure 6.4b the same sample that was compressed to a strain of 0.4 in Figure 6.4a is now compressed beyond that previous maximum to a new maximum compressive strain of 0.8. Notice that up to the previous maximum strain the stress response is that of a preconditioned material, but as soon as that threshold (0.4) is passed the material returns to the "primary loading path" and behaves as though it were not compressed previously. Figure 6.4c shows the primary loading path that was constructed by combining the stress-strain response for the first loading path (which stopped at 0.4 strain) with the later first compressive cycle to exceed that strain (which went to 0.8). Notice that combining the first compression from 0 to 0.4 strain with the first compression from 0.4 to 0.8 strain results in an uninterrupted path. That is, the material proceeds through a separate preconditioning phase from 0.4 to 0.8 regardless of the earlier preconditioning to 0.4. After several cycles to 0.8 strain, the steady-state response is reached (shown as the dashed line in Figure 6.4c). All of this is a direct consequence of the locality of preconditioning that results from the reorientation of individual CNTs [156] followed by the formation of collective buckles (Figure 6.3). Any time a previous maximum strain is exceeded, local microstructural rearrangements are necessary to allow for buckle formation along a portion of the height that has not previously rearranged in any way, necessitating the return to the primary loading path (e.g., the solid line in Figure 6.4c).

This combination of a hysteretic stress-strain response, preconditioning, and dependence on previous maximum strains is analogous to the Mullins effect as observed in rubbers [162]. It has been observed previously in CNT arrays undergoing indentation [114], and has been first pointed out for the case of compression in our previous modeling work [152, 164] (the experimental part of this is discussed in more detail in Section 2.2 and the mathematical details of the model are provided in Appendix A).

In addition to this Mullins-like behavior that we have described previously, we here show strain rate independence of the compressive response (both for the primary loading curve as well as the subsequent preconditioned cycles) over a range of 10^{-4}–10^{-1} s^{-1}. This has important implications regarding the physical mechanisms causing

the dissipative response of CNT arrays in quasistatic compression, as will be discussed in Section 6.2.4.

6.2.2 Experimental results

We synthesized arrays of nominally-aligned CNTs using a common vapor-phase (or "floating catalyst") procedure using a thermal chemical vapor deposition (CVD) system [26]. A solution of ferrocene and toluene was made at a concentration of 0.02 g ml^{-1} and injected into the 827 °C heating zone of the CVD furnace at 1 ml min^{-1} using a syringe pump. The ferrocene decomposes in the heating zone to release Fe, which acts as the catalyst for CNT growth, and the toluene acts as a carbon source. CNT arrays were synthesized to a thickness of approximately 1 mm (which took approximately 50 minutes) in a flow gas consisting of 50% argon and 50% hydrogen at atmospheric pressure. The arrays ultimately consist of multi-wall CNTs of outer diameters of approximately 20 nm and often 20 or so concentric walls [40]. Samples were subsequently removed from their growth substrates by razor blade prior to quasistatic compression testing with an Instron E3000.

We compressed the samples at strain rates from $\dot{\epsilon}$ =10^{-4} to 10^{-1} s^{-1}. First the samples were compressed three times to a strain of ϵ =0.4 followed by three compressive cycles to maximum strain ϵ =0.8. Figure 6.5 shows the stress-strain response for samples compressed at each of these strain rates. Figure 6.5a shows the stress-strain relationship for the first compressive cycle to strain ϵ =0.8, after the samples were preconditioned up to strain ϵ =0.4. As shown in Figure 6.4, this means that up to ϵ =0.4 the response is that of the preconditioned material and above ϵ =0.4 the response is that of the pristine material, along the primary loading path.

Samples at all four strain rates clearly respond very similarly. Importantly, however, as we have discussed in our previous work, both the maximum stress reached [52] and the area of the hysteresis (energy dissipated) [40] are linearly dependent on the bulk density of the samples. Though we took the samples used in these tests from directly adjacent portions of their growth substrate, we have observed that the density

does vary systematically even within a growth substrate [52]. It is therefore useful to normalize the stress response by sample bulk density, as we have done in Figure 6.5b for the data displayed in Figure 6.5a. Notice that in this case the responses are even more similar, almost entirely covering one another, both in the preconditioned region and along the primary loading path. To further lend clarity to the preconditioning region, we show the stress-strain response of the fully preconditioned material (all the way up to ϵ =0.8) and this same data normalized by density in Figure 6.5 panels c and d, respectively.

We can therefore conclude that the compressive response of CNT arrays is strain-rate invariant over the range of $\dot{\epsilon}$ =10^{-4}–10^{-1} s^{-1}. This observation is in accord with other related work in the literature, such as rate-independent shearing of disordered CNT agglomerates [172] and temperature-invariant viscoelasticity of disordered CNT networks over a range of $\sim$ 1200 °C [173], which will be discussed more in Section 6.2.4.

To understand the extent of the strain rate independence it would be important to experimentally explore higher strain rates, above the 10^{-1} s^{-1} that we have looked at via quasistatic compression. As discussed elsewhere (e.g., Sec. 3.2), we have performed low-energy impact tests at strain rates of approximately 10^{3} s^{-1}. However, due to the gap in strain rates between $\sim 10^{-1}$ to $\sim 10^{3}$ s^{-1} it has remained unclear how to rigorously relate the dissipation observed in quasistatic compression to dissipative parameters, such as the coefficient of restitution, for the case of the impact tests. Establishing additional experimental methods to bridge this gap is an important goal for future work.

6.2.3 Generalized model

As developed by Fraternali et al. [71], the multiscale features of their one-dimensional model allow it to capture both the global constitutive response of CNT arrays in compression and the local buckling that occurs due to the gradient in physical features along the height of the structures. With the original scheme it is assumed that the material fully recovers its initial height after compression, and that it can be

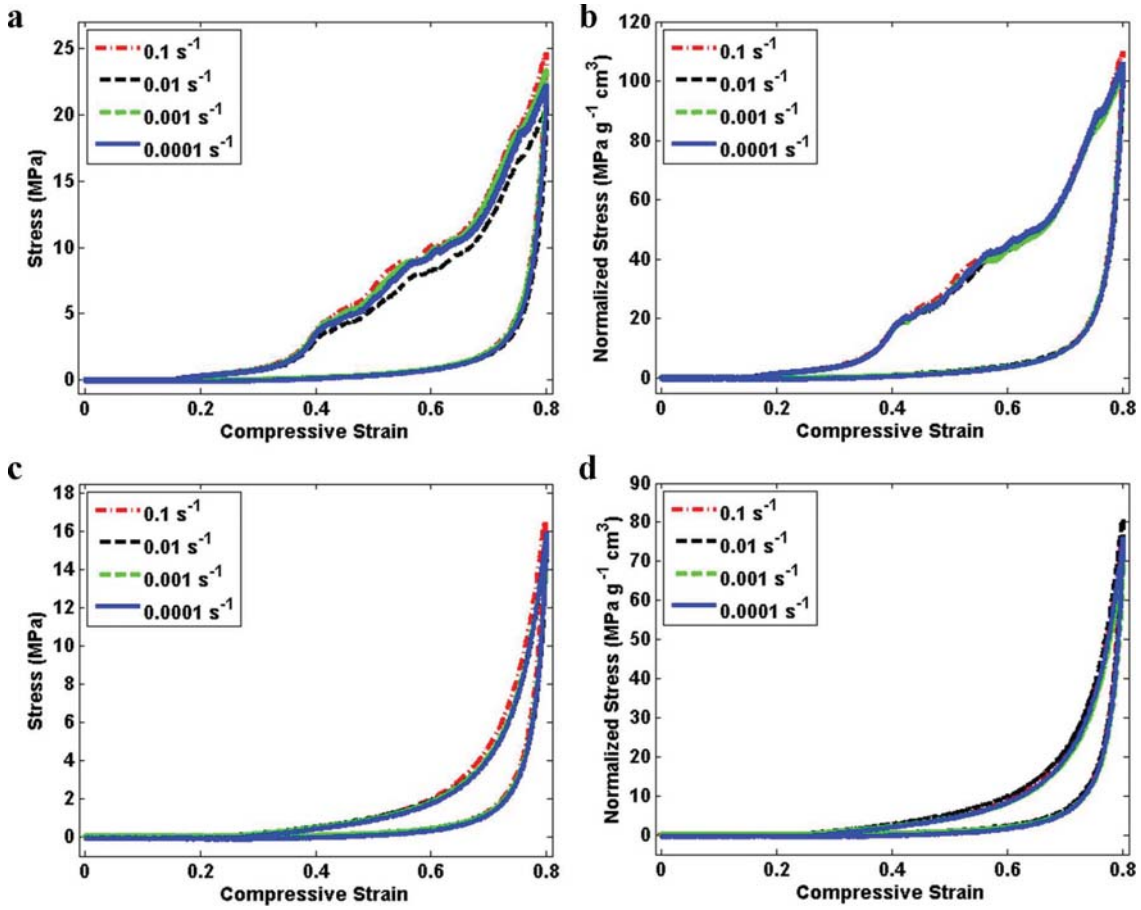

Figure 6.5: The stress-strain data for CNT arrays compressed from 10^{-4}–10^{-1} s^{-1}; (a) the first compressive cycles to a strain of 0.8, such that the material is already preconditioned for strains up to 0.4 but pristine above this point; (b) the data of panel a normalized by sample density; (c) the compressive cycle after preconditioning to 0.8 strain for each sample; (d) the preconditioned cycles of panel c normalized by density

subsequently compressed with the exact same constitutive response as observed in the first cycle. However, as discussed in Sections 6.2.1 and 6.2.2, real CNT arrays exhibit some additional features that are not captured by those assumptions. Namely, (1) there are permanent microstructural rearrangements that lead to preconditioning, by which repeated compressive cycles to a given strain exhibit less dissipation than the first; and (2) this "damage" or microstructural rearrangement is a local effect, only occurring in the buckling regions (leading to a Mullins-like response).

In subsequent work that built on the work of Fraternali et al. [71], we therefore

extended the model to account for these additional effects [152, 164]. In Ref. [164] we introduced a parameter $0 < \beta \leq 1$, which indicates the fraction of undamaged microscopic springs within a given mesoscopic element. By this definition, a fraction $1 - \beta$ of microscopic springs are damaged, with β a function of the number of past compressive cycles and the maximum strains of those cycles. As we have shown in detail (in Ref. [152] and in Appendix A), this allows for the successful modeling of material damage and the Mullins-like behavior of CNT arrays in compression.

For illustrative purposes, the effect of β is shown in Figure 6.6 (corresponding to changes in the response of a mesoscopic spring). The fraction $1 - \beta$ of microscopic springs is deemed to be irreversibly damaged, with all such springs set to have nearly zero stiffness. It is very important to note, however, that because of the form of the spring potential (Eq. 6.2) these springs can still bear finite stress. Additionally, it is convenient that, as illustrated in Figure 6.6, the "activation strain" (the strain up to which the stress response will be zero due to the deactivated springs), is equivalent to the fraction of annihilated springs, $1 - \beta$.

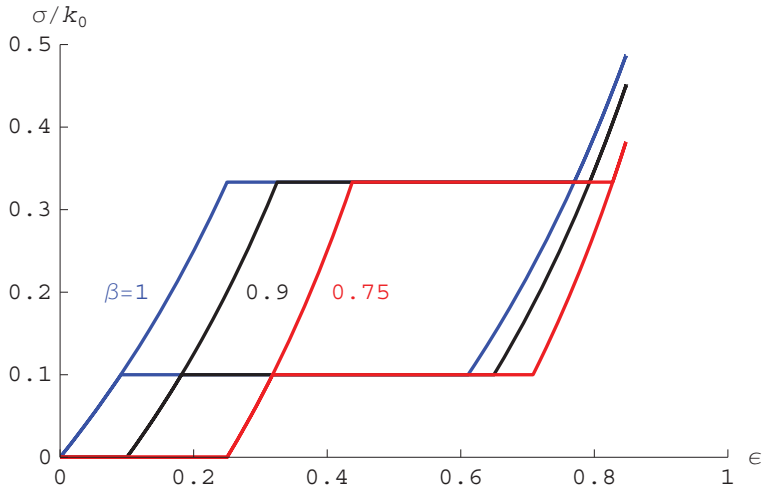

Figure 6.6: Overall limiting stress-stain pattern ($N \to \infty$) for different values of β (fixed material constants: $k_0 = k_c = 50.00 \times 10^6$ Pa; $k_b = -22.44 \times 10^6$ Pa; $\varepsilon_a = 0.25$; $\varepsilon_* = 0.52$; $\delta = 50.00 \times 10^2$ Pa)

While β captures the phenomenological "damage" associated with changes in the stress-strain response (i.e., a decline in stress levels after the first compressive cycle,

residual strain, etc., as discussed earlier), it is important to note that these changing features of the stress-strain response are a result of complex microstructural changes and not literal damage to the individual CNTs. SEM and TEM have shown no damage to the individual CNTs after quasistatic compression of the sort we have performed on our systems, a result of the extreme bendability known to exist in CNTs [73]. Rather, the phenomenological "damage" that is observed at a structural level is a result of a reordering of the CNTs, which is necessary for the formation of collective buckles under compression [156]. Though the CNT arrays continue to recover much of their height in subsequent cycles, and therefore in an important sense the formation of buckles is reversible, the reorientation of the CNTs that is necessary for the formation of these collective buckles is permanent [117, 156]. It is this latter effect that is being captured by β in our model. The twisting and sliding of the individual CNTs relative to one another that occurs during this permanent reordering results in higher observed stress and energy dissipation during earlier compressive cycles (e.g., when the material is entirely "undamaged" with $\beta = 1$) relative to later cycles. The higher energy dissipation during the first cycle could be explained by an increased frequency of the formation and breaking of van der Waals interactions as a result of this twisting and sliding during reorientation of the CNTs, similar to what was recently studied in Ref. [172]).

The Mullins-like behavior that we seek to capture with β is observed in a variety of contexts, from biological materials [163] to solid rocketry [242]. In all cases, the challenge remains linking the phenomenological "damage" that is evident in the constitutive response under repeated loading with physical microstructural changes. In some efforts, no attempt is made to establish such a link [163, 242, 243]. Perhaps it is with rubbers where the most plausible connection between microstructure (or nanostructure) and a Mullins response has been established, thanks to decades of study of the material and related polymers. In this case there is an understanding that the Mullins behavior is a result of the "finite extensibility" of the individual polymeric chains and the damage to the individual chains that must therefore occur when the bulk material is subject to tension [244]. In our case, there is a qualitative

understanding of the relationship between microstructural damage and the parameter β that we use to model the "damage" exhibited in the constitutive response. However, further study is necessary to establish a rigorously quantitative connection. A plausible course toward that end could include a characterization of CNT alignment using x-ray techniques (e.g., see Ref. [65]) before and after compression, to quantify changes in CNT alignment before and after a porion of a CNT array has buckled (and subsequently recovered).

In addition to the parameter β, we further allow for a hardening response within a mesoscopic element to more closely match the continuous physical gradient along the height of real structures of CNT arrays (as discussed in Section 6.2.1). Notice that without such a provision, e.g., in Figure 6.6, the response of a mesoscopic element is constrained to exhibit a perfectly plastic plateau, both during loading and unloading. For this reason we use the additional quantities k_{p+} and k_{p-}, which give the slopes of the "plastic" loading and unloading plateaux, respectively (as discussed in detail in Ref. [152] and Appendix A). With these final additions to the model, we obtain the following constitutive response for a generic mesoscopic spring (indicated as mesoscopic spring # i):

$$\sigma^i = \begin{cases} 0, \quad \text{for } \varepsilon^i \leq (1-\beta^i); \\ \\ \sigma^{(a,i)} \;=\; k_0^i\,(\varepsilon_i - (1-\beta^i))/(1-\varepsilon^i), \\ \text{for } ((1-\beta^i) < \varepsilon^i < \bar{\varepsilon}_a^i) \text{ or} \\ ((\bar{\varepsilon}_a^i < \varepsilon^i < \varepsilon_\beta^i) \text{ and } (\text{flag}^{(k-1)} \neq c)); \\ \\ \sigma^{(c,i)} \;=\; k_c^i\,(\varepsilon^i - (1-\beta^i) - \beta^i\varepsilon_*^i)/(1-(\varepsilon^i - \beta^i\varepsilon_*^i)), \\ \text{for } (\varepsilon^i > \varepsilon_c^i) \text{ or} \\ ((\bar{\varepsilon}_c^i < \varepsilon^i < \varepsilon_c^i) \text{ and } (\text{flag}^{(k-1)} \neq a)); \\ \\ \sigma^{(d,i)} \;=\; \sigma_a^i \;+\; k_{p+}^i(\varepsilon^i - \varepsilon_a^i), \\ \text{for } (\varepsilon_a^i \leq \varepsilon^i \leq \varepsilon_c^i) \text{ and } (\text{flag}^{(k-1)} = a); \\ \\ \sigma^{(e,i)} \;=\; \bar{\sigma}_c^i \;+\; k_{p-}^i(\varepsilon^i - \bar{\varepsilon}_c^i), \\ \text{for } (\bar{\varepsilon}_a^i \leq \varepsilon^i \leq \bar{\varepsilon}_c^i) \text{ and } (\text{flag}^{(k-1)} = c); \end{cases} \tag{6.7}$$

where, at the generic step k of a quasistatic loading process

$$\text{flag}^{(k)} = a \quad \text{if } \sigma^i = \sigma^{(a,i)}; \text{flag}^{(k)} = c, \text{ if } \sigma^i = \sigma^{(c,i)}; \text{ flag}^{(k)} = \text{flag}^{(k-1)} \text{ otherwise.}$$

The stress-strain equation (6.7) is characterized by the independent parameters β^i, k_0^i, k_c^i, k_{p+}^i, k_{p-}^i, ε_a^i, ε_c^i, and $\Delta\sigma^i = \sigma_a^i - \bar{\sigma}_c^i$. Parameters k_0^i and k_c^i represent the slopes of the branches (a) and (c) at zero stress, respectively, as in Figure 6.7, with (a') representing the case of $\beta^i = 1$. The parameters ε_a^i and ε_c^i represent the transition strains from (a') to (d) and from (d) to (c), respectively.

6.2.4 Discussion

As noted earlier (Section 2.2), it is known that the behavior associated with deformation and energy dissipation differs from the first compressive cycle to later cycles. The

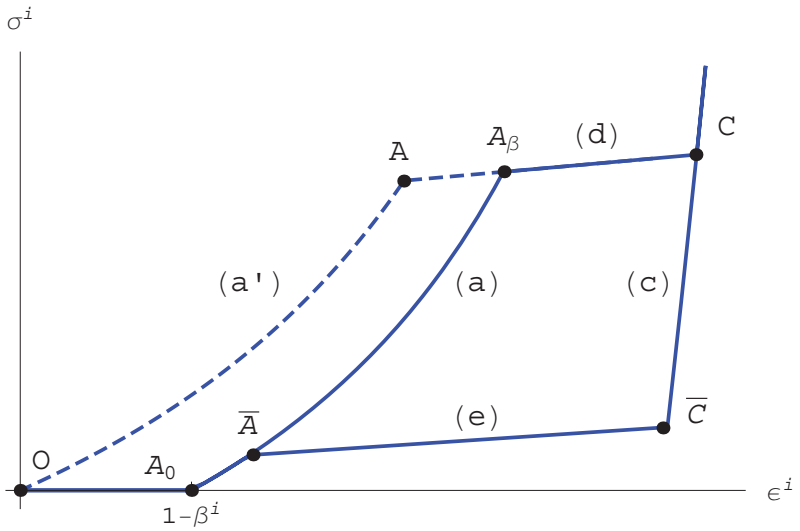

Figure 6.7: Modified mesoscopic model accounting for material hardening during the "plastic" phase transitions (d) and (e), and different rigidities of phases (a) and (c)

first cycle, during which much more dissipation occurs than in later cycles, involves reorientation of individual CNTs [156]. The permanent nature of these changes is evidenced both by the significant decrease in the stress from the first to all later cycles and by permanent changes in electrical resistance from this to later cycles, which we have observed previously [140]. Additionally, as seen in Figure 6.4, this is supported by the fact that the experimental data show rising/falling in the stress-strain response during the primary loading cycle (corresponding with instabilities, slipping, and the initial formation of the buckles) but not in any of the later cycles (despite the fact that there is still the formation/release of buckles in later cycles). This matches the one-time reorientation of individual CNTs in preparation for the formation of buckles, which has been observed previously [156]. During compression tests these stress drops can actually be audible to the human ear, and are therefore observed to only occur during the first cycle both by the stress-strain response and audibly.

The permanent microstructural rearrangements of the primary cycle, though responsible for a large part of the energy dissipation observed for compressed CNT arrays, only explain the quantity of energy dissipation associated with preconditioning. Some models of, for example, tensile tests of rubber stop at this point, approximating the stress-strain response as the "idealized Mullins effect" in which any

subsequent loading of the material after the first cycle is assumed to follow along the first cycle's unloading path [245]. That is, the simplifying assumption is that the hysteretic response is solely a phenomenon of the first cycle, and thus later cycles are not dissipative. However, it is clear by our experiments (e.g., Figure 6.4) and by those discussed in the literature [117, 118] that a hysteretic response remains for subsequent cycles and therefore that additional energy mechanisms beyond those of permanent microstructural changes or damage must be considered. It is therefore a great strength of the generalized model discussed in Section 6.2.3 that it accounts for the large decline in dissipation from the first to later cycles without over-simplifying the preconditioned response of later cycles as non-dissipative.

One can therefore posit two separate categories for the various dissipative mechanisms: one set that is associated with these permanent structural changes and that is only relevant to the first cycle, and another set that explains the steady-state energy dissipation and continues in importance for any number of compressive cycles. By the experimental data we presented in Section 6.2.2 it is clear that the mechanical response during both the primary loading cycle and the subsequent preconditioned response for later cycles are independent of strain rate in the quasistatic regime from $\dot{\epsilon}$ =10^{-4}–10^{-1} s^{-1}. Therefore both categories of dissipative mechanisms are also strain-rate independent in this regime.

The above discussion provides useful information regarding the specific nature of the underlying physical mechanisms of the dissipative response. Early reports of the foam-like energy dissipation of compressed CNT arrays attributed the source of the dissipation to friction between the CNTs and the flow of air through the porous network [117]. Treating a CNT array as an open cell foam, as is commonly done, the latter effect would be expected to have a linear dependence on strain rate [153]. However, we observe no such dependence for our material in the quasistatic regime over several orders of magnitude of strain rates. This and the rapid recovery of the CNT arrays from a compressed state [117, 119] lead us to conclude that viscous flow of air is a negligible source of dissipation in our system at quasistatic strain rates (for both the primary loading cycle and subsequent preconditioned cycles).

In addition to ruling out this source of viscous dissipation as a major contributor to the response of the system, we also rule out any significant contribution from the permanent damage of individual CNTs. Though such an effect might be expected (especially during the first compressive cycle), after examining dozens of CNT array samples with SEM or TEM, we have observed no evidence of this resulting from our low-strain-rate quasistatic compression tests (in contrast with impact tests, which have shown the capability to cause damage to individual CNTs [114]). The well-known flexibility of CNTs [68, 246] supports our experimental observations that quasistatic bending and buckling of CNTs will not cause internal damage.

There are two dissipative physical mechanisms discussed in the literature which occur at short enough time scales that the compressive response of CNT arrays in the quasistatic regime would be expected to appear rate independent. First, CNTs have been shown to reversibly form kinks under compression or bending [68–70]. This involves bending followed by asymmetric kinking associated with negative stiffness and a dissipative response. Second, networks of CNTs have been shown to very rapidly break and form van der Waals interactions between individual CNTs [172]. Both mechanisms allow for the "transformational plasticity" [170] that serves as a motivation for the multiscale bistable spring model that we use. In this scheme, the nanoscale rapid physical events that allow for dissipation correspond to the microscale spring elements discussed earlier (Section 6.1). These events occur at time scales orders of magnitude more rapid than the external deformation of the system (e.g., the breaking/formation of van der Waals interactions occurs in the sub-nanosecond time scale [172]). Thus the quasistatic response observed in the stress-strain data as in Figure 6.5, corresponding to a series of mesoscopic spring elements as described in Section 6.2.3, is dissipative in a manner that is independent of the rate of external loading.

The kinking described in Refs. [68–70] is not expected to provide a significant contribution to the dissipative response. First, because of the nature of our compressive experiments, there is no reason to expect that kinks will rapidly form and unform, as would be necessary to provide sufficient dissipation to explain the global response.

In contrast, the twisting and rearrangement of individual CNTs [156] and the continued formation of buckles [117] would allow for a single CNT to form and unform numerous van der Waals interactions with other CNTs during a single compressive cycle. Second, thick multi-wall CNTs such as those that make up our samples predominantly deform via non-dissipative small-amplitude rippling on the inner (compressed) wall rather than via the formation of kinks [74]. We therefore expect that van der Waals interactions explain the dissipative response in a similar manner as explained in Ref. [172].

6.2.5 Conclusion

We have explored the compressive response of CNT arrays following both experimental and modeling approaches. We have verified experimentally that the quasistatic compressive response is independent of strain rate from $\dot{\epsilon}$ =10^{-4}–10^{-1} s^{-1}, and have related this to known rate-independent mechanisms from the literature, particularly the rapid breaking and formation of van der Waals interactions between adjacent CNTs as examined by Yang et al. [172], which occurs at a time scale orders of magnitude shorter than the time scale of compression. We have additionally recently extended (see Refs. [152, 164] and Appendix A) the model originally developed by Fraternali et al. [71], and have here related our generalized model to the complicated physical response of CNT arrays. This extended model captures both the Mullins-like behavior of the material in repeated compression and the observed permanent deformation, in addition to the rate-independent stress response of the original model. Future work will include an investigation of the dynamic response of CNT arrays with the goal of understanding at what point the response becomes dependent on strain rate.

6.3 Modeling and *in situ* identification of material parameters for layered structures based on carbon nanotube arrays

Abstract

We test and model the mechanical response of a multilayer composite structure composed of alternating layers of aligned carbon nanotubes and copper foils under compression[1]. We employ a bistable mass-spring model to capture the three-phase hysteretic response of the loading curve with excellent agreement with the experimental observations. An *in situ* identification procedure is proposed to quantify the material parameters corresponding to the mesoscopic scale of the structure. We refine the results using a genetic algorithm and compare the response of two different models based on three and four springs in series. The localization of deformation can be accurately captured by these simplified models, which hold promise for the design of novel materials with tailored deformation responses.

6.3.1 Introduction

The non-uniform buckling and hysterestic behavior observed experimentally in arrays of CNTs have been recently modeled using a multi-scale mass-spring model. The model employs 1D chains of bistable springs to describe phenomena both at the microscopic and mesoscopic scales [71]. This model mathematically describes the heterogeneous, multiscale nature of aligned CNT structures, and captures the resulting sequential collapse of the material from the base upward. Here, we extend this model to the case of multilayer structures of aligned CNTs, in which multiple layers of aligned CNTs are joined by copper foil interlayers. Multilayer specimens are expected to provide superior damping performance in dynamic conditions as compared to their

[1] This section has been previously published as Ref. [72] by J.R. Raney, F. Fraternali, A. Amendola, and C. Daraio and is here reproduced with the publisher's permission. JRR and FF wrote the manuscript. JRR performed the experimental component of the work. FF and AA conducted the numerical modeling. All authors contributed to the analysis of the results.

single-layer counterparts. Multilayer structures of aligned CNTs are therefore interesting from a practical point of view, as potential light-weight components in laminar composites for energy absorption and protective systems. The multilayer structures examined in this study are constructed so that the copper interlayers between CNT arrays have a minimal influence in the overall mechanical response of the system, allowing for a clearer picture of the CNT mechanics. The understanding of these systems will enable future study of more complex structures in which aligned CNTs could be partially [114] or fully [133] embedded in various polymeric matrices.

Additionally, we present in this work an *in situ* identification procedure to experimentally determine the material constants that characterize the mesoscopic scale of the model proposed in [71]. To identify the material parameters, we inspect the local deformation of the CNTs through the thickness of a multilayer structure during collapse. We show that in addition to capturing the global stress-strain data obtained from experiments (as in [71]), the model can be used to capture the local deformation response at multiple length scales. To incorporate local deformation data from experiments we used a high-resolution CCD camera to measure local strain while the material was quasistatically compressed. This allowed a first approximation of the experimental parameters, which can be effectively used to run a successive parameter optimization procedure based on genetic algorithms (GA) [247–249], leading to highly accurate theory-experiment matching.

The rest of this section is organized as follows: we begin by outlining the mechanical model in Section 6.3.2. This is followed, in Section 6.3.3, by an explanation of our *in situ* procedure for estimating the material characteristics that are later used as starting points for parameter optimization. In Section 6.3.4 we discuss an application of these techniques for a specific experiment based on a structure consisting of four layers of aligned CNTs separated by copper interlayers. Specifically, Section 6.3.4.1 utilizes a four-spring model to approximate the sample and Section 6.3.4.2 repeats the analysis for a three-spring model, revealing that the number of springs does not need to match the number of physical layers for successful theory-experiment matching. Finally, concluding remarks are given in Section 6.3.5.

6.3.2 Mechanical model

Following Section 6.1 and Ref. [71], we model a multilayer CNT structure as a 1D mass-spring chain with $N+1$ lumped masses $m^0, \ldots, m^N$ connected by N nonlinear springs ($N \geq 2$). As before, the mesoscopic spring element, which represents a finite portion of the CNT array structure, consists of the continuum limit $N \to \infty$ of microscopic springs. Unlike in Section 6.2, we will forego the use of the parameter β in order to simplify the discussion here (this means that we will only be considering the response of the first compressive cycle). To allow for mechanical preconditioning, we introduce "initial strains" $\varepsilon_0^i \geq 0$, and "elastic strains" $\underline{\varepsilon}^i = \varepsilon^i - \varepsilon_0^i$ in each spring. The generic spring represents a mesoscopic dissipative element, which corresponds to the continuum limit of a lower-level (microscopic scale) chain of bistable elastic springs [71]. The constitutive equations for each spring are:

$$\sigma^i = \begin{cases} \sigma^{(a,i)} = k_0^i \, \underline{\varepsilon}_i/(1-\underline{\varepsilon}^i), \\ \text{for } (\underline{\varepsilon}^i < \hat{\varepsilon_a}^i) \text{ or} \\ ((\hat{\varepsilon_a}^i < \underline{\varepsilon}^i < \varepsilon_a^i) \text{ and } (\text{flag}^{(k-1)} \neq c)); \\ \\ \sigma^{(d,i)} = \sigma_a^i + k_{h+}^i(\underline{\varepsilon}^i - \varepsilon_a^i), \\ \text{for } (\varepsilon_a^i \leq \underline{\varepsilon}^i \leq \hat{\varepsilon}_c^i) \text{ and } (\text{flag}^{(k-1)} = a); \\ \\ \sigma^{(e,i)} = \bar{\sigma}_c^i + k_{h-}^i(\underline{\varepsilon}^i - \bar{\varepsilon}_c^i), \\ \text{for } (\hat{\varepsilon}_a^i \leq \underline{\varepsilon}^i \leq \bar{\varepsilon}_c^i) \text{ and } (\text{flag}^{(k-1)} = c); \\ \\ \sigma^{(c,i)} = k_c^i \, (\underline{\varepsilon}^i - \varepsilon_*^i)/(1-(\underline{\varepsilon}^i - \varepsilon_*^i)), \\ \text{for } (\underline{\varepsilon}^i > \hat{\varepsilon_c}^i) \text{ or} \\ ((\bar{\varepsilon}_c^i < \underline{\varepsilon}^i < \hat{\varepsilon}_c^i) \text{ and } (\text{flag}^{(k-1)} \neq a)); \end{cases} \tag{6.8}$$

where σ^i is the corresponding stress and, at each loading step k, it results that $\text{flag}^{(k)} = a$, if $\sigma^i = \sigma^{(a,i)}$; $\text{flag}^{(k)} = c$, if $\sigma^i = \sigma^{(c,i)}$; and $\text{flag}^{(k)} = \text{flag}^{(k-1)}$, otherwise.

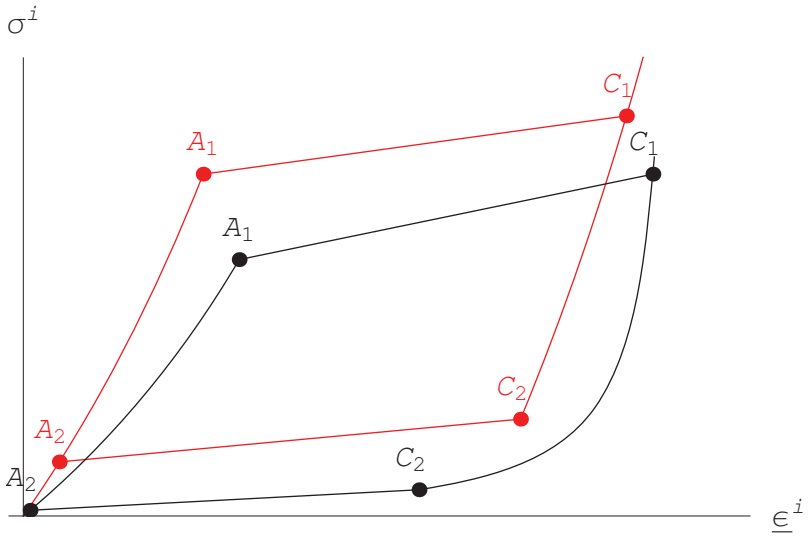

Figure 6.8: Stress-strain curve of the generic spring for two different sets of material properties

The quantities k_0^i and k_c^i appearing on the right-hand side of (6.8) represent the slopes $d\sigma^i/d\underline{\varepsilon}^i$ at $\sigma^i = 0$ ("initial stiffnesses") of the the bilateral branches $O \rightleftharpoons A_1$ (branch a) and $C_1 \rightleftharpoons C_2$ (branch b) shown in Figure 6.8 (O denoting the origin of the σ^i-$\underline{\varepsilon}^i$ axes). Such branches describe the initial elastic regime and the final densification phase of the portion of the structure pertaining to the ith spring, respectively. In the same equation, the quantity k_{h+}^i represents the slope of the unilateral branch $A_1 \rightarrow C_1$, which instead describes the snap-buckling and the initial densification of such a region during loading; the quantity k_{h-}^i represents the slope of the unilateral branch $C_2 \rightarrow A_1$. The latter models the snap-back of the same region during unloading.

Concerning the stress and strain quantities appearing in (6.8), we remark that σ_a^i represents the stress corresponding to point A_1; $\bar{\sigma}_c^i$ represents the stress corresponding to C_2; the quantities ε_a^i, $\hat{\varepsilon}_c^i$, $\bar{\varepsilon}_a^i$, and $\hat{\varepsilon}_a^i$ indicate the strains corresponding to A_1, C_1, C_2, and A_2, respectively. The constitutive Eq. (6.8) can be expressed in terms of the independent parameters k_0^i, k_c^i, k_{h+}^i, k_{h-}^i, ε_a^i, $\hat{\varepsilon}_c^i$, and $\Delta\sigma^i = \sigma_a^i - \bar{\sigma}_c^i$ [71].

It is worth noting that such an equation doesn't allow for accumulation of permanent strain, which often affects real CNT structures (e.g., see [117]), but just for reversible (or "transformational") plasticity [71, 170]. The model could be easily gen-

eralized to capture such a phenomenon, by allowing that the snap-back of one or more springs leads to permanent deformation, and not to phase (a) Figure 6.8.

6.3.3 *In situ* parameter identification

The proposed *in situ* material parameter identification procedure requires an experimental apparatus that allows the characterization of the CNT morphology alongside the load-displacement curve (e.g., by using a high-resolution CCD camera as in this study, or a scanning electron microscope as in [120]). Specifically, we obtain high-resolution images from the side of the structure, such that its whole height can be viewed in detail. In hard-device conditions, the order parameter of a quasistatic compression test will be the global strain ε, and the stress σ will be approximatively constant along the thickness of the structure. We suppose that ε and σ are continuously recorded during the test. Frames taken from an *in situ* video of the experiment can be used to track the local deformation of vertical portions (or segments) $\mathcal{S}^i$ of the CNT structure ($i = 1, ..., N$). Such regions of deformation can correspond to individual CNT arrays, groups of arrays, and/or portions of individual arrays. Let h^i denote the undeformed length of $\mathcal{S}^i$, and h^i_{def} its current deformed length (Figure 6.9). An approximation to the local strain ε^i of $\mathcal{S}^i$ is given by $(h^i - h^i_{def})/h^i$.

$$\varepsilon^i \approx \frac{h^i - h^i_{def}}{h^i} \tag{6.9}$$

On using (6.9), and supposing $\sigma^i \approx const = \sigma$, one can easily record a local stress-strain curve σ^i vs. ε^i for each of the elements $\mathcal{S}^1, ..., \mathcal{S}^N$.

We employ the theoretical stress-strain response described by Eq. (6.8) and depicted in Figure 6.8 to model such experimental responses, up to the instants marking the snap-back of the CNTs from a buckled to an unbuckled state (disregarding permanent deformation effects). In particular, with reference to the generic element $\mathcal{S}^i$, we identify the point denoted by A_1 in Figure 6.8 with the state immediately preceding the snap-buckling (or initial densification) of such a portion of the structure. Similarly, we identify C_1 with the state marking the beginning of the final densifi-

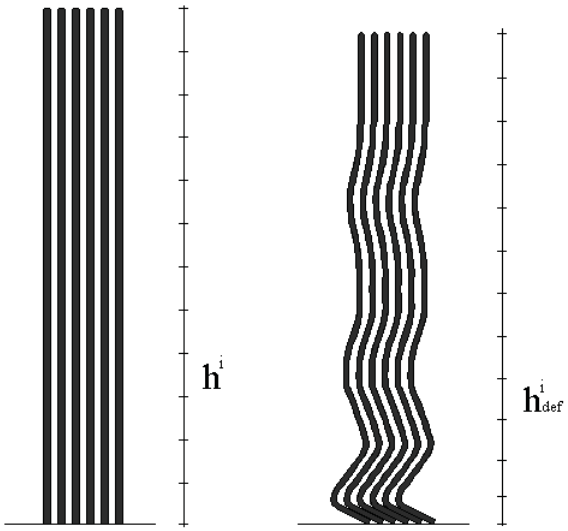

Figure 6.9: Tracking of the local deformation along the axis of the carbon nanotubes

cation phase; and C_2 with the state immediately preceding the local snap-back of the CNTs to an unbuckled state. Since the video frames are synchronized with the global stress-strain data, we obtain the local stress-strain response for any arbitrary segment. The three necessary points mentioned above are in this way determined for each segment, based on visual inspection of the video frames and the local stress-strain responses. By constraining the stress-strain response (6.8) to pass through the three "experimental" points A_1, C_1, and C_2, we determine the six constitutive parameters k_0^i, k_c^i, k_{h+}^i, ε_a^i, $\hat{\varepsilon}_c^i$, and $\Delta\sigma^i$, which completely characterize the portion $OA_1C_1C_2$ of the path shown in Figure 6.8.

6.3.4 Estimation of the mechanical parameters of a four-layer structure

We estimate the material parameters of a multilayer structure composed of alternating layers of vertically aligned multi-walled CNTs and copper tape, which consists of copper foil and a thin layer of adhesive on each side. The CNTs were grown by chemical vapor deposition (CVD) using ferrocene and toluene as precursors. The height of each CNT layer was approximately 1.3 mm and the area was about 25 mm^2. The

average diameter of the as-grown CNTs was about 50 nm. The multilayer structure was constructed using a total of four CNT layers (labelled as layers 1–4, numbered from bottom to top). Compression tests were performed at a strain rate of 0.01 s^{-1} to a total strain ε of 0.4 using an Instron E3000. The parameter estimates hereafter refer to the first loading cycle.

6.3.4.1 Four-spring model

In the first instance, we modeled the four-layer structure as a collection of four springs, with one spring for each layer of aligned CNTs (Figure 6.10). The theoretical stress-strain curves σ^i vs. ε^i $(i = 1, ..., 4)$ obtained via the *in situ* identification procedure (Model # 1) are shown in Figure 6.11. It is seen from such a figure that the largest strains occur in correspondence with spring (or layer) # 2, where the major CNT collapse was observed during the experiment (see Figure 6.16). The same figure also shows that the stiffest layers are the topmost and the bottommost ones, and that the central layers exhibit a rather compliant response. It has been observed that the stiffness of aligned arrays of CNTs can vary, even within a particular growth substrate, and that this variation in stiffness correlates with a variation in bulk density [52]. Prior to the assembly of the four CNT layers into a unified structure, their bulk densities were separately computed (by measuring the mass and dividing it by the volume). It was found that the bulk densities for the middle two layers were less than those for the top and bottom layers. Thus the increased stiffness of the top and bottom layers is explained by their higher bulk densities, in accordance with previous observations. The correlation between bulk density and stiffness is not perfect, with layer 2 showing more deformation than layer 3 despite a somewhat higher density.

Figure 6.12 shows a comparison between the overall σ vs. ε response predicted by Model # 1 and the corresponding experimental response. The theoretical response was determined on the basis of the local stress-strain curves shown in Figure 6.11, and a time-integration procedure based on the dynamic relaxation of the discrete equilibrium problem [71]. Such a procedure describes the evolution of the system during the examined experiment through two different time scales. An external time ("macro"

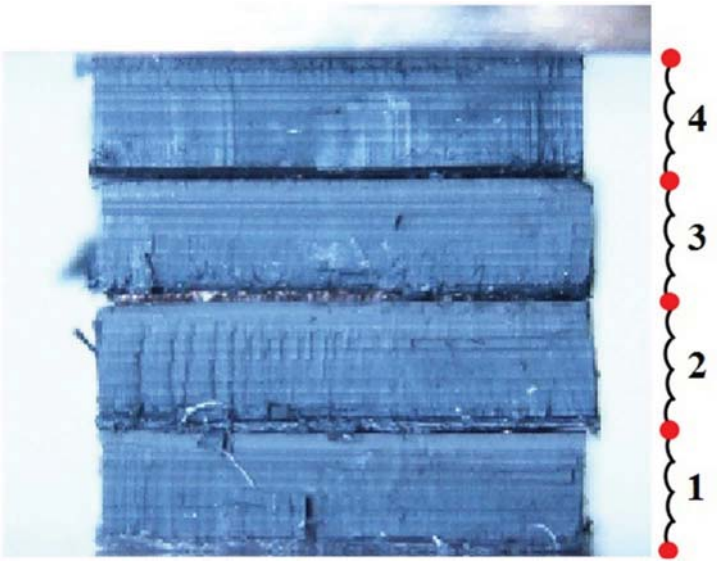

Figure 6.10: A four-spring scheme, in which each spring represents exactly one CNT layer, is used for Models # 1 and # 2

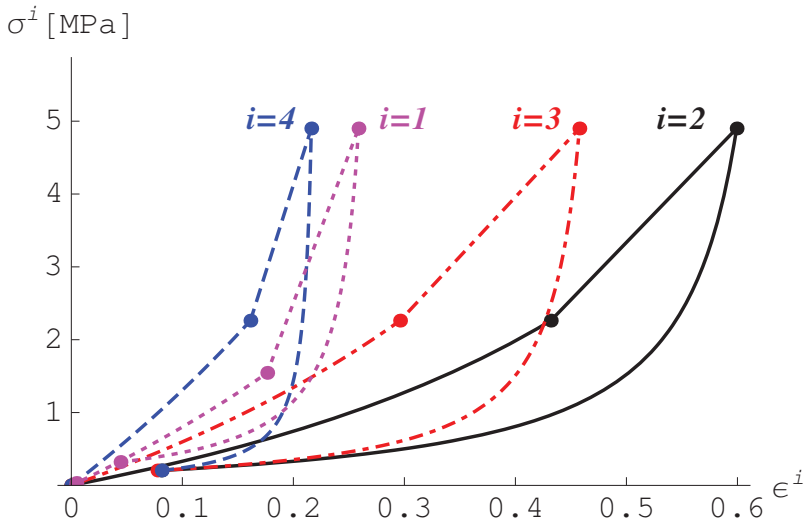

Figure 6.11: *In situ* identification of the stress-strain curves of the four springs forming Model # 1

steps) rules the quasistatic (slow) evolution of the applied deformation history, while an internal time ("meso" steps) rules the (viscous) dynamics of the microstructural rearrangements occurring at the mesoscopic level during the macro steps. The latter are induced by the "plastic snaps" of the individual springs and determine the

macroscopic hysteresis of the system [71].

Since we examined loading from the pristine state, we assumed $\varepsilon_0^i = 0$ in each spring (no preconditioning). The fitness performance f of such a model was measured through the maximum norm of the difference between the overall predicted and experimental stress-strain curves (up to the first snap-back point), obtaining $f = 1.19$ MPa. We observe in Figure 6.12 agreement between Model # 1 and the experimental response, with major deviations occurring for the largest strain values ($\varepsilon \geq 0.3$). We were able to significantly improve the theory-experiment matching by running a GA fitting procedure. More specifically, we employed the Breeder Genetic Algorithm (BGA) presented in [249], which has been successfully used as a parameter identification tool in previous work dealing with the constitutive modeling of CNT foams [71], granular protectors [250], and soft biological tissues [251]. BGAs differ from other available GAs due to their selection mechanism, which mimics animal breeding and selects only from among the best elements of the current population (in most other GAs, selection is instead stochastic and meant to mimic Darwinian evolution). Such a feature ("truncation" selection scheme) improves the ability of BGAs when dealing with large search spaces, as compared to standard GAs (see, e.g., [248]). For the present and the following fitting procedures, we employed a population size of 50 "individuals" (candidate solutions); a truncation rate of 15%; extended intermediate recombination [248]; and a mutation rate of 50%. We let the BGA run up to 600 generations and included in the first generation an individual with genes corresponding to the material parameters of the *in situ* identified model (Model # 1, in the present case). The BGA optimization of Model # 1 led to an improved model (Model # 2), with fitting performance $f = 0.13$ MPa. The plots shown in Figure 6.12 highlight a rather good agreement between Model #2 and the experimental response. The material parameters of Models # 1 and # 2 are provided in Table 6.1.

6.3.4.2 Three-spring model

As previously mentioned, the largest deformation of the CNT structure collapse was observed in experiments at the bottom of layer # 2. At the same time, the remaining

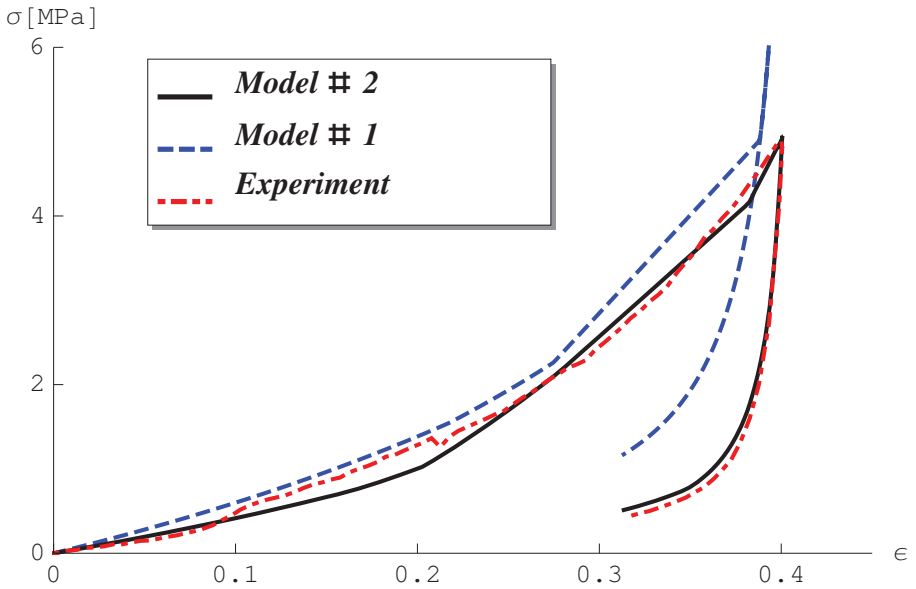

Figure 6.12: Comparison between the overall stress-strain curves predicted by Models # 1 and # 2, and the recorded experimental response

portions of the multilayer structure underwent smaller deformations (see Figure 6.16). Within an individual layer of aligned CNTs under compression, buckling begins on the side nearest the substrate, resulting in the localization of strain in this region [117, 120]. Specifically, with the detail provided by scanning electron microscope as in [120], it was observed that, apart from the buckling taking place at the base of the aligned CNTs, the rest of the structure remains undeformed. That is, this would correspond to a model of compression in which all springs except one remain of nearly constant length with only one experiencing a large deformation. To design a model that would capture more closely the local deformation noted experimentally, we constructed a three-spring model in which one spring was placed in correspondence with the heavily buckled region, and two other springs modeled the behavior of the remaining portions of the material below and above the deformed region (Figure 6.13). Specifically, we considered a model in which the topmost spring (spring # 3) corresponds to the union of layers # 4 and # 3 plus a portion of layer # 2 (total height $h^3 = 3.24$ mm); the middle spring (spring # 2) corresponds to the remaining portion of layer # 2 ($h^2 = 0.68$ mm), in which maximum deformation was

Model # 1 ($f = 1.19$ MPa)

spring	k_0^i (MPa)	k_c^i/k_0^i	k_{h+}^i/k_0^i
4	11.76	0.003	4.09
3	5.38	0.026	3.04
2	2.98	0.092	5.30
1	7.21	0.014	5.66
	ε_a^i	$\hat{\varepsilon_c}^i$	$\Delta\sigma^i/\sigma_a^i$
4	0.16	0.21	-0.91
3	0.30	0.43	-0.91
2	0.43	0.54	-0.91
1	0.18	0.22	-0.79

Model # 2 ($f = 0.13$ MPa)

spring	k_0^i (MPa)	k_c^i/k_0^i	k_{h+}^i/k_0^i
4	8.82	0.008	3.20
3	3.83	0.009	3.20
2	2.23	0.033	5.32
1	3.96	0.007	5.70
	ε_a^i	$\hat{\varepsilon_c}^i$	$\Delta\sigma^i/\sigma_a^i$
4	0.11	0.17	-0.87
3	0.36	0.52	-0.98
2	0.32	0.59	-0.98
1	0.16	0.16	-0.94

Table 6.1: Material constants of Models # 1 and # 2

observed experimentally; and the bottom spring (spring # 1) corresponds to layer # 1 ($h^1 = 1.24$ mm).

The theoretical stress-strain curves obtained for the single springs through the *in situ* identification procedure (Model # 3) are shown in Figure 6.14. It is worth noting that such stress-strain curves capture the deformation mechanism described above, with very large strains in correspondence with spring # 2 (up to almost 90%), and stiffer responses in correspondence with springs # 1 and # 3.

Figure 6.15 shows a good agreement between the overall σ vs. ε response predicted by Model # 3 and the corresponding experimental response, with fitting performance $f = 1.15$ MPa. In the present case, most of the theory-experiment deviation is localized in a very narrow region corresponding to the final portion of the densification regime ($\varepsilon \geq 0.35$). A BGA optimization of Model # 3 led to the response denoted as Model # 4 in Figure 6.15, which shows an excellent agreement with the experimental

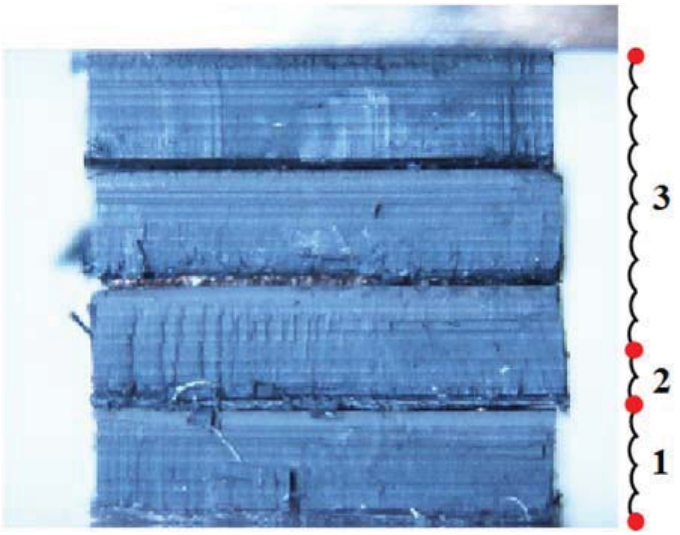

Figure 6.13: A three-spring scheme is used for Models # 3 and # 4

one and fitting performance $f = 0.09$ MPa. The material parameters of Models # 3 and # 4 are provided in Table 6.2, while selected frames from the videos for the experiment and the response of Model # 4 are shown in Figure 6.16.

Upon comparison of the optimized 4-spring and 3-spring models (i.e., Models # 2 and # 4, respectively) it is clear that the fitness performance is not driven by the number of springs so much as it is driven by the extent to which the springs correspond to the distinct behavior of the portions of the physical structure. From the experimental video, it is clear the this particular structure consists of a thin soft region surrounded by two thicker firm regions. The fitness performance of Model # 4 is superior to that of Model # 2 even though the former consists of fewer springs exactly because its springs more closely match the firm-soft-firm arrangement of the sample in question. Thus a careful viewing of the experimental recording allows one to quickly choose an appropriate, though not necessarily optimal, model. A model with a much larger number of springs could certainly be utilized, with the only limitation being the resolution of the video recording. Though this approach could be used to capture even more of the subtlety of the heterogeneous collapse of the structure, and thereby to obtain improved fitting performance, the computational time would rapidly increase. The better approach is to find the model with the minimum

number of springs that provides a "good enough" agreement with experiment, as with our three-spring models in this case.

The mechanical response of CNT arrays can vary dramatically between different growth processes. More work must be done to understand how this mechanical response depends on measurable physical characteristics (e.g., bulk density). Until this relationship is understood in detail, it is not possible to use the model for accurate experimental predictions.

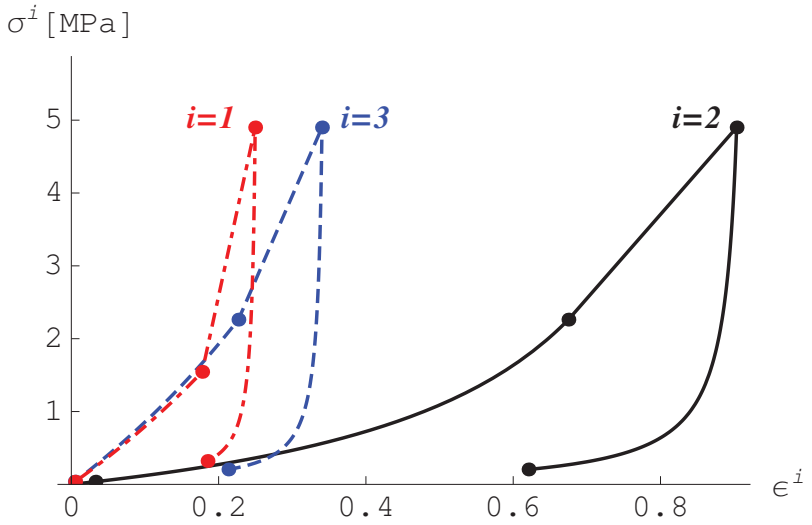

Figure 6.14: *In situ* identification of the stress-strain curves of the three springs forming Model # 3

6.3.5 Concluding remarks

We have presented in this work an *in situ* identification procedure for the mesoscopic mass-spring model of carbon nanotube foams recently proposed in [71]. The given procedure allows one to obtain the mechanical properties of the different springs forming such a model through experimental characterization of local deformation of the aligned CNTs alongside a given load-displacement curve. We applied the model to characterize the mechanical reponse of a four-layer CNT structure, tracking the local deformation of the layers under compression.

Model # 3 ($f = 1.15$ MPa)

spring	k_0^i (MPa)	k_c^i/k_0^i	k_{h+}^i/k_0^i
3	7.71	0.004	3.02
2	1.09	0.081	10.60
1	7.15	0.003	6.53
	ε_a^i	$\hat{\varepsilon_c}^i$	$\Delta\sigma^i/\sigma_a^i$
3	0.23	0.33	-0.91
2	0.67	0.88	-0.91
1	0.18	0.24	-0.79

Model # 4 ($f = 0.09$ MPa)

spring	k_0^i (MPa)	k_c^i/k_0^i	k_{h+}^i/k_0^i
3	7.69	0.005	3.02
2	0.69	0.056	10.6
1	8.00	0.003	6.52
	ε_a^i	$\hat{\varepsilon_c}^i$	$\Delta\sigma^i/\sigma_a^i$
3	0.21	0.33	-0.87
2	0.63	0.98	-0.86
1	0.17	0.22	-0.82

Table 6.2: Material constants of Models # 3 and # 4

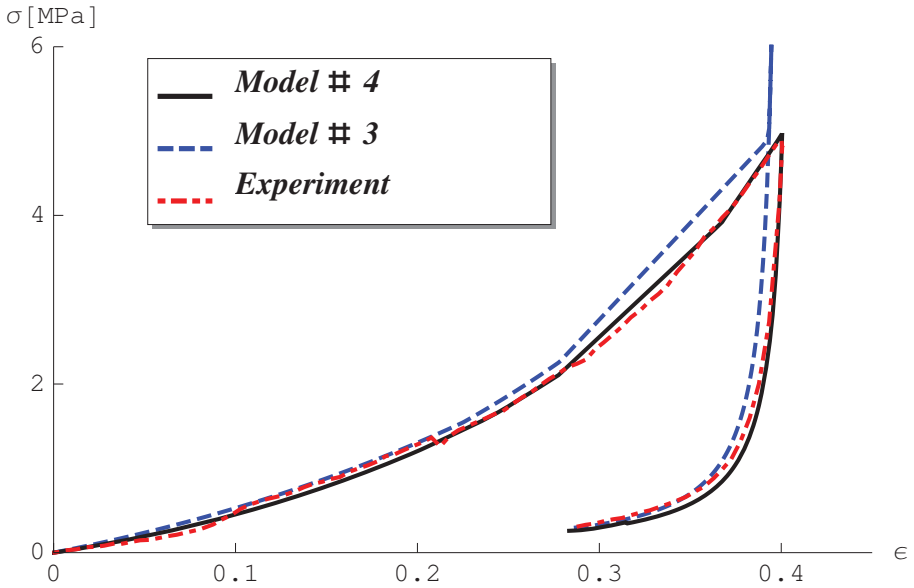

Figure 6.15: Comparison between the overall stress-strain curves predicted by Models # 3 and # 4, and the recorded experimental response

The presented results show that the given identification procedure is able to produce a first approximation of the experimental response, capturing its main features

and reproducing the localization of the buckling deformation. This approximation can be usefully refined through a successive GA optimization of material parameters [71]. We found that a suitable choice of the fitting model (number and localization of the springs) significantly improves the theory-experiment matching.

Additionally, we have extended the work proposed in [71], which was limited to a single array of aligned CNTs, to the case of multilayer composites based on alternating layers of aligned CNTs and copper foils. In other experiments we have found that similar multilayer structures give superior response under impact when compared to a single CNT array. Modeling structures such as these is a necessary first step toward the construction of light-weight multilayer CNT-based laminar composites with tailored collapse and energy-dispersive properties.

A generalization of the procedure presented here to account for permanent deformation and time dependence will be addressed in future work. Additional study of the response of CNT arrays at the microscopic scale (based on characterization of the local deformation with scanning electron microscopy) is also planned.

Acknowledgments

CD acknowledges support from the Institute for Collaborative Biotechnologies under contract W911NF-09-D-0001 with the Army Research Office. FF acknowledges the support of the University Centre for Risk Prediction and Prevention (CUGRI) in association between the Universities of Salerno and Napoli Federico II, Italy. FF also thanks the Graduate Aerospace Laboratory at the California Institute of Technology (GALCIT) for the hospitality during his visit. JRR gratefully acknowledges the U.S. Department of Defense and the Army Research Office for their support via a National Defense Science & Engineering Graduate (NDSEG) Fellowship.

$\varepsilon = 0.15$

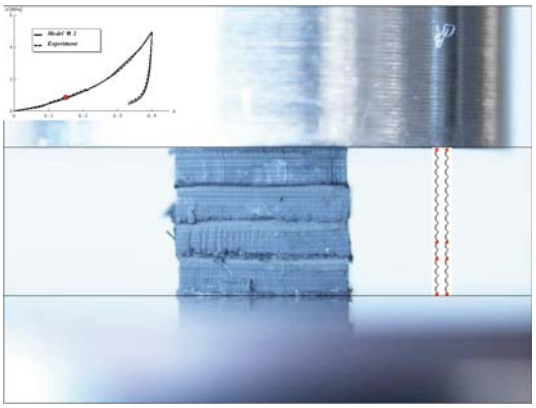

$\varepsilon = 0.29$

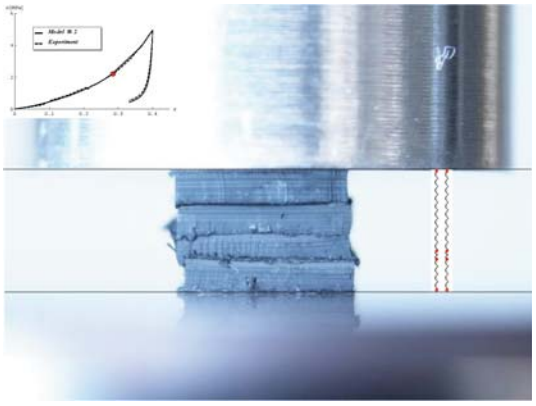

$\varepsilon = 0.40$

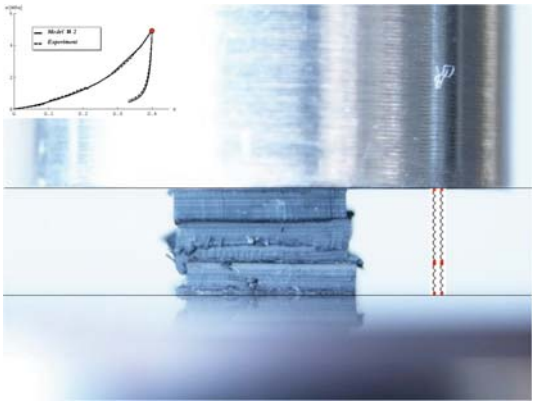

Figure 6.16: Comparison between frames from the videos for the experiment and the response of Model # 4 for different values of the overall strain ε

Chapter 7

Conclusion

7.1 Summary

Carbon nanotubes hold much potential due to their individual properties [1], but it remains a challenge to realize that potential in bulk materials due to the difficulty in manipulating them and getting them to interact well with surrounding materials. As discussed in Chapter 1, there are a variety of approaches to achieving these advances. It is hoped that the work developed in this dissertation contributes to that effort. In Chapter 2 the mechanics of CNT arrays in compression was discussed. This chapter summarized the present state of the literature on the mechanics of CNT arrays, and expanded upon this foundation through the analysis of our own data. Of note:

- CNT arrays in compression exhibit behavior analogous to the Mullins effect in rubbers [162]; this behavior is a result of (1) a preconditioning effect by which the first compressive cycle differs significantly from subsequent cycles, and (2) local buckling that accommodates all of the compressive strain through the sequential formation of buckles from the base upward. The locality of the observed preconditioning means that when the material is compressed beyond its previous maximum strain it responds as if it had never been compressed previously.

- Stress relaxation and creep tests revealed that CNT arrays show nonlinear viscoelastic behavior; unlike linear viscoelastic materials, which show a constant

rate of decay in stress (for stress relaxation tests) or a constant rate of increase in strain (for creep tests) regardless of the magnitude of the applied deformation/load, the material presents a decay rate that is dependent on the applied deformation/load.

- We found that the energy dissipation that occurs during a standard quasistatic compression experiment is > 200 times that of commercial polymeric foams of comparable density (e.g., foams used in packaging materials) [140].

- The hysteretic stress-strain response of CNT arrays in compression is rate independent over the range that we tested (10^{-4}-10^{-1} s^{-1}), both for the primary cycle and the subsequent preconditioned cycles.

In addition to these contributions to understanding the mechanics of CNT arrays, we also provided several experimental/synthesis procedures to allow for the synthesis of arrays with large variations in properties. These include control of physical properties, such as the bulk density, as well as mechanical properties. Both the global response, as indicated by the compressive stress-strain behavior, and the local response are able to be varied.

To illustrate the effective range over which the global mechanical response can be varied, Figure 7.1 gives the stress-strain response for two samples compressed to 0.8 strain. These represent practical upper and lower bounds on the stress response using the procedures that we developed here, with our procedures able to provide samples that behave anywhere within these bounds. The curve represented by the blue dashed line corresponds to a sample that was synthesized following the procedure discussed in Chapter 4 for the placement of MnO_2 nanoparticles on the surfaces of the individual CNTs. The curve represented by the red solid line corresponds to a sample that was synthesized following the procedure discussed in Section 3.1, with a flow gas consisting of 50%–50% argon/hydrogen. Corresponding values for various properties are provided in Table 7.1.

Note that following these two distinct processes results in a factor of 8 difference in bulk density, and a corresponding factor of over 40 for certain mechanical properties

(namely the peak stress reached at a maximum strain of 0.8 and the energy dissipated per unit volume, synonymous with the area of the stress-strain hysteresis that results in compression).

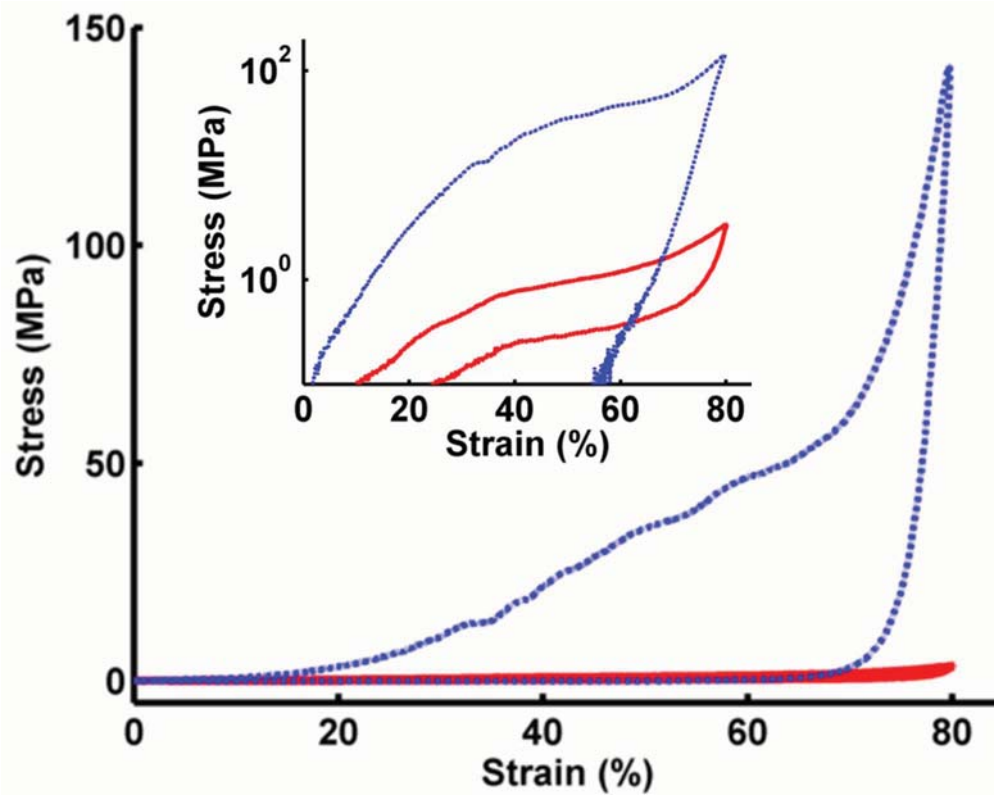

Figure 7.1: Tunability of the global mechanical response of CNT arrays (inset is the same but with a logarithmic axis for stress); the dashed line is the compressive stress-strain response of a CNT array that has been reinforced with MnO_2 nanoparticles, using the process described in Chapter 4; the solid line is the stress-strain response of a CNT array that was synthesized with a high concentration of hydrogen in the flow gas, using the process described in Section 3.1; the former has more than 40 times the hysteresis area and peak stress of the latter, as detailed in Table 7.1

The materials developed in this dissertation are modified either during synthesis (Chapter 3) or after synthesis (Chapters 4 and 5). Though the procedures can be categorized in this way, it is perhaps physically clearer to categorize them by whether they affect only the global structure/properties or if they also affect local properties. In this case, controlling structure by hydrogen concentration (Section 3.1) or by the addition of nanoparticles (Chapter 4) only affects the global response; in contrast,

Prep. method	Density (g cm^{-3})	Peak stress (MPa)	Unloading mod. (MPa)	En. dissip (MJ m^{-3})	Details
MnO_2 particles	0.602	140.9	4446	19.9	Chapter 4
H_2	0.075	3.4	157	0.4	Section 3.1

Table 7.1: Measured properties of two extreme samples synthesized using the procedures developed in this dissertation; these represent the bounds on the tuning that is readily possible following the procedures described herein, and correspond to the stress-strain curves shown in Figure 7.1. Note that "peak stress" refers to the stress at maximum strain, which was 0.8 in this case

controlling heterogeneities along the height of the structure (either at the microscale, as in Section 3.2, or at the millimeter scale, as in Chapter 5 and Section 6.3) affects the local structure/response. As shown in Figure 1.1, together these procedures allow for control of the structural hierarchy of the system over length scales of 5 or 6 orders of magnitude.

Finally, this work (specifically in Chapter 6) contributed to the use of a one-dimensional bistable spring model that was originally developed by Fraternali et al. for use with CNT arrays [71]. In particular, this model was extended (see Section 6.2 and Appendix A for details) to account for permanent damage, partial strain recovery, and the Mullins-like behavior that we observed experimentally. The model presented in Ref. [71], which was developed for single-layer structures of CNT arrays, was applied to multilayer structures in Section 6.3. In this same section, an *in situ* identification scheme was developed to more directly link experiments with the model. This allowed the model to better capture not only the global constitutive response of CNT array-based materials, but also the strain localization that arises from the gradient in physical properties along the height of the individual CNT arrays (and the heterogeneities that result from using CNT arrays of differing properties in multilayer structures). This identification procedure also greatly decreased the time necessary for the parameter search that is necessary for the model to successfully reproduce the experimental response.

7.2 Future directions

In the course of developing the work presented in the various chapters of this dissertation, several other avenues of potentially fruitful work were started (but not completed at the time of the completion of the dissertation). A few brief summaries of these are provided here which may be of interest to the reader.

7.2.1 Electromechanical stiffening

Samples were constructed from CNT arrays with poly(dimethyl siloxane) (PDMS) anchoring layers that also contained bucky-paper thin films, similar to the multilayer samples described earlier (Chapter 5). The bucky-paper/PDMS layers were designed to have sufficient length ($\sim$ 2–3 cm) that they extended outside the compression area during compression tests of the CNT arrays. The bucky-paper/PDMS was connected to the electric probes of a current source to allow simultaneous mechanical and electrical manipulation and measurement.

It is noteworthy that not only did the electrical resistance of the structure change during compression (as discussed in Chapter 5) but also the flow of electrical current resulted in a stiffening of the material, such that the application of current resulted in a sudden elevation of stress even while the material was being held at a constant strain (Figure 7.2). This is in keeping with the observation that individual CNTs can act as actuators [81]. Figure 7.2 shows stress spikes that correspond to current pulses. Other experiments showed that the increase in stress is maintained as long as current is applied, and immediately ceases when the current is turned off.

In order to understand the mechanism associated with the observed stiffening, we also tested unanchored CNT samples that did not have any polymer or bucky-paper components. In these cases we used conductive silver epoxy to attach the CNT arrays to copper foil, and this foil was of sufficient length to connect to electric probes outside of the compression region. In this configuration, with the copper playing the role that buckypaper played in the original tests, there was no variation in stress during the application of electrical current. Either the bucky-paper itself or else the interaction of

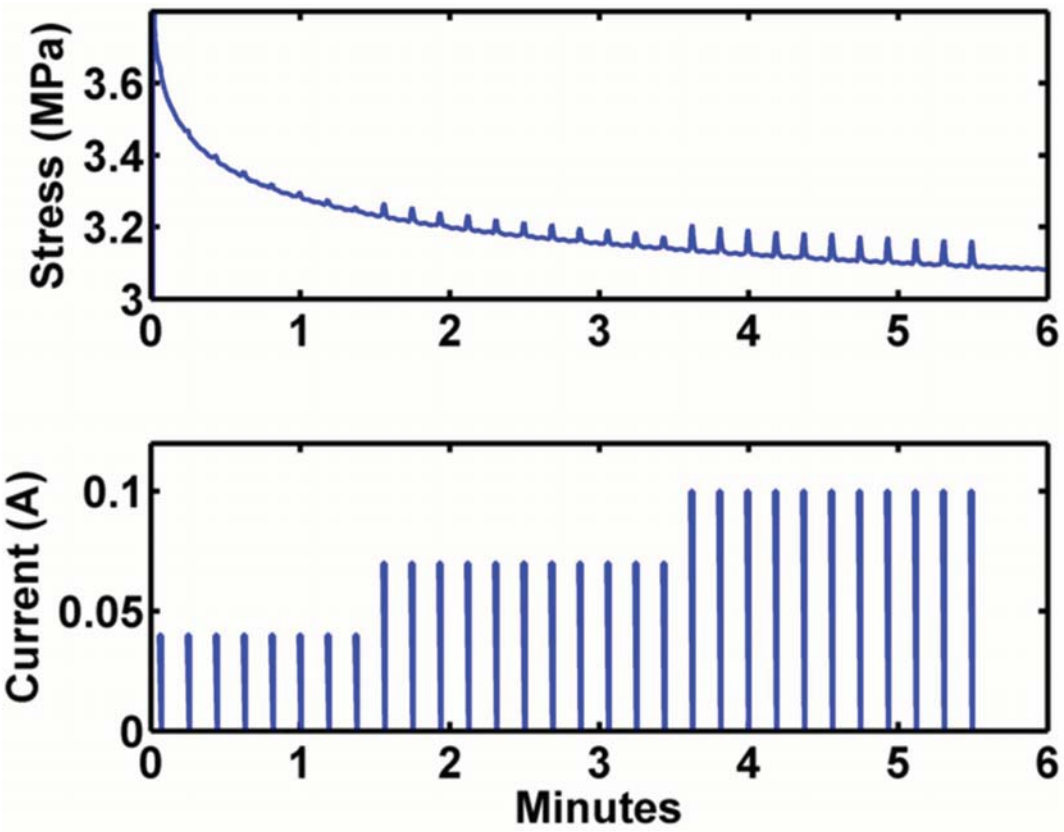

Figure 7.2: Current was pulsed through the sample during a typical stress relaxation test, resulting in a temporary rise in stress

the bucky-paper with the CNT arrays seems to be the source of the stiffening behavior, but as yet this has not been clearly identified. There is also much need to understand how the stiffening effect might change at various compressive strains, given that the mechanical response passes through three distinct regimes during loading (as verified both in the stress-strain response [117] and in the viscoelastic response [151]).

7.2.2 Designing multilayer structures for controlled deformation

It was noted earlier that certain properties associated with the mechanical response of CNT arrays depend nearly linearly on density (Chapter 2). Additionally, the procedures outlined in Chapters 3 and 4 allow for the structure and the mechanical response

of CNT arrays to be tuned broadly. Because of these variations it is easy to imagine that multilayer structures of CNT arrays could be assembled (as in Chapter 5 and Section 6.3) with very different properties from layer to layer. As briefly mentioned in Section 6.3, this could allow the design of multilayer structures with planned strain localization characteristics.

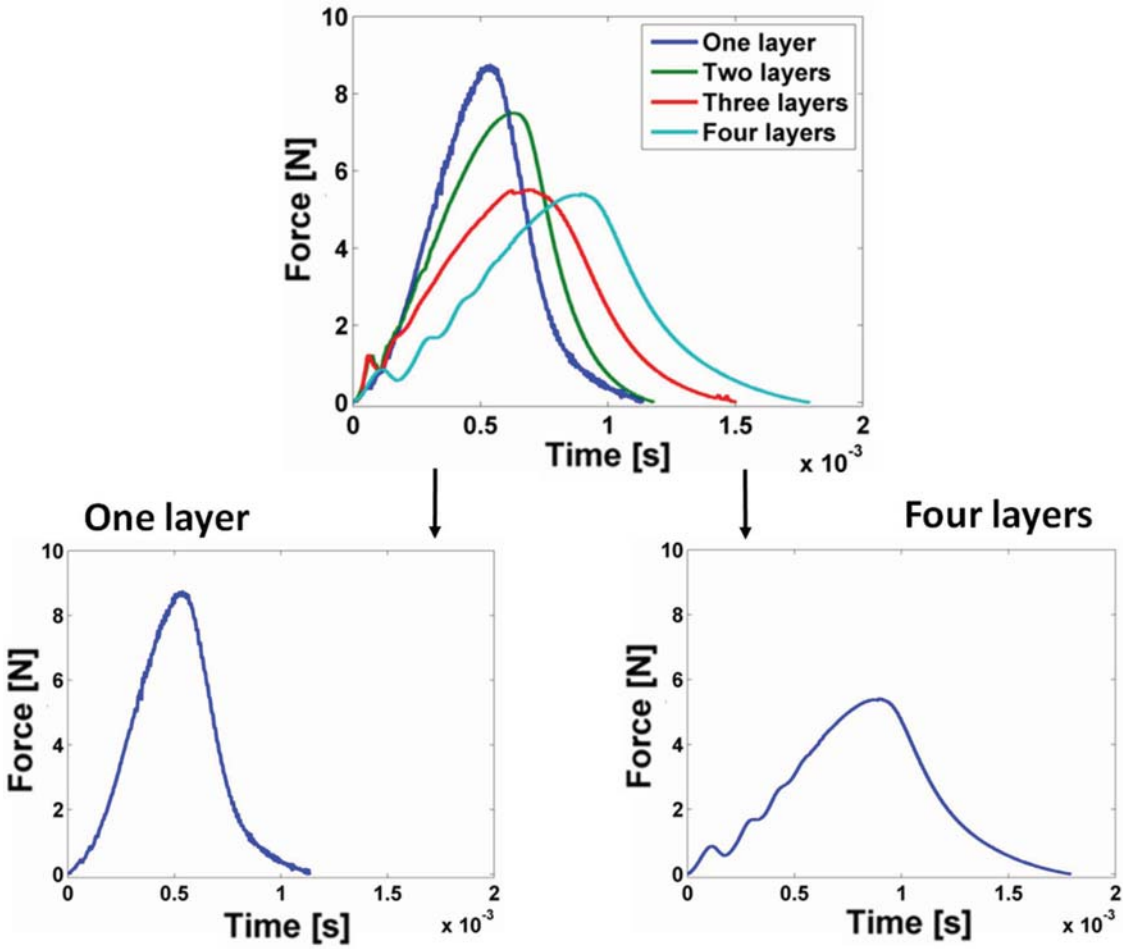

Figure 7.3: The force-time response of structures that were made from multiple layers of CNT arrays connected by copper foils and tested in low-energy impact

This possibility was explored in some preliminary impact tests (in addition to the quasistatic tests of Section 6.3). Figure 7.3 shows the force-time response for samples under low-energy impact. These samples consisted of one, two, three, or four CNT arrays, with the multilayer samples held together by copper foils with thin (and weak) adhesives. Notice that the force-time response reveals a rise and fall in the

force during contact between the striker and the sample. In the case of the single-layer sample, the pattern is unsurprising, with a typical rise and fall in the force-time response. For the multilayer samples (most clearly for the four-layer structure, but also for the two- and three-layer structures), however, there are smaller amplitude instances of rising/falling during the early stages of contact which are superimposed upon the larger, expected rise and fall. These small amplitude changes in force are thought to correspond to separate collapse events in the distinct layers.

In continuing studies in this area it will be important to understand the effects of various boundary layers, such as the PDMS layers used in Chapter 5 versus the copper foil used in Section 6.3. We do know that the PDMS does affect the manner of buckling/collapse for anchored CNTs at high strains (see, e.g., Figure 5.3) and therefore expect that it could affect stress wave propagation in multilayer CNT structures.

7.2.3 Varying [H_2] discretely during synthesis for heterogeneous layered structures

As discussed in Section 3.1, the use of higher concentrations of hydrogen in the flow gas results in CNTs of narrower average diameter. Though that work involved the study of how different hydrogen concentrations led to CNTs of different properties, the hydrogen concentration was always kept constant during any given round of synthesis. This idea can be extended one step further by allowing the hydrogen concentration to vary within a single round of synthesis.

Figure 7.4 shows an annotated scanning electron microscope (SEM) image of such a material. In this case, the injection of the carbon/catalyst precursor solution was paused (similar to the procedure discussed in Section 3.2) periodically, with the hydrogen concentration only adjusted during this pause and held constant during the synthesis of the subsequent CNT layer. This was done so that any effect of the change would be clearly demarcated for easy visualization, though in principle continual gradations should be allowable.

Note first that the different layers have different average CNT diameters (Fig-

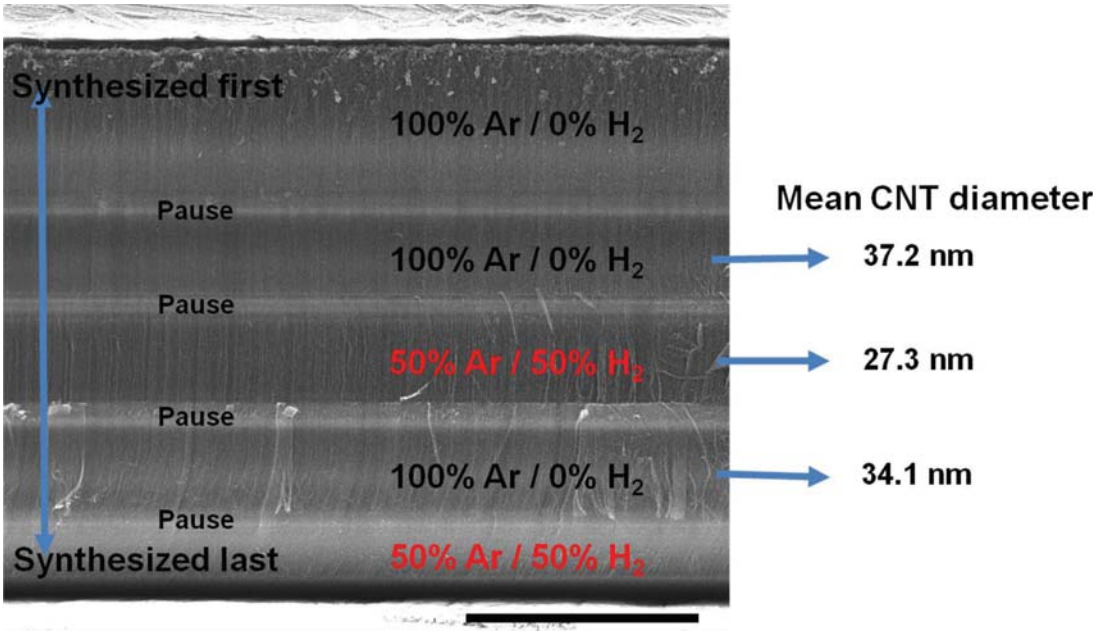

Figure 7.4: A heterogeneous, layered structure that results from a combination of varied hydrogen concentration in the flow gas and pauses in the input of carbon/catalyst for visualization; the scale bar indicates 200 μm

ure 7.4). This was determined by using high-resolution SEM images, which allowed statistical comparisons to be made among layers. Normally, the CNT diameter would be expected to increase from the base to the top (hence the increase in diameter when comparing the layer second from bottom to that second from top, which were synthesized under the same conditions) [38]. For this reason, the average diameter observed for the middle layer, synthesized with H_2 present, is anomalous relative to the typical expectation. Presumably, the decrease in diameter observed for this layer is a result of the hydrogen that was present during its synthesis, which would result in narrower diameter CNTs both from smaller catalyst particle size and decreased contribution from pyrolysis (Section 3.1).

Additionally, samples synthesized as in Figure 7.4 were placed in a steel vise to hold the sample compressed during SEM imaging. It was observed that buckling did indeed preferentially occur in the lower density layers (analogous to the observations in Section 3.2) that were synthesized with H_2 present. One of the next steps for this work would be to study the dynamic response of the material, with the expec-

tation that the heterogeneities in these samples would result in an improved impact protection response similar to that observed previously (Section 3.2). It would be particularly interesting to determine if the combination of higher H_2 concentration (i.e., Section 3.1) with a higher input rate of the carbon/catalyst precursor (i.e., Section 3.2) would lead to even lower density/diameters in desirable ways. This procedure is one more way in which strain localization can be manipulated, primarily for length scales of ~ 100 μm or greater.

7.2.4 Control of mesoscale structure utilizing substrate patterning and solvent wetting

Because the process we used for CNT synthesis utilizes standard (thermally oxidized) silicon wafers, the well-established techniques of photolithography can be used to produce patterned CNT forests. As a proof of concept, a negative masking procedure was followed, which involved placing a chromium thin film (~ 20 nm) everywhere that CNT growth was not desired on the substrate. For example, the CNT bundles in Figure 7.5 were synthesized as follows: First, a simple photomask was designed using a CAD program. Because of the relatively large size of the features (> 10 μm) it was sufficient to use a flexible transparency with the design printed with a high-resolution laser printer. Second, positive photoresist was spin-coated onto a typical growth substrate (a thermally oxidized silicon wafer), which was then exposed to UV light in a mask aligner. Since the pattern consisted of solid black circles everywhere the CNT growth was desired, the UV exposure predominantly occurred only where growth was not desired. The developer solution therefore resulted in the removal of photoresist everwhere that growth was not desired. Third, a chromium thin film was evaporated onto this surface, using an electron beam evaporator. Finally, the whole surface was exposed to acetone, which removed the remaining photoresist (and hence the chromium where it was on top of the photoresist), leaving only the chromium thin film where CNT growth was not desired. CNT synthesis then followed the typical procedure.

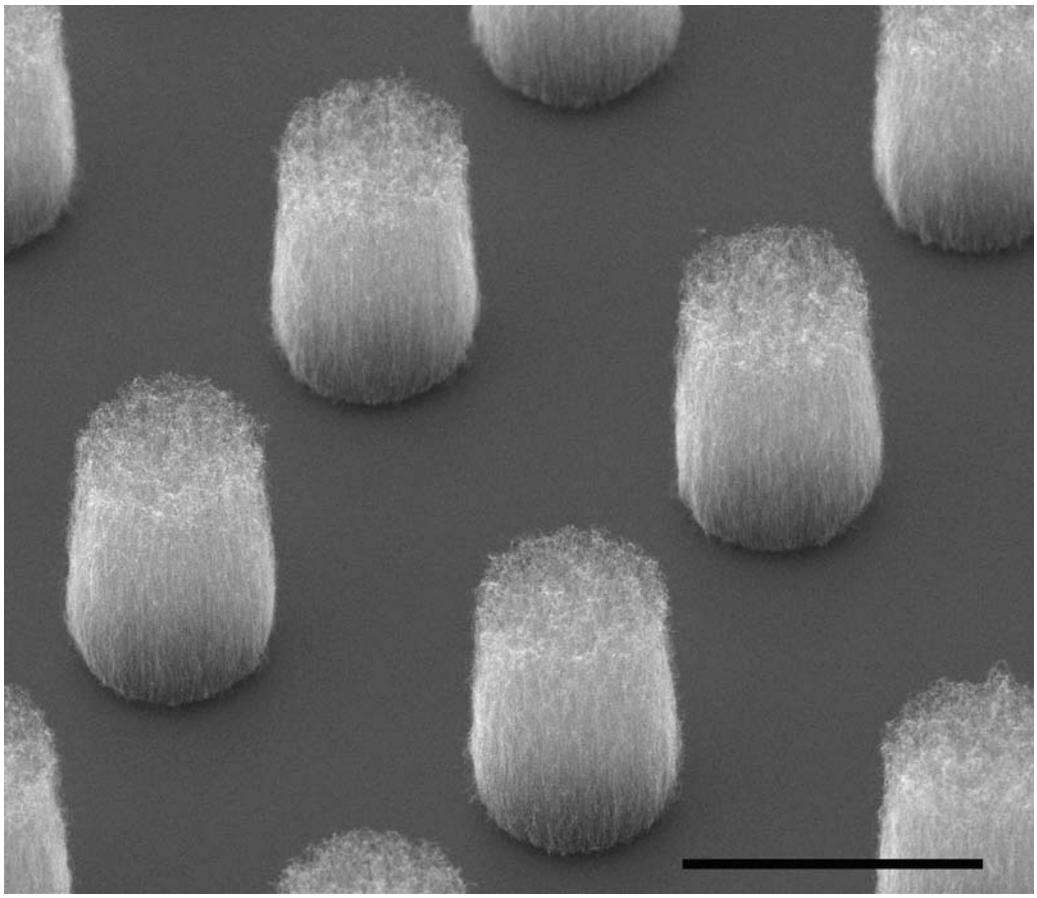

Figure 7.5: CNT bundles synthesized on a patterned substrate (a chromium mask is present everywhere that there is no growth); the scale bar indicates 100 μm

This procedure is quite robust in allowing for a wide variety of patterns. This could potentially allow for the integration of aligned CNT architectures into more complicated systems (e.g., through wafer interconnects [105]) in which the CNT bundles are merely components.

Though it has been previously noted that solvent effects can cause the formation of filamentous mesoscale structures in CNT-based materials (e.g., Ref. [52]), this is especially noticeable in patterned microscale CNT bundles, in which the structure changes drastically. A combination of substrate patterning and solvent effects could be useful in manipulating the mesoscale structure of systems of CNTs. Figure 7.6 illustrates one example of this, in which bundles similar to those in Figure 7.5 were exposed to a small quantity of acetone. Because of the high vapor pressure of ace-

tone, the liquid rapidly evaporates, but leaves behind CNT bundles with modified architectures. The bundles in the top left of Figure 7.6 were exposed to acetone while those in the bottom right were not. Notice that the constraint that results from the substrate allows for the structure to vary as a function of height.

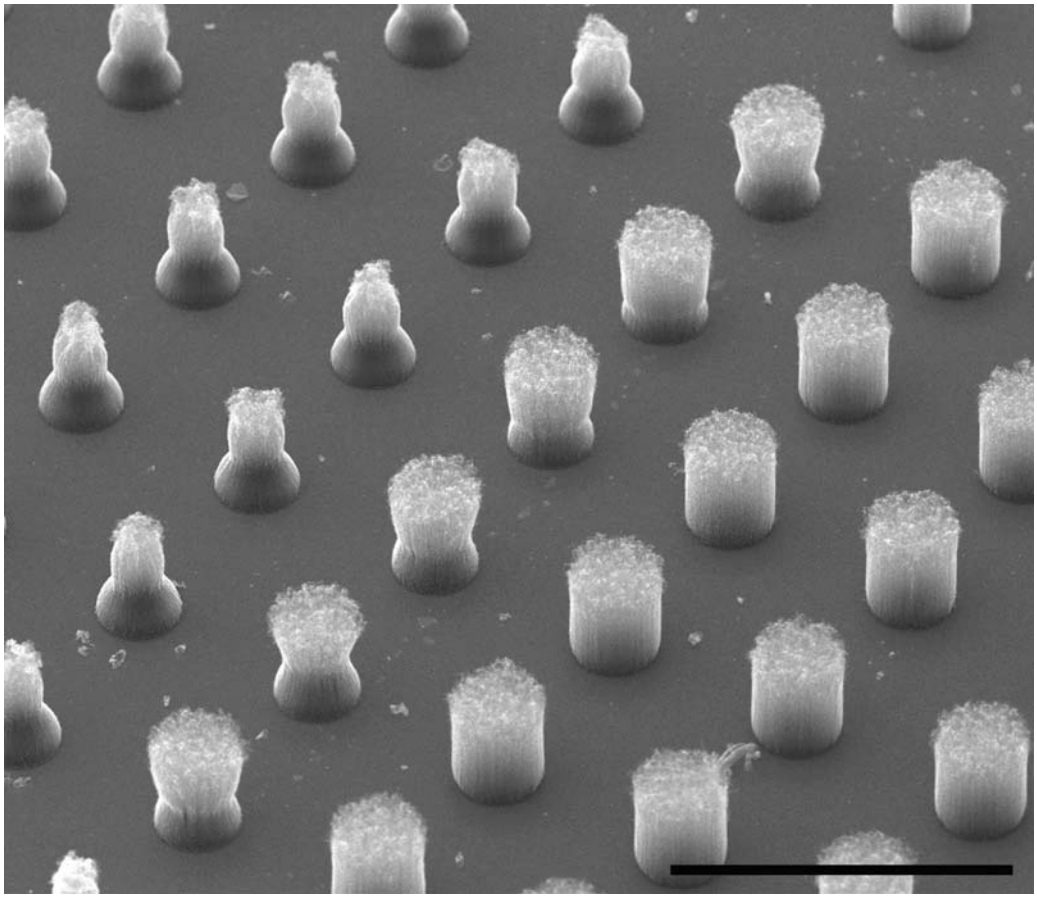

Figure 7.6: CNT bundles that had been exposed to acetone (top left of image) and some that were not (bottom right); the scale bar indicates 400 μm.

Bibliography

[1] Baughman, R. H., Zakhidov, A. A., and Heer, W. A. d. *Science* **297**(5582), 787–792 (2002).

[2] Radushkevich, L. V. and Lukyanovich, V. M. *Zhurnal Fizicheskoi Khimii* **26**, 88–95 (1952).

[3] Oberlin, A., Endo, M., and Koyama, T. *Journal of Crystal Growth* **32**(3), 335–349 (1976).

[4] Iijima, S. *Nature* **354**(6348), 56–58 (1991).

[5] Chopra, N. G., Benedict, L. X., Crespi, V. H., Cohen, M. L., Louie, S. G., and Zettl, A. *Nature* **377**(6545), 135–138 (1995).

[6] Ruoff, R. S., Tersoff, J., Lorents, D. C., Subramoney, S., and Chan, B. *Nature* **364**(6437), 514–516 (1993).

[7] Charlier, J. C. *Accounts of Chemical Research* **35**(12), 1063–1069 (2002).

[8] Dresselhaus, M. S., Jorio, A., Hofmann, M., Dresselhaus, G., and Saito, R. *Nano Letters* **10**(3), 751–758 (2010).

[9] Dresselhaus, M. S., Dresselhaus, G., Charlier, J. C., and Hernández, E. *Philosophical Transactions of the Royal Society of London—A* **362**(1823), 2065–2098 (2004).

[10] Ebbesen, T. W., Lezec, H. J., Hiura, H., Bennett, J. W., Ghaemi, H. F., and Thio, T. *Nature* **382**(6586), 54–56 (1996).

[11] Wang, C. M., Zhang, Y. Y., Xiang, Y., and Reddy, J. N. *Applied Mechanics Reviews* **63**(3), 030804 (2010).

[12] Lu, J. P. *Journal of Physics and Chemistry of Solids* **58**(11), 1649–1652 (1997).

[13] Qian, D., Wagner, G. J., Liu, W. K., Yu, M.-F., and Ruoff, R. S. *Applied Mechanics Reviews* **55**(6), 495–533 (2002).

[14] Tibbetts, G. G. *Journal of Crystal Growth* **66**(3), 632–638 (1984).

[15] Park, S., Srivastava, D., and Cho, K. *Nano Letters* **3**(9), 1273–1277 (2003).

[16] Wei, X., Wang, M.-S., Bando, Y., and Golberg, D. *Science and Technology of Advanced Materials* **12**(4), 044605 (2011).

[17] Kim, P., Shi, L., Majumdar, A., and McEuen, P. L. *Physical Review Letters* **87**(21) (2001).

[18] Berber, S., Kwon, Y.-K., and Tománek, D. *Physical Review Letters* **84**(20), 4613 (2000).

[19] Thostenson, E. T., Ren, Z., and Chou, T.-W. *Composites Science and Technology* **61**(13), 1899–1912 (2001).

[20] Terrones, M., Grobert, N., Olivares, J., Zhang, J. P., Terrones, H., Kordatos, K., Hsu, W. K., Hare, J. P., Townsend, P. D., Prassides, K., Cheetham, A. K., Kroto, H. W., and Walton, D. R. M. *Nature* **388**(6637), 52–55 (1997).

[21] Ren, Z. F., Huang, Z. P., Xu, J. W., Wang, J. H., Bush, P., Siegal, M. P., and Provencio, P. N. *Science* **282**(5391), 1105–1107 (1998).

[22] Feng, X., Liu, K., Xie, X., Zhou, R., Zhang, L., Li, Q., Fan, S., and Jiang, K. *The Journal of Physical Chemistry C* **113**(22), 9623–9631 (2009).

[23] Sinnott, S. B., Andrews, R., Qian, D., Rao, A. M., Mao, Z., Dickey, E. C., and Derbyshire, F. *Chemical Physics Letters* **315**(1–2), 25–30 (1999).

[24] Nessim, G. D., Hart, A. J., Kim, J. S., Acquaviva, D., Oh, J., Morgan, C. D., Seita, M., Leib, J. S., and Thompson, C. V. *Nano Letters* **8**(11), 3587–3593 (2008).

[25] Chakrabarti, S., Kume, H., Pan, L., Nagasaka, T., and Nakayama, Y. *The Journal of Physical Chemistry C* **111**(5), 1929–1934 (2007).

[26] Andrews, R., Jacques, D., Rao, A. M., Derbyshire, F., Qian, D., Fan, X., Dickey, E. C., and Chen, J. *Chemical Physics Letters* **303**(5–6), 467–474 (1999).

[27] Conroy, D., Moisala, A., Cardoso, S., Windle, A., and Davidson, J. *Chemical Engineering Science* **65**(10), 2965–2977 (2010).

[28] Sampedro-Tejedor, P., Maroto-Valiente, A., Nevskaia, D. M., Múñoz, V., Rodríguez-Ramos, I., and Guerrero-Ruíz, A. *Diamond and Related Materials* **16**(3), 542–549 (2007).

[29] Das, N., Dalai, A., Soltan Mohammadzadeh, J. S., and Adjaye, J. *Carbon* **44**(11), 2236–2245 (2006).

[30] Mukhopadhyay, S. M., Karumuri, A., and Barney, I. T. *Journal of Physics D: Applied Physics* **42**(19), 195503 (2009).

[31] Pal, S. K., Talapatra, S., Kar, S., Ci, L., Vajtai, R., Borca-Tasciuc, T., Schadler, L. S., and Ajayan, P. M. *Nanotechnology* **19**(4), 045610 (2008).

[32] Seah, C.-M., Chai, S.-P., and Mohamed, A. R. *Carbon* **49**(14), 4613–4635 (2011).

[33] Jung, Y. J., Wei, Vajtai, R., Ajayan, P. M., Homma, Y., Prabhakaran, K., and Ogino, T. *Nano Letters* **3**(4), 561–564 (2003).

[34] Li, Q. W., Zhang, X. F., DePaula, R. F., Zheng, L. X., Zhao, Y. H., Stan, L., Holesinger, T. G., Arendt, P. N., Peterson, D. E., and Zhu, Y. T. *Advanced Materials* **18**(23), 3160–3163 (2006).

[35] Fan, S., Chapline, M. G., Franklin, N. R., Tombler, T. W., Cassell, A. M., and Dai, H. *Science* **283**(5401), 512–514 (1999).

[36] Reilly, P. T. A. and Whitten, W. B. *Carbon* **44**(9), 1653–1660 (2006).

[37] Abbaslou, R. M. M., Soltan, J., and Dalai, A. K. *Applied Catalysis A—General* **372**(2), 147–152 (2010).

[38] Li, X. S., Zhang, X. F., Ci, L. J., Shah, R., Wolfe, C., Kar, S., Talapatra, S., and Ajayan, P. M. *Nanotechnology* **19**(45), 455609 (2008).

[39] Kim, K.-E., Kim, K.-J., Jung, W. S., Bae, S. Y., Park, J., Choi, J., and Choo, J. *Chemical Physics Letters* **401**(4–6), 459–464 (2005).

[40] Raney, J. R., Misra, A., and Daraio, C. *Carbon* **49**(11), 3631–3638 (2011).

[41] Aksak, M. and Selamet, Y. *Applied Physics A: Materials Science & Processing* **100**(1), 213–222 (2010).

[42] Zhang, H., Cao, G., Wang, Z., Yang, Y., Shi, Z., and Gu, Z. *The Journal of Physical Chemistry C* **112**(33), 12706–12709 (2008).

[43] Dong, L. F., Jiao, J., Foxley, S., Tuggle, D. W., Mosher, C. L., and Grathoff, G. H. *Journal of Nanoscience and Nanotechnology* **2**(2), 155–160 (2002).

[44] Cao, A., Zhang, X. F., Xu, C. L., Liang, J., Wu, D. H., and Wei, B. Q. *Journal of Materials Research* **16**(11), 3107–3110 (2001).

[45] Hata, K., Futaba, D. N., Mizuno, K., Namai, T., Yumura, M., and Iijima, S. *Science* **306**(5700), 1362–1364 (2004).

[46] Maghrebi, M., Khodadadi, A., Mortazavi, Y., Sane, A., Rahimi, M., Shirazi, Y., Tsakadze, Z., and Mhaisalkar, S. *Applied Physics A: Materials Science & Processing* **97**(2), 417–424 (2009).

[47] Tapasztó, L., Kertész, K., Vértesy, Z., Horváth, Z. E., Koós, A. A., Osváth, Z., Sárközi, Z., Darabont, A., and Biró, L. P. *Carbon* **43**(5), 970–977 (2005).

[48] Bajpai, V., Dai, L., and Ohashi, T. *Journal of the American Chemical Society* **126**(16), 5070–5071 (2004).

[49] Gui, X., Wei, J., Wang, K., Cao, A., Zhu, H., Jia, Y., Shu, Q., and Wu, D. *Advanced Materials* **22**(5), 617–621 (2010).

[50] Liu, X. Y., Huang, B. C., and Coville, N. J. *Fullerenes Nanotubes and Carbon Nanostructures* **10**(4), 339–352 (2002).

[51] Maghrebi, M., Khodadadi, A. A., Mortazavi, Y., Rahimi, M., Sane, A., Tsakadze, Z., and Mhaisalkar, S. *Materials Chemistry and Physics* **124**(2–3), 1139–1145 (2010).

[52] Misra, A., Raney, J. R., Craig, A. E., and Daraio, C. *Nanotechnology* **22**, 425705 (2011).

[53] Maghrebi, M., Khodadadi, A. A., Mortazavi, Y., and Mhaisalkar, S. *Applied Surface Science* **255**(16), 7243–7250 (2009).

[54] Kuwana, K., Endo, H., Saito, K., Qian, D., Andrews, R., and Grulke, E. A. *Carbon* **43**(2), 253–260 (2005).

[55] Lee, C. J., Lyu, S. C., Kim, H.-W., Park, C.-Y., and Yang, C.-W. *Chemical Physics Letters* **359**(1–2), 109–114 (2002).

[56] Endo, M., Kim, Y. A., Fukai, Y., Hayashi, T., Terrones, M., Terrones, H., and Dresselhaus, M. S. *Applied Physics Letters* **79**(10), 1531–1533 (2001).

[57] Bai, X., Li, D., Wang, Y., and Liang, J. *Tsinghua Science & Technology* **10**(6), 729–735 (2005).

[58] Singh, C., Shaffer, M. S. P., and Windle, A. H. *Carbon* **41**(2), 359–368 (2003).

[59] Li, Y., Kim, W., Zhang, Y., Rolandi, M., Wang, D., and Dai, H. *The Journal of Physical Chemistry B* **105**(46), 11424–11431 (2001).

[60] Halonen, N., Kordas, K., Toth, G., Mustonen, T., Maklin, J., Vahakangas, J., Ajayan, P. M., and Vajtai, R. *Journal of Physical Chemistry C* **112**(17), 6723–6728 (2008).

[61] Zhang, H., Liang, E., Ding, P., and Chao, M. *Physica B: Condensed Matter* **337**(1–4), 10–16 (2003).

[62] Kim, Y. A., Hayashi, T., Endo, M., Kaburagi, Y., Tsukada, T., Shan, J., Osato, K., and Tsuruoka, S. *Carbon* **43**(11), 2243–2250 (2005).

[63] Kuwana, K., Li, T., and Saito, K. *Chemical Engineering Science* **61**(20), 6718–6726 (2006).

[64] Wasel, W., Kuwana, K., and Saito, K. *Chemical Physics Letters* **422**(4–6), 470–474 (2006).

[65] Pinault, M., Pichot, V., Khodja, H., Launois, P., Reynaud, C., and Mayne-L'Hermite, M. *Nano Letters* **5**(12), 2394–2398 (2005).

[66] Li, X., Cao, A., Jung, Y. J., Vajtai, R., and Ajayan, P. M. *Nano Letters* **5**(10), 1997–2000 (2005).

[67] Iijima, S., Brabec, C., Maiti, A., and Bernholc, J. *The Journal of Chemical Physics* **104**(5), 2089–2092 (1996).

[68] Yakobson, B. I., Brabec, C. J., and Bernholc, J. *Physical Review Letters* **76**(14), 2511 (1996).

[69] Yap, H. W., Lakes, R. S., and Carpick, R. W. *Nano Letters* **7**(5), 1149–1154 (2007).

[70] Yap, H. W., Lakes, R. S., and Carpick, R. W. *Physical Review B* **77**(4) (2008).

[71] Fraternali, F., Blesgen, T., Amendola, A., and Daraio, C. *Journal of the Mechanics and Physics of Solids* **59**(1), 89–102 (2011).

[72] Raney, J. R., Fraternali, F., Amendola, A., and Daraio, C. *Composite Structures* **93**(11), 3013–3018 (2011).

[73] Falvo, M. R., Clary, G. J., Taylor, R. M., Chi, V., Brooks, F. P., Washburn, S., and Superfine, R. *Nature* **389**(6651), 582–584 (1997).

[74] Arroyo, M. and Belytschko, T. *Physical Review Letters* **91**(21), 215505 (2003).

[75] Pantano, A., Boyce, M. C., and Parks, D. M. *Physical Review Letters* **91**(14), 145504 (2003).

[76] Chesnokov, S. A., Nalimova, V. A., Rinzler, A. G., Smalley, R. E., and Fischer, J. E. *Physical Review Letters* **82**(2), 343–346 (1999).

[77] Treacy, M. M. J., Ebbesen, T. W., and Gibson, J. M. *Nature* **381**(6584), 678–680 (1996).

[78] Lourie, O., Cox, D. M., and Wagner, H. D. *Physical Review Letters* **81**(8), 1638 (1998).

[79] Yu, M.-F., Lourie, O., Dyer, M. J., Moloni, K., Kelly, T. F., and Ruoff, R. S. *Science* **287**(5453), 637–640 (2000).

[80] Sazonova, V., Yaish, Y., Ustunel, H., Roundy, D., Arias, T. A., and McEuen, P. L. *Nature* **431**(7006), 284–287 (2004).

[81] Baughman, R. H., Cui, C. X., Zakhidov, A. A., Iqbal, Z., Barisci, J. N., Spinks, G. M., Wallace, G. G., Mazzoldi, A., De Rossi, D., Rinzler, A. G., Jaschinski, O., Roth, S., and Kertesz, M. *Science* **284**(5418), 1340–1344 (1999).

[82] Ajayan, P. M. and Tour, J. M. *Nature* **447**(7148), 1066–1068 (2007).

[83] Ajayan, P., Suhr, J., and Koratkar, N. *Journal of Materials Science* **41**(23), 7824–7829 (2006).

[84] Tang, W., Santare, M. H., and Advani, S. G. *Carbon* **41**(14), 2779–2785 (2003).

[85] Xie, X.-L., Mai, Y.-W., and Zhou, X.-P. *Materials Science and Engineering R: Reports* **49**(4), 89–112 (2005).

[86] Gu, Z., Peng, H., Hauge, R. H., Smalley, R. E., and Margrave, J. L. *Nano Letters* **2**(9), 1009–1013 (2002).

[87] Liang, F., Sadana, A. K., Peera, A., Chattopadhyay, J., Gu, Z., Hauge, R. H., and Billups, W. E. *Nano Letters* **4**(7), 1257–1260 (2004).

[88] Tasis, D., Tagmatarchis, N., Bianco, A., and Prato, M. *Chemical Reviews* **106**(3), 1105–1136 (2006).

[89] Lee, J. U., Huh, J., Kim, K. H., Park, C., and Jo, W. H. *Carbon* **45**(5), 1051–1057 (2007).

[90] Zou, J. H., Khondaker, S. I., Huo, Q., and Zhai, L. *Advanced Functional Materials* **19**(3), 479–483 (2009).

[91] Veedu, V. P., Cao, A., Li, X., Ma, K., Soldano, C., Kar, S., Ajayan, P. M., and Ghasemi-Nejhad, M. N. *Nature Materials* **5**(6), 457–462 (2006).

[92] Duong, H. M., Yamamoto, N., Papavassiliou, D. V., Maruyama, S., and Wardle, B. L. *Nanotechnology* **20**(15), 155702 (2009).

[93] Yamamoto, N., John Hart, A., García, E. J., Wicks, S. S., Duong, H. M., Slocum, A. H., and Wardle, B. L. *Carbon* **47**(3), 551–560 (2009).

[94] Jiang, K., Li, Q., and Fan, S. *Nature* **419**(6909), 801–801 (2002).

[95] Zhang, M., Fang, S. L., Zakhidov, A. A., Lee, S. B., Aliev, A. E., Williams, C. D., Atkinson, K. R., and Baughman, R. H. *Science* **309**(5738), 1215–1219 (2005).

[96] Whitby, R. L. D., Fukuda, T., Maekawa, T., James, S. L., and Mikhalovsky, S. V. *Carbon* **46**(6), 949–956 (2008).

[97] Liu, L., Ma, W., and Zhang, Z. *Small* **7**(11), 1504–1520 (2011).

[98] Zhang, M., Atkinson, K. R., and Baughman, R. H. *Science* **306**(5700), 1358–1361 (2004).

[99] Lebental, B., Chainais, P., Chenevier, P., Chevalier, N., Delevoye, E., Fabbri, J. M., Nicoletti, S., Renaux, P., and Ghis, A. *Nanotechnology* **22**(39) (2011).

[100] Jung, Y. J., Kar, S., Talapatra, S., Soldano, C., Viswanathan, G., Li, X., Yao, Z., Ou, F. S., Avadhanula, A., Vajtai, R., Curran, S., Nalamasu, O., and Ajayan, P. M. *Nano Letters* **6**(3), 413–418 (2006).

[101] Leroy, C. M., Carn, F., Backov, R., Trinquecoste, M., and Delhaes, P. *Carbon* **45**(11), 2317–2320 (2007).

[102] Niu, C., Sichel, E. K., Hoch, R., Moy, D., and Tennent, H. *Applied Physics Letters* **70**(11), 1480–1482 (1997).

[103] Izadi-Najafabadi, A., Yasuda, S., Kobashi, K., Yamada, T., Futaba, D. N., Hatori, H., Yumura, M., Iijima, S., and Hata, K. *Advanced Materials* **22**(35), E235–E241 (2010).

[104] Liu, H., Zhai, J., and Jiang, L. *Soft Matter* **2**(10), 811–821 (2006).

[105] Xu, T., Wang, Z., Miao, J., Chen, X., and Tan, C. M. *Applied Physics Letters* **91**(4) (2007).

[106] Cross, R., Cola, B. A., Fisher, T., Xu, X., Gall, K., and Graham, S. *Nanotechnology* **21**(44) (2010).

[107] Kordás, K., Tóth, G., Moilanen, P., Kumpumäki, M., Vähäkangas, J., Uusimäki, A., Vajtai, R., and Ajayan, P. M. *Applied Physics Letters* **90**(12) (2007).

[108] Teo, E. H. T., Yung, W. K. P., Chua, D. H. C., and Tay, B. K. *Advanced Materials* **19**(19), 2941–2945 (2007).

[109] Wirth, C. T., Hofmann, S., and Robertson, J. *Diamond and Related Materials* **17**(7–10), 1518–1524 (2008).

[110] Zhao, Y., Tong, T., Delzeit, L., Kashani, A., Meyyappan, M., and Majumdar, A. *Journal of Vacuum Science & Technology B* **24**(1), 331–335 (2006).

[111] Cao, A., Veedu, V. P., Li, X., Yao, Z., Ghasemi-Nejhad, M. N., and Ajayan, P. M. *Nature Materials* **4**(7), 540–545 (2005).

[112] Tóth, G., Mäklin, J., Halonen, N., Palosaari, J., Juuti, J., Jantunen, H., Kordás, K., Sawyer, W. G., Vajtai, R., and Ajayan, P. M. *Advanced Materials* **21**(20), 2054–2058 (2009).

[113] Johnson, R. D., Bahr, D. F., Richards, C. D., Richards, R. F., McClain, D., Green, J., and Jiao, J. *Nanotechnology* (6), 065703 (2009).

[114] Misra, A., Greer, J. R., and Daraio, C. *Advanced Materials* **21**(3), 334–338 (2009).

[115] Jakubinek, M. B., White, M. A., Li, G., Jayasinghe, C., Cho, W., Schulz, M. J., and Shanov, V. *Carbon* **48**(13), 3947–3952 (2010).

[116] Pavese, M., Musso, S., and Pugno, N. M. *Journal of Nanoscience and Nanotechnology* **10**(7), 4240–4245 (2010).

[117] Cao, A. Y., Dickrell, P. L., Sawyer, W. G., Ghasemi-Nejhad, M. N., and Ajayan, P. M. *Science* **310**(5752), 1307–1310 (2005).

[118] Suhr, J., Victor, P., Ci, L., Sreekala, S., Zhang, X., Nalamasu, O., and Ajayan, P. M. *Nature Nanotechnology* **2**(7), 417–421 (2007).

[119] Bradford, P. D., Wang, X., Zhao, H., and Zhu, Y. T. *Carbon* **49**(8), 2834–2841 (2011).

[120] Hutchens, S. B., Hall, L. J., and Greer, J. R. *Advanced Functional Materials* **20**(14), 2338–2346 (2010).

[121] Qiu, A., Bahr, D. F., Zbib, A. A., Bellou, A., Mesarovic, S. D., McClain, D., Hudson, W., Jiao, J., Kiener, D., and Cordill, M. J. *Carbon* **49**(4), 1430–1438 (2011).

[122] Wardle, B. L., Saito, D. S., García, E. J., Hart, A. J., de Villoria, R. G., and Verploegen, E. A. *Advanced Materials* **20**(14), 2707–2714 (2008).

[123] Al-Khedher, M. A., Pezeshki, C., McHale, J. L., and Knorr, F. J. *Nanotechnology* **18**(35), 355703 (2007).

[124] Malik, H., Stephenson, K. J., Bahr, D. F., and Field, D. P. *Journal of Materials Science* **46**(9), 3119–3126 (2011).

[125] Wang, B. N., Bennett, R. D., Verploegen, E., Hart, A. J., and Cohen, R. E. *The Journal of Physical Chemistry C* **111**(48), 17933–17940 (2007).

[126] Borowiak-Palen, E., Bachmatiuk, A., Rümmeli, M. H., Gemming, T., Kruszynska, M., and Kalenczuk, R. J. *Physica E: Low-Dimensional Systems and Nanostructures* **40**(7), 2227–2230 (2008).

[127] Jackson, J. J., Puretzky, A. A., More, K. L., Rouleau, C. M., Eres, G., and Geohegan, D. B. *ACS Nano* **4**(12), 7573–7581 (2010).

[128] Suhr, J., Koratkar, N., Keblinski, P., and Ajayan, P. *Nature Materials* **4**(2), 134–137 (2005).

[129] Abot, J. L., Song, Y., Schulz, M. J., and Shanov, V. N. *Composites Science and Technology* **68**(13), 2755–2760 (2008).

[130] Abot, J. L. and Song, Y. *Journal of Reinforced Plastics and Composites* **29**(22), 3401–3410 (2010).

[131] Ci, L., Suhr, J., Pushparaj, V., Zhang, X., and Ajayan, P. M. *Nano Letters* **8**(9), 2762–2766 (2008).

[132] García, E. J., Hart, A. J., Wardle, B. L., and Slocum, A. H. *Nanotechnology* **18**(16), 165602 (2007).

[133] García, E. J., Hart, A. J., Wardle, B. L., and Slocum, A. H. *Advanced Materials* **19**(16), 2151–2156 (2007).

[134] García, E. J., Wardle, B. L., and Hart, A. J. *Composites Part A: Applied Science and Manufacturing* **39**(6), 1065–1070 (2008).

[135] Cebeci, H., Villoria, R. G. d., Hart, A. J., and Wardle, B. L. *Composites Science and Technology* **69**(15-16), 2649–2656 (2009).

[136] Tawfick, S., Deng, X. P., Hart, A. J., and Lahann, J. *Physical Chemistry Chemical Physics* **12**(17), 4446–4451 (2010).

[137] Shin, M. K., Oh, J., Lima, M., Kozlov, M. E., Kim, S. J., and Baughman, R. H. *Advanced Materials* **22**(24), 2663–2667 (2010).

[138] Sansom, E. B., Rinderknecht, D., and Gharib, M. *Nanotechnology* **19**(3) (2008).

[139] Zhang, Q., Zhao, M., Liu, Y., Cao, A., Qian, W., Lu, Y., and Wei, F. *Advanced Materials* **21**(28), 2876–2880 (2009).

[140] Misra, A., Raney, J. R., De Nardo, L., Craig, A. E., and Daraio, C. *ACS Nano* **5**(10), 7713–7721 (2011).

[141] Tantra, R. and Cumpson, P. *Nanotoxicology* **1**(4), 251–265 (2007).

[142] Cena, L. G. and Peters, T. M. *Journal of Occupational and Environmental Hygiene* **8**(2), 86–92 (2011).

[143] Jaurand, M. C. F., Renier, A., and Daubriac, J. *Particle and Fibre Toxicology* **6** (2009).

[144] Liu, A., Sun, K., Yang, J., and Zhao, D. *Journal of Nanoparticle Research* **10**(8), 1303–1307 (2008).

[145] Bergamaschi, E., Bussolati, O., Magrini, A., Bottini, M., Migliore, L., Bellucci, S., Iavicoli, I., and Bergamaschi, A. *International Journal of Immunopathology and Pharmacology* **19**(4 Suppl), 3–10 (2006).

[146] Blazer-Yost, B. L., Banga, A., Amos, A., Chernoff, E., Lai, X., Li, C., Mitra, S., and Witzmann, F. A. *Nanotoxicology* **5**(3), 354–371 (2011).

[147] Muller, J., Huaux, F., Fonseca, A., Nagy, J. B., Moreau, N., Delos, M., Raymundo-Piñero, E., Béguin, F., Kirsch-Volders, M., Fenoglio, I., Fubini, B., and Lison, D. *Chemical Research in Toxicology* **21**(9), 1698–1705 (2008).

[148] Poland, C. A., Duffin, R., Kinloch, I., Maynard, A., Wallace, W. A. H., Seaton, A., Stone, V., Brown, S., MacNee, W., and Donaldson, K. *Nature Nanotechnology* **3**(7), 423–428 (2008).

[149] Thurnherr, T., Brandenberger, C., Fischer, K., Diener, L., Manser, P., Maeder-Althaus, X., Kaiser, J. P., Krug, H. F., Rothen-Rutishauser, B., and Wick, P. *Toxicology Letters* **200**(3), 176–186 (2011).

[150] Bello, D., Hart, A. J., Ahn, K., Hallock, M., Yamamoto, N., García, E. J., Ellenbecker, M. J., and Wardle, B. L. *Carbon* **46**(6), 974–977 (2008).

[151] Lattanzi, L., Raney, J. R., De Nardo, L., Misra, A., and Daraio, C. *Journal of Applied Physics* **111**, 074314 (2012).

[152] Blesgen, T., Fraternali, F., Raney, J. R., and Daraio, C. *In review* (2012).

[153] Gibson, L. J. and Ashby, M. F. *Cellular solids: structure and properties*. Cambridge University Press, (1999).

[154] Yaglioglu, O. *Carbon Nanotube Based Electromechanical Probes*. PhD thesis, Massachusetts Institute of Technology, Cambridge, Massachusetts, (2007).

[155] Pushparaj, V. L., Ci, L., Sreekala, S., Kumar, A., Kesapragada, S., Gall, D., Nalamasu, O., Pulickel, A. M., and Suhr, J. *Applied Physics Letters* **91**(15), 153116 (2007).

[156] Zbib, A. A., Mesarovic, S. D., Lilleodden, E. T., McClain, D., Jiao, J., and Bahr, D. F. *Nanotechnology* **19**(17), 175704 (2008).

[157] Deck, C. P., Flowers, J., McKee, G. S. B., and Vecchio, K. *Journal of Applied Physics* **101**(2), 023512 (2007).

[158] Ge, L., Ci, L., Goyal, A., Shi, R., Mahadevan, L., Ajayan, P. M., and Dhinojwala, A. *Nano Letters* **10**(11), 4509–4513 (2010).

[159] Zhang, Q., Lu, Y. C., Du, F., Dai, L., Baur, J., and Foster, D. C. *Journal of Physics D: Applied Physics* **43**(31), 315401 (2010).

[160] Maschmann, M. R., Zhang, Q., Du, F., Dai, L., and Baur, J. *Carbon* **49**(2), 386–397 (2011).

[161] Cao, C., Reiner, A., Chung, C., Chang, S.-H., Kao, I., Kukta, R. V., and Korach, C. S. *Carbon* **49**(10), 3190–3199 (2011).

[162] Mullins, L. *Journal of Rubber Research* **16**(12), 275–289 (1947).

[163] Peña, E. *Journal of the Mechanics and Physics of Solids* **59**, 1808–1822 (2011).

[164] Blesgen, T., Fraternali, F., Raney, J. R., Amendola, A., and Daraio, C. *In review* (2012).

[165] Dorfmann, A. and Ogden, R. W. *International Journal of Solids and Structures* **41**, 1855–1878 (2004).

[166] Flamm, M., Spreckels, J., Steinweger, T., and Weltin, U. *International Journal of Fatigue* **33**, 1189–1198 (2011).

[167] McCarter, C., Richards, R., Mesarovic, S., Richards, C., Bahr, D., McClain, D., and Jiao, J. *Journal of Materials Science* **41**(23), 7872–7878 (2006).

[168] Maschmann, M. R., Zhang, Q., Wheeler, R., Du, F., Dai, L., and Baur, J. *ACS Applied Materials & Interfaces* **3**(3), 648–653 (2011).

[169] Waters, J. F., Riester, L., Jouzi, M., Guduru, P. R., and Xu, J. M. *Applied Physics Letters* **85**(10), 1787–1789 (2004).

[170] Puglisi, G. and Truskinovsky, L. *Journal of the Mechanics and Physics of Solids* **53**(3), 655–679 (2005).

[171] Pampolini, G. and Del Piero, G. *Journal of Mechanics of Materials and Structures* **3**(5), 969–981 (2008).

[172] Yang, X., He, P., and Gao, H. *Nano Research* **4**(12), 1191–1198 (2011).

[173] Xu, M., Futaba, D. N., Yamada, T., Yumura, M., and Hata, K. *Science* **330**(6009), 1364–1368 (2010).

[174] Li, X., Ci, L., Kar, S., Soldano, C., Kilpatrick, S. J., and Ajayan, P. M. *Carbon* **45**(4), 847–851 (2007).

[175] Mesarovic, S. D., McCarter, C. M., Bahr, D. F., Radhakrishnan, H., Richards, R. F., Richards, C. D., McClain, D., and Jiao, J. *Scripta Materialia* **56**(2), 157–160 (2007).

[176] Pathak, S., Cambaz, Z. G., Kalidindi, S. R., Swadener, J. G., and Gogotsi, Y. *Carbon* **47**(8), 1969–1976 (2009).

[177] Qiu, A., Fowler, S. P., Jiao, J., Kiener, D., and Bahr, D. F. *Nanotechnology* **22**(29) (2011).

[178] Xu, M., Futaba, D. N., Yumura, M., and Hata, K. *Advanced Materials* **23**(32), 3686–3691 (2011).

[179] Gogotsi, Y. *Science* **330**(6009), 1332–1333 (2010).

[180] Koratkar, N., Wei, B. Q., and Ajayan, P. M. *Advanced Materials* **14**(13–14), 997–1000 (2002).

[181] Findley, W. N., Lai, J. S., and Onaran, K. *Creep and Relaxation of Nonlinear Viscoelastic Materials*. Elsevier Science Publishing Co, Inc, (1976).

[182] Green, M. J., Behabtu, N., Pasquali, M., and Adams, W. W. *Polymer* **50**(21), 4979–4997 (2009).

[183] Hadid, M., Rechak, S., and Tati, A. *Materials Science and Engineering A* **385**(1–2), 54–58 (2004).

[184] Provenzano, P., Lakes, R., Keenan, T., and Vanderby, R. *Annals of Biomedical Engineering* **29**(10), 908–914 (2001).

[185] Lakes, R. S. and Vanderby, R. *Journal of Biomechanical Engineering* **121**(6), 612–615 (1999).

[186] Li, W. Z., Xie, S. S., Qian, L. X., Chang, B. H., Zou, B. S., Zhou, W. Y., Zhao, R. A., and Wang, G. *Science* **274**(5293), 1701–1703 (1996).

[187] Lee, C. J., Park, J., Huh, Y., and Yong Lee, J. *Chemical Physics Letters* **343**(1–2), 33–38 (2001).

[188] de Heer, W. A., Chatelain, A., and Ugarte, D. *Science* **270**(5239), 1179–1180 (1995).

[189] Tong, T., Zhao, Y., Delzeit, L., Kashani, A., Meyyappan, M., and Majumdar, A. *Nano Letters* **8**(2), 511–515 (2008).

[190] Cui, X., Wei, W., Harrower, C., and Chen, W. *Carbon* **47**(15), 3441–3451 (2009).

[191] Wasel, W., Kuwana, K., Reilly, P. T. A., and Saito, K. *Carbon* **45**(4), 833–838 (2007).

[192] Liu, Q., Ren, W., Chen, Z.-G., Wang, D.-W., Liu, B., Yu, B., Li, F., Cong, H., and Cheng, H.-M. *ACS Nano* **2**(8), 1722–1728 (2008).

[193] Okita, A., Suda, Y., Oda, A., Nakamura, J., Ozeki, A., Bhattacharyya, K., Sugawara, H., and Sakai, Y. *Carbon* **45**(7), 1518–1526 (2007).

[194] Romo-Negreira, A., Cott, D. J., De Gendt, S., Maex, K., Heyns, M. M., and Vereecken, P. M. *Journal of the Electrochemical Society* **157**(3), K47–K51 (2010).

[195] Zhang, G., Mann, D., Zhang, L., Javey, A., Li, Y., Yenilmez, E., Wang, Q., McVittie, J. P., Nishi, Y., Gibbons, J., and Dai, H. *Proceedings of the National Academy of Sciences of the United States of America* **102**(45), 16141–16145 (2005).

[196] Dresselhaus, M. S., Dresselhaus, G., Saito, R., and Jorio, A. *Physics Reports* **409**(2), 47–99 (2005).

[197] Raney, J. R., Wang, R. Y., and Daraio, C. *In review* (2012).

[198] Chakrabarti, S., Gong, K., and Dai, L. *The Journal of Physical Chemistry C* **112**(22), 8136–8139 (2008).

[199] Sun, G., Li, G., Hou, S., Zhou, S., Li, W., and Li, Q. *Materials Science and Engineering: A* **527**(7–8), 1911–1919 (2010).

[200] Suresh, S. *Science* **292**(5526), 2447–2451 (2001).

[201] Miserez, A., Schneberk, T., Sun, C., Zok, F. W., and Waite, J. H. *Science* **319**(5871), 1816–1819 (2008).

[202] Daraio, C., Nesterenko, V. F., and Jin, S. *Applied Physics Letters* **85**(23), 5724–5726 (2004).

[203] Raney, J. R., Zhang, H.-L., Morse, D. E., and Daraio, C. *Carbon* **In press** (2012).

[204] Deck, C. P. and Vecchio, K. S. *The Journal of Physical Chemistry B* **109**(25), 12353–12357 (2005).

[205] Cao, A., Zhang, X., Wei, J., Li, Y., Xu, C., Liang, J., Wu, D., and Wei, B. *The Journal of Physical Chemistry B* **105**(48), 11937–11940 (2001).

[206] Ajdari, A., Nayeb-Hashemi, H., and Vaziri, A. *International Journal of Solids and Structures* **48**(3–4), 506–516 (2011).

[207] Wang, E., Gardner, N., and Shukla, A. *International Journal of Solids and Structures* **46**(18–19), 3492–3502 (2009).

[208] Cui, L., Kiernan, S., and Gilchrist, M. D. *Materials Science and Engineering: A* **507**(1–2), 215–225 (2009).

[209] Kiernan, S., Cui, L., and Gilchrist, M. D. *International Journal of Non-Linear Mechanics* **44**(5), 456–468 (2009).

[210] Zhang, H.-L. and Morse, D. E. *Journal of Materials Chemistry* **19**(47), 9006–9011 (2009).

[211] Guo, G., Guo, J., Tao, D., Choy, W. C. H., Zhao, L., Qian, W., and Wang, Z. *Applied Physics A: Materials Science & Processing* **89**(2), 525–528 (2007).

[212] Moon, S. Y., Kusunose, T., Tanaka, S.-i., and Sekino, T. *Carbon* **47**(12), 2924–2932 (2009).

[213] Bittencourt, C., Felten, A., Ghijsen, J., Pireaux, J. J., Drube, W., Erni, R., and Van Tendeloo, G. *Chemical Physics Letters* **436**(4–6), 368–372 (2007).

[214] Liu, Y., Tang, J., Chen, X., Chen, W., Pang, G. K. H., and Xin, J. H. *Carbon* **44**(2), 381–383 (2006).

[215] Zhao, B., Yadian, B. L., Li, Z. J., Liu, P., and Zhang, Y. F. *Surface Engineering* **25**(1), 31–35 (2009).

[216] Eder, D. *Chemical Reviews* **110**(3), 1348–1385 (2010).

[217] Kuang, Q., Li, S.-F., Xie, Z.-X., Lin, S.-C., Zhang, X.-H., Xie, S.-Y., Huang, R.-B., and Zheng, L.-S. *Carbon* **44**(7), 1166–1172 (2006).

[218] Han, W.-Q. and Zettl, A. *Nano Letters* **3**(5), 681–683 (2003).

[219] Jin, X., Zhou, W., Zhang, S., and Chen, G. *Small* **3**(9), 1513–1517 (2007).

[220] Ma, S.-B., Ahn, K.-Y., Lee, E.-S., Oh, K.-H., and Kim, K.-B. *Carbon* **45**(2), 375–382 (2007).

[221] Ng, K. C., Zhang, S., Peng, C., and Chen, G. Z. *Journal of the Electrochemical Society* **156**(11), A846–A853 (2009).

[222] Otieno, G., Koos, A. A., Dillon, F., Wallwork, A., Grobert, N., and Todd, R. I. *Carbon* **48**(8), 2212–2217 (2010).

[223] Chandrashekar, A., Ramachandran, S., Pollack, G., Lee, J. S., Lee, G. S., and Overzet, L. *Thin Solid Films* **517**(2), 525–530 (2008).

[224] Neocleus, S., Pattinson, S. W., Motta, A. M. M., Windle, A. H., and Eder, D. *Functional Materials Letters* **4**(1), 83–89 (2011).

[225] Wang, W., Epur, R., and Kumta, P. N. *Electrochemistry Communications* **13**(5), 429–432 (2011).

[226] Mylvaganam, K. and Zhang, L. C. *Applied Physics Letters* **89**(12), 123127 (2006).

[227] Ramachandra, S., Sudheer Kumar, P., and Ramamurty, U. *Scripta Materialia* **49**(8), 741–745 (2003).

[228] Han, C. and Sun, C. T. *Journal of Sound and Vibration* **243**(4), 747–761 (2001).

[229] Kireitseu, M. *Advances in Science and Technology* **50**, 31–36 (2006).

[230] Kireitseu, M. V. and Bochkareva, L. *ASME Conference Proceedings* **2007**(42703), 21–26 (2007).

[231] Gama, B. A., Bogetti, T. A., Fink, B. K., Yu, C. J., Claar, T. D., Eifert, H. H., and Gillespie, J. W. *Composite Structures* **52**(3–4), 381–395 (2001).

[232] Liu, M., Sun, J., Sun, Y., Bock, C., and Chen, Q. *Journal of Micromechanics and Microengineering* **19**(3), 035028 (2009).

[233] Ajayan, P. M., Schadler, L. S., Giannaris, C., and Rubio, A. *Advanced Materials* **12**(10), 750–753 (2000).

[234] Barker, M. K. and Seedhom, B. B. *Rheumatology* **40**(3), 274–284 (2001).

[235] Loret, B. and Simoes, F. M. F. *Mechanics of Materials* **36**(5–6), 515–541 (2004).

[236] Yang, J., Chiou, R., Ruprecht, A., Vicario, J., MacPhail, L. A., and Rams, T. E. *Dentomaxillofacial Radiology* **31**(5), 313–316 (2002).

[237] Naraghi, M., Filleter, T., Moravsky, A., Locascio, M., Loutfy, R. O., and Espinosa, H. D. *ACS Nano* **4**(11), 6463–6476 (2010).

[238] Zhou, J., Shrotriya, P., and Soboyejo, W. O. *Mechanics of Materials* **36**(8), 781–797 (2004).

[239] San Marchi, C., Despois, J. F., and Mortensen, A. *Acta Materialia* **52**(10), 2895–2902 (2004).

[240] Puglisi, G. and Truskinovsky, L. *Journal of the Mechanics and Physics of Solids* **50**(2), 165–187 (2002).

[241] Tans, S. J., Verschueren, A. R. M., and Dekker, C. *Nature* **393**(6680), 49–52 (1998).

[242] Gurtin, M. E. and Francis, E. C. *Journal of Spacecraft and Rockets* **18**, 285–286 (1981).

[243] Ogden, R. W. and Roxburgh, D. G. *Proceedings: Mathematical, Physical and Engineering Sciences* **455**(1988), 2861–2877 (1999).

[244] Horgan, C. O., Ogden, R. W., and Saccomandi, G. *Proceedings of the Royal Society of London. Series A: Mathematical, Physical and Engineering Sciences* **460**(2046), 1737–1754 (2004).

[245] De Tommasi, D. and Puglisi, G. *Journal of Rheology* **50**(4), 495–512 (2006).

[246] Pantano, A., M. Parks, D., and Boyce, M. C. *Journal of the Mechanics and Physics of Solids* **52**(4), 789–821 (2004).

[247] Holland, J. H. *Journal of the ACM* **9**(3), 297–314 (1962).

[248] Mühlenbein, H. and Schlierkamp-Voosen, D. *Evolutionary Computation* **1**(4), 335–360 (1993).

[249] De Falco, I., Del Balio, R., Della Cioppa, A., and Tarantino, E. In *Proceedings of the Second Workshop on Evolutionary Computing (WEC2)*, 29–32, (1996).

[250] Fraternali, F., Porter, M. A., and Daraio, C. *Mechanics of Advanced Materials and Structures* **17**(1), 1–19 (2010).

[251] El Sayed, T., Mota, A., Fraternali, F., and Ortiz, M. *Journal of Biomechanics* **41**(7), 1458–1466 (2008).

[252] Bertotti, G. *Physical Review Letters* **76**(10), 1739–1742 (1996).

[253] Fisher, D. S. *Physics Reports* **301**(1–3), 113–150 (1998).

[254] He, Y. J. and Sun, Q. P. *International Journal of Solids and Structures* **47**(20), 2775–2783 (2010).

[255] Petryk, H. and Stupkiewicz, S. *Journal of the Mechanics and Physics of Solids* **58**(3), 390–408 (2010).

[256] De Tommasi, D., Puglisi, G., and Saccomandi, G. *Biophysical Journal* **98**(9), 1941–1948 (2010).

[257] Forcadel, N., Imbert, C., and Monneau, R. *Discrete and Continuous Dynamical Systems* **23**(3), 785–826 (2009).

Appendix A

Multiscale mass-spring models of carbon nanotube arrays accounting for Mullins-like behavior and permanent deformation

Abstract

Based on a one-dimensional discrete system of bistable springs, we introduce a mechanical model to describe plasticity and damage in carbon nanotube arrays[1]. We investigate analytically the energetics of the mechanical system, derive the stress-strain law, and compute the mechanical dissipation in the system, both for the discrete case as well as for the continuum limit. Macroscopic portions of the material are investigated using numerical homogenization and dynamic relaxation. To validate the model, we simulate a cyclic compression experiment on CNT foams, considering both the material response during the primary loading path from the virgin state, and the damaged response after preconditioning. The model developed captures the multiscale features of the experimental response, including a Mullins-like behavior at

[1] This chapter is adapted from our recent work, Ref. [152] by T. Blesgen, F. Fraternali, J.R. Raney, and C. Daraio, which is currently in review under the same title. It is included for those interested in understanding more of the mathematical basis of the model discussed in Chapter 6, especially the generalized model of Section 6.2. TB developed the mathematical framework, FF performed numerical modeling, and JRR conducted experiments, with each author leading the writing of the portion of the manuscript corresponding to his topic. All authors contributed to the discussions and the writing of the manuscript.

different loading conditions.

A.1 Introduction

The local rearrangements and buckling associated with preconditioning and the Mullins-like behavior of CNT arrays (as discussed in Section 2.2) give rise to an important mechanism for energy dissipation during the first few compressive cycles. In some past efforts to model the Mullins effect in reinforced rubber, this source of energy dissipation has been treated as the exclusive source of dissipation (referred to as the *idealized Mullins effect*), with the material behaving elastically after the preconditioning cycles (e.g., Ref. [245]). Yet the material continues to exhibit a hysteretic response after preconditioning, as do rubbers, and therefore a model that accounts for both the initial preconditioning cycles (and the Mullins-like strain dependence), as well as the latter hysteretic response of the material is needed. The energy dissipation observed in compressed CNT arrays is a result of the interplay of several distinct mechanisms, including friction and entanglement between CNTs [117]. Additionally, individual CNTs have been observed in axial compression to undergo elastic shell buckling, with an unstable kinking regime associated with negative stiffness and resulting dissipation [69, 70]. This latter mechanism leads to a form of rate-independent hysteresis (or "transformational plasticity") at the macroscopic scale, which is similar to that observed in metals, shape memory alloys, and open-cell foams (refer, e.g., to Refs. [170, 171] and references therein).

Bistable spring models in the context of plasticity were first introduced in [240]; see also [170] for the investigation of a variety of material behaviors. Typical for such systems is a large number of almost degenerate metastable configurations resulting in a sequence of bifurcations during monotone loading. In magnetism, this kind of mechanism is referred to as the Barkhausen effect [252]. A deeper understanding of how the different length scales interact physically was obtained by the investigation of the pinning and depinning patterns of inhomogeneous materials like superconductors, the occurrence of Bloch walls in ferromagnets, or the formation of crack lines [253].

The approach of bistable springs is in particular appealing for systems undergoing cyclic loading with hysteresis, see, e.g., the recent articles [254] and [255] among others. In Ref. [256], bistable springs have also been applied to plastically deformed spider silks, also investigating damage. But different to the model presented here, the stress-strain law is linked to the microstructure. A homogenization of the discrete model is found in Ref. [257].

Multiscale mass-spring models of CNT structures have been recently proposed in Refs. [71, 72] in order to account for the hysteretic response of single- and multi-layer structures within an effective one-dimensional framework. Such models are able to capture some distinctive features of the microstructural rearrangements that have been discussed so far, namely:

- strain localization due to local buckling of the tubes;
- rate-independent hysteresis induced by the succession of infinitesimal, negative-stiffness events of viscous nature at the microscopic scale (refer also to [170]); and
- multiscale response related to graded mechanical properties along the height of the structure (e.g., [72, 155]).

In the present work, we show that a suitable generalization of the above models leads us to capture some other relevant phenomena, such as:

- material damage induced by Mullins-like response to preconditioning, and
- permanent deformation of the structure.

We start by describing the primary loading path of a CNT array under uniform compression through the multiscale mass-spring model presented in Ref. [71]. Subsequently, we introduce some preconditioning-induced material damage by setting to zero the stiffness of a suitable percentage of microscopic springs. Such a position also allows us to model permanent axial deformation of the structure. The latter follows

from the irreversible "annihilation" of the springs with zero stiffness and coincides with the "activation" strain of the mesoscopic response. As in Ref. [71], we introduce an intermediate mesoscopic scale between the microscopic scale of an infinitesimal vertical portion of the structure and the scale of the entire structure. This allows us to account for grading of material damage along the thickness of the structure. The mesoscopic response is obtained through an analytic approach, on computing the limiting response of the bistable spring model adopted at the microscopic scale.

An analytic approach to damage in CNT arrays is already given in Ref. [164], where the passage from microscale to mesoscale is studied both numerically and analytically in the framework of Γ-convergence for the elastic energy functional. We extend this analysis here by studying the branching mechanism during the minimization process and by computing the dissipated energy, also for the continuum limit of infinitely many springs.

We use an information-passing technique in Section A.2.3 to formulate a mechanical model of the macroscopic response of the structure. We address to future work the modeling of the transient response of CNT arrays during preconditioning, and account for progressive deterioration of the mechanical properties at the microscopic level.

The remainder of this appendix is organized as follows: first, we summarize an earlier model by the authors where bistable mass-spring models have been used to describe the plastic behavior of CNT arrays. In Section A.2.2, we extend this model to incorporate damage, i.e., the mechanical failure of certain springs. Therein we also study the energy landscape, derive the stress-strain law, and compute the dissipated energy, both for the discrete system as well as for the idealized continuum limit of infinitely many springs. In Section A.2.3, we develop an information-passing approach to deal with macroscopic sections of a CNT material. These concepts are then combined in Section A.3 to do simulations for experimental data on multicycle compression tests with very good agreement. We end with an evaluation of the results and an outlook.

A.2 Multiscale mass-spring models of CNT arrays

A.2.1 Bistable spring model at the microscopic scale

We model an infinitesimal portion of a CNT foam through the bistable spring model diffusely described in Ref. [71], which we briefly summarize below. We assume that an infinitesimal portion of the foam can be described as a chain of $N+1$ lumped masses $m^0, \dots, m^N$, with m^N clamped at the bottom of the chain. The adjacent masses are connected with each other through bistable springs characterized by the axial strains

$$\varepsilon^i = \varepsilon^i(u_N) = \frac{u_N^{i-1} - u_N^i}{h_N}, \qquad i = 1, \dots, N, \tag{A.1}$$

where u_N^i denotes the axial displacement of the mass m^i (positive upward), and we set $u_N := \{u_N^0, \dots, u_N^N\}$. The potential V^i and stress σ^i vs. strain ε^i laws of the generic spring are defined by

$$V^i(\varepsilon^i) = \begin{cases} V_a^i(\varepsilon^i) := -k_0^i[\varepsilon^i + \ln(1-\varepsilon^i)], & \varepsilon^i < \varepsilon_a^i, \\ V_b^i(\varepsilon^i) := c_1 + \sigma_a^i \varepsilon^i + \frac{1}{2} k_b^i (\varepsilon^i - \varepsilon_a^i)^2, & \varepsilon_a^i \le \varepsilon^i \le \bar{\varepsilon}_c^i, \\ V_c^i(\varepsilon^i) := c_2 - k_c^i[\varepsilon^i - \varepsilon_*^i + \ln(1-(\varepsilon^i - \varepsilon_*^i))], & \bar{\varepsilon}_c^i < \varepsilon^i, \end{cases} \tag{A.2}$$

$$\sigma^i(\varepsilon^i) = V^{i\prime}(\varepsilon^i) = \begin{cases} k_0^i \frac{\varepsilon^i}{1-\varepsilon^i}, & \varepsilon^i < \varepsilon_a^i, \\ \sigma_a^i + k_b^i(\varepsilon^i - \varepsilon_a^i), & \varepsilon_a^i \le \varepsilon^i \le \bar{\varepsilon}_c^i, \\ \frac{k_c^i(\varepsilon^i - \varepsilon_*^i)}{1-(\varepsilon^i - \varepsilon_*^i)}, & \bar{\varepsilon}_c^i < \varepsilon^i \end{cases} \tag{A.3}$$

where $k_0^i > 0$, $k_b^i < 0$, $k_c^i > 0$, $\varepsilon_a^i > 0$, and $\varepsilon_c^i \ge \varepsilon_a^i$ are constitutive parameters (five independent parameters); the constants $c_1 < 0$ and $c_2 > 0$ are such that $V_a^i(\varepsilon_a^i) = V_b^i(\varepsilon_a^i)$, $V_b^i(\bar{\varepsilon}_c^i) = V_c^i(\bar{\varepsilon}_c^i)$. This results in

$$\varepsilon_*^i = \varepsilon_c^i - \frac{\sigma_a^i}{k_c^i + \sigma_a^i}, \tag{A.4}$$

$$\bar{\varepsilon}_c^i = \frac{\varepsilon_c^i(k_c^i + \sigma_a^i)}{k_c^i + \sigma_c^i} + \frac{(\sigma_c^i - \sigma_a^i)(k_c^i + \varepsilon_c^i k_c^i + \varepsilon_c^i \sigma_a^i)}{(k_c^i + \sigma_a^i)(k_c^i + \sigma_c^i)}, \tag{A.5}$$

with

$$\sigma_a^i = k_0^i \frac{\varepsilon_a^i}{1 - \varepsilon_a^i}, \qquad \sigma_c^i = \sigma_a^i + k_b^i(\bar{\varepsilon}_c^i - \varepsilon_a^i). \tag{A.6}$$

The stress-strain response (A.3) is graphically illustrated in Figure 6.1.

A.2.2 Response at the mesoscopic scale

We study a dynamic switching process at the microscopic scale between the phases (a) and (c) described by branches $0\bar{A}A$ and $\bar{C}C$ in Figure 6.1, respectively. This is in line with the ideas in Refs. [170, 240]. Following [170], we name a response of the material *plastic*, if the strain ε^i of a single spring exceeds the critical value ε_a^i. For a chain of N springs, this can be characterized by the occurrence of loading and unloading stress plateaux. However, we notice that our analysis excludes accumulation of permanent deformation, therefore the end point of one hysteresis cycle coincides with the start point of the next cycle. In this sense, the present hysteresis model is time independent.

Within the current section, we rescale for simplicity L to unity; name (b) the unstable phase described by branch $A\bar{C}$ in Figure 6.1; and regard a mesoscopic element of a CNT array as the limit for $N \to \infty$ of a series of N microscopic springs.

Let us refer to the steady-state dissipation following preconditioning as the "hysteretic shakedown" of the material. We assume that the application of a given number m of hysteretic shakedowns (up to different maximum strains) has severely weakened the stiffness of $(1 - \beta(m))N$ microscopic springs for a given number $0 < \beta(m) \leq 1$,

and that at the current time for all $m \in \mathbb{N}$ it holds

$$
\begin{aligned}
&(A1) \quad k_c^i = k_0^i \quad \text{for all } i \in \mathbb{N} \\
&(A2) \quad k_0^1 = k_0^2 = \ldots = k_0^{\lfloor \beta N \rfloor} = k_0, \qquad k_0^{\lfloor \beta N+1 \rfloor} = \ldots = k_0^N = \delta \\
&(A3) \quad \varepsilon_i^* = \varepsilon_* \quad \text{for } 1 \leq i \leq \beta N \\
&(A4) \quad \varepsilon_a^i = \overline{\varepsilon}_c^i \quad \text{for } \beta N + 1 \leq i \leq N.
\end{aligned}
$$

Condition (A1) stipulates the *symmetry* of the microscopic springs. By (A2), we may differentiate between the springs $1, \ldots, \lfloor \beta N \rfloor$, which we call from now on *undamaged*, and the remaining springs $\lfloor \beta N + 1 \rfloor, \ldots, N$, subsequently named *damaged*. The parameter δ is a small, positive constant and it will become clear later why this parameter has been introduced.

The above model with the assumptions (A1)–(A4) has already been introduced in [164], where also the Γ-limit of the energy has been computed. In this appendix, we extend the analysis and investigate the branch-switching during the minimizing of the total mechanical energy, in particular computing the dissipation of an array with N masses, and perform the dissipation limit when $N \to \infty$.

For the later analysis we also require a certain smallness condition on ε_a^i and $\overline{\varepsilon}_c^i$ relating to strong pinning that disappears in the limit $N \to \infty$ [240].

We define the mechanical energy of the structure as

$$
E_N(u_N) = \frac{1}{N} \sum_{i=1}^{N} V^i(\varepsilon^i(u_N)) \tag{A.8}
$$

with the effective potentials V^i given by (A.2).

Let σ be the given total stress. The mesoscopic average strain is simply

$$
\varepsilon(u_N) := \frac{1}{N} \sum_{i=1}^{N} \varepsilon^i(u_N),
$$

where ε^i is the strain associated with the i-th spring.

We model plasticity by the gradient flow equations [170]

$$\nu\,\dot{\varepsilon}^i(u_N) = -\frac{\partial \Phi_N}{\partial \varepsilon^i}(\varepsilon^1(u_N), \dots, \varepsilon^N(u_N)) \tag{A.9}$$

with the total energy

$$\Phi_N(\varepsilon^1, \dots, \varepsilon^N) := \frac{1}{N}\sum_{i=1}^{N} \left[V^i(\varepsilon^i) - \sigma\varepsilon^i\right].$$

The evolution equation (A.9) lets ε^i evolve towards local minimizers of Φ_N. We are interested in the limit $\nu \to 0$ which amounts to infinitely fast evolution such that $\varepsilon(u_N)$ attains a local minimizer of Φ_N. First we construct the equilibrium points. Inside the i-th spring element, the strain must satisfy the condition $(V^i)'(\varepsilon^i) = \sigma$. For given total stress σ, there are at most the three local minimizers (using (A3))

$$\breve{\varepsilon}^i_a(m) = \frac{\sigma}{k^i_0 + \sigma}, \tag{A.10a}$$

$$\breve{\varepsilon}^i_b(m) = \frac{\sigma - \sigma_a}{k^i_b} + \varepsilon^i_a, \tag{A.10b}$$

$$\breve{\varepsilon}^i_c(m) = \frac{\sigma(1+\varepsilon_*) + k^i_0\varepsilon_*}{k^i_0 + \sigma} = \breve{\varepsilon}^i_a(m) + \varepsilon_*. \tag{A.10c}$$

For the derivation of (A.10), it is necessary that δ be positive.

In a loading or unloading experiment, the first spring located closer to the bottom of the structure is the softest and yields first, changing its phase [72]. Next, the second spring yields, and so forth, until the βN-th spring. (Note that in accordance with (A2), the springs $\beta N + 1, \dots, N$ with zero spring constant do not flip.) Therefore, similar to the case of N identical springs, the total state of the series of springs is still completely specified by two scalar parameters p and q and the additional parameter β. Here, p, q, $1-p-q$ denote the phase fractions of the minimizers a, b, and c, which correspond to having βNp, βNq, and $\beta N(1-p-q)$ springs in phase a, b, and c, respectively. We assumed here that $\beta Np \in \mathbb{N}$.

As $\varepsilon \mapsto V^i(\varepsilon)$ is concave in Regime b for all $i \in \mathbb{N}$, if the elongation of a spring

in the local minimum $\breve{\varepsilon}_b^i$ is altered by an arbitrarily small perturbation, it will move (according to the sign of the perturbation) to either $\breve{\varepsilon}_a^i$ or $\breve{\varepsilon}_c^i$. In consequence, any system of N springs with $q \neq 0$ is unstable and we can restrict our study to the case $q = 0$.

The average strain of a system with βN springs in equilibrium and the first $\beta N p$ springs in phase a fulfills the identity

$$\begin{aligned}\varepsilon(m) &= \frac{1}{N}\left[\sum_{i=1}^{\beta N p}\breve{\varepsilon}_a^i(m) + \sum_{i=\beta N p+1}^{\beta N}\breve{\varepsilon}_c^i(m) + \sum_{i=\beta N+1}^{N}\frac{\sigma}{k_0^i+\sigma}\right] \\ &= \frac{1}{N}\sum_{i=1}^{\beta N}\breve{\varepsilon}_a^i(m) + \frac{1}{N}\sum_{i=\beta N p+1}^{\beta N}\varepsilon_* + \frac{1}{N}\sum_{i=\beta N+1}^{N}\frac{\sigma}{\delta+\sigma}.\end{aligned}$$

Let us restrict to the limiting case $\delta \searrow 0$ where there is no small contribution by the damaged springs. In this case, we obtain

$$\begin{aligned}\varepsilon(m) &= \frac{\beta\sigma(m)}{k_0+\sigma(m)} + (1-\beta) + \beta(1-p)\varepsilon_* \\ &= \frac{\sigma(m) + (1-\beta)k_0}{k_0+\sigma(m)} + \beta(1-p)\varepsilon_*, \end{aligned} \tag{A.11}$$

where we used (A1)–(A4), (A.3), and (A.10); especially $\breve{\varepsilon}_c^i = \breve{\varepsilon}_a^i + \varepsilon_*$.

Resolving (A.11), we obtain the stress-strain relationship for a system with N springs

$$\sigma(\varepsilon, m) = \frac{k_0(\varepsilon - \varepsilon_p + \beta - 1)}{1 - (\varepsilon - \varepsilon_p)} \tag{A.12}$$

with

$$\varepsilon_p(m) := \beta(1-p)\varepsilon_*.$$

This quantity can in a natural way be identified with the plastic strain. From (A.12) we see that σ only depends on m and on the elastic strain $\varepsilon_{\mathrm{el}} := \varepsilon - \varepsilon_p$.

For the energy of the equilibrium configuration with the first Np springs in phase

a we find

$$\begin{aligned}\widehat{E}_p(\varepsilon,m) &= \frac{1}{N}\left[\sum_{i=1}^{\beta Np} V^i(\breve{\varepsilon}_a^i(m)) + \sum_{i=\beta Np+1}^{\beta N} V^i(\breve{\varepsilon}_c^i(m))\right] \\ &= \frac{1}{N}\sum_{i=1}^{\beta N}(-k_0^i)\Big[\frac{\sigma(\varepsilon,m)}{k_0^i+\sigma(\varepsilon,m)} + \ln\Big(\frac{k_0^i}{k_0^i+\sigma(\varepsilon,m)}\Big)\Big] + (1-p)c_2.\end{aligned}$$

Since

$$\frac{\sigma(\varepsilon,m)}{k_0+\sigma(\varepsilon,m)} = \frac{\varepsilon-\varepsilon_p(m)+\beta-1}{\beta}, \qquad \frac{k_0}{k_0+\sigma(\varepsilon,m)} = \frac{1-(\varepsilon-\varepsilon_p(m))}{\beta},$$

we end up with

$$\begin{aligned}\widehat{E}_p(\varepsilon,m) = (-k_0)\Big[\varepsilon-\beta(1-p)\varepsilon_* + \beta - 1 + \beta\ln\Big(\frac{1-(\varepsilon-\varepsilon_p(m))}{\beta}\Big)\Big] \\ + \beta(1-p)c_2.\end{aligned}$$

By straightforward computations, we find for the derivative

$$\frac{\partial\widehat{E}_p(\varepsilon,m)}{\partial\varepsilon} = (k_0)\frac{\varepsilon-\varepsilon_p(m)+\beta-1}{1-(\varepsilon-\varepsilon_p(m))}.$$

For fixed m, the functionals $\widehat{E}_p$ constitute a family of convex functionals with a finite number of local minimizers (depending on the parameter p). The switching takes place between branches that differ in exactly one element in the phase state and the succession of N such steps describes the transition from one homogeneous state to the next. Each of these steps can be thought of as the combination of an elastic part and a plastic part.

The stress-strain curve of the structure follows a sawtooth pattern as illustrated in Figure A.1 [164]. The symbols P^i denote the final states of the *elastic steps* ($Q^i \to P^{i+1}$) where the system remains on the same metastable branch as long as possible. The *plastic steps* ($P^i \to Q^i$) are characterized by the fact that the total strain is fixed and the system switches between metastable branches that are neighbors

($[Np] = 1$, and $[(\cdot)]$ generically denotes the jump of a quantity $(\cdot)$). It is worth observing that stress is zero for $\varepsilon \leq 1-\beta$, and that, conversely, the system is able to bear stresses $\sigma > 0$ for $\varepsilon > 1-\beta$, even in presence of $(1-\beta)N$ springs with stiffness k_0^i tending to zero. This is possible because the local strain ε^i in such springs tends to unity as the corresponding stiffness tends to zero.

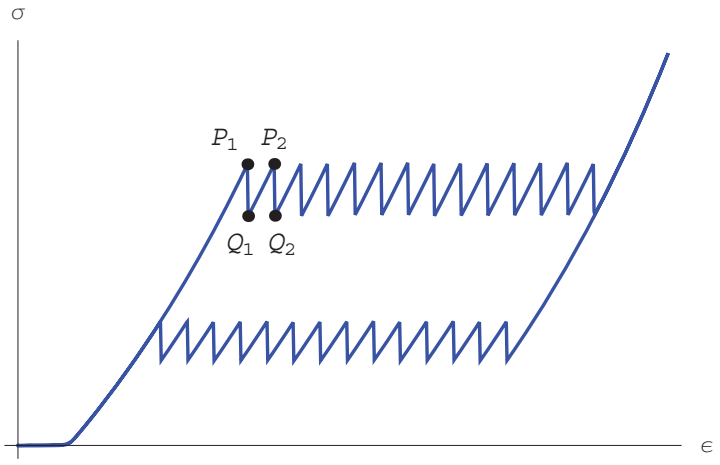

Figure A.1: Overall stress-strain pattern of a finite series of microscopic springs

For the next step of the analysis, additional to (A1)–(A4), we assume

$$(A5) \quad \varepsilon_a^i \equiv \varepsilon_a,\ \varepsilon_c^i \equiv \varepsilon_c \quad \text{for all } i \in \mathbb{N}. \tag{A.13}$$

The above considerations then lead for $1 \leq i \leq N$ to the representation

$$P^i = \Big(\varepsilon_{P_i}, \frac{k_0(\varepsilon_a+\beta-1)}{1-\varepsilon_a}\Big), \quad Q^i = \Big(\varepsilon_{P_i}, \frac{k_0(\varepsilon_a-\beta\varepsilon_*/N+\beta-1)}{1-\varepsilon_a+\beta\varepsilon_*/N}\Big)$$

in the (ε, σ)-diagram, where

$$\varepsilon_{P_i} := \varepsilon_a + \frac{i-1}{N}\beta\varepsilon_*. \tag{A.14}$$

So we can compute that a plastic step is characterized by

$$[\varepsilon] = 0, \quad [Np] = 1, \quad [\sigma] = -(\beta^2 k_0)\frac{\varepsilon_*}{N(1-\varepsilon_a)(1-\varepsilon_a+\beta\varepsilon_*/N)},$$

whereas an elastic step fulfills

$$[\varepsilon] = \beta\frac{\varepsilon_*}{N}, \quad [Np] = 0, \quad [\sigma] = (\beta^2 k_0)\frac{\varepsilon_*}{N(1-\varepsilon_a)(1-\varepsilon_a+\beta\varepsilon_*/N)}.$$

The evolution equation (A.9) lets ε^i evolve towards local minimizers of Φ_N.

Now we want to look at the energetics of the plastic and the elastic regime. For an elastic step we have the energy difference

$$\begin{aligned}\Delta\widehat{E}_N = \beta k_0\Big[&\ln\big(1-\varepsilon_a+\beta\varepsilon_*(1-N)/N\big)\\ &-\ln\big(1-\varepsilon_a+\beta\varepsilon_*(2-N)/N\big)\Big] + \frac{k_0\beta}{N}\varepsilon_*.\end{aligned} \tag{A.15}$$

In the same spirit, we calculate that for a system with $N \geq 1$ springs, the plastic dissipation is

$$\begin{aligned}D_N &= \beta k_0\Big[\ln\big(1-\varepsilon_a+\beta\varepsilon_*(2-N)/N\big)\\ &\qquad -\ln\big(1-\varepsilon_a+\beta\varepsilon_*(1-N)/N\big)\Big] - \frac{\beta(c_2+k_0\varepsilon_*)}{N}\\ &= \beta k_0\frac{1}{\xi_N}\frac{\beta\varepsilon_*}{N} - \frac{\beta(c_2+k_0\varepsilon_*)}{N}\end{aligned} \tag{A.16}$$

for a parameter

$$\xi_N \in \Big(1-\varepsilon_a+\frac{1-N}{N}\beta\varepsilon_*, 1-\varepsilon_a+\frac{2-N}{N}\beta\varepsilon_*\Big).$$

Clearly, $\xi_N \to 1-\varepsilon_a-\beta\varepsilon_*$ for $N\to\infty$.

In one hysteresis cycle, there are βN steps where the stress is increased and βN steps where the material yields. So, overall, $2\beta N$ steps dissipate energy. The total dissipated energy D in a cycle becomes in the limit $N\to\infty$

$$D = \lim_{N\to\infty}\big(2\beta N D_N\big) = 2\beta^2\Big(\frac{\beta k_0\varepsilon_*}{1-\varepsilon_a-\beta\varepsilon_*} - c_2 - k_0\varepsilon_*\Big). \tag{A.17}$$

The limit stress-stain pattern for $N\to\infty$ is shown in Figure 6.6 for different values of the parameter β. It corresponds to a "perfectly plastic" behavior with stress plateaux at $\sigma=\sigma_a$ (loading plateau) and $\sigma=\sigma_c=\sigma_a+\Delta\sigma$ (unloading plateau) [164].

We emphasize again that this ansatz only works for rate-independent plasticity where the energy only depends on start point and end point of the evolution, but not on the evolution path itself. The limit dissipation (A.17) equals the area enclosed by the limit stress-strain response. As already observed, the behavior shown in Figure 6.6 refers to a mesoscopic spring element, which represents a finite portion of the array thickness. It is worth observing that equation (A.12) is still valid in the limit $N \to \infty$, with $\varepsilon_p = \beta\varepsilon_*$. This implies that the stress is zero for $\varepsilon \leq 1-\beta$ in the limiting behavior. We can therefore refer to the quantity $1-\beta$ as the "activation strain" of the mesoscopic response (or "damage" parameter). Conversely, the quantity β can be regarded as an "integrity" parameter of the material at the mesoscopic scale.

A.2.3 Macroscopic response

We model the macroscopic mechanical response of a CNT array through an information-passing approach, adopting a mass-spring chain composed of a finite number of mesoscopic springs, and a suitable modification of the analytical model derived in the previous section for each spring.

We already noted that the assumption (A1) introduced in Section A.2.2 implies that the phases (a) and (b) of the microscopic response (Figure 6.1) are "symmetric", while Assumptions (A2)–(A3) imply that the microscopic springs have uniform mechanical properties.

It is known, however, that real CNT foams exhibit a gradient in density along the height of the tubes, which typically increases from the base to the top (e.g., [120, 155]); and Mullins-like behavior characterized by different stiffness during loading and unloading [114]. In particular, the density gradient typically induces bottom-to-top increasing local buckling loads and progressive tube collapse starting from the bottom [117, 120]. We show in Figure A.2 the overall stress-strain response that we numerically determined for chains showing 9 undamaged and 1 damaged springs, and, alternatively, constant material properties ("p.plastic" response), or linearly increasing buckling loads along the thickness ("hardening" response). It is seen that the

"hardening" response actually features a sawtooth stress-strain diagram characterized by a progressive increase of the stress σ during the plastic steps, while the "p.plastic" response features a sawtooth stress-strain diagram showing constant average stress (see the previous section about the second behavior).

In order to account for graded material properties and different stiffness during loading and unloading, we slightly modify the limiting mesoscopic behavior illustrated in Figure 6.6, describing the generic mesoscopic spring (say, the i-th one) through the following constitutive equation (Figure 6.7)

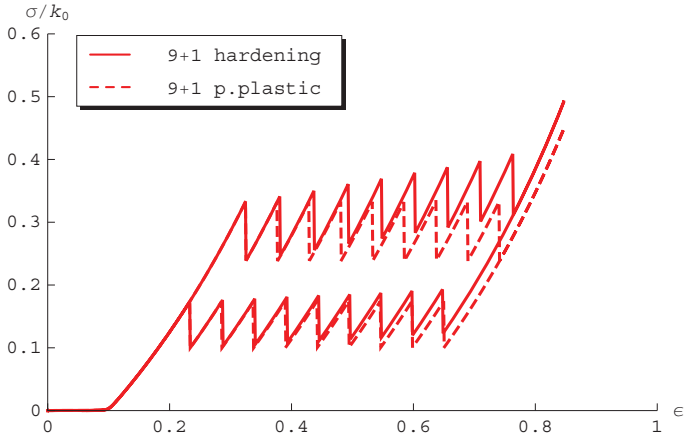

Figure A.2: Overall stress-strain pattern of chains showing 9 undamaged and 1 damaged springs ($\beta = 0.9$). The "p.plastic" response refers to constant ε_a (i.e., constant buckling load, see Figure 6.1) in each spring, while the "hardening" response refers to ε_a linearly varying along the thickness of the chain. Chosen spring constants: $k_0 = k_c = 50.00 \times 10^6$ Pa; $k_b = -22.44 \times 10^6$ Pa; $\varepsilon_a = \text{const} = 0.25$ in the "p.plastic" chain; ε_a varying from 0.25 to 0.29 (step 0.05) in the "hardening" chain; $\varepsilon_* = 0.52$; $\delta = 50.00 \times 10^2$ Pa

$$\sigma^i = \begin{cases} 0, \quad \text{for } \varepsilon^i \leq (1-\beta^i); \\ \\ \sigma^{(a,i)} \;=\; k_0^i\ (\varepsilon_i - (1-\beta^i))/(1-\varepsilon^i), \\ \text{for } ((1-\beta^i) < \varepsilon^i < \bar{\varepsilon}_a^i) \text{ or} \\ ((\bar{\varepsilon}_a^i < \varepsilon^i < \varepsilon_\beta^i) \text{ and } (\text{flag}^{(k-1)} \neq c)); \\ \\ \sigma^{(c,i)} \;=\; k_c^i\ (\varepsilon^i - (1-\beta^i) - \beta^i\varepsilon_*^i)/(1-(\varepsilon^i - \beta^i\varepsilon_*^i)), \\ \text{for } (\varepsilon^i > \varepsilon_c^i) \text{ or} \\ ((\bar{\varepsilon}_c^i < \varepsilon^i < \varepsilon_c^i) \text{ and } (\text{flag}^{(k-1)} \neq a)); \\ \\ \sigma^{(d,i)} \;=\; \sigma_a^i \;+\; k_{p+}^i(\varepsilon^i - \varepsilon_a^i), \\ \text{for } (\varepsilon_a^i \leq \varepsilon^i \leq \varepsilon_c^i) \text{ and } (\text{flag}^{(k-1)} = a); \\ \\ \sigma^{(e,i)} \;=\; \bar{\sigma}_c^i \;+\; k_{p-}^i(\varepsilon^i - \bar{\varepsilon}_c^i), \\ \text{for } (\bar{\varepsilon}_a^i \leq \varepsilon^i \leq \bar{\varepsilon}_c^i) \text{ and } (\text{flag}^{(k-1)} = c); \end{cases} \tag{A.18}$$

where, at the generic step k of a quasistatic loading process, it results

$$\text{flag}^{(k)} = a \quad \text{if } \sigma^i = \sigma^{(a,i)}; \text{flag}^{(k)} = c, \text{ if } \sigma^i = \sigma^{(c,i)}; \text{ flag}^{(k)} = \text{flag}^{(k-1)} \text{ otherwise.}$$

The stress-strain equation (A.18) can be characterized in terms of the independent parameters β^i, k_0^i, k_c^i, k_{p+}^i, k_{p-}^i, ε_i^a, ε_c^i, and $\Delta\sigma^i = \sigma_a^i - \bar{\sigma}_c^i$. The quantities k_0^i and k_c^i represent the slopes of the branches (a) and (c) at zero stress, respectively (Figure 6.7). The quantities k_{p+}^i and k_{p-}^i instead denote the slopes of the "plastic" transition branches (d) and (e), respectively. As already discussed, we allow for nonzero stiffness of such branches in order to account for graded mechanical properties of the foam at the microscopic scale. Let (a') denote the particularization of branch (a) for $\beta^i = 1$ (Figure 6.7), and set $\sigma^{(a',i)} = k_0^i\varepsilon^i/(1-\varepsilon^i)$. The parameters ε_a^i and ε_c^i represent the transition strains from phase (a') to phase (d) and from phase (d) to

phase (c), respectively. Finally, $\beta^i \in (0,1]$ represents the integrity parameter of the current spring; the quantity $1-\beta^i \in [0,1)$ denotes the activation strain (or damage parameter), while $\Delta\sigma^i$ represents the stress drop moving from point A to point $\bar{C}$ (Figure 6.7).

The remaining quantities appearing in (A.18) can easily be derived from the above independent parameters. In particular, one computes ε^i_β, ε^i_*, $\bar{\varepsilon}^i_c$, and $\bar{\varepsilon}^i_a$ by solving the equations

$$\begin{aligned}
\sigma^{(a,i)}(\varepsilon^i = \varepsilon^i_\beta) &= \sigma^{(d,i)}(\varepsilon^i = \varepsilon^i_\beta),\\
\sigma^{(a,i)}(\varepsilon^i = \varepsilon^i_a) &= \sigma^{(c,i)}(\varepsilon^i = \varepsilon^i_a),\\
\sigma^{(c,i)}(\varepsilon^i = \bar{\varepsilon}^i_c) &= \sigma^{(e,i)}(\varepsilon^i = \bar{\varepsilon}^i_c),\\
\sigma^{(e,i)}(\varepsilon^i = \bar{\varepsilon}^i_a) &= \sigma^{(a,i)}(\varepsilon^i = \bar{\varepsilon}^i_a)
\end{aligned}$$

for such variables, respectively. It can be seen from Figure 6.7 that the "damaged" stress-strain response ($\beta < 1$) returns to the primary loading path (a')–(d) for $\varepsilon \geq \varepsilon^i_\beta$.

From now on, we use the symbol N to denote the number of mesoscopic springs that form the macroscopic mass-spring model. At a given loading step k (that is, for a given prescribed displacement $\bar{u}_k$ of the topmost mass), we compute the corresponding (macroscopic) equilibrium configuration of the system through a dynamic relaxation procedure. The latter is founded upon the integration with respect to a virtual (or "internal") time t of the following equations of motion

$$m^i\ \ddot{\hat{u}}^i_N \ + \ \gamma^i\ \dot{\hat{u}}^i_N \ = \ \sigma^{i+1} \ - \ \sigma^i, \quad i = 1, \ldots, N, \tag{A.19}$$

under the initial boundary conditions

$$\hat{u}^i_N(t=0) \ = \ (u^i_N)^{(k-1)}, \quad i = 0, \ldots, N-1; \quad \hat{u}^N_N(t=0) \ = \ \bar{u}_k;$$

$$\dot{\hat{u}}^i_N(t=0) \ = \ 0, \quad i = 0, \ldots, N. \tag{A.20}$$

Here, $\hat{u}_N^i = \hat{u}_N^i(t)$ denote transient displacement histories of the masses $m^0, \ldots, m^N$ forming the macroscopic model; a superimposed dot denotes a derivative with respect to t; and, $\gamma^1, \ldots, \gamma^N$ denote the ("critical") damping coefficients

$$\gamma^i \;=\; 2\,\sqrt{m^i\;k^i},$$

where $k^i = d\sigma^i/d\varepsilon^i$ indicates the stiffness of the i-th spring at the beginning of the current loading step. Equations (A.19) are numerically integrated through a fourth-order Runge-Kutta integration scheme, up to an internal time t_1 such that it results ([71])

$$|\sigma^{i+1} - \sigma^i| \leq 10^{-6}|\sigma^N| \quad \text{for all } i \in \{1, \ldots, N-1\}.$$

A.3 Applications

We illustrate the macroscopic model formulated in the previous section by applying it to the simulation of the cyclic compression experiment illustrated in Figure 2.4. Such an experiment was performed on a single-layer CNT array with 0.847 mm thickness, which was synthesized using a vapor phase (or "floating catalyst") thermal chemical vapor deposition (CVD) system, as described elsewhere [26, 40]. Following past work, the composition of the flow gas used during synthesis has a large effect on the resulting structure and mechanical response of the CNT arrays [40]. An inert gas such as argon is typically used during CVD synthesis of CNTs, with a reducing agent such as hydrogen sometimes included to prevent impurities. It has been observed that increasing the H_2/Ar ratio can result in CNTs of narrower diameters and CNT arrays with a much more compliant response [40]. The compression test in Figure 2.4 was performed on a sample synthesized in 50% Ar, 50% H_2, with CNTs of diameter $\sim$ 18 nm. The compression tests were performed quasistatically at strain rates of $\dot{\epsilon} = 0.03s^{-1}$ using a commercial materials testing system (Instron E3000). The sample was compressed three times to a maximum overall strain of $\epsilon = 0.4$ and then three times to a maximum strain of $\epsilon = 0.8$.

We focus our attention on the first loading-unloading path to $\varepsilon = 0.4$ (1st cycle to 0.4 in Figure 2.4, hereafter also denoted as *np*), and the first loading-unloading path to $\varepsilon = 0.8$, which follows preconditioning at $\varepsilon = 0.4$ (1st cycle to 0.8 in Figure 2.4, hereafter also denoted as *wp*). We fit the mechanical properties of single-spring and multispring models to the experimental stress-strain curves, making use of the Genetic Algorithm procedure illustrated in Ref. [71], and the following normalized root-mean-square deviation (NRMSD)

$$f = \frac{\sqrt{\frac{\sum_{k=1}^{N_{\text{data}}} (\sigma_k^{\text{mod}} - \sigma_k^{\text{exp}})^2}{N_{\text{data}}}}}{(\sigma_{\text{max}}^{\text{exp}} - \sigma_{\text{min}}^{\text{exp}})} \tag{A.21}$$

as fitting performance. In (A.21), N_{data} denotes the number of experimental data points, σ_k^{exp} the experimental value of the stress in correspondence with the loading step $\varepsilon = \varepsilon_k$, and σ_k^{mod} denotes the predicted stress for $\varepsilon = \varepsilon_k$.

In Figures A.3 and A.4, comparisons between experimental and best-fit overall stress-strain curves are shown, while the best-fit values of the mechanical properties of the fitting models are provided in Tables A.1 and A.2, together with the corresponding fitting performances.

We obtain rather good fitting performances already through single-spring models (NRMSD equal to 4.3% and 4.8% for the cases *np* and *wp*, respectively). In such a case, the behavior after preconditioning (*wp* model) corresponds to $\beta = 0.83$ (Table A.1), which implies an activation strain $\varepsilon = 0.17$ (Figure A.3). Snapshots of the deformation history of the single spring *np* and *wp* models are illustrated in Figure A.5. One can easily recognize that the first loaded ($\sigma > 0$) equilibrium configuration of the *wp* model (first configuration in Figure A.3,*wp*) features total height $h_{\text{wp}} = 0.83 h_{\text{np}}$, where h_{np} denotes the undeformed height of the *np* model.

Appreciable improvements of the fitting performance are observed in the five-spring models, which indeed show NRMSD equal to 3.2% and 4.4% in the *np* and *wp* cases, respectively (see Figure A.4 and Table A.2). The fitting algorithm adopted for such a model includes a grading-constraint which requires that the springs placed at the bottom of the chain collapse before those placed at the top (we number the

springs progressively from bottom to top, see Section A.2.1). This choice is based on the physical gradients that are known to exist in these materials (see below). It is worth noting that the examined models feature uniform stiffness parameters $k_0 = 4.27$ MPa and $k_c = 15.7k_0$ in each spring (Table A.2). The results shown in Table A.2 and Figure A.6 highlight that the five-spring model localizes in the bottom-most spring ($\#1 - wp$) all the preconditioning damage corresponding to the wp case. Such a spring exhibits a local activation strain $\varepsilon^1 = 0.90$ (the corresponding integrity parameter β^1 is indeed 0.10, see Table A.2), while the overall activation strain is approximatively 0.17 (Figure A.4). The bottom-top collapse mechanisms of the five-spring models (Figure A.6) follow from the increasing values of the transition strains ε_a^i of the different springs (Table A.2). In particular, Figure A.6 shows that the five-spring np model features sequential collapse of the springs #1, #2, #3, and #4 (Figure A.6). The topmost spring #5 np instead jumps from phase (a) to phase (c) without collapsing (see Table A.2 and Figure A.6). On the other hand, the five-spring wp model first features the complete collapse of the pre-damaged spring #1 (configuration #2 in Figure A.6, wp), and next the sequential collapse of springs #2, #3, and #4 (cf. configuration #3 to #5 in Figure A.6, wp). As in the np case, spring #5 jumps from phase (a) to phase (c) without collapsing (Table A.2 and Figure A.6).

This matches previous work with real CNT foams in which the same sequential buckling from the base upward is observed. Clear images of this phenomenon can be observed in Ref. [120], closely matched by the configuration of springs seen in Figure A.6. Physically, this strain localization arises due to known gradients in certain physical properties along the height of the structures, such as in density [155] and CNT diameter [38]. Because of the lateral interactions of CNTs, this localized strain is accommodated by the formation of buckles, which result from the reorientation and collective buckling of CNTs [156]. Additionally, these physical gradients are sufficiently large—and therefore the mechanical properties vary significantly as a function of height—that while a buckle is in the process of forming at the base of the structure the rest of the structure remains undeformed. Thus the strain localization observed

in Figure A.6 is in agreement with experimental observations.

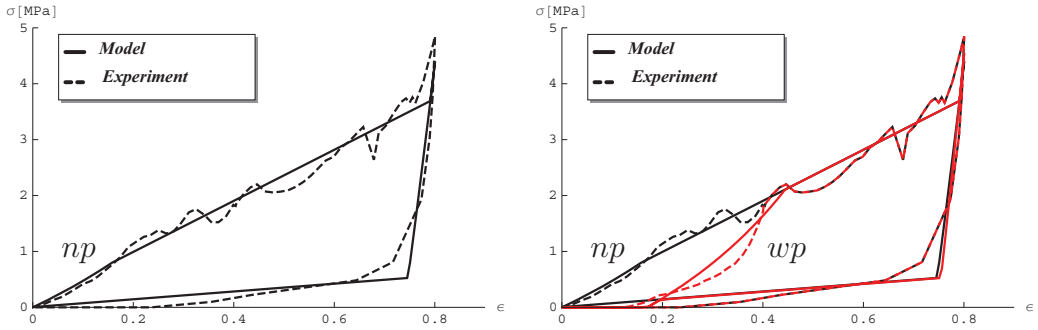

Figure A.3: Fitting of the experimental response illustrated in Figure 2.4 to single-spring models, without preconditioning (*np*: black curves), and with preconditioning at $\varepsilon = 0.4$ (*wp*: red curves); spring properties in Table A.1

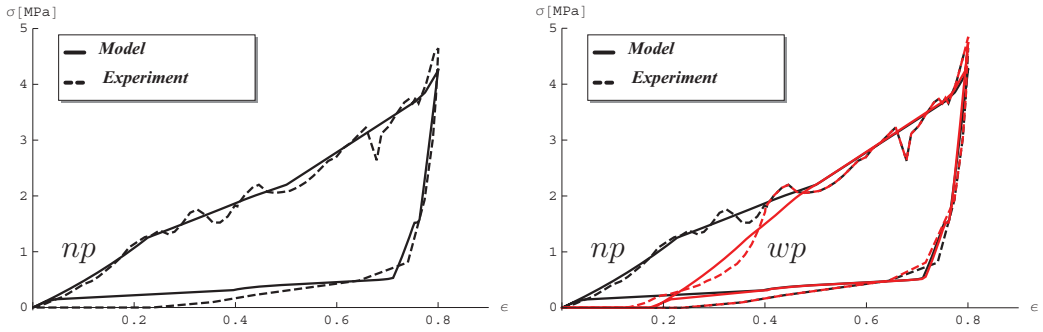

Figure A.4: Fitting of the experimental response illustrated in Figure 2.4 to five-spring models, without preconditioning (*np*: black curves), and with preconditioning at $\varepsilon = 0.4$ (*wp*: red curves); spring properties in Table A.2

A.4 Concluding remarks

We proposed a bistable-spring ansatz capable of incorporating the effect of damage in plastically deformed materials. In comparison to the model recently introduced in [71], we added a hysteresis dependence and allowed for the possible failure of material bondings, represented by the weakening of certain springs in the one-dimensional network. We have demonstrated that this new ansatz is capable

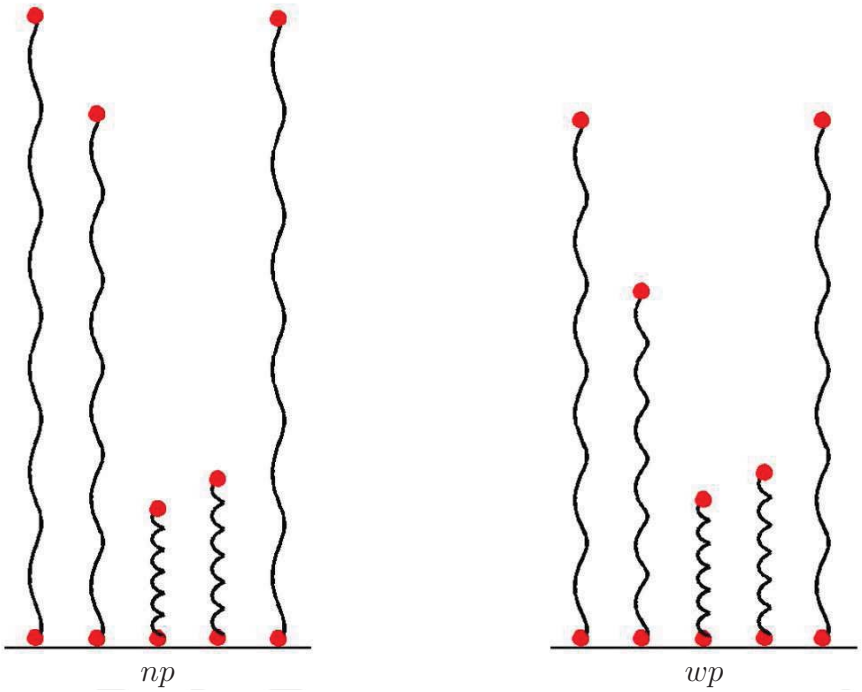

Figure A.5: Snapshots of the deformation histories of the single-spring models; spring properties in Table A.1

spring #	β	k_0 [MPa]	$\Delta\sigma/\sigma_a$	ε_a	ε_c	k_{p+}/k_0	k_{p-}/k_0	k_c/k_0	f
$1-np$	1.000	4.270	-0.338	0.157	0.791	1.069	0.159	15.700	0.043
$1-wp$	0.830	4.270	-0.338	0.157	0.791	1.069	0.159	15.700	0.048

Table A.1: Mechanical properties of single-spring models fitting results in Figure 2.4, without preconditioning (np) and with preconditioning (wp) at $\varepsilon = 0.4$

of handling preconditioning-induced material damage, characterized by a non-zero activation strain, permanent deformation, and a reduction in the energy dissipation capacity. The change in the permanent deformation goes along with a change of the activation strain. As a benefit, we are now in the position to extend the concept of "transformational plasticity" given in Ref. [170] from time-independent hysteretic behavior to fatigue-type material damage. This opens a large class of new applications, in particular those materials with Mullins-like behavior [162] that include, besides carbon nanotube arrays, rubber-like and soft biological materials.

The bistable springs model presented here is an interesting generalization of the fundamental mechanism developed in [170]. In contrast to the theory presented

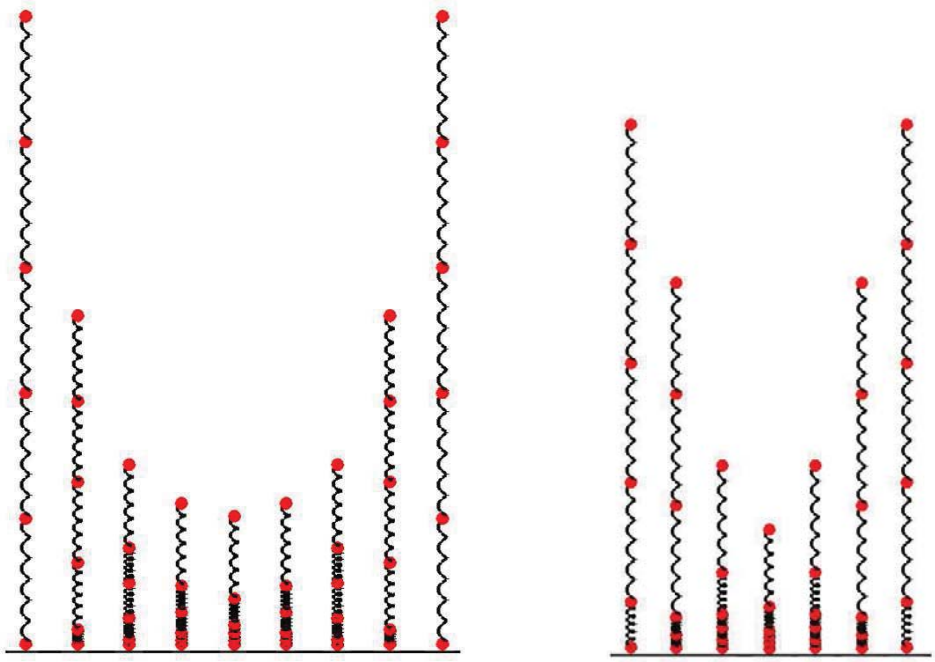

Figure A.6: Snapshots of the deformation histories of the five-spring models; spring properties in Table A.2

therein, due to considering nonlinear kinematics, we can derive a stress-strain law of the stable branches (a) and (c), permitting us to have in the limit $\delta \searrow 0$ springs with zero stiffness bearing non-zero stresses. The internal damage parameter is related to the number of hysteretic shakedowns applied to the material during the previous loading history (up to different maximum strains). As a result, we obtain a fatigue-type damage model that is rate-independent and contemplates the return of the material to the primary loading path for a suitable value of the overall strain, which is suitably larger than the activation strain.

The macroscopic model formulated in Section A.2.3 allowed us to generalize the analytic mesoscopic model developed in Section A.2.2, in order to account for graded material properties along the height of the structure [120, 155]. The numerical simulation of a compression experiment on a real CNT foam has shown that such a model is actually able to capture the experimental macroscopic stress-strain behavior, before and after preconditioning; damage localization at the basis of the structure; and se-

spring #	β	k_0 [MPa]	$\Delta\sigma/\sigma_a$	ε_a	ε_c	k_{p+}/k_0	k_{p-}/k_0	k_c/k_0	f
$5-np$	1.000	4.270	-0.228	0.317	0.317	0.851	0.046	15.700	
$4-np$	1.000	4.270	-0.737	0.317	0.788	0.851	0.046	15.700	
$3-np$	1.000	4.270	-0.749	0.317	0.939	0.851	0.046	15.700	
$2-np$	1.000	4.270	-0.749	0.227	0.942	0.851	0.046	15.700	
$1-np$	1.000	4.270	-0.749	0.227	0.942	0.310	0.046	15.700	0.031
$5-wp$	1.000	4.270	-0.228	0.317	0.317	0.851	0.046	15.700	
$4-wp$	1.000	4.270	-0.737	0.317	0.788	0.851	0.046	15.700	
$3-wp$	1.000	4.270	-0.749	0.317	0.939	0.851	0.046	15.700	
$2-wp$	1.000	4.270	-0.749	0.227	0.941	0.851	0.046	15.700	
$1-wp$	0.100	4.270	-0.749	0.227	0.941	0.310	0.046	15.700	0.044

Table A.2: Mechanical properties of five-spring models fitting results in Figure 2.4, without preconditioning (np) and with preconditioning at $\varepsilon = 0.4$ (wp)

quential buckling from the base upward. These phenomena are well recognized in the literature dealing with the experimental behavior of CNT foams [38, 120, 155, 156].

We leave to future work the modeling of the transient mechanical response of CNT structures during preconditioning, accounting for progressive deterioration of the material stiffness at different scales, and the time-dependent response. Future research lines also include an analytic study on the limiting dissipative behavior of bistable spring chains featuring nonuniform material properties; the modeling of the mechanical response of multilayer CNT structures; and the *in situ* identification of material properties, to be carried out through high-resolution camera- and/or SEM-assisted laboratory tests [72, 120].

Acknowledgments

The authors gratefully acknowledge the support received by Ada Amendola (Department of Civil Engineering, University of Salerno) during the course of the present work. FF acknowledges the support of the Italian Network of Seismic Engineering Laboratories (ReLUIS) and the Italian Civil Protection Department (DPC), through the ReLUIS-DPC grant 2010/2013. TB acknowledges the support of the German Research Community (DFG) through grant BL 512 4/1. JRR gratefully acknowledges the U.S. Department of Defense and the Army Research Office for their support via a National Defense Science & Engineering Graduate (NDSEG) Fellowship.

CD acknowledges support from the Institute for Collaborative Biotechnologies under contract W911NF-09-D-0001 with the Army Research Office.